The Removal of Inorganic Contaminants Using Nanofiltration and Reverse Osmosis

Laura Ann Richards

Submitted for the degree of Doctor of Philosophy

Heriot-Watt University

School of Engineering and Physical Sciences

Department of Mechanical Engineering

Edinburgh, United Kingdom

April 2012

Abstract

Improved methods of providing safe drinking water are essential in an era in which demand for water is increasing but surface water supplies remain scarce. Desalination of brackish groundwater via membrane filtration with nanofiltration and reverse osmosis (NF/RO) offers a solution to this problem. As such, the overall motivation of this study was to improve mechanistic understanding of NF/RO. The first main aim was to evaluate the performance of a renewable energy membrane system previously tested with real groundwater and varying energy conditions. Given sufficient solar availability, the system reliably removed salts and inorganic contaminants, although solute retention varied with energy (and consequently pressure and flow) and pH, depending on dominant retention mechanisms. The second main aim was to assess the specific impact of pH on inorganic contaminant removal in a bench-scale filtration system. The speciation of boron, fluoride and nitrate was linked with ion retention as a function of pH, with results suggesting that there may be important mechanisms such as ion dehydration controlling transport in NF/RO, which would explain the high retention of fluoride when compared to nitrate. The third main aim was to determine the importance of ion hydration in determining transport using molecular dynamics simulations of monovalent anions transporting through an idealized pore. Simulations demonstrated that energy barriers of transport were strongly dependent on ion properties and pore size and were directly attributable to dehydration. The final aim was to experimentally verify molecular dynamics simulations by quantifying energy barriers for ion transport in NF membranes. Experimentally-determined energy barriers were also solute and membrane-specific, with fluoride having a higher barrier than other solutes. Comparison of results with expected dehydration trends and molecular dynamics corroborated that energy barriers in nanofiltration may be due to dehydration. The results obtained in this thesis provide new insight into NF/RO transport mechanisms, which may contribute to improvements in current technologies and predictive models.

For those that believed, especially when I did not.

Acknowledgements

This PhD has been an opportunity and adventure for me, having led me to learn immensely, experience living in different countries, work with a diverse group of people and pursue my career goals. Thank you to my PhD supervisors, Profs. Andrea Schäfer and Bryce Richards, for making this possible. Your vision, guidance, knowledge, time and input have each contributed to me acquiring the skills necessary to make this PhD a success. In addition to scientific input, I appreciate you pointing me towards non-research opportunities, such as Oxford Leadership Academy and Landmark Forum. The journey has been difficult, humbling and empowering, and as a result, I have grown professionally and personally. Thank you for constantly challenging me; I am now better equipped to meet future challenges and open future doors. I hope to pass on some of what I have learned from you to other journeyers.

As part of my PhD I was fortunate enough to visit the University of Western Australia for four months. This was a very positive experience for me and I attribute much of the success of this PhD to that visit. A/Prof. Ben Corry is an inspiration for me. Thank you, Ben, for your patience and for welcoming me to the world of molecular dynamics.

Thanks to my fellow students, past and present, for the endless support and laughs over the last few years. It has been an adventure! A special thanks to Gavin Park – I cannot imagine a better friend and colleague with whom to have started (and ended!) this journey. Ime Akanyeti, Dave Ross, Dr. Andrea Semião, Helfrid Schulte-Herbrüggen, Annalisa De Munari, Helen Cope, Dr. Laura Banasiak, Dr. Peta Neale, Dalila Capão, Payam Malek and Than Hieu Ngo: much gratitude for your smiles and support! Thanks also to Dr. Michael Thomas, Evelyne Deplazes and Sasha Nemkevich (University of Western Australia) for welcoming me into their research group in Perth. To Berkley, Bren, Suz, Gudrun and Curtis: my sincerest thanks for your friendship and perspective.

I have had fruitful discussions with a number of other people at various stages of my PhD. My PhD examiners Prof. Anthony Szymczyk (Université de Rennes) and Prof. Raffaella Ocone (Heriot-Watt University) provided very valuable feedback on my work and I am grateful for their time and input. Thank you to Prof. Nico van der Vegt

ACADEMIC REGISTRY
Research Thesis Submission

Name*:*	Laura Ann Richards		
School/PGI:	School of Engineering and Physical Science		
Version: *(i.e. First, Resubmission, Final)*	Final	Degree Sought (Award **and** Subject area)	PhD, Mechanical Engineering

Declaration

In accordance with the appropriate regulations I hereby submit my thesis and I declare that:

1) the thesis embodies the results of my own work and has been composed by myself
2) where appropriate, I have made acknowledgement of the work of others and have made reference to work carried out in collaboration with other persons
3) the thesis is the correct version of the thesis for submission and is the same version as any electronic versions submitted*.
4) my thesis for the award referred to, deposited in the Heriot-Watt University Library, should be made available for loan or photocopying and be available via the Institutional Repository, subject to such conditions as the Librarian may require
5) I understand that as a student of the University I am required to abide by the Regulations of the University and to conform to its discipline.

* *Please note that it is the responsibility of the candidate to ensure that the correct version of the thesis is submitted.*

Signature of Candidate*:*		Date:	

Submission

Submitted By *(name in capitals):*	LAURA ANN RICHARDS
Signature of Individual Submitting:	
Date Submitted:	

For Completion in the Student Service Centre (SSC)

Received in the SSC by (name in capitals):			
1.1 Method of Submission (Handed in to SSC; posted through internal/external mail):			
1.2 E-thesis Submitted (mandatory for final theses)			
Signature:		Date:	

Contents

List of Symbols

In order of appearance:

$\Delta G_{hydration}$	free energy of hydration (kcal.mol^{-1})
$\Delta H_{hydration}$	enthalpy of hydration (kcal.mol^{-1})
$\Delta S_{hydration}$	entropy of hydration (kcal.mol^{-1})
r_s	Stokes radius (m)
k_B	Boltzmann constant (J.mol^{-1}.K^{-1})
η	viscosity (kg.m^{-1}.s^{-1})
T	temperature (K)
D	diffusion coefficient (m^2.s^{-1})
dc/dx	concentration gradient across the membrane (mol.m^{-4})
$J_{diffusive}$	diffusive flux (mol.h^{-1}.m^{-2})
$J_{co\text{-}ions}$	co-ion flux (mol.h^{-1}.m^{-2})
$J_{counter\text{-}ions}$	counter-ion flux (mol.h^{-1}.m^{-2})
ΔP	hydrostatic pressure difference (bar)
$\Delta \pi$	osmotic pressure difference (bar)
R_{tot}	total resistance (m)
c_m	concentration at the membrane surface (mol.L^{-1})
c_b	concentration in the bulk (mol.L^{-1})
c_p	concentration in the permeate (mol.L^{-1})
k_f	mass transfer coefficient (m.s^{-1})
pK_a	acid dissociation constant (--)
k	solute flux (mol.h^{-1}.m^{-2})
A	Arrhenius pre-exponential factor (--)
R	gas constant (kcal.mol^{-1}.K^{-1})
E_a	energy barrier or activation energy (kcal.mol^{-1})
$j_{i,total}$	solute flux of solute i (mol.s^{-1}.m^{-2})
$j_{i,diffusion}$	diffusive solute flux (mol.s^{-1}.m^{-2})
$j_{i,convection}$	convective solute flux (mol.s^{-1}.m^{-2})

$j_{i,charge}$ solute flux due to electromigration (mol.s^{-1}.m^{-2})

$D_{i,p}$ hindered diffusivity (m^2.s^{-1})

$D_{i,\infty}$ diffusion coefficient in bulk water (m^2.s^{-1})

$K_{i,d}$ diffusive hydrodynamic coefficient (--)

λ_i ratio of Stokes radius to pore radius (--)

z_i ionic valence (--)

c_i^m average concentration in the membrane (mol.m^{-3})

F Faraday's constant (C.mol^{-1})

R gas constant (J.mol^{-1}.K^{-1})

φ_m potential across the active layer (V)

$K_{i,c}$ convective hydrodynamic coefficient (--)

J_v volumetric flux (m^3.m^{-2}.s^{-1})

γ activity (mol.m^{-3})

F_{xi} force on the ith particle from a given direction (kg.m.s^{-2})

m_i mass of the ith particle (kg)

x_i coordinate of the ith particle (--)

a_i acceleration of the ith particle (m.s^{-2})

t time (s)

V_{total} total potential energy (kcal)

$V_{internal}$ internal energy potential (kcal)

$V_{external}$ external energy potential (kcal)

b instantaneous bond length (Å)

θ instantaneous angle (deg)

b_0 equilibrium bond length (Å)

θ_0 equilibrium bond angle (deg)

k_b bond force constant (kcal.mol^{-1}.Å^{-2})

k_θ angular force constant (kcal.mol^{-1}.rad^{-2})

k_t torsion force constant (kcal.mol^{-1}.rad^{-2})

n multiplicity (--)

σ phase (deg)

ε_{ij} potential energy well depth (kcal)

$R_{min/2,ij}$ distance between two ions with minimum LJ interaction energy (m)

q charge of an ion

r_{ij} distance between two ions (m)

ε_D	dielectric constant (--)
R_p	effective pore radius (m)
L	membrane active layer thickness (m)
ε	membrane porosity (--)
Φ	distribution coefficient (--)
$\langle J_s \rangle$	radial average solute flux (mol.s^{-1}.m^{-2})
Pe	membrane Peclet number (--)
$\langle V \rangle$	radial average fluid velocity (m.s^{-1})
c_m	concentration at the membrane surface (mol.m^{-3})
c_p	concentration in the permeate (mol.m^{-3})
R_r	real retention (%)
ζ	zeta potential (mV)
U_s	streaming potential (mV)
P	applied pressure (bar)
μ	dynamic viscosity (kg.m^{-1}.s^{-1})
ε_0	permittivity of free space (C^2.J^{-1}.m^{-1})
$\varepsilon_{solution}$	relative permittivity of test solution (--)
$L_{channel}$	channel length (m)
$A_{xsection}$	channel cross-sectional area (m^2)
$R_{channel}$	channel resistance (m)
Ra	mean roughness (m)
Rq	root mean square roughness (m)
J_v or J	volumetric flux (L.h^{-1}.m^{-2})
Q	flow of the permeate (L.h^{-1})
A	membrane surface area (m^2)
L	permeability (L.h^{-1}.m^{-2}.bar^{-1})
$P_{applied}$	applied pressure (bar)
k_f	salt mass transfer coefficient (m.s^{-1})
π	osmotic pressure (bar)
SEC	specific energy consumption (kWh.m^{-3})
I	current (A)
U	voltage (V)
TMP	transmembrane pressure (bar)

δ	uncertainty (units vary)
M_{dep}	mass deposited (of precipitate) (g)
R_{hyd}	hydrated radius (10^{-10} m)
R_p	pore radius based on center of carbon atoms, MD (10^{-10} m)
R_{eff}	effective pore radius available to water, MD (10^{-10} m)
RDF_{min}	minimum in the radial distribution function (--)
$R_{ion,oxygen}$	ionic radius of oxygen (10^{-10} m)
r_{radial}	distance from the central pore axis (10^{-10} m)
Z	vertical position along trajectory (10^{-10} m)

Publications

The following publications were produced from this work:

Accepted

Richards, L. A.; Richards, B. S.; Rossiter, H. M. A.; Schäfer, A. I., Impact of Speciation on Fluoride, Arsenic and Magnesium Retention by Nanofiltration/Reverse Osmosis in Remote Australian Communities. *Desalination* 2009 248, 177 - 183.

Richards, L. A.; Vuachère, M.; Schäfer, A. I., Impact of pH on the removal of fluoride, nitrate and boron by nanofiltration/reverse osmosis. *Desalination* 2010, 261, 331 - 337.

Richards, L. A.; Richards, B. S.; Schäfer, A. I., Renewable energy powered membrane technology: Salt and inorganic contaminant removal by nanofiltration/reverse osmosis. *Journal of Membrane Science* 2011, 269, 188 - 195.

Richards, L. A.; Richards, B. S.; Schäfer, A. I., Renewable energy powered membrane systems: Inorganic contaminant removal from Australian groundwaters. *Membrane Water Treatment* 2011, 2(4).

Richards, L. A.; Schäfer, A. I.; Richards, B. S.; Corry, B.; The importance of dehydration in determining ion transport in narrow pores. *Small* (accepted 01/2012).

In Preparation

Richards, L. A.; Corry, B.; Richards, B. S.; Schäfer, A. I., Experimental energy barriers to anions transporting through nanofiltration membranes *(in preparation for Journal of Membrane Science, 2012)*

Richards, L. A.; Schäfer, A. I.; Richards, B. S.; Corry, B.; Quantifying barriers to anion transport in narrow pores *(in preparation for Physical Chemistry Chemical Physics, 2012)*

Chapter 1

Introduction

"Water is fundamental for life and health. The human right to water is indispensable for leading a healthy life in human dignity. It is a pre-requisite to the realization of all other human rights" – United Nations Committee on Economic, Cultural and Social Rights, 2002

This chapter introduces the broad context of this research project. The provision of safe drinking water is critical in an era in which the world's population is increasing rapidly but safe water supplies remain scarce. Further, in a number of remote locations, water and energy are inextricably linked and, thus, the synergy between them must be addressed when considering either. Often the only water available in these areas is brackish groundwater which requires treatment before consumption in order to reduce levels of bacterial and chemical contaminants to safe levels. Nanofiltration and reverse osmosis (NF/RO) membranes are able to effectively remove a number of contaminants from drinking water. NF/RO systems powered by renewable energy provide a promising technology for water treatment in remote areas due to their independence from grid electricity, generally high removal of contaminants, low energy consumption and modularity. This chapter provides the context and motivation for the rest of the work presented in this thesis and concludes with a description of the overall

thesis structure. This introduction sets the stage for a detailed literature review of ion transport in NF/RO membranes, which is the subject of Chapter 2.

1.1 Motivation: The World Water Crisis

The world population is increasing at an alarming rate which has been significantly higher in the last hundred years than ever before (Figure 1-1) [1]. The population achieved seven billion in 2011 and is expected to exceed nine billion by 2040. As shown on Figure 1-1, this population growth is not equally distributed between developed and developing countries. In fact, growth in developing regions of Africa and the Middle East is often more than three times greater than in other parts of the world (Figure 1-2). A major concern with population growth arises because the earth's resources are limited and also unequally distributed, and thus it is becoming increasingly difficult to match resources with the growing demand. In particular, this is a concern for resources such as water, oil and food. Water scarcity is the focus of the work presented in this thesis.
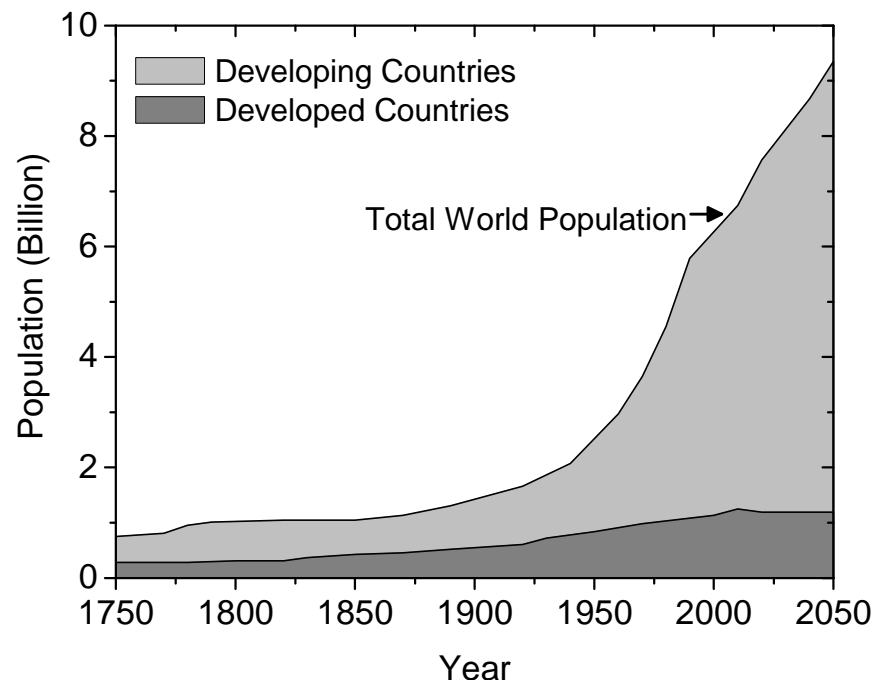
Figure 1-1. World population from 1750 to 2050, adapted from [1].
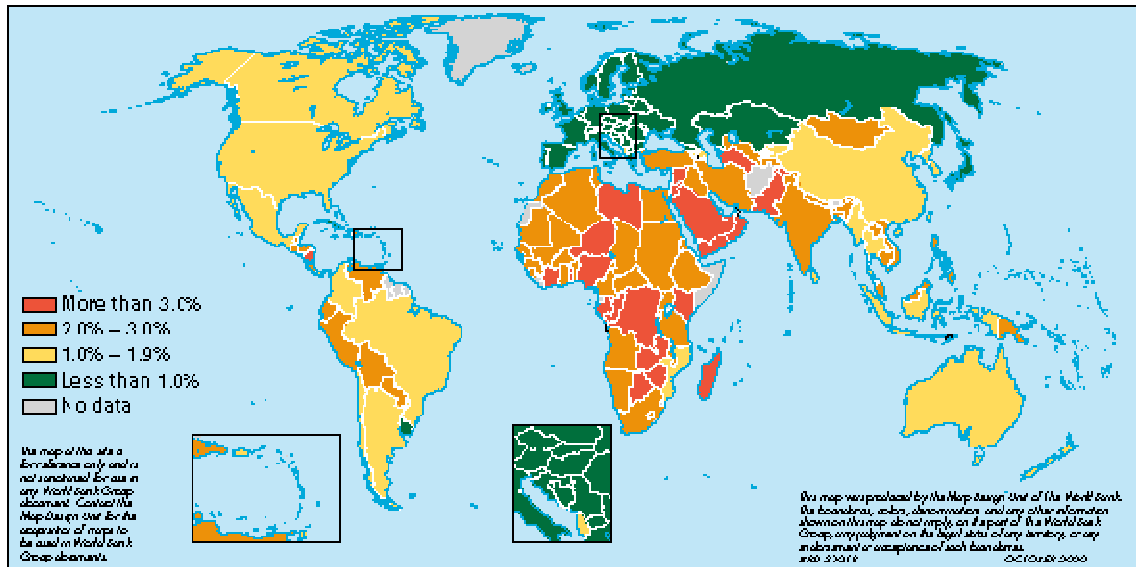
Figure 1-2. Population growth distribution [2].

Water scarcity is already a significant global concern, and the current population growth will only exasperate the problems if nothing is done. Currently, 884 million people lack access to an improved drinking water source [3], which is only defined as a public standpipe within one kilometre of one's dwelling. The people affected by the lack of access to drinking water are often disproportionately women and children, who are generally responsible for water collection. This is furthered because men sometimes take employment in places away from the home with more-developed infrastructure. The great majority of people without access to improved water sources, 84%, live in rural areas where generally infrastructure is lacking and poverty is prevalent [4]. An estimated 3,900 children are killed every day from illness related to unsafe drinking water and inadequate sanitation [5]. The statistics are even worse for the number of people living in water-stressed areas. An astounding 2.3 billion people live in water-stressed areas (Figure 1-3), and this number is expected to climb to 3.5 billion by 2050 [6]. In addition to direct effects on human health [7], increased concerns about water scarcity are also linked to ecological effects such as threatened river biodiversity [8]. These harrowing statistics highlight the severity and urgency of the current water crisis and put forward a call to action for a concerted effort to do everything we can to help ourselves and our global community.
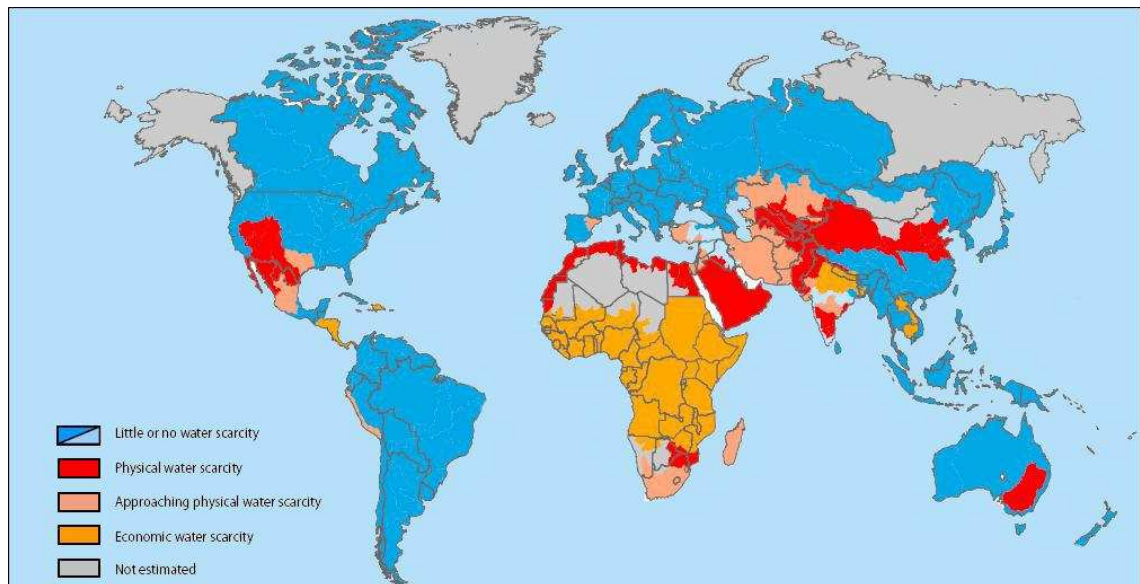
Figure 1-3. Areas of physical and economic water scarcity. Red: physical water scarcity (more than 75% of river flows are allocated); Light red: physical water scarcity (more than 60% of river flows are allocated); Orange: Economic water scarcity; Blue: Abundant water resources relative to use (less than 25% of water from rivers is withdrawn for human purposes); Grey: not evaluated [9].

As a result of this global water crisis, the United Nations has declared the years 2005 to 2015 to be the International Decade for Action 'Water for Life' [10]. The purpose of this declaration was to promote efforts to fulfil international commitments made on water and sanitation issues by the year 2015. At the largest-ever gathering of world leaders at the United Nations Millennium Summit in 2000, an integrated set of time-bound targets were developed to be met by 2015. These targets are collectively called the Millennium Development Goals and their overall aim was to extend the benefits of globalization to the world's poorest citizens. The specific objective of Target 10 was to cut in half the proportion of people without sustainable access to safe drinking water [4]. In 2002, this target was further expanded to include basic sanitation, as water as a resource was recognized as being critically integral to meet each and every one of the Millennium Development Goals. While progress has been made in achieving these goals, significant work is still necessary, particularly in sub-Saharan Africa where goals will not be met if current trends continue. A very positive note is that improvements in drinking water and sanitation are currently estimated to reduce the number of children who die each year by 2.2 million [3].

1.2 *The Synergy Between Water and Energy*

In rural communities, where the majority of people are lacking access to clean water, natural water sources such as groundwater, surface water (rivers and lakes) and rainwater are often used to meet water requirements. These sources of water often contain bacterial and chemical contaminants which can be dangerous for human consumption [11], and frequently, these water sources are left untreated. There are a number of reasons for this, a significant one being that the location away from population centres makes remote areas naturally prone to reduced infrastructure and management capabilities. In the absence of water infrastructure, community or household level solutions are necessary, which often do not effectively happen due to high costs (economies of scale cannot be exploited at the household/community level), lack of materials (*eg.* for chemical treatment), technical difficulty, lack of maintenance plans or know-how, lack of education, inappropriate storage techniques leading to re-contamination or other socio-cultural factors [12]. Problems are compounded by the fact that rural areas are frequently not considered during central energy planning, either. Of the 1.5 billion people with no access to electricity, 85% live in rural areas in developing countries [13]. This leaves a significant population who live in remote areas without access to *either* electricity or clean water. In these areas, which also overlap with regions of highest population growth, water and energy must be addressed together and addressed urgently.

The synergy between water and energy is not limited to remote communities. In fact, the concerns are wide-spread and relevant to industrial areas too, where water demand is higher. With the increasing population and increasing demand of all resources, water needs to be secured in different ways than has been done previously, in remote and populated areas alike [6, 14]. In arid parts all over the world, groundwater resources are dwindling and thus the supplies that remain are becoming increasingly brackish as withdrawal continues to increase. The increasing withdrawal of water is clearly see when a comparison is made between 1995 and projected data in 2025 (Figure 1-4) [6], and a challenge remains in defining and managing location-specific sustainable extraction rates for groundwater. Consequently, increasing interest in the desalination of brackish groundwater and seawater has led desalination to be at the forefront of current research efforts [6, 15]. A particular research interest is to increase the

performance and decrease the energetic expense of desalination by novel technologies such as more efficient membranes and carbon nanotubes [16].
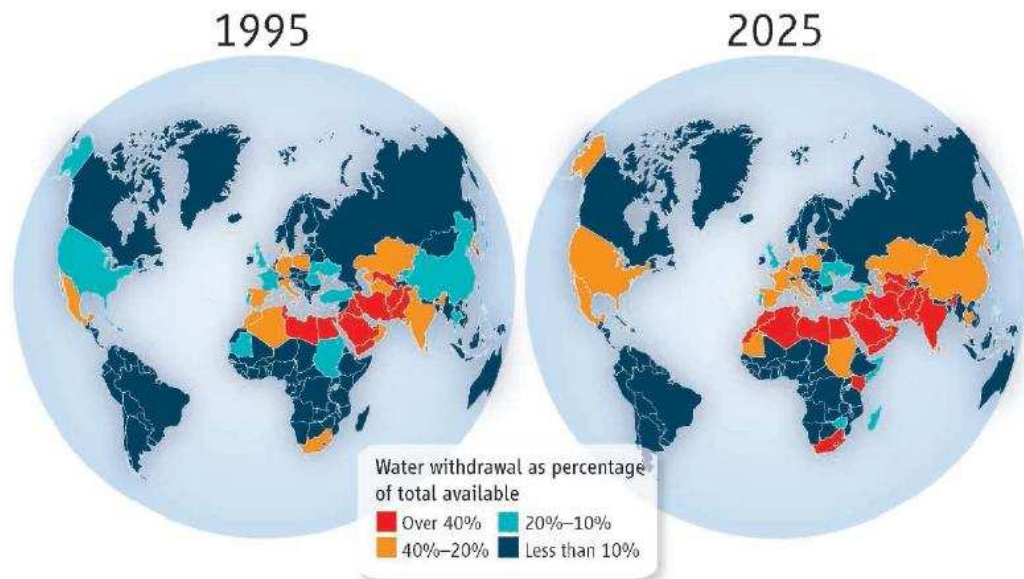
Figure 1-4. Water withdrawal in 1995 and 2025 [6].

1.3   *Contaminants in Drinking Water*

As previously mentioned, the presence of potentially health-threatening bacterial and chemical contaminants is an important concern with remote drinking water supplies. Surface water (lakes, rivers and streams) is one common source of drinking water in developing countries. Raw surface water often contains bacteria, protozoa or larvae which make the water unsafe for drinking without treatment [11], however chemical disinfection or filtration can be effective in removing these contaminants. Bacterial surface water contaminants were not dealt with in this study, but a brief mention remained warranted.

As a safer alternative to surface water, groundwater is frequently used and considered to be the most affordable, sustainable and secure water supply in rural areas [17]. Groundwater constitutes more than 97% of global fresh water [18]. Groundwater is stored beneath the earth's surface in underground aquifers, rock, and soil, and thus must be pumped up to the surface for access. Boreholes of depths roughly around 100 m are required to reach deep water aquifers and many types of pumps (electrical, hand, bike)

have been used to deliver water from boreholes [19]. A major advantage of groundwater is that it is generally protected from contamination by microbial pollutants [20, 21]. Additionally, because it is stored deeply in the earth, groundwater is less affected by drought and seasonable variations than surface or rain water. Another advantage is that a groundwater well, if there is sufficient water, can be located relatively close to its point of use, as compared to a surface water resource which can require hours of collection time in dry regions such as sub-Saharan Africa.

However, the use of groundwater also has disadvantages and associated concerns. Although groundwater does not typically have microbial contaminants, it does contain a number of inorganic salts and trace contaminants which can be health-threatening if consumed. These will be discussed specifically in the next paragraph. The majority of these inorganic contaminants are naturally-occurring; however anthropogenic activities such as agriculture and mining can also cause leaching of nitrogen-rich fertilizers, dangerous pesticides and other chemical contaminants into groundwater. A significant concern is the contamination of wells, in particular from shallow aquifers, from sanitation facilities like pit latrines. Rapid industrialization and population expansion are leading to the contamination of shallow aquifers being an increasingly widespread problem [21]. A major issue with groundwater is that current sources are becoming depleted and increasingly saline, due to over-withdrawal in certain areas. Higher salt levels in the groundwater may become even more serious due to climate change which is predicted to affect groundwater supplies by increased salt intrusion due to rising sea levels [22].

Many naturally-occurring inorganic compounds can be present in groundwater. Because groundwater characteristics depend on a complex combination of geology, weather patterns and geomorphology (the processes which shape landforms), the chemical composition and availability of groundwater is highly variable throughout the world [23]. Some groundwater contaminants are dangerous for human consumption, and in light of this the World Health Organization (WHO) and other individual governments have developed drinking water standards to advise of adverse health concerns and acceptable levels of contaminants [11]. Consumption of solutes such as arsenic, boron, copper, fluoride, nitrite and nitrate above recommended guideline values can lead to significant health impacts [11, 24, 25]. For example, millions of people

worldwide are at risk of acute chronic arsenic poisoning due to arsenic naturally found in groundwater [26-28]. Well-known high arsenic groundwater areas include Argentina, Chile, Mexico, China, Hungary, West Bengal, Bangladesh and Vietnam – with more than 40 million people drinking water containing excessive arsenic concentrations in the Bengal Basin alone [29]. In Ghana, concentrations of iron, manganese, arsenic, fluoride, lead and chromium all have been found to exceed the WHO drinking water guidelines [28]. These contaminants may be naturally present in the groundwater, or may be caused by land-use and industry. Most notably, Ghana has a long history of gold mining, and an undesired consequence of the mining is the contamination resulting from the release of contaminants such as arsenic and mercury into both water and air in the surrounding and downstream areas [28, 30]. Other compounds, such as calcium, chloride, magnesium, manganese, phosphate, potassium, sodium, and sulphur, have no currently known negative health impacts at the concentrations typically found in drinking water but may have aesthetic consequences such as taste and smell that make the water less desirable for consumption [11, 24, 25]. In order for remote drinking water supplies to be most beneficial to communities, it is important that the water is desirable from both health and aesthetic perspectives.

The inorganic contaminants boron, fluoride, nitrate and nitrite are of particular relevance to this project so the potential health-threats of these natural groundwater constituents will be discussed individually. Boron exposure is associated with short-term irritant and organ effects, however chronic toxicity in humans has not been clearly defined. The recommended guideline value for boron is 2.4 mg.L^{-1}, but as boron is very difficult to remove using conventional water treatment processes, the recommendation is that local regulatory and health authorities should consider a value in excess of 2.4 mg.L^{-1} by making a rough estimate of exposure from other sources [31]. Fluoride exposure via drinking water of concentrations above 1.5 mg.L^{-1} can lead to dental fluorosis (which affects teeth enamel), and greater than 10 mg.L^{-1} can lead to skeletal fluorosis (which affects bones) [32]. Nitrate in drinking water is of concern mainly due to its reduction to nitrite, a toxic contaminant leading to methaemoglobinaemia (baby blue syndrome), which causes reduced oxygen transport to bodily tissues and is particularly dangerous for infants [11]. The guideline value for nitrate in drinking water is 50 mg.L^{-1} and for nitrite is 3 mg.L^{-1} (short-term exposure) and 0.2 mg.L^{-1} (provisional long-term exposure) [11, 33]. A summary of the chemical contaminants which were the

focus of the work in this thesis is shown on Table 1-1. The presence of inorganics in groundwaters is spread over the world, and as an example, the distribution of fluoride in concentrations exceeding the guideline value of 1.5 mg.L^{-1} is shown in Figure 1-5.

Table 1-1. Summary of selected chemical drinking water contaminants with WHO guidelines and associated health concerns [11]. Fluoride, nitrate and nitrite were the primary focus of the work completed in this thesis.

Contaminant	WHO Guideline (mg/L)	Health Concern
Arsenic	0.01[a]	toxicity, dermal legions, vascular disease, carcinogenic (skin, bladder, lung). Arsenic is most commonly present in water as As^{+5} but is likely to be As^{+3} in anaerobic conditions. As^{+3} is considered the most toxic form.
Barium	0.7	hypertension
Boron	2.4[b]	short-term irritant and organ effects
Chromium	0.05[a]	possible carcinogen
Fluoride	1.5	dental and skeletal fluorosis
Manganese	0.4	none, guideline is aesthetic-based
Nitrate	50	reduces to nitrite
Nitrite	3 (short-term); 0.2 (provisional long-term)	toxic, leads to methaemoglobinaemia (particularly dangerous for infants)
Selenium	0.01	long-term toxic effects in humans (hair, liver, nails)
Uranium	0.015[a]	possible carcinogen

[a]Provisional guideline due to scientific uncertainties regarding toxicology/epidemiology and/or due to difficulties regarding technical achievability; [b]Recommended guideline
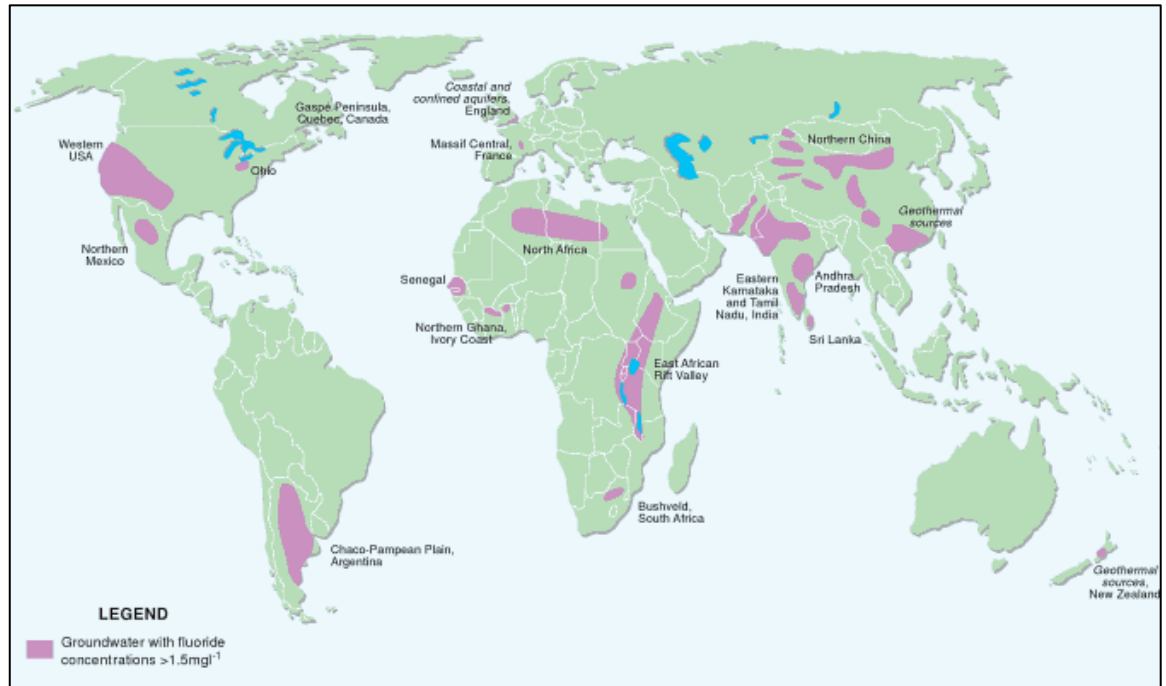
Figure 1-5. Locations where the fluoride levels in groundwater exceed the guideline value of 1.5 mg.L^{-1} (taken from [34]).

1.4   The Case for Membranes

A number of conventional and advanced water treatment technologies exist which can reduce concentrations of both bacterial and chemical contaminants in drinking water. Conventional treatment methods generally involve a combination of coagulation, flocculation, clarification, filtration and disinfection [35], which are effective for some chemical contaminants but less-so for others.   A broad comparison of different processes and the water quality problems addressed is shown on Table 1-2. Advanced water treatment technologies include methods such as advanced oxidation, ultraviolet disinfection and membrane processes. Advanced water treatment technologies have been developed in order to achieve better performance or efficiency (in terms of energetic, economic or physical space) than conventional treatment processes. One type of advanced water treatment technology, membrane processes, is the focus of this work.

Table 1-2. Summary of main water treatment processes and the water quality problems addressed [35]. Membrane processes are shown in bold.

Process	Primary Treatment Objective[*]												
	1	2	3	4	5	6	7	8	9	10	11	12	13
Coarse screening	x												
Fine screening	x												
Raw-water storage		x								x			
Preliminary settlement		x											
Aeration					x	x							
Air stripping									x				
Coagulation and flocculation			x	x		x				x		x	
Gravity clarification			x	x		x				x		x	
Dissolved Air Flotation			x	x		x				x		x	
Slow sand filtration			x	x		x				x		x	
Rapid gravity filtration			x	x		x				x		x	
Microfiltration			**x**	**x**						**x**		**x**	
Ultrafiltration				**x**						**x**			
Reverse osmosis/Nanofiltration							**x**	**x**	**x**		**x**		
Activated carbon adsorption				x	x			x					
Pre-ozonation				x	x			x	x			x	
Post-ozonation								x	x				
Ion exchange							x						
Chemical oxidation						x							
pH control						x							x
Phosphate dosing													
Chlorination						x							x
Ultraviolet Disinfection										x		x	x

[*]1: Debris; 2: High sediment load; 3: Turbidity; 4: Color; 5: Taste and odor; 6: Iron and manganese; 7: Nitrate; 8: Pesticides; 9: Volatile organic compounds; 10: Cryptosporidium; 11: Salinity; 12: Algae; 13: Microbiological quality

The term "membrane processes" collectively refers to a number of different types of membrane technology, namely reverse osmosis (RO), nanofiltration (NF), ultrafiltration (UF) and microfiltration (MF). Membranes are essentially a selective barrier which separates different dissolved solutes or particles in water to varying degrees. Particles or solutes removed range in size from tiny single ions (as small as $1 \cdot 10^{-10}$ to $3 \cdot 10^{-10}$ m radius) to molecules, bacteria, and even larger particles (up to 100 μm) [35]. A schematic showing these different membrane types and their general distinctions follows in Figure 1-6. Because the primary interest in this project was to remove dissolved salts and inorganic contaminants, as are relevant to desalination, the discussion will focus on RO and NF. RO membranes are roughly defined as those which near-completely remove all mono- and multi-valent ions. NF membranes are

roughly defined as those which are slightly more open than RO, having slightly higher fluxes and letting most monovalent ions pass. The distinctions between RO and NF are certainly not hard and set, but RO is generally accepted to be a denser material with higher retention and lower flux, as compared to NF which is more porous and has lower retention and higher flux. A point of controversy remains in the field about where actual nanofiltration "pores" lie in the spectrum between discrete pore (micro/ultrafiltration) and dense material (reverse osmosis) [36-38], but the presence of "void space" within membrane polymers is generally accepted. These differences are clearly seen on the scanning electron microscopy surface images of a microfiltration and reverse osmosis membrane (Figure 1-7).
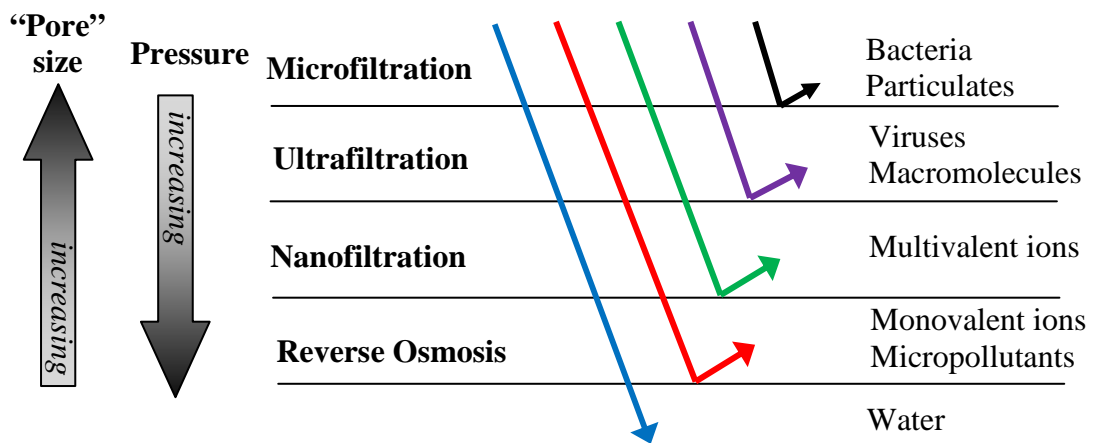
Figure 1-6. Schematic of membrane types.

RO membranes were originally developed for seawater desalination in the 1960s [39]. Shortly after, they were also applied to brackish water for desalination [40]. These early RO membranes produced very good quality permeate, but required high pressures and had high energy consumption (>10 kWh.m^{-3}) [40]. Numerous improvements were made to the membranes, and in the 1980s, NF membranes were developed with higher water permeability, reduced energy consumption and lower solute rejection [41-43]. The technologies have continued to improve dramatically, with the aim for the ultimate membrane to be able to provide very high water flux, very high solute rejection, low specific energy consumption and low cost. Currently, even though properties have become much more desirable in recent years, there is still much potential and ongoing effort in improving and developing new membrane materials (such as carbon nanotube
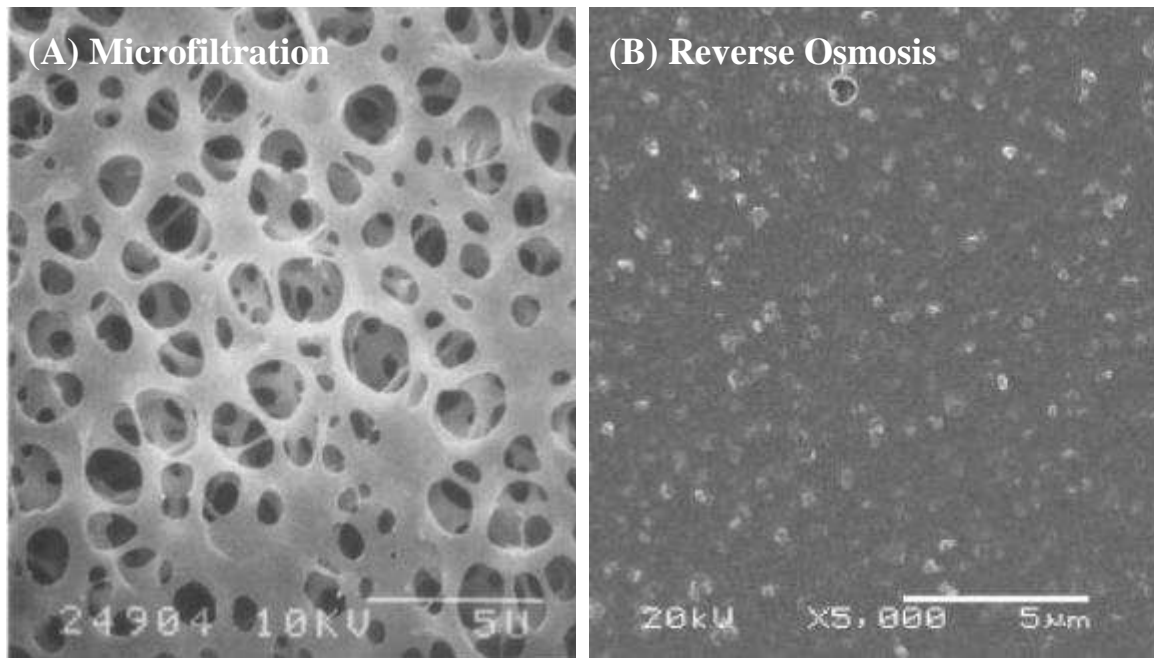
Figure 1-7. Scanning electron microscope images of (A) microfiltration membrane Sartorius SM 11127 (0.2 μm) at 5000x magnification [44] and (B) reverse osmosis membrane LP21 at 5000x magnification [45].

membranes). In particular, the development of ultralow pressure membranes has allowed the specific energy consumption of some membranes to become closer to the minimum theoretical thermodynamic limit, when the applied pressure is equal to the osmotic pressure of the concentrate (around 1.0 kWh.m^{-3} for seawater at 50% recovery) [15, 46]. In fact, an energy consumption rate of 1.8 kWh.m^{-3} using new, high-permeability SWRO membrane elements at 50% recovery has recently been demonstrated [15].

RO/NF membranes were initially made from cellulose acetate and variations thereof, but subsequently a wide range of polymer materials are in use, such as polyamide, polysulfone and polyurea [35]. Thin film polyamide materials have been particularly successful because their thin nature creates less head loss across the membrane, thus lowering the pressure required. The two most common forms of membranes used are spiral wound modules and hollow fibre modules. Spiral wound modules are flat sheet membranes layered with spacers and then wound tightly and contained in a module. Hollow fibre modules encase a group of cylindrical membrane "straws" which contact feed water on one side (usually the outside) and clean water permeates through the membrane material. The differences are shown on Figure 1-8.
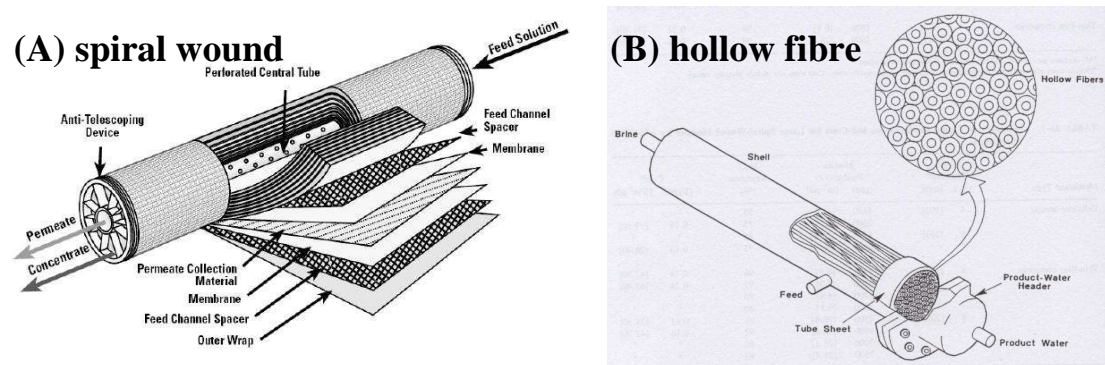
Figure 1-8. Diagram of a membrane module which is (A) spiral wound [47] and (B) hollow fibre [48].

Membranes have several distinct advantages compared to conventional water treatment processes involving a combination of coagulation, flocculation, clarification, filtration and disinfection, as previously shown on Table 1-2. Further specific advantages are that membranes have:

- Higher inorganic trace contaminant removal, in particular for boron [49, 50], fluoride [32, 51, 52], nitrate and nitrite [43, 53-55];
- Effective removal of salt for the desalination of brackish groundwater and sea water, which has become increasingly important [40, 56, 57];
- Possibility for single-stage treatment of some surface and groundwaters;
- Modular in design; and
- Smaller physical foot-print as compared to equipment for conventional water treatment.

A common misconception of membranes is that a major disadvantage is cost, however significant improvements have been made in this area and are expected to continue as materials further develop. The unit cost of water from large-scale seawater RO production has decreased from nearly 5.00 USD.m^{-3} in the late 1970s to less than 1.00 USD.m^{-3} in 2004 [40]. A recent plant in Israel (Ashkelon plant) produces water costing only 0.53 USD.m^{-3} in 2005 [40]. Brackish water desalination costs less than seawater due to less electrical power required for production, and ranges from 0.10 USD.m^{-3} to 1.00 USD.m^{-3} [40]. Especially when economies of scale are considered for larger systems, cost is no longer a major barrier to the use of NF/RO [40, 58]. Cost for

14

membrane desalination plants can be broken into capital cost and operation and maintenance costs (*eg.* membrane replacement, energy consumption, labor, and chemicals). In the Ashkelon seawater desalination plant in Israel, the capital costs were 59% of the total expenditure, whereas the capital cost of a comparable brackish water plant (Metropolitan plant in California) was 43%. The capital costs of the seawater plant were five times greater than the brackish water plant due to more extensive pre-treatment equipment and higher pumping requirements. Energy costs were also five times greater for the brackish plant due to higher pressures and lower recovery, but chemical costs were similar. Membrane replacement costs were higher for the seawater plant because seawater membranes typically have shorter lifetimes due to higher fouling [40]. Disadvantages of membranes include potential membrane fouling (eventually leading to membrane replacement and thus additional cost) and the requirement of occasional chemical cleaning (and associated costs). A concern with utilizing membranes in remote locations is the lack of local availability of suitable materials. Another concern is the relatively high energetic requirement of desalination, however, as discussed above, energy consumption of membrane processes has drastically improved recently. Further, renewable energy powered membrane systems/plants avoid the negative environmental consequences of an energetically expensive process and are gaining great momentum. These systems are discussed in the next section.

NF/RO membranes utilize a number of different mechanisms to create the separation between water and dissolved solutes, which will be discussed in detail in Chapter 2. The basic principle of NF/RO is that a hydrostatic pressure must be applied which is in excess of the osmotic pressure of the feed water, which reverses the natural drive of osmosis, as shown in Figure 1-9 [40, 59]. This drives water through the membrane barrier but leaves certain solutes behind. Specific separation mechanisms are dependent on solute and membrane properties and can include size exclusion, charge repulsion, convection, diffusion and adsorptive interactions.
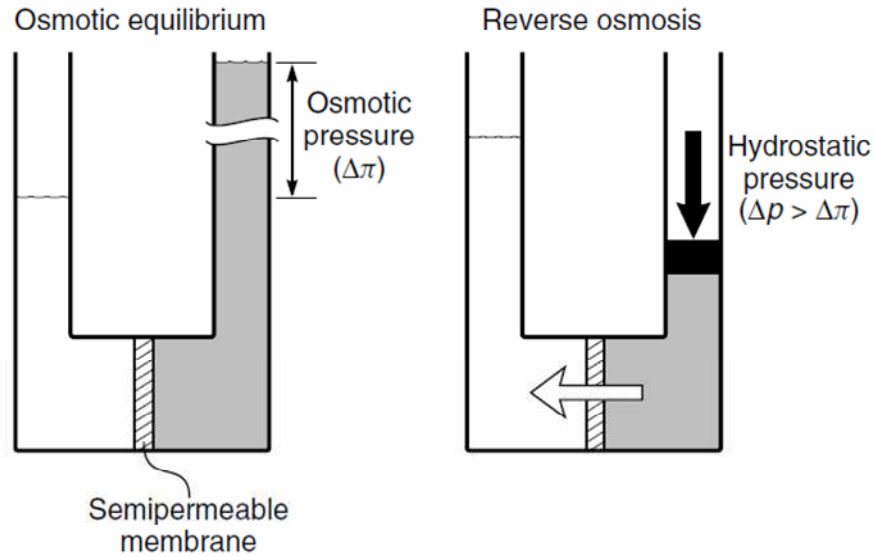
Figure 1-9. Basic principle of RO [59].

One key parameter in understanding specific separation (or retention) mechanisms is solute speciation. Speciation refers to the chemical form in which a solute is present in solution, and one particular solute (calcium or fluoride, for example) can take on different forms in solution depending on environmental factors such as ionic strength and pH. Specifically, pH has a complex effect on retention mechanisms because it not only affects the speciation of a solute, but also the properties of a membrane. This is very important to understanding charge interactions in membrane processes. The literature surrounding the effect of pH on solute speciation and retention is discussed in detail in Chapter 2.1.3 and 2.3.5, and this topic is the subject of the experimental work presented in Chapter 5.

Information about retention mechanisms can be further gathered experimentally by accessing the specific impact of parameters such as ion type, pressure, temperature, flow and concentration on solute retention. These operating parameters affect system hydrodynamics, conditions at the membrane surface, and the chemical properties of the solution, thus affecting retention mechanisms. This topic is reviewed in detail in Chapter 2.2 and 2.3 and is the subject of experimental results in Chapter 7.

Molecular dynamics is a powerful tool that can be used to understand fundamental chemical and physical interactions. This has direct applications to membrane processes,

16

where mechanisms can be difficult to understand from experimental results due to very complex interactions and limitations in measurement capabilities. Molecular dynamics, as will be discussed in Chapter 2.5, has been used to understand the transport of ions in ion channels and carbon nanotubes, but the techniques have not yet been directly applied to understanding the removal of health threatening contaminants in NF/RO. This is the subject of Chapter 6.

1.5   Renewable Energy Powered Membrane Systems

The majority of membrane development has focused on large scale application, hindering it largely inaccessible for small-scale systems in developing countries [60]. However, this is quickly changing as recent effort has focused on the development of renewable energy powered membrane systems (RE-membrane) [61-64]. The integration of renewable energy with membrane technology has the dual benefit of being more resource-friendly and the potential to be located in remote locations that are away from grid electrical connections [61-64].

There are several key factors commonly described when developing a secure and suitable water supply for a remote community [17]:

- the water is of sufficient quality for human consumption;
- the supply is sufficient and reliable throughout the year (including changes in availability as well as in demand);
- the water is accessible to the whole community and within a reasonable distance from households;
- the supply is affordable; and
- the supply can be easily maintained.

A well-designed and well-integrated RE-membrane system would meet most of the criteria for use in a remote community in developed and developing regions alike. In fact, RE-membrane systems offer one of the most promising options for removing salts, microbial and chemical pollutants from groundwaters in communities in off-grid locations [16]. However, it should be noted that acquisition of equipment such as

membrane modules and renewable energy equipment such as solar panels can be more challenging in developing areas. RE-membrane systems were first used approximately 30 years ago [65] and technology has developed since the first protocols into systems for remote areas which are now cost-competitive with other water supply technologies [58, 63, 64]. Systems of varying sizes operated with photovoltaic (PV) and/or wind energy have now been tested across the world in Australia [66], Saudi Arabia [67], Jordan [68], Hawaii [69] and Gran Canaria [68]. PV-membrane systems are now at the applications and advanced research and development stages, and total costs for brackish water and seawater desalination range from $6.50 - 9.0$ USD.m^{-3} and $11.60 - 15.50$ USD.m^{-3}, respectively [70]. Costs are higher than grid-powered systems both because the systems are generally much smaller (and thus cannot take advantage of economies of scale) and more capital is required for renewable energy equipment. Recently, 14 leading European organizations have been brought together in a project called ProDes (Promotion of Renewable Energy for Water Production through Desalination) to support the market development of renewable energy desalination [70].

In order to avoid the effect of energy fluctuations on operational performance, most RE-membrane systems have used batteries to provide a constant energy source [66-68, 71]. However, batteries are also undesirable for several reasons: decreased system efficiency; decreased performance at high temperatures and thus higher maintenance costs; difficulty and expense of replacing batteries in remote locations; and higher life-cycle costing [72]. Additionally, not using batteries eliminates the chance of the system's batteries being used for other purposes and thereby rendering such a drinking water production system useless. Therefore, it is better for system cost and efficiency to operate the system with no energy storage and such systems have subsequently been developed [66, 69, 72-75]. A RE-membrane system is the focus of the results presented in Chapter 4.

1.6 Thesis Overview

In summary, there is a great need for improved water treatment solutions with the increasing demand on resources and the changing climate. NF/RO membranes are excellent treatment options because of their ability to remove contaminants at the ionic

level, which is appropriate for desalination of sea and brackish water. However, there are still improvements to be made with these technologies such as widespread integration of renewable energy with membrane processes, improved materials and better mechanistic understanding (which will be discussed in Chapter 2). This therefore makes the area of NF/RO an exciting research area with the potential for real contribution to the challenges presented by the world water crisis.

The overall aim of this research project was to contribute to the understanding of NF/RO processes, with the motivation that the technical knowledge obtained could contribute to solutions to the water problem. A broad description of the four core parts of this project follows (and will be described in more technical detail after the relevant literature is reviewed in Chapter 2):

- The performance of a renewable energy powered membrane system was evaluated with real varying energy conditions and natural groundwater. This was be achieved by determining (i) the impact of varying energy on the retention of inorganic solutes; (ii) the role of pH in this process; (iii) the dominant mechanisms of ion retention; and (iv) system performance at different locations. The data evaluated by the PhD candidate was previously produced during a field trial in Australia in 2005 (Chapter 4).

- The specific impact of pH on the removal of selected inorganic contaminants was determined, as pH is a very important parameter to NF/RO performance and varies naturally widely. This was achieved by completing a study initiated by a previous student that linked solute speciation of boron, fluoride and nitrate with retention with six different NF/RO membranes (Chapter 5).

- The importance of ion hydration on determining the transport of monovalent anions (fluoride, chloride, nitrate and nitrite) was analyzed using molecular dynamics simulations. This is a very poorly understood mechanism in NF/RO and new information in this area would provide insight into what determines separation. This was achieved by determining hydration structure and energy barriers as a function of pore size, ion type and surface charge (Chapter 6).

- Experimental evidence of the proposed mechanism of partial ion dehydration was sought. This was achieved by determining solute flux and Arrhenius

activation energy barriers for each ion type and two membranes, and linking results to molecular dynamics simulations (Chapter 7).

This thesis is structured as shown in Figure 1-10. The purpose of this introduction chapter was to paint a broad overview of the topic at hand. A specific, in-depth, literature review of principles and mechanisms of ion transport in NF/RO will follow in Chapter 2. Chapter 2 will conclude with the detailed research objectives undertaken in this research project. Experimental methods and materials are described in Chapter 3. The first results are presented in Chapter 4, which discusses the field performance of a renewable energy membrane system with specific regard to varying energy and pH. Simplified bench-scale experiments were conducted to assess the effect of pH on the retention of inorganic contaminants and boron, and these are discussed in Chapter 5. Chapter 6 presents molecular dynamics results that assessed the specific impact of ion hydration/dehydration when ions transport through pores. The final experimental chapter, Chapter 7, attempts to link experimental energy barriers according to ion and membrane type with expected trends for dehydration determined with the molecular dynamics simulations. The thesis concludes with a summary of results obtained and recommendations for future work (Chapter 8).

Chapter 1. Introduction

Chapter 2. Ion Transport Principles: A Review

Chapter 3. Experimental Methods and Materials:

Chapter 4. Renewable Energy Powered Membrane Systems

Key Points
- System effectively removed inorganic contaminants over real energy and pH conditions
- Energy fluctuations affected operating parameters and hence retention where diffusion/convection mechanisms dominated
- Groundwater pH was important for contaminants dominated by charge mechanisms

Relevant Publications: Richards *et al.*, Desalination (2009); Richards *et al.*, Journal of Membrane Science (2011); Richards *et al.*, Membrane Water Treatment (2011)

Chapter 5. Impact of pH on Inorganic Contaminant Removal

Key Points
- Chemical speciation in different water matrices was predicted for boron, fluoride and nitrate
- Retention trends strongly correlated to speciation and membrane properties as a function of pH
- The selectivity of fluoride and nitrate cannot be explained by charge interactions alone nor size exclusion according to the size of the bare ion

Relevant Publication: Richards *et al.*, Desalination (2010)

Chapter 6. The Importance of Dehydration in Determining Ion Transport in Narrow Pores

Key Points
- Energy barriers are strongly dependent on pore size
- Energy barriers are strongly dependent on ion type (and hence hydration properties)
- Molecular dynamics simulations show that dehydration is the main barrier to anion transport in narrow pores

Relevant Publications: Richards *et al.*, Small (2012, accepted); Richards *et al.*, Physical Chemistry Chemical Physics (*in preparation*)

Chapter 7. Experimental Determination of Energy Barriers to Ion Transport

Key Points
- Energy barriers can be determined experimentally using Arrhenius activation energies
- Energy barriers depend on ion type and membrane type
- Energy barriers are compared to those determined using molecular dynamics simulations

Relevant Publication: Richards *et al.*, Journal of Membrane Science (*in preparation*)

Chapter 8. Conclusions and Future Recommendations

Figure 1-10. Thesis structure.

Chapter 2

Ion Transport Principles: A Review

Having highlighted the water crisis and synergetic energy crisis in Chapter 1, membrane technology was offered as a solution to partially help address this urgent need. This chapter offers a more thorough description of the current state of knowledge surrounding nanofiltration and reverse osmosis (NF/RO). Firstly, ion properties in bulk water are described, as this is fundamental to understanding the behaviour of these ions in more complicated membrane processes. Secondly, a description of various NF/RO mechanisms is given, followed by an explanation of how various operating parameters affect NF/RO performance. A discussion of current NF/RO models is then given, including their limitations, and suggestions on how these models may be improved by use of molecular dynamics. Finally, this chapter describes, with more detail, the specific research aims and objectives that were originally outlined in Chapter 1.

2.1 Ion Properties in Aqueous Solutions

In order to understand how the mass transport of inorganic ions works in membrane processes, first the ion properties in bulk aqueous solutions must be understood. When ions are in aqueous solution, they interact with the solution around them and thus exhibit properties that are different than if the ion was alone. For the purposes of this

research, only ion properties in water (*eg.* not other aqueous solutions) will be discussed. The basic principles of ion behaviour in bulk water follow.

2.1.1 Ion Hydration

To understand the role membranes have in removing contaminants from water it is first necessary to understand the interactions of ions and water molecules. When ions are in water, they are surrounded by a "shell" of water molecules due to the dipole nature of water [76]. This shell of water is referred to as a hydration shell or hydrated layer. A generic schematic of hydration layers around a large and small anion is shown on Figure 2-1 [77]. This process of hydration results in the kinetic entity no longer being the bare ion but the ion accompanied by its associated hydrated shell [76]. When the hydrated shell is considered, the effective ion size is larger than the bare ion alone, and the radius of the entity is known as the hydrated radius.

The strength of the attractive interactions between the bare ion and the hydrated shell is known as the Gibbs free energy of hydration ($\Delta G_{hydration}$, kcal.mol^{-1})

$$\Delta G_{hydration} = \Delta H_{hydration} - T\Delta S_{hydration} \, , \qquad \text{Equation 1}$$

where H represents enthalpy (kcal.mol^{-1}) and S entropy (kcal.mol^{-1}). The free energy of hydration is defined as the change in chemical potential of a solute molecule, upon formation of an infinitely dilute aqueous solute from components in their standard states (*eg.* gaseous for the solute and pure liquid for the solvent). This parameter therefore represents how favourable the interactions are between a dissolved solute (*eg.* fluoride) and water, and has both enthalpic and entropic energetic contributions [78]. A highly negative $\Delta G_{hydration}$ indicates very strong attractive forces and less negative $\Delta G_{hydration}$ means the ion is more weakly hydrated. Small ions have strong hydration energies because their charge density is higher, which causes stronger attractive interactions with the water molecules. There can be more than one distinct hydration shell around an ion if the attractive forces are strong enough to affect more-distant water molecules.

large anion (*eg.* nitrate
ΔG_{hyd} = -71.6 kcal.mol^{-1})

small anion (*eg.* fluoride,
ΔG_{hyd} = -119.7 kcal.mol^{-1})
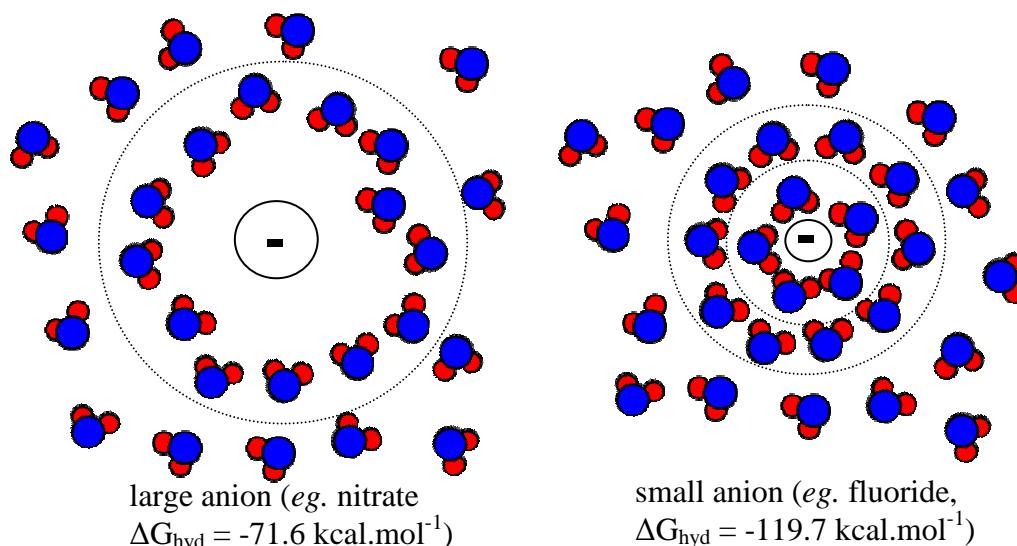
Figure 2-1. Generic schematic of the hydration around a large and small anion (adapted from Tansel *et al.* [77]). A small ion such as fluoride has a much higher hydration energy than a relatively large ion such as nitrate due to the higher charge density and thus stronger interaction energies with surrounding water molecules.

small cation (*eg.* sodium,
ΔG_{hyd} = -88.6 kcal.mol^{-1})

small anion (*eg.* fluoride,
ΔG_{hyd} = -119.7 kcal.mol^{-1})
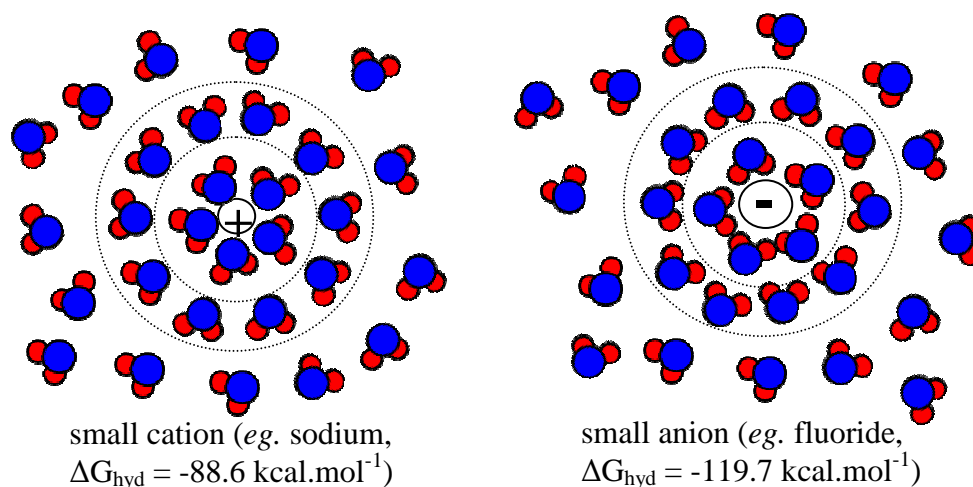
Figure 2-2. Generic schematic of the hydration comparing a small cation with a small anion (adapted from Tansel *et al.* [77]). Note that the water molecules orient their oxygen atom towards the cation, and their hydrogen atoms toward the anion.

Cations and anions are hydrated differently because they attract the water towards themselves in different manners (Figure 2-2) [79]. With mono-atomic cations, which are positively charged, water molecules orient with their oxygen atom (containing lone pairs of electrons) pointing towards the cation. In this case, the oxygen atoms in the water molecules act as electron donors and the cations as acceptors. Conversely, with

anions, the water molecules orient one or both of their hydrogen atoms towards the anion and hydrogen bonds can be created, as shown on Figure 2-1. The size, shape, and charge all affect how the interactions between ion and water molecule occur [79]. Hydration involves complicated interactions, with contributions from all thermodynamic functions such as entropy, enthalpy and available volume [76, 79-81].

Significant effort has been made over a number of years, starting in the 1900s, to quantify what the kinetic entity of an ion is in electrolyte solutions, as this has importance to a number of applications in chemistry, biology and medicine [76]. However, this has proven very challenging, time consuming, and at times ambiguous because of the difficulty in experimentally measuring or simulating these free energies of hydration and/or structures. Experimental measurements can be made using crystallographic techniques including vibration potentials and Volta potentials [79]. Much of the difficulty arises because a single correlation or model to exactly represent the hydration phenomena is not expected [82], although some models have been developed that match reasonably well with a wide number of similar ion types [79, 80]. These early correlations characterized an ion by its charge and radius, and made no distinction between cations and anions with the same radius and charge. They also divided the surrounding water into two regions: (1) a hydration shell where water is immobilized and electro-restricted and (2) bulk water which is under the influence of the electric field [79, 80]. With these models, elongated, non-spherical ions (such as nitrate or nitrite) are approximated by a sphere [79].

Determining accurate hydration information remains a challenge, and although vast steps forward have been made in this arena, recent efforts are still ongoing to accurately represent even monovalent ions in solution [83, 84]. To properly understand ionic interaction in solution, it is necessary to be able to simultaneously reproduce many properties such as ionic structure, dynamics, solvation, ion-ion interaction and ion-molecule interaction. Some of the best current models employ a simple additive, nonpolarizable and pairwise potential for atomic interaction [83], and the most recent updates involve further developing the ion-interactions within the pairwise Couloumbic and Lennard-Jones framework which give more accurate representations of interactions

between the ion of interest and surrounding water molecules [83]. A particular focus has been placed on alkali (Li^+, Na^+, K^+, Rb^+ and Cs^+) and halide ions (F^-, Cl^-, Br^- and I^-) which are most relevant to biological phenomena. A lack of updated information remains for many contaminants relevant to drinking water treatment such as nitrate and nitrite.

Despite the fact that values for hydrated radius and strength can vary according to the type of experiment or simulation and point of reference, the general order of the ions properties remains the same. A summary of available hydration data for ions relevant to NF/RO follows in Table 2-1. This shows that some hydration information exists in the literature for a number of ions, but the information is often not comprehensive nor consistent [77, 80, 82, 85]. Ideally, a consistent source is best for comparison. As such, hydrated radii provided by Nightingale [82] are used to discuss the results in Chapter 4 and 5, as there is information provided for most of the ions of interest. Data from Nightingale [82] is listed as the first line for each ion in Table 2-1. In Chapter 6 and 7, more detailed parameters about hydration structure are required and thus updated information is used for chloride and fluoride from the current literature [83] and developed from scratch for nitrate and nitrite from crystallographic experimental hydration energies [80] (details discussed where appropriate). The theory of ionic hydration and obtaining consistent information remains a challenge and some scientists claim that final answers may never be reached [86, 87]!

Table 2-1. Molecular weight, ionic and hydrated radii for relevant ions, arranged according to valence charge and number.

Species	Molecular Weight (g.mol^{-1})	Ionic Radius (10^{-10} m)	Hydrated Radius (10^{-10} m)	Gibbs Free Energy of Hydration (kcal.mol^{-1})	Ref.
Cl^-	35.45	1.81[a]	3.32	--	[82]
		1.98	3.24	--	[88]
		1.81	1.95	--	[89]
		1.81	2.24[b]	-81.2[c]	[80]
		1.81	--	-82.9	[90]
		--	3.13	-89.6	[83]
		--	--	-89.1	[86]
		--	3.29	-89.2	[84],[83][d]
		--	3.187	-81.2	[79],[83][d]
		1.81	--	-88.0	[91]

F[-]	19.00	1.36 [a]	3.52	--	[82]
		1.28	3.48	--	[88]
		1.19	2.84	--	[89]
		1.33	2.12[b]	-111.0[c]	[80]
		1.26	--	-112.7	[90]
		--	2.63	-119.7	[83]
		--	--	-119.7	[86]
		--	2.80	-115.8	[84],[83][d]
		--	2.63	-111.0	[79],[83][d]
		1.36	--	-126.1	[91]
NO$_3$[-]	62.00	2.64[a]	3.35	--	[82]
		1.79	2.23[b]	-71.6[c]	[80]
		2.00	--	-73.1	[90]
NO$_2$[-]	46.01	1.92	2.29[b]	-78.8[c]	[80]
		1.87	--	-81.0	[90]
MoO$_4$[2-]	159.94	3.23[a]	3.85	--	[82]
SeO$_4$[2-]	142.96	3.05[a]	3.84	--	[82]
SO$_4$[2-]	96.06	2.90[a]	3.79	--	[82]
		2.15	3.00	--	[89]
		2.30	2.73[b]	-257.9[c]	[80]
		2.18	--	-260.3	[90]
K^{+}	39.10	1.33[a]	3.31	--	[82]
		1.48	2.75	--	[88]
		1.38	2.01	--	[89]
		1.38	2.12[b]	-70.5[c]	[80]
		--	2.75	-70.7	[83]
		--	--	-71.2	[86]
		--	2.86	-61.5	[84],[83][d]
		--	2.798	-70.5	[79],[83][d]
		1.33	--	-66.0	[91]
Na^{+}	22.99	0.95[a]	3.58	--	[82]
		0.99	2.99	--	[88]
		1.02	1.78	--	[89]
		1.02	2.18[b]	-87.2[c]	[80]
		--	2.38	-88.7	[83]
		--	--	-88.6	[86]
		--	2.49	-78.8	[84],[83][d]
		--	2.356	-87.2	[79],[83][d]
		0.95	--	-82.7	[91]
Sr^{2+}	87.62	1.13 [a]	4.12	--	[82]
		1.36	2.80	--	[89]
		1.13	2.63[b]	-329.5[c]	[80]
Ni^{2+}	58.69	0.70[a]	4.04	--	[82]
		0.60	3.11	--	[89]
		0.69	3.02[b]	-472.8[c]	[80]
Ca^{2+}	40.08	0.99[a]	4.12	--	[82]
		1.23	2.53	--	[89]
		1.00	2.71[b]	-359.4[c]	[80]
Cu^{2+}	63.55	0.72[a]	4.19	--	[82]
		0.73	2.97[b]	-480.0[c]	[80]

Zn^{2+}	65.39	0.74[a]	4.30	--	[82]
		0.74	2.80	--	[89]
		0.75	2.95[b]	-466.9[c]	[80]
Mg^{2+}	24.31	0.65[a]	4.28	--	[82]
		0.72	3.00	--	[89]
		0.72	2.99[b]	-437.0[c]	[80]
Mn^{2+}	54.94	0.80[a]	4.38	--	[82]
		0.83	2.86[b]	-420.3[c]	[80]

[a]Crystal radii reported by Nightingale [82]

[b] Manually calculated as ionic radius plus the width of shell from Table 1 in [80]

[c]Experimental values that were converted to absolute values with the choice of $\Delta_{hyd}G°[H^+]$=-252.2 kcal.mol^{-1}

[d]As reported by [83] using TIP3P water model

2.1.2 Definitions of Solute Radius

A major challenge in understanding ion behaviour in bulk solution, and subsequently in understanding membrane processes, lies in the definition of solute radius. As shown on Table 2-1, there can be considerable discrepancy in reported values, even of the same type, due to differences in measurement techniques and assumptions. Generally reported values of ionic radius (or "crystal" radius if determined with crystallography) are fairly consistent; however this is an inaccurate representation of the effective size when in water due to hydration. Even the definition of "hydrated" radius varies. For example, when determined with molecular dynamics simulations that reproduce experimental hydration energies, sometimes the hydrated radius is defined as the first *peak* of the oxygen density profile away from the centre of the ion (called a Radial Distribution Function, as shown on Figure 2-3), and other times it is defined as the first *base* of the first oxygen density profile. This further supports that it is best to use data reported by one source so that trends are consistent.
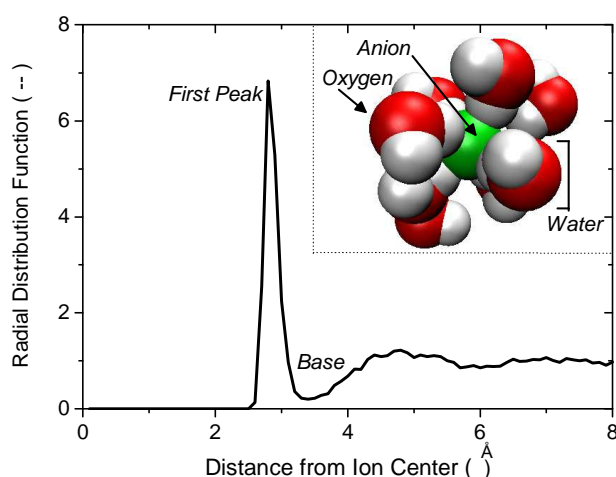
Figure 2-3. Example radial distribution function showing the possible definitions of hydrated radius made from the first peak (most common) or base of the oxygen density profile away from the centre of an ion.

For membrane applications, the Stokes radius is commonly used to describe the effective ion size [36, 92, 93]. Stokes radius represents the effective size of a theoretical solid sphere that diffuses at the same speed as the ion of interest [81]. An ion with high mobility will have a small Stokes radius and vice versa. Although Stokes radius represents mobility, it is inherently unrealistic as it is not a measurement of the physical size of the hydrated entity. Stokes radius, r_s (m) is calculated as

$$r_s = \frac{k_B T}{6\pi\eta D},$$
<div align="right">Equation 2</div>

where k_B is the Boltzmann constant (J.mol^{-1}.K^{-1}), η is viscosity (kg.m^{-1}.s^{-1}), T is temperature (K) and D is the solute diffusion coefficient (m^2.s^{-1}). Other radii which are sometimes reported are Born's radius, cavity radius and Pauling radius, but as these are not used anywhere in this thesis they will not be described.

Obviously, this discrepancy in understanding the effective size of a solute has major implications for understanding fundamental ion behaviour. Hussain *et al.* [92] evaluated the effect of different ion sizes on the prediction of NF systems and found that it, unsurprisingly, has a considerable effect. Understanding how ions interact at a fundamental level, and in particular with membranes, remains a challenge. Improvements in this area would provide a valuable contribution to the field.

2.1.3 Impact of pH on Ion Properties

Inorganic contaminants are significantly impacted by water quality characteristics, and in particular, pH. Solution pH has a significant role in the speciation of elements as the number of hydrogen atoms available for interaction as well as oxidation-reduction transformations will determine what type, relative amount, charge, and form of a species is present [72, 94]. For example, Smedley and Kinniburgh determined two main triggers leading to arsenic release in natural waters. First, the development of high pH conditions (pH >8.5) in semi-arid or arid environments leads to desorption of adsorbed arsenic (especially As^{+5}) from mineral oxides. The second trigger occurs at near neutral pH values with strongly reducing conditions, which again results in the desorption of arsenic (As^{+3} is relatively abundant in this case) [29]. Typical pH values of groundwaters vary significantly globally, and thus an understanding of how inorganic trace contaminants behave at varying pH levels is important to understanding how to best reduce them to safe levels [72]. The specific effect of pH on contaminant speciation and filtration with NF/RO will be discussed in Section 2.3.5 and will be the subject of results presented in Chapters 4 and 5.

2.1.4 Ion Pairing

Another phenomenon worth mentioning about the interaction of ions in bulk water is ion pairing. Ion pairing occurs when oppositely-charged ions are close together and the energy of their mutual electrical attraction is considerably greater than their thermal energy ($2kT$, for a 1:1 electrolyte). The electrical attraction pulls the ions together while the thermal energy causes the motion of the ions. Therefore, when the electrical attraction is attractive enough, a new entity is formed which is which is stable enough to persist through a number of collisions with solvent molecules [76]. For a 1:1 symmetrical electrolyte, like sodium chloride, the resulting ion pair has no net charge, but is still has a dipole moment due to its polarization [76]. For this type of electrolyte, the rule of thumb for the critical distance where ion pairing can potentially occur is at a distance of $q = 2kT = 3.57 \cdot 10^{-10}$ m (at 25 °C). At distances greater than this, the attractive forces between the ions are not strong enough for pairing to occur [76]. Of

course, like all ion interactions, this becomes complicated because ion pairing is more likely for some electrolytes than others [76]. Optimal conditions for ion pairing occur when a cation is weakly hydrated (potassium is much more likely to pair than sodium), and an anion, especially polyatomic, has an inherently polarizable structure. In this situation with a weakly hydrated cation and very polarizable anion, the attractive forces between the ions can more easily overcome the hydration forces of each individual ion. Given these optimal conditions, pairing is likely for potassium nitrate in water. This is because nitrate has a planar configuration which may allow a cation (in particular weakly hydrated potassium) to approach in one direction with distances less than the critical distance of roughly $3.57 \cdot 10^{-10}$ m. It has been roughly estimated that about 3% of 0.1 M potassium nitrate is paired in bulk solution, but this is very difficult to measure [76].

Molecular dynamics simulations have been used to examine potential ion pairing in alkali halide solutions to overcome the limitations of experimental measurements [95-97]. Fennell *et al.* [95] showed that there are a number of different ways in which alkali halides can be paired: contact ion pairing, solvent-shared ion pairing and solvent-separated ion pairing, which are shown in Figure 2-4 [95, 97]. Different types of pairing involve different interactions with the hydrated later of the paired ions and are driven by the most energetically favourable arrangement. Although ion pairing is not the focus of this work, it is mentioned as it is directly related to ion hydration, ion interactions and ion properties in water.
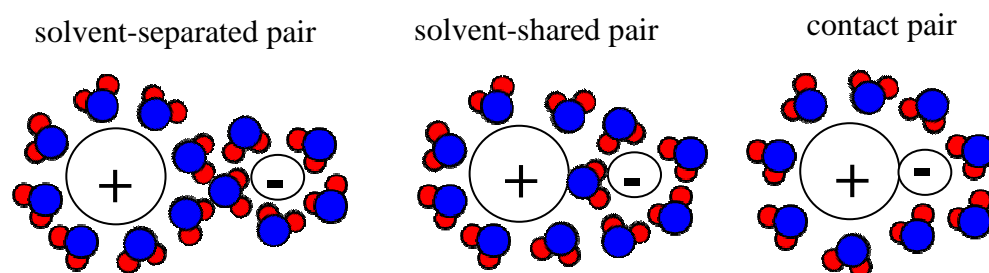
Figure 2-4. Different types of ion pairing adapted from [97].

The properties of ions in water were described in order to provide a basis for understanding transport mechanisms of NR/RO. Ion properties are affected by

interactions with water molecules and environmental factors such as pH and the presence of other ions. As such, these parameters will also affect the transport of ions through membranes. The next section discusses the use of NF/RO for the removal of inorganic contaminants.

2.2 *Nanofiltration and Reverse Osmosis for Inorganic Contaminant Removal*

NF/RO membranes are well-accepted water treatment technologies capable of desalination and reducing concentrations of other compounds found in natural waters. NF removes multivalent ions and has high organics removal, while RO retains both mono- and multivalent ions. NF/RO membranes are typically hydrophilic, negatively-charged polymers, and removal of ions tends to be specific to the particular membrane and ion characteristics and speciation [94]. NF/RO membranes can be quite effective at reducing nitrate, arsenic, aluminium, fluoride, boron, and uranium concentrations in natural waters [53, 57, 98-103].

The underlying separation principles of NF/RO membranes involve the combination of electrostatic and steric interactions associated with charge shielding, Donnan exclusion, and ion hydration as well as other effects such as diffusion and convection [54, 94, 98]. Ion transfer through NF/RO is therefore affected by membrane characteristics, operation parameters, and feed water characteristics. Specifically, membrane surface charge, chemistry, thickness, pore size and age of membrane, transmembrane pressure, and hydrodynamics regimes as well as feed water composition, pH, and temperature all contribute in varying degrees to ion passage through the membrane [104].

This section will discuss the primary mechanisms of NF/RO and how operating conditions affect them.

2.2.1 Steric Hindrance

Size exclusion, or steric hindrance, is an important mechanism of ion retention that is based on the physical size of a solute. Size exclusion refers to the process in which the size of a solute is larger than the pore size. Thus, the solute can not fit through the membrane pore and is retained, as shown on Figure 2-5. In this case, both ions are too large to "fit" into the membrane pore. This is like a sieving phenomenon, but in reality the interactions are complex because the neither the size of the solutes nor pores is uniform [105]. The transport and removal of ions during the membrane process is significantly impacted by hydrated radii and strength of hydration shells because the variations in hydrated ion size determine which ions will be able to pass through the membrane pores via convection or diffusion [77, 106, 107]. Ions with relatively small crystal radii have higher charge, higher hydration numbers, larger hydrated radii, and hold hydration shells more strongly [77]. Conversely, ions with larger crystal radii have weaker hydration shells and smaller hydrated radii, and hence may be able to detach from their hydration layer when passing through the membrane [77]. In Figure 2-5, both the ions alone and the ions with their associated first hydration shell are larger than the pore, but this is not always the case.
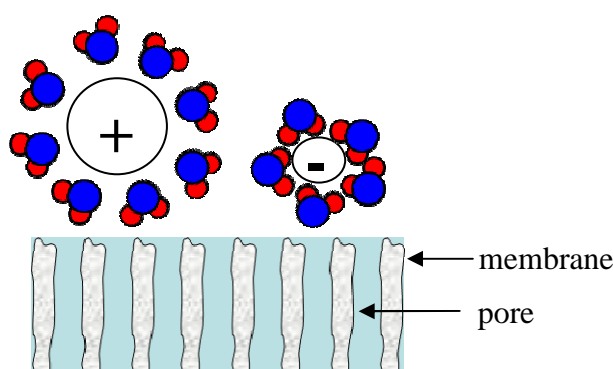
Figure 2-5. Simplified schematic of ions retained by the steric hindrance mechanism in a membrane with uniform pore sizes.

Tansel *et al.* showed that the ion permeability through NF is strongly correlated with hydrated radii (shown on Table 2-1) [77]. Ions with relatively small crystal radii, high hydration number, strong energies of hydration and large hydrated radii (*eg.* Mg^{2+} and Ca^{2+}) were effectively removed by both dead-end and cross flow NF modules.

Alternatively, ions with larger crystal radii such as K^+ and Na^+ have weaker hydration shells and smaller hydrated radii, and hence may be able to detach from their hydration layer while passing through the NF membrane unretained [77]. For example, Favre-Réguillon *et al.* explain that higher rejection of Mg^{2+} compared with Ca^{2+} in a NF experiment may be due to the fact that magnesium ions, although smaller, display larger hydrated diameters than those of calcium ions [100]. The strength of hydration is impacted by ionic structure and water composition as well as environmental factors such as pH, ionic strength, and temperature [77, 108]. Results from another study indicate that if retention trends are not consistent with the size of the hydrated ions, charge exclusion is likely the predominant mechanism [108]. Thus, the effective solute size directly impacts size exclusion and it is very important to understand the role of hydration in this process in order to know which ions may be excluded under what conditions. If dehydration occurs during transport, this reduces the effective solute size and hence reduces retention due to size exclusion.

2.2.2 Charge Interactions

Another prevailing NF/RO mechanism, and the only established non-sieving mechanism, is charge interactions. Charge interactions between the charged membrane and ions in solution occur [77, 109-111]. This results in charge exclusion between the typically negatively-charged membrane surface and the ions present in solution. This phenomenon is called the Donnan potential. Anions are repelled from the membrane's surface, thus increasing anion rejection by the membrane, as shown on Figure 2-6 [77, 98, 101, 104]. The Donnan potential is impacted by surface charge and chemistry (membrane specific), feed water composition (including pH, electrolyte concentrations, and ionic strength), as well as flux and hydrodynamic conditions [77, 111-113]. The membrane charge density depends on ionic strength and concentration, and can be partially attributed to ion adsorption on the membrane surface [114].
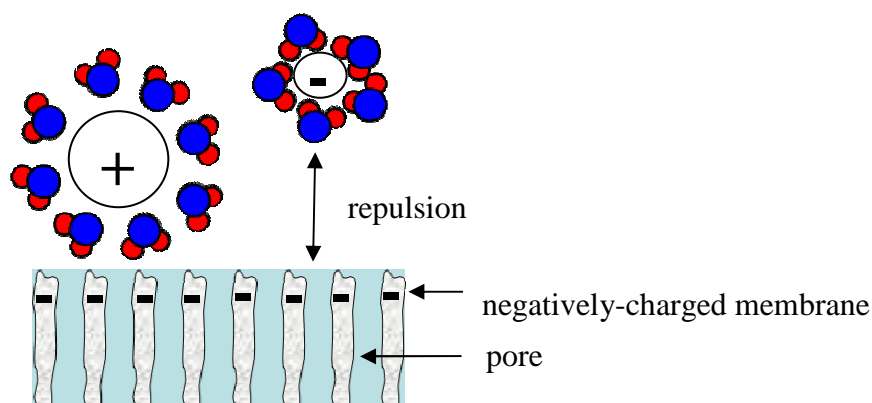
Figure 2-6. Simplified schematic of an anion repelled from a negatively charged membrane surface.

In the Donnan exclusion model, the rejection of the multicharge anions by a negatively charged membrane is highest, whereas that of the bivalent or monovalent cations is the lowest [100]. The Donnan potential is impacted by the membrane surface charge and chemistry as well as the feed water composition [77, 98, 101, 104]. Membrane surface charge in particular is an important parameter impacting compound retention. Most thin film composite membranes have a negative surface charge at neutral pH due to deprotonated acidic functional groups, but surface charge has been found to vary between membranes and is dependent upon feed water chemistry including pH, electrolyte concentrations, and the presence of natural organic matter. The rejection of inorganic ions is reported to increase during conditions favouring a membrane surface charge that can electrostatically repulse the ion being studied [111]. Increased feed water ionic strength, especially in the form of divalent cations such as calcium and magnesium, results in a reduced negative surface charge since the ions can bind to the negatively charged membrane surface, subsequently resulting in a reduced rejection of inorganic ions [111]. Bellona and Drewes [111] hypothesized that charged organic compounds with molecular weight similar to the molecular weight cut-off of a membrane are less affected by these decreased electrostatic interactions due to the dominant role of steric exclusion in the rejection of these compounds. However, the removal of charged compounds of smaller molecular weight than the molecular weight cut-off can be affected by the reduced negative surface charge of a membrane [111]. Minimum salt rejection has been observed at the isoelectric point (point of zero charge) of the NF membrane surface [115] which is likely due to the minimal ionic interactions between the membrane surface and the solutes at that point. This demonstrates that

charge interactions are very important for membrane filtration and depend both on membrane and solute properties.

The electroneutrality condition requires that charge must be balanced on either side of the membrane. This means that in the case of a negatively charged membrane, the negatively charged co-ion would be the limiting concentration here (because of repulsion) and thus the transport of positively charged ions will have to balance that of the co-ions. Thus, ions with a higher or lower permeability affect the permeability of other ions in order to maintain electrostatic neutrality. A similar principle could be linked to dehydration, where transport may be limited according to solute properties such as hydrated size or strength, while electroneutrality requirements must still be maintained.

Dielectric exclusion is another charge interaction that is a proposed cause for ion rejection in NF. Dielectric exclusion occurs due to the polarization at the water/membrane interface [109, 116, 117]. It is caused by the interactions of ions with the bound electric charges induced at the interfaces of media of different dielectric constants (*eg*. water and polymer). Dielectric exclusion can actually enhance Donnan exclusion making these net charge interactions significant under certain conditions.

Charge interactions will be considered throughout this thesis, and particularly in Chapters 4 and 5 where pH is a key variable (pH directly impacts charge interactions as will be discussed in Section 2.3.5).

2.2.3 Diffusion and Convection

Diffusion is a balance of two forces: (1) the gradient of chemical potential for a particular ionic species and (2) an electric field created by the motion of oppositely charged ions [76]. Electroneutrality requires that anions and cations must move at the same overall speed. Thus, less mobile ions must speed up and more mobile ones must slow down in order to keep the forces balanced [76]. Even in bulk solutions, diffusive interactions become very complicated in non-dilute (>0.01 M) solutions because the motion of solvent molecules must be considered as well as that of the solute [76].

Diffusion is a concentration driven process that follows the general form of Fick's first law:

$$J_{diffusive} = -D\frac{dc}{dx},$$

Equation 3

where $J_{diffusive}$ is the diffusive flux (mol.h^{-1}.m^{-2}), dc/dx is the concentration gradient across the membrane (mol.m^{-4}) and D is the diffusion coefficient (m^2.s^{-1}) of the solute of interest. In NF models, the diffusion coefficient is corrected for the hindered nature of the pore and this will be described in Section 2.4.

Diffusion in membranes is hindered but the fundamental process remains the same: for ions to move from a concentrated side (the feed) to a dilute side (the permeate). The difference is that there now is a membrane in between. Interactions with the membrane affect diffusion [118], and also the concentration of water in the membrane (degree of swelling) [119, 120]. This is obviously membrane-specific and because it depends on the structure and chemical nature of the polymer, there is significant variation [119]. The predictive ability of theoretical models remains very limited because they are not able to account for the very individual character of polymer-solvent-solute interactions and the exact polymer composition of commercial membranes is proprietary [119]. Diffusion is a dominant salt transport mechanism in many NF/RO membranes.

Convective transport involves the solutes being "carried" in the solvent stream through the membrane. In convection, larger solutes are better retained via steric hindrance. Convective transport is directly related to permeate flux (and thus applied pressure) and concentration.

Diffusion and convection are difficult to separate from each other in pressure driven systems because both occur simultaneously. Both are affected by the solute properties and concentration. However, different operating conditions, and in particular pressure, lead conditions to be more conducive to the dominant effect of one over the other. This will be discussed in more detail in Section 2.2.8.

As both diffusion and convection are strongly influenced by solute size, again the necessity for a better understanding of the effective size of a hydrated ion during membrane transport is highlighted.

2.2.4 Precipitation

Accumulation of solutes on the membrane surface can result from precipitation due to concentrations at the membrane surface exceeding solubility limits [121]. Deposit formation and the possible consequent variation of membrane characteristics affect apparent retention. The actual concentration at the surface (or boundary layer concentration) depends on membrane characteristics, solution chemistry (*eg.* feed concentration and pH), and operating conditions (*eg.* pressure, cross flow velocity, hydrodynamics), and cannot be measured. Deposition on the membrane surface can result in membrane scaling, which reduces permeate flux and quality, requires chemical cleaning, and may lead to physical damage of the membranes and hence a reduced lifetime. This is of particular interest for the filtration of natural groundwaters, which is the subject of Chapter 4, because carbonate-based solutes (*eg.* $MgCO_3$), common in natural waters, are highly insoluble and thus may precipitate during filtration which can affect both retention and flux.

2.2.5 Dehydration

The specific role of hydration in controlling transport in NF is not yet well-understood. A number of studies have correlated ion transport with hydrated radius [77, 122] or hydration energy [122], rather than ionic radius. It has been observed several times that ions with smaller ionic radii have higher hydration energy and larger hydrated radii which retards their transport through the membrane [77, 85, 100, 122-124]. As such, it is not the ionic size that dictates transport, but the hydrated size. Further, ions with less strongly bound shells may actually detach from their hydration layer while passing through membrane [77, 125]. This has direct implication on the size exclusion mechanism (Section 2.2.1) if the effective size of the ion is actually changing during the transport process. The effective ion size (and hydration state) thus directly impacts all mechanisms of transport.

Due to the inability to measure this effect directly experimentally, some simulations have been conducted to study the effect of potential dehydration through narrow pores. This effect has been simulated in carbon nanotube membranes, where ions were shown to have different energy barriers depending on ion type, pore size and pressure when entering hydrophobic pores as a consequence of dehydration [126, 127]. The energetic expense of chloride transport in cylindrical Si_3N_4 nanopores was also related to the stripping of ion hydration layers [128]. Most of the work in this area has focused on ions relevant to biological channels such as potassium and sodium [129, 130]. The results of the relevant simulations will be discussed in Section 2.5. A primary objective of this thesis is to explore the effect of dehydration on ions relevant to drinking water purification, namely fluoride, chloride, nitrate and nitrite, which will provide new understanding of membrane selectivity.

Understanding the role of hydration/dehydration in ion transport is very important because it essentially affects all of the retention mechanisms discussed. Namely, the effective size will be affected according to hydration state (hydrated, dehydrated or partially hydrated), and thus steric interactions will be impacted. Diffusion and convection will also be affected by hydration state. Charge interactions may also be affected as strong hydration layers may shield charge repulsion.

2.2.6 Ion Pairing

An NF/RO mechanism which has been proposed is that ions can transport through membranes paired together [131]. The rationale for this is that the difference conditions near the membrane surface (in particular the increased concentration) can make ion pairing more amenable for certain ions (such as potassium nitrate). If 1:1 ions are paired, the net charge of the paired entity is neutral so charge repulsion would be minimized. Matsumoto *et al.* [131] demonstrated that ion pairing was substantial in a charged, low-water-content membrane both theoretically and experimentally. Ion pairing was used to explain the greater rejection of Na_2SO_4 (< 1 % paired) as compared to $MgSO_4$ (16 – 17 % paired) [132]. However, another study concluded that ion-pairing was not responsible for the transport of NaCl, Na_2SO_4, $MgCl_2$ or $CdSO_4$ in commercial polar RO and NF membranes [133]. Rather, it was suggested that coupled

transport occurs where individual ions partition and transport in a way that maintains the electroneutrality requirement [133]. This remains an area which is not yet well-understood, and although it is not the focus of this work, it is relevant to fundamental ion transport in membranes.

2.2.7 Sorptive Interactions

Although sorptive interactions are not a focus of this work, it is important to mention them for the sake of completeness. Adsorption is primarily related to the organic solutes and generally occurs when they have a high hydrogen bonding capacity and are sparingly soluble in water [134]. This allows them to have attractive interactions with the membrane material. Water flux in RO membranes is also believed to be due in part to a sorption-diffusion process and thus greatly dependent on the waters ability to form hydrogen bonds with the hydrophilic groups of the membrane polymer [135]. This adsorptive water binding to the membrane can hinder the flux. Although usually associated with organic solutes, higher partitioning of nitrate compared with chloride on a thin film composite membrane has been observed [136]. For inorganic contaminants, sorptive interactions are generally much smaller than dominate charge and size interactions which are the focus of this work.

2.2.8 Interplay Between Mechanisms

In pressure driven NF/RO, there is rarely only one mechanism that affects transport. The interplay between mechanisms is complex and strongly depends on operating parameters, solute properties and membrane properties. The dominant retention mechanism depends on the specific compound characteristics, feed solution chemistry, membrane characteristics (especially charge), and operational parameters (in particular applied pressure) [37, 107, 108, 137-143]. Theoretical models using the extended Nernst-Planck (ENP) equation have been used to predict the relative influence of contributing mechanisms, namely convection (pressure gradient), diffusion (concentration gradient) and electromigration (electric potential gradient) [109, 144-147] and these models will be explained in more detail in Section 2.4. If dehydration occurs as a part of transport, it will directly impact the effective solute size and thus

directly contribute to both convective and diffusive interactions. A summary of the mechanisms discussed is shown in Table 2-2 with general guidelines of when one particular mechanism may be dominant. In practice, the dominant mechanism is highly dependent on operating parameters, solute properties and membrane properties and thus this general summary is not applicable to every circumstance.

Table 2-2. NF/RO mechanism and conditions which are amenable to that particular mechanism. Note that this is meant to be qualitative and general, as conditions for a particular mechanism to be dominant are highly dependent on operating parameters, solute properties and membrane properties.

Mechanism	Conditions When Dominant
Steric Hindrance	when the size of the solute (both hydrated and ionic size) are much larger than the narrowest part of the pore
Charge Repulsion/ Electromigration	when the membrane is highly charged (typically at high pH values) and multivalent ions are freely present in solution, at high membrane thickness to porosity ratios
Diffusion	when the size of the solute (both hydrated and ionic size) are smaller than the narrowest part of the pore (or in non-porous membranes), at low pressure conditions, at low membrane thickness to porosity ratios.
Convection	at high pressure and flow conditions (*eg.* high flux), especially when pore is larger than the solute, at high membrane thickness to porosity ratios. The contribution of convection to salt transport in the active layer of most thin film composite NF/RO membranes is small [148-152]. The relative contribution of diffusion and convection can be estimated by the Peclet (Pe) number. Typical values for NF membranes for volumetric flux and the thickness to porosity ratio, respectively, are on the order of 10^{-5} m.s^{-1} and 10^{-6} m. If Pe is calculated from the typical value of ion diffusivity in bulk water (on the order of 10^{-9} m^2.s), Pe $\approx 10^{-2}$, suggesting that the contribution of convection is small and diffusion dominates (since Pe $<$ 1). However, if pore diffusivities are used in this calculation (on the order of 10^{-11} to 10^{-13}, as determined using diffusion cell experiments), Pe is in the range of 0.1 to 10, and the conclusion about if diffusion or convection dominates may be different. The balance between diffusion and convection is thus complex and cannot be generally concluded for every case.
Precipitation	at concentrations above saturation level at the membrane surface for insoluble solutes such as Ca_2CO_3 or Mg_2CO_3
Dehydration	yet to be evaluated, but expected to be dependent on hydrated size to pore size ratio, and hydration strength of the solute
Ion Pairing	yet to be evaluated, but expected only at very high concentrations
Sorptive Interactions	when there are highly favourable interactions between membrane polymers and organic solutes

Szymczyk *et al.* [144] conducted a thorough review of the impact of specific parameters (pore size, membrane charge density, volumetric flux, and thickness to porosity ratio) on the relative contributions of convection, diffusion and electromigration to electrolyte transport. This review used the framework of the Donnan steric pore model (DSPM) based on the ENP equation (the details of the model will be discussed in Section 2.4). In summary, it was found that diffusive transport is expected to be dominant under conditions with low permeate flux, low membrane thickness to porosity ratio, and high membrane charge. Convection is expected to be dominant with high permeate flux and membrane thickness to porosity ratio and/or low membrane charge density. Electromigration never dominated transport when cations and anions had identical diffusion coefficients. With unequal diffusion coefficients (the case in practice) electromigration was the dominant mechanism for certain values of membrane charge.

A schematic of how convection, diffusion and electromigration all occur at the same time is shown in Figure 2-7 [145]. Here, there is a positive convective and diffusive drive from a pressure and concentration gradient for both co-ions (same charge as the membrane) and counter-ions (opposite charge as the membrane). The electromigration attraction of the counter-ions to the membrane surface results from attractive charge interactions between, for example, a membrane with fixed negatively charged groups and positive ions (or vice versa). Thus, co-ions are excluded from the membrane and counter-ions are attracted, resulting in lower concentration of co-ions than counter-ions in the membrane. Note that all transport is in the direction of the permeate side with the exception of the electromigration of counter-ions oriented towards the feed solution. For any electrolyte, the sum of the total co-ion flux ($J_{co\text{-}ion}$, mol.h^{-1}.m^{-2}) must be equal to the total counter-ion flux ($J_{counter\text{-}ion}$, mol.h^{-1}.m^{-2}) [145]. Because the total flux of co-ions must equal that of the counter-ions to maintain electroneutrality, the convective flux of counter-ions must be larger in magnitude in order to balance the charge repulsion.
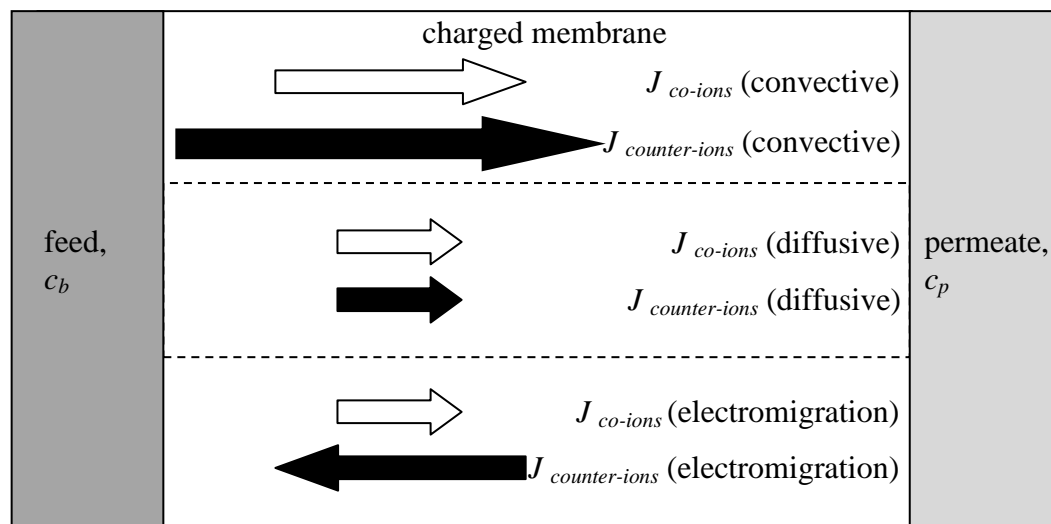
Figure 2-7. Schematic of interplay between diffusion, convection and electrostatic interactions in the case of positive retention and attraction of counter-ions to fixed charge groups on the membrane (adapted from [145]).

To illustrate potential interactions schematically in a different way, Figure 2-8 is provided. This figure shows a number of different interactions and mechanisms that can occur during transport. For example, the negative surface attracts positive cations towards it and repels negative ions (charge repulsion and Donnan equilibrium). Attractive forces can occur between fixed charge groups on the membrane material and positive cations. An ion may become dehydrated while transporting through the narrowest part of the pore (dehydration and/or size exclusion). Ion pairing can occur in free solution, while transporting or with fixed charged groups on the membrane. This shows the complexity of the interactions which are even further complicated when driving forces such as pressure, concentration and temperature are involved (which affect convection, diffusion and electromigration simultaneously, as shown on Figure 2-7).

Applied pressure

NF membrane with
negative functional groups

Membrane pore

Ion-pair

Free co-ion
Hydrated ion
Free counter-ion

$\bigoplus$ Counter-ion

$\bigominus$ Co-ion

$\bigominus$ Fixed charge
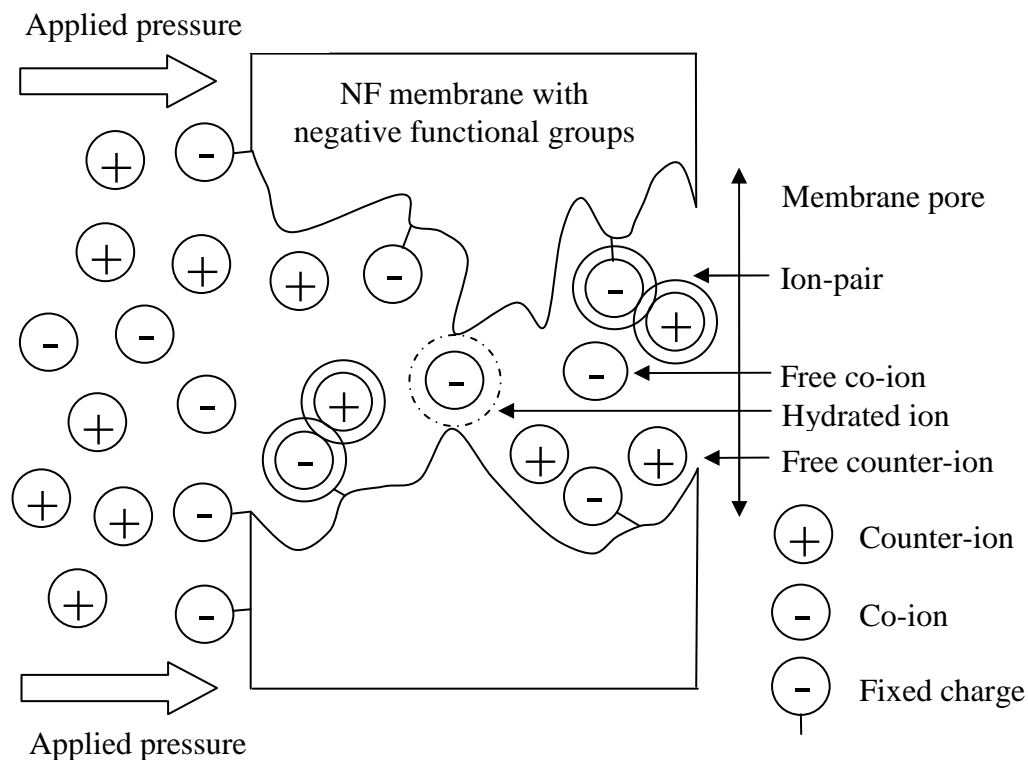
Applied pressure

Figure 2-8. Exaggerated schematic of potential interactions (adapted from [131]). A tortuous pore with fixed negative functional groups interacts with ions in solution, which are driven in the direction of flow due to an applied pressure.

2.3 *Impact of Operating Parameters on Inorganic Mass Transport in NF/RO*

Operating parameters such as pressure, flow, concentration, pH and temperature strongly affect mass transport. They affect the dominant mechanisms, the properties of the membrane, the properties of the solute and conditions at the membrane surface. The effect of each key operating parameter will be reviewed. Pressure, flow and concentration are discussed as these are relevant to Chapter 4, where changing renewable energy conditions impact each of these things. The importance of pH is discussed, as this is the subject of parts of Chapter 4 and Chapter 5. The impact of temperature and energy barriers on ionic transport are the subject of Chapter 7.

2.3.1   Impact of Pressure

Applied pressure directly influences the performance of NF/RO. Pressure is the driving force for convective flux and thus strongly impacts both flux and retention of solutes. Volumetric flux (J_v) is directly related to pressure by

$$J_v = \frac{\Delta P - \Delta \pi_{membrane}}{\eta R_{tot}}$$

Equation 4

where ΔP is the applied hydrostatic pressure (bar), $\Delta \pi$ is the osmotic pressure difference across the membrane (bar) (dependent on concentration and temperature), η is viscosity (mol.m^{-1}.s^{-1}) and R_{tot} (m) is the total resistance which includes the membrane itself and resistance due to other factors such as concentration polarization or fouling. The applied pressure must be larger than osmotic pressure at the membrane surface to induce transport.

Concentration polarization is a phenomenon that occurs in pressure-driven processes such as NF/RO [153, 154]. The retained, or partially retained, solutes can accumulate at the membrane surface where their concentration gradually increases. A schematic of a concentration profile is shown in Figure 2-9. Concentration polarization results in the concentration at the membrane surface (c_m) being higher than the concentration in the bulk (c_b). This effect is most significant at low flow and high pressure conditions. Backwards diffusion then occurs from the concentration at the membrane surface towards the bulk solution.
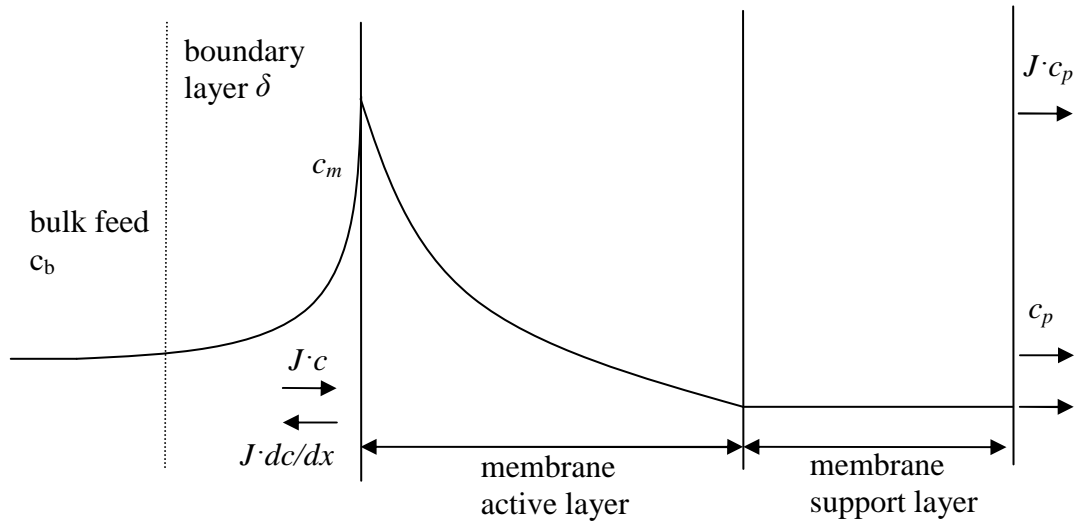
Figure 2-9. Generic schematic of concentration polarization (adapted from [153]). Note that the membrane support later is much thicker than the active layer in NF/RO but this was not shown on this schematic as the concentration drop occurs in the active layer when pressure is applied.

The concentration at the membrane surface can be calculated [153]. This is derived from film theory considering the steady state conditions which occur when the convective transport of the solute to the membrane equals the sum of the permeate flow and the diffusive back transport of the solute, as in

$$J_v c + D\frac{dc}{dx} = J_v c_p \, , \qquad\qquad \text{Equation 5}$$

where c is concentration (mol.L^{-1}), D is the diffusion coefficient (m^2.s^{-1}), dc/dx is the change in concentration across the membrane (mol.L^{-1}), and cp is permeate concentration (mol.L^{-1}). When Equation 5 is integrated across the boundary layer with the boundary conditions of $c = c_m$ at $x = 0$ and $c = c_b$ at $x = \delta$, this yields

$$\frac{c_m - c_p}{c_b - c_p} = exp\left(\frac{J_v \delta}{D}\right) = exp\left(J_v k_f\right) \qquad\qquad \text{Equation 6}$$

where δ/D is the mass transfer coefficient k_f (m.s^{-1}) which can be experimentally determined [154]. The relationship provided in Equation 6 can be used to correct

experimentally measured retention (using bulk and permeate concentrations that can be measured) for concentration polarization.

Concentration polarization results in increased osmotic pressure, which reduces the pressure driving force across the membrane. Thus, flux decreases and there can be an increased risk of scaling, which is an operational problem that can reduce membrane life. The conditions where concentration polarization is greatest is for high pressures and low crossflow velocity [155].

The impact of pressure on retention has been well-documented in the literature [38, 108, 140, 156-160]. In most cases, a increase in retention with pressure is reported [38, 108, 140, 156, 158-160], which can be explained by the increased flux at higher pressures. At infinite fluxes, intrinsic retention approaches the reflection coefficient and observed retention tends to zero, according to film theory. The contribution of diffusion remains constant with pressure and the increase in water flux surmounts the increase in convective transport of the solute, and as such retention increases. Occasionally a decrease in retention with pressure is reported [38] or constant retention with pressure [108, 156] which can occur for relatively large solutes (as compared to the pore size), which are excluded due to their large size.

2.3.2 Impact of Concentration

The impact of concentration is closely linked to the impact of pressure due to concentration polarization. The retention of NaCl decreases with increasing concentration, which can be explained by the fact that the increased osmotic pressure difference results in a decrease in flux (and thus higher concentrations in the permeate). Another explanation is that at high concentrations of NaCl (and thus high ionic strengths), the electrical double layer of the membrane becomes thinner [143, 161]. This, in effect, implies that the membrane charge (and thus charge repulsion) has less influence as the concentration of salt increases [143, 161]. The thickness of the double layer is called the Debye length (κ^{-1}), and is defined as the thickness of the mobile layer where the potential has decreased to a value of the potential at the Stern plane (ψ_D) divided by e (e = 2.718). Debye length represents the distance from a charged surface where the electrical energy and thermal energy are balanced, and the physical

significance of this is shown on Figure 2-10. Debye length is concentration dependent. Detailed discussion of Debye length and the corresponding theories can be found in aquatic chemistry textbooks such as Stumm and Morgan [162]. For membranes with small pore sizes (such as Dow Filmtec BW30 or NF90), the effect of increasing concentration on retention is very small [143, 161]. On the other hand, the normalized flux of these same membranes was strongly reduced when concentration was increased [161]. This was explained because due to the shielding of the membrane charge by high ionic strength, the repulsion in the pores will decrease. This results in more pore blocking and hence lower fluxes. The most hydrophilic membrane still had the highest fluxes. In addition, increasing concentration increases the diffusive driving force across the membrane. It's important to consider the impacts of concentration both in bulk solution and at the membrane surface.
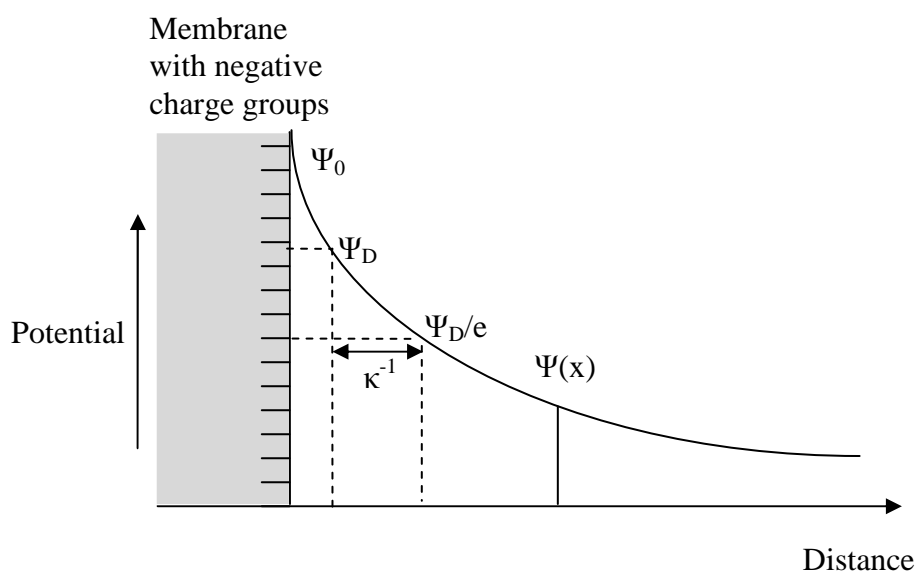
Figure 2-10. **Physical significance of Debye length (κ^{-1}, nm) represented by chemical potential decreasing with distance away from the membrane surface (adapted from [94, 110, 153]). Surface potential is ψ_0; the Stern potential is ψ_D, the transition from fixed to mobile charge, the actual potential affecting charged solutes and cannot be measured; and κ^{-1} is defined as the thickness of the mobile layer where $\psi = \psi_D/e$.**

2.3.3 Impact of Flow

Flow impacts concentration polarization in addition to pressure. Crossflow velocity directly affects hydrodynamic conditions. Mass transport at the membrane surface is

theoretically related to fluid mechanics parameters such as crossflow velocity, solution viscosity, diffusion coefficients and dimensions of the inlet. These interactions can be represented by empirical hydrodynamic relationships such as the Sherwood, Reynolds and Schmidt number [153, 154, 163, 164], however they are highly dependent on equipment setup due to hydrodynamic variability. In order to avoid this discrepancy, the concentration polarization level can be determined experimentally using a simple method described by Sutzkover *et al.* [154] which represents a net impact of all of the conditions affecting the membrane surface (flow, pressure and concentration). This method is described in Chapter 3.5 because it is based on experimental measurements. Koyuncu and Topacik [165] observed that increased crossflow velocity resulted in higher rejection of NaCl, which is attributed to less concentration polarization under high-flow conditions. This was most noticeable for low salt concentrations [165].

2.3.4 Impact of Varying Energy

As shown in the previous sections, operating conditions (in particular pressure, flow and concentration) significantly affect membrane performance and mechanisms. When a renewable energy source is used to directly power NF/RO (without battery storage), the fluctuations in power input consequently lead to direct changes in pressure and flow. Therefore, conditions at the membrane surface are continually changing and all mechanisms are subsequently affected. Consequently, varying energy leads to complicated non-steady state interactions and it becomes very difficult to isolate particular mechanisms.

There is minimal information in the literature that describes what impacts fluctuating energy may have on the effectiveness of the NF/RO membranes, particularly with regard to inorganic trace contaminants. One early study showed that variable feed flow velocities have very little effect upon the quality or quantity of the water, provided that the feed velocity is not reduced to zero [166]. Another study suggests that if flow through the membrane was discontinued for any great length of time (not formally assessed), the pressure dropped considerably when the system was restarted and the permeate salt concentration would overshoot to high values before returning to normal [167]. Park *et al.* [168] used wind energy to power a reverse osmosis system over

fluctuating conditions (wind speed, wind turbulence intensity and period of oscillation). For a feed water containing 2750 mg.L^{-1} NaCl, the system produced good quality permeate (< 600 mg.L^{-1}) for all conditions. At a higher feed concentration of 5500 mg.L^{-1} NaCl, fluctuations had a larger impact on performance and an average wind speed of > 7 m.s^{-1} was required to produce adequate permeate (< 1000 mg.L^{-1}). The studies which have been conducted on fluctuating energy have not evaluated the impact on trace contaminants. The area of RE-membrane systems opens an exciting realm of research questions and has importance in application-based design.

2.3.5 Impact of pH

As already discussed, NF/RO retention highly depends on both solute and membrane characteristics as well as operating conditions [169, 170]. Solution pH is very important because it affects not only the different forms (species) in which a solute is present in a solution (changing properties such as size, charge and hydration), but membrane characteristics (such as charge and pore size) as well [143]. Thus, pH can impacts both water flux and solute retention mechanisms (namely charge and size interactions), making pH an important parameter for ion retention in NF/RO [107, 112, 141, 171, 172].

Solute speciation depends on the specific conditions of the feed solution, including pH, ionic strength, total elemental concentrations, temperature, and pressure [173]. Different species of the same solute have different characteristics such as size and charge, which affect retention mechanisms. For example, if an uncharged solute is deprotonated at its acid dissociation constant (pK_a), charge exclusion may become significant. A change in species affects hydration state and consequently hydrated radius, thus impacting retention when size exclusion is important [37, 77].

Membrane characteristics such as zeta potential [174] and hence retention properties are affected by pH. Solution chemistry, in particular the presence of salts containing divalent ions, impacts zeta potential due to the preferential adsorption of divalent cations rather than divalent anions to the membrane surface especially in the higher pH range [174]. Generally, increasing feed water pH results in an increasingly negative

surface charge for most polymeric membranes. Subsequently, electrostatic interaction between ionic compounds and the membrane surface vary according to solution pH [143], with minimal retention typically occurring around the isoelectric point of the membrane surface due to the minimized electrostatic effects [104, 111, 138, 141, 172]. Additionally, pH impacts the dissociation of the functional groups on the membrane surface which can impact the "openness" of the pores [143]. A study by Childress and Elimelech [143] observed NaCl retention was directly related to membrane pore charge (rather than the membrane surface), with minimum retention at the isoelectric point of the membrane pores. However, this is not the case for all membranes [143]. The importance of pore charge is particularly important for "loose" membranes, when the hydrated radius of the solute is smaller than the pore radius [124, 143]. These studies show that pH can affect both the charge and pore size of the membrane.

Many of the current research efforts towards understanding pH impact have focused on evaluating arsenic removal specifically because of increased attention to this particular contaminant as millions of people worldwide are at risk of acute or chronic arsenic poisoning due to arsenic naturally occurring in groundwater [27, 28, 175]. One study concluded that pH control for RO membrane feed water is essential for the successful removal of arsenic but that the effect of solution pH on antimony removal is negligible, largely due to the chemistry of both compounds' species in natural waters [176]. Another study looked at arsenic species individually, determining that the removal of arsenate (As^{5+}) was nearly steady from pHs in the range of 3 to 10, but that arsenite (As^{3+}) rejection increased approximately above pH 7. These results were explained by the chemical equilibrium of arsenic compounds [177]. Other studies have also concluded that pH affects arsenic removal, with total arsenic rejection increasing with increasing pH [175, 178, 179].

Several studies have also assessed the impact of pH on the removal of other trace contaminants. A study evaluating the rejection of anionic model substances with NF determined that the extent of retention of multivalent salts significantly depends on pH and membrane characteristics [38]. Other studies have focused specifically on boron removal, and have determined that the rejection of boron also depends greatly on pH, with highest rejection occurring at pH above approximately 10.5 to 11 [99, 180].

Nitrate rejection was shown to increase with pH between 5 and 9 for some membranes in a study that varied pH, nitrate and sulphate ion concentration [54]. Ballet *et al.* concluded that phosphate retention increased from 40% to 95% when the pH of solution increases from 2.8 to 6 and then the phosphate rejection remained almost constant from pH 6 to 10 [108]. The large increase in rejection observed at low pHs is likely caused by a combination of the increase of phosphate ions (mostly $H_2PO_4^-$) and the membrane charge becoming increasingly positive [108]. The subsequent levelling-off of retention is explained because an increasingly negative surface can only reject negatively charged solutes to a certain level before the effect is offset by pore expansion or membrane swelling [108]. Bellona and Drewes made a similar observation when they assessed the impact of pH on the retention of several organic acids [111]. Increasing feed water pH from 3 to 7 resulted in a significant increase in rejection of organic acids which closely follows the percentage of the deprotonated species for each of the compounds and can be explained by a combination of the solutes becoming more deprotonated and the membrane charge becoming increasingly negative resulting in an increased degree of electrostatic repulsion [111]. The maximum rejection of lactate was found at a neutral pH, since the increase of charge repulsion at higher pH was cancelled by a decreased sieving effect through membrane swelling as the pH increased [111]. Bellona and Drewes hypothesized that the increase in permeability as a result of increased surface electronegativity may offset the expected increase in electrostatic repulsion between the membrane and solute [111]. Based on their experiments, it appears that an increasingly negative surface charge can only reject negatively charged solutes to a certain level before the effect is offset by pore expansion or membrane swelling [111]. Other studies have also reported that rejection of organic acids increased as the pH approached the pK_a [181, 182]. All of these results emphasize the importance of pH on trace contaminant removal. This will thus be the subject of Chapter 4, where the impact of pH on the retention of real groundwater is evaluated, and subsequently the subject of Chapter 5 where the impact of pH specifically on the removal of nitrate, fluoride and boron is addressed.

2.3.6 Impact of Temperature

Temperature also affects transport in NF/RO. Primarily, temperature increases the process of diffusion because molecules at higher temperature have more internal energy. By increasing energy, the proportion of solutes with energy greater than the activation energy of transport is significantly higher, so the overall transport increases. The activation is due to the hindered nature of transport that occurs when membrane pores are similar to the ionic and/or hydrated size of water and dissolved solutes. Because transport through the pores can be substantially hindered, transport is subsequently an "activated process". Each of the mechanisms contributes to the net activation energy, which is the energy barrier that needs to be overcome in order for transport to occur. Because of the strong influence of temperature on internal energy, temperature is a driver which easily affects the proportion of ions with sufficient energy to overcome the barrier to transport. The increase in ion transport with temperature is usually explained by a reduction in solvent viscosity, an increase in solvent diffusion coefficient, an increase in polymer chain mobility [163, 183-185] or a change in pore size/membrane structure (*eg.* swelling) [136, 183, 185-187].

Although NF/RO are conventionally operated at ambient temperatures, a rapid increase in proposed NF/RO applications such as water treatment in the sugar and textile industry and purification of condensate water from power generators have instilled interest in understanding the effect of temperature on NF/RO transport phenomena [163]. Further, temperature can be an important parameter if a membrane system is run in the field due to the ambient temperature and pumping heat.

2.3.7 Arrhenius Energy Barriers

Because temperature directly impacts NF/RO performance by increasing diffusion and changing polymeric properties, Arrhenius theory has been applied to NF/RO. This is important because Arrhenius theory allows a relationship to be established between temperature and mass transport or reaction rate by the determination of activation energy barriers. The temperature dependence of water and solute transport through

membranes and dense films has been described by the Arrhenius relationship in a number of cases [118, 119, 184, 186, 188-193]. The Arrhenius relationship relates temperature and solute flux, allowing a determination of the energy barrier from flux and temperature measurements [78] according to

$$\ln(k) = \ln(A) - \left(\frac{E_a}{R} \cdot \frac{1}{T} \right),$$ Equation 7

where k is solute flux (mol.h^{-1}.m^{-2}), A is a pre-exponential factor (--), R is the gas constant (kcal.mol^{-1}.K^{-1}), T is temperature (K) and E_a is the activation energy or energy barrier (kcal.mol^{-1}). The slope of a linear plot of ln(k) versus T^{-1} gives the energy barrier.

Activation energies for the transport of water and various solutes have been reported. However, thus far, energy barriers for NF have not been linked to energy requirements for the partial of full dehydration of an ion. This is important because experimentally determined energy barriers can be compared with fundamental energetics of ion hydration and ion transport. This is the interest of the current work (Chapter 7). A review of the activation energies that have been reported in the literature for transport in NF follow.

Activation energies of pure water permeation for RO and inorganic NF membranes have ranged from around 4.3 to 7.2 kcal.mol^{-1} [118, 163, 183, 188]. Another study reported energy barriers for pure water varied from that for Poiselle pore flow (4.6 kcal.mol^{-1}) for membranes with little or no salt rejection to nearly 6 kcal.mol^{-1} for membranes with salt rejections in the order of 99% [188]. For an aromatic polyamide membrane (Filmtec NF-200B), activation energy for pure water was around 6.0 kcal.mol^{-1} and about 8.4 kcal.mol^{-1} for a mixture of 9% (w/v) NaCl and 2% (w/v) lactate at pH 3 [190]. The increase in activation energy with concentrated solutions was explained by the degree of swelling of the polymeric membrane decreasing, thus becoming more geometrically constrained [119].

Energy barriers have also been reported for the transport of some neutral organic solutes. Neutral solutes were selected because they are well defined and lack complex

54

charge interactions [183]. Consistent with free volume theory of activated gas transport, activation energies of the permeability of neutral organic solutes (*eg.* sucrose, dextrose, glycerol, ethanol, methanol) in aqueous systems increased with Stokes radius and molecular weight indicating hindered diffusion in membrane pores [183]. Rejection of neutral solutes (raffinose) decreased with temperature due to steric hindrance/molecular sieving (resulting in relatively large energy barriers) [163].

For salt transport, apparent activation energies of salt transport in RO membranes have been reported in the range of 4.8 to 7.2 kcal.mol^{-1} [118, 188]. The energy barrier of potassium chloride ranged from 11.9 to 12.9 kcal.mol^{-1} in NF (NF200) from an ion-exchanged solution containing potassium clavulanate [193]. Tsuru *et al.* [163] compared the activation energy of different neutral and charged solutes in nanoporous titania membranes on the basis of molecular sieving and charge effects. They determined that the energy barrier for neutral solutes is actually larger than for electrolytes because neutral solutes have a more tortuous path through the membrane, where as charged solutes are "protected" by a double layer so they just pass quickly through the membrane. The electrolytes NaCl and MgCl$_2$ remained constant with temperature, which indicated charge effect (Donnan exclusion) was approximately constant and resulted in comparatively small energy barriers [163].

Energy barriers experimentally determined represent the net transport process, although some efforts have been made to split these into enthalpic and entropic thermodynamic contributions [136]. Enthalpy values were 3 – 5 times larger than entropic, suggesting a enthalpy-driven process [136]. Viscous and non-viscous contributions to energy barriers can be also be calculated [163, 183, 184]. If the activation energies are greater than just the viscous contribution to bulk diffusion, transport across the membrane is considered hindered [163, 183]. Non-viscous contributions to activation energies for pure water transport across two polymeric thin film composite NF membranes were calculated to be 0.931 and 1.53 kcal.mol^{-1} [183]. Although energy barriers have been looked at in a number of cases, there has been no link made yet to the potential dehydration of ions during pore transport.

2.4 Modelling of Ion Transport in Nanofiltration and Reverse Osmosis

A number of models are used to attempt to understand and predict ion transport in NF/RO, and a brief review of the typical descriptive models follows. There are different categories of NF/RO models, namely the irreversible thermodynamic model [194, 195], the Stefan-Maxwel model [196], and the hydrodynamic model (which has many slight variations based upon the same core principles). By far, the most widely used is the hydrodynamic model, which is based off the extended Nernst Planck (ENP) equation. A summary of available models is shown on Table 2-3.

The irreversible thermodynamic model and the Stefan-Maxwel model, although represented by different equations, are equivalent and consider the membrane to be a black box when deriving phenomenological equations [196]. The hydrodynamic model differs by assuming a geometrical model of the membrane, thus deriving all of the transport equations based on this geometry [105]. The hydrodynamic model has been widely used for NF pore size characterization because of its direct derivation from physical geometry [197-199] and reasonable ability to described NF performance [198]. The hydrodynamic model was used in this thesis to characterize membrane pore sizes (Chapter 3.2.3), and the details are discussed in the next section.

Alternatively, RO membranes are often considered to be dense, non-porous materials. As such, the pore assumption made in the hydrodynamic model is not applicable. Permeation is slower and rejection is not due to sieving but instead the solution diffusion mechanism. In these circumstances, sorption-diffusion is the most widely accepted explanation of water transport in RO membranes, and the solution diffusion model is commonly used to explain transport [135]. Some argue that in tight NF membranes of pore radius between 0.25 and 0.5 nm, both pore flow and sorption diffusion can occur [135]. However, the majority of the work presented in this thesis deals with NF and assumes that a pore (of some definition is present), and thus the hydrodynamic model is best because it accounts for this geometry.

Table 2-3. Summary of available models for transport in NF/RO.

Transport Model	Primary Application	Basis	Comments	Reference
Irreversible thermodynamic model	RO	Black box	Membrane assumed to be a black box, not possible to characterize structural or electrical properties	[194, 195]
Solution-diffusion model	RO	Black box	Solutes dissolve in the membrane material and then diffuse through the membrane according to a concentration gradient. Assumes uniform pressure within membrane and chemical potential is expressed only as a pressure gradient.	[135]
Stefan-Maxwell model	RO	Black box	Force balance conducted where sum of force on a molecule is balanced by friction. Based on diffusion. Application is low due to mathematical complexity.	[196]
Hydrodynamic model: Electrokinetic space-charge model	NF	ENP	Describes creeping flow of charged species through charged capillaries. Ions are treated as point charges defined by Poisson-Boltzmann equation. Ion transport across pore guided by the extended Nernst Planck equation. Application is limited by the numerical complexity of the calculations.	[200-203]
Hydrodynamic model: Improvements to the space-charge model	NF	ENP	Derived from space-charge models but with the approximation of radially homogenous ion concentration and potential across the pore (valid when surface charge density is relatively small and pores are sufficiently narrow, *eg.* normal NF conditions). There are many similar versions of this model.	[36, 199, 204-206]

Hydrodynamic model: Donnan-Steric Pore model	NF	ENP	Ion transport described by extended Nernst Planck, slightly modified to include hindered transport and equilibrium partitioning to a combination of electrical (Donnan) and sieving (steric) mechanisms. Most commonly used NF model.	[36]
Hydrodynamic model: Donnan-Steric Pore model with Dielectric Exclusion	NF	ENP	Based on DSPM model with incorporation of non-ideality of electrolyte solutions and concentration polarization at the membrane/feed solution interface. A program for numerical integration is provided by Geraldes and Brites Alves [164]	[164]

2.4.1 Extended Nernst Planck (ENP) Hydrodynamic Model

NF is often studied using models originally built on fundamental principles of hindered transport [207] and solution diffusion [135]. Currently, most NF models are based on numerically solving the ENP equation and include separate terms for diffusive, convective and electrostatic contributions [143, 144, 198, 208-211]. Detailed effects such as concentration polarization [212] and charge adsorption inside pores [213] are now being included in transport models. These models assume that NF membranes have pores [36, 37], yet a point of controversy remains about where actual NF 'pores' lie in the spectrum between discrete pore and dense material [38].

The Donnan steric partitioning pore model (DSPM), originally developed by Bowen *et al.* [210], is recognized as the most commonly used and has proven to be useful in describing relatively simple systems in NF [198]. This model is based on the ENP equation and accounts for ionic contributions from convection, diffusion and electromigration through cylindrical membrane pores. It is coupled with an assumption of electroneutrality within the membrane as well as Donnan equilibrium at both interfaces between the solution and membrane (*eg.* bulk and permeate side). The membrane is assumed to be a charged porous structure characterized by pore radius,

thickness to porosity ratio and charge density. The volumetric flux within the pore is assumed to follow a Hagan-Poiseuilli parabolic profile.

The principle of ENP is that solute flux ($j_{i,total}$, mol.m^{-2}.s^{-1}) of a particular solute i results from the sum of contributions from diffusion ($j_{i,diffusion}$, mol.m^{-2}.s^{-1}), convection ($j_{i,convection}$, mol.m^{-2}.s^{-1}) and electromigration ($j_{i,charge}$, mol.m^{-2}.s^{-1}) as in

$$j_{i,total} = j_{i,diffusion} + j_{i,charge} + j_{i,convection} .$$
<div align="right">Equation 8</div>

The detailed form of this equation, where the first term is diffusive, the second electrostatic and the third convective, is

$$j_i = -D_{i,p} \frac{dc_i}{dx} - \frac{z_i c_i D_{i,p} F}{RT} \frac{d\varphi_m}{dx} + K_{i,c} c_i J_v .$$
<div align="right">Equation 9</div>

Here, $D_{i,p}$ (m^2.s^{-1}) represents hindered diffusivity as defined by

$$D_{i,p} = K_{i,d} \cdot D_{i,\infty} ,$$
<div align="right">Equation 10</div>

where $D_{i,\infty}$ (m^2.s^{-1}) is the diffusion coefficient in bulk water and $K_{i,d}$ (dimensionless) is the diffusive hydrodynamic coefficient, which is dependent on the ratio of Stokes radius to pore radius (λ_i, dimensionless). It is very important to note that the solute size here is based on Stokes radius. In Equation 9, the difference in concentration across the membrane active layer is dc_i/dx (mol.m^{-4}). The charge term contains ionic valence (z_i, dimensionless), concentration in the membrane (c_i, mol.m^{-3}), Faraday's constant (F, C.mol^{-1}), the gas constant (R, J.mol^{-1}.K^{-1}), temperature (T, K) and the change of the potential across the active layer ($d\varphi_m/dx$, V.m^{-1}). The convective term contains the convective hydrodynamic coefficient $K_{i,c}$ (dimensionless) which is again dependent on λ_i, and the volumetric flux J_v (m^3.m^{-2}.s^{-1}). The relative contribution from each mechanism can be calculated by dividing the particular term ($j_{i,diffusion}$, $j_{i,convection}$, $j_{i,charge}$) by the total value of solute flux ($j_{i,total}$).

Another form of the expression is shown in

$$j_i = -D_{i,p} \frac{dc_i}{dx} - \frac{z_i c_i D_{i,p} F}{RT} \frac{d\varphi_m}{dx} + K_{i,c} c_i J_v - c_i D_{i,p} \frac{d[ln\,\gamma_i]}{dx} - \frac{c_i D_{i,p}}{RT} V_i \frac{dP}{dx}, \qquad \text{Eqn 11}$$

where all terms are as previously described, γ (mol.m^{-3}) is activity and *dP/dx* is a "pressure diffusion" term which comes from the pressure dependence of chemical potential [94, 214]. The two additional terms on this equation are not considered in the common NF models because they are considered to be negligible [204, 214] and for reasons of numerical simplicity.

One challenge in solving the ENP equation is the determination of hydrodynamic drag coefficients $K_{i,c}$ and $K_{i,d}$. Solutes moving in free solution are affected by a drag force, which is amplified when solutes move into a confined space where transport in hindered, such as a membrane pore. The restricted hydrodynamic coefficients include both a convective ($K_{i,c}$) and diffusive ($K_{i,d}$) term and are functions of the ratio of Stokes radius to pore radius (λ_i). Theoretical consideration of hindered transport in pores has been through reviewed [105] and there are a number of simplified correlations offered in the literature for specific values of λ_i. However, most of these expressions cover only a small range of λ_i which limits their use generally to ultrafiltration and microfiltration scale. The most complete expressions, valid for $0 \leq \lambda_i \leq 1$, were used in membrane characterization and were provided by Bungay and Brenner [215, 216], and reviewed by Deen [105]. The Nanofiltran program [164] for numerical integration utilized coefficients provided by Dechadilok and Deen [217], Mavrovouniotis and Brenner [218], and Ennis *et al.* [219].

Although the use of ENP theory was not the primary objective of this thesis, the principles outlined here were used to determine the relative mechanistic contributions of selected experimental data. Membrane characterization was completed using the method for neutral organic solutes outlined by Nghiem *et al.* [216] to determine membrane pore size and thickness to porosity ratio (described in detail in Chapter 3.2.3). During the analysis of experimental results presented in Chapter 7, the full ENP equation including charge was solved for ionic species using the Nanofiltran numerical

solver program developed by Geraldes and Brites Alves [164] in order to get a relative idea of the predicted mechanistic contributions (detailed results are not presented).

2.4.2 Limitations of Current Models

A major limitation in current NF models is the definition of solute size because most models use Stokes radius [36] or ionic radius [210], but this is inherently inaccurate due to the process of hydration. Ions are hydrated by a shell of dipolar water molecules, which means that the mobile entity is the ion with its hydrated shell rather than just the bare ion [76]. Despite the fact that hydration is neglected in NF models, the importance of hydration has been demonstrated numerous times experimentally, as discussed in detail in Sections 2.2.1 and 2.2.5 [77, 85, 122-125].

Hydration during pore transport processes is not addressed in NF models for a number of reasons. Firstly, the lack of available hydration data relevant to NF is a major limitation. Determining information about hydration free energies and structure is difficult. While data exists for a variety of ions [80-82], these lists are not comprehensive [85] and there is considerable discrepancy on reported values due to differing methods and assumptions used, as shown in Table 2-1. Data is insufficient for many drinking water contaminants, such as nitrite or nitrate. Secondly, hydration during pore transport includes complex interactions with the membrane; hence information on hydration in bulk solution cannot be applied within the pore. Thirdly, if partial or complete dehydration occurs during the process of transport [77, 125, 126], the hydrated radius is therefore a transient parameter, and very little is known about how to account for this in transport models. A more detailed approach is thus required that incorporates the interaction of water molecules with the ion as well as the interaction between the hydrated ion and the pore.

2.5 *Modelling of Ion Transport Using Molecular Dynamics*

Another tool that can be used in the modeling of ion transport is molecular dynamics (MD). The motivation is that MD may be used to specifically examine the impact of ion hydration on transport through membranes, which is an issue that is not addressed by current NF/RO models. MD is a classical simulation technique which allows the

determination of dynamic processes and interactions occurring at the atomic level in a given system [220, 221]. Much recent effort has been placed on examining the transport of water and ions through modelled biological ion channels and carbon nanotubes using MD [56, 222-225], however the application of MD techniques directly to NF has not largely been realized. The aim of Chapter 6 is to conduct MD simulations in order to look at the specific role of ion hydration during transport through generic pores of similar size to NF pores. Most of the focus in this area has been given to biological ion channels, so the influence of ion hydration in biological channels will be discussed. The hope is to extend the knowledge obtained in these studies to be relevant to NF.

The concepts and algorithms underlying MD are inherently complex, and thus, a balance must be made between accuracy and processing capabilities. Modern MD has been developed in enable high-performance simulation of molecules in environments of 100,000 atoms or more at realistic time scales (*eg.* 10^{-9} s for atoms) [220, 226]. This involves programmed algorithms for efficient numerical integration of Newtonian equations of motion, statistical mechanism methods for controlling temperature and pressure, efficient evaluation of electrostatic forces and the calculation of alchemical free energy differences. A program called NAMD [226] is a popular high-performance molecular dynamics simulation technique that has been successfully employed in a number of applications, especially in membrane biophysics [126, 127, 227, 228].

In biological ion channels, the molecular basis of selectivity is due in part to the ion's hydration properties [229-232]. Specific binding sites are located in selective transport proteins which identify the ions in their partially or fully dehydrated forms. Selection depends upon how well the interactions with the protein in this binding site can compensate for the energetic cost of ion dehydration [229]. The selectivity of most classes of anion channels corresponds to the lyotropic sequence, with weakly hydrated anions (*eg.* nitrate) showing a higher permeability than strongly hydrated anions (*eg.* fluoride) due to the dehydration energy required for transport [233, 234]. However, the majority of work on anionic selectivity in ion channels has largely focused on chloride because chloride is the only halogen ion used in abundance in biological systems. Chloride transport is typically controlled by chloride channel transport proteins which have an hourglass-shaped chloride selectivity filter which forms a row of binding sites

for the fully or partially dehydrated chloride ion [235, 236]. This filter is not highly selective between chloride and bromide [237], but this is not required in nature.

Alternatively, cation channels are highly selective and are constructed differently than the chloride channel proteins by having large aqueous vestibules within the transmembrane spanning portion of the membrane [229]. Differences in hydration are important in explaining the extremely precise selectivity in potassium channels (and other cation channels) that are up to 1000 times more permeable to potassium than sodium. Although sodium is a smaller ion, the energy required to remove the hydration shell is greater than the energy gained by interacting with the carbonyl oxygen in the channels as compared to potassium [238]. The ease of constraining a hydrated potassium ion inside a narrow pore relative to hydrated sodium or lithium is highly dependent on pore radius [239].

In carbon nanotube membranes, ions were shown to have different energy barriers depending on ion type, pore size and pressure when entering hydrophobic pores as a consequence of dehydration [126, 127]. The energetic expense of chloride transport in cylindrical Si_3N_4 nanopores was also directly related to the stripping of ion hydration layers [128].

The knowledge and techniques utilized in these MD simulations is highly relevant to NF, but very few studies have yet applied these principles to drinking water contaminants. The limited studies have involved simulating the transport of water and/or ions such as chloride in carbon nanotubes [126, 127, 223-225]. This presents an exciting opportunity to apply the knowledge of the transport of hydrated ions in biological channels to drinking water contaminants and NF.

2.5.1 Molecular Dynamics Theory

A brief review of the theory of MD is provided. Dynamic processes and fundamental atomic interactions are determined with MD [220, 221]. Successive configurations of the system over a series of time steps are generated using Newton's laws of motion, which can be stated as:

1. A body continues to move in a straight line at constant velocity unless a force acts upon it.

2. Force equals the rate of change of momentum.

3. To every action there is an equal and opposite reaction.

Trajectories are obtained using Newton's Second Law,

$$F_i = m_i \cdot a_i$$ Equation 12

by solving the differential equations embodied within it:

$$\frac{d^2 x_i}{dt^2} = \frac{F_{x_i}}{m_i}.$$ Equation 13

The trajectory can then be determined for any particle, i, of mass m_i (kg) along one coordinate x_i, with acceleration a_i (m.s^{-2}) and F_{xi} (kg.m.s^{-2}) being the force on that particle from a given direction. To clarify nomenclature, a "particle" in the MD context refers to the specific atom, ion or molecule under consideration, and does not refer to a colloidal solid of considerable size as sometimes described in the membrane field.

2.5.2 Force Field Parameters

In order to understand the motion of a given particle at each coordinate of a trajectory, the forces acting upon that particle must be known. One way in which these forces can be determined is by the use of a force field. The force on a particular atom is calculated at any given coordinate or trajectory within a system from the gradient of the energy potential,

$$F_i = \nabla V_{total}.$$ Equation 14

The simplified potential energy function ($V_{total,}$ kcal) incorporates both bonded ($V_{internal,}$ kcal) and non-bonded ($V_{external,}$ kcal) interactions [221] such that

64

$$V_{total} = V_{internal} + V_{external}.$$ Equation 15

The internal energy contributions ($V_{internal}$) are associated with covalently bonded atoms and is expressed as

$$V_{internal} = \sum_{bonds} k_b(b - b_0)^2 + \sum_{angles} k_\theta(\theta - \theta_0)^2 + \sum_{dihedrals} k_t[1 + cos(nt - \sigma)],$$ Equation 16

where b (Å) and θ (deg) are bond length and angle, respectively, subscript 0 signifies the equilibrium value, k is the associated force constant, n is multiplicity (dimensionless), t is torsion angle (deg) and σ is the phase (deg), each of which is described in the following text. The internal contributions account for covalent interactions between atoms in close proximity. In order to best explain these interactions, a generic schematic of a molecule showing these interactions is provided in Figure 2-11. The first two terms in Equation 16 define the bond stretching and angle terms which are treated harmonically. This keeps the bonds and angles values (b and θ, respectively) near the equilibrium points (b_0 and θ_0). Force constants k_b (kcal.mol^{-1}.Å^{-2}) and k_θ (kcal.mol^{-1}.rad^{-2}) are like spring constants associated with each term. The final bonding term, torsion, is applicable when there are 4 or more atoms in a molecule and it describes, for example, the angle between atoms 1-2 and 3-4 when viewed along the 2-3 bond. This angle is known as the torsion angle, t, and it is periodic in nature. The torsion force constant is k_t (kcal.mol^{-1}.rad^{-2}), n is multiplicity or periodicity and σ is the phase. The periodicity indicates the number of cycles per full rotation around the dihedral. The phase dictates the location of the maxima in the dihedral energy surface allowing for the location of the minima for a dihedral of $n=2$ to be shifted from 0° to 90°. Typically the phase is either 0° or 180°.
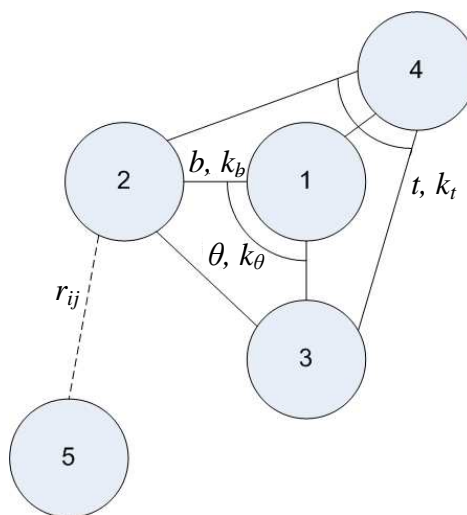
Figure 2-11. Generic representation of molecules to illustrate the various force field parameters (adapted from [221]).

Nonbonded interactions occur between all atoms in a system and strongly impact the behaviour of any atom. The external energy ($V_{external}$) represents nonbonded or intermolecular interactions between atoms and is calculated from

$$V_{external} = \sum_{\substack{nonbonded \\ atom\ pairs}} \left(\varepsilon_{ij} \left[\left(\frac{R_{\min/2,ij}}{r_{ij}} \right)^{12} - \left(\frac{R_{\min/2,ij}}{r_{ij}} \right)^{6} \right] + \frac{q_i q_j}{\varepsilon_D r_{ij}} \right), \qquad \text{Equation 17}$$

where ε_{ij} (kcal) is the potential energy well depth, $R_{min/2,ij}$ (m) is the distance between atoms i and j of minimum interaction energy, r_{ij} is the distance between atoms (m), q is ionic charge and ε_D is the dielectric constant. The term in square brackets in Equation 17 corresponds to the van der Waals (VDW) interactions. VDW interactions are typically reported as the Lennard-Jones (LJ) 6-12 term, which is the form shown in Equation 17. The r_{ij}^{-12} term represents the exchange repulsion between atoms due to overlapping electron clouds (the Pauli exclusion principle), which is a very strong function of distance. The negative r_{ij}^{-6} term represents favourable London's dispersion interactions or instantaneous dipole-induced dipole interactions. In this LJ form, there are two parameters. The first is the potential energy well depth (ε_{ij}) describing the magnitude of the London's dispersion interactions between atoms i and j. The second parameter is $R_{min/2,ij}$ which is the distance between atoms i and j where the minimum LJ interaction energy occurs. Typically, ε_{ij} and $R_{min/2,ij}$ are not determined for every single atom pair in a system, but rather for the types of individual atoms (for example for all

oxygens in water). A general schematic showing the qualitative meaning of ε_{ij} and $R_{min/2,ij}$ follows in Figure 2-12. The quantitative values are obviously dependent on the two atoms interacting.
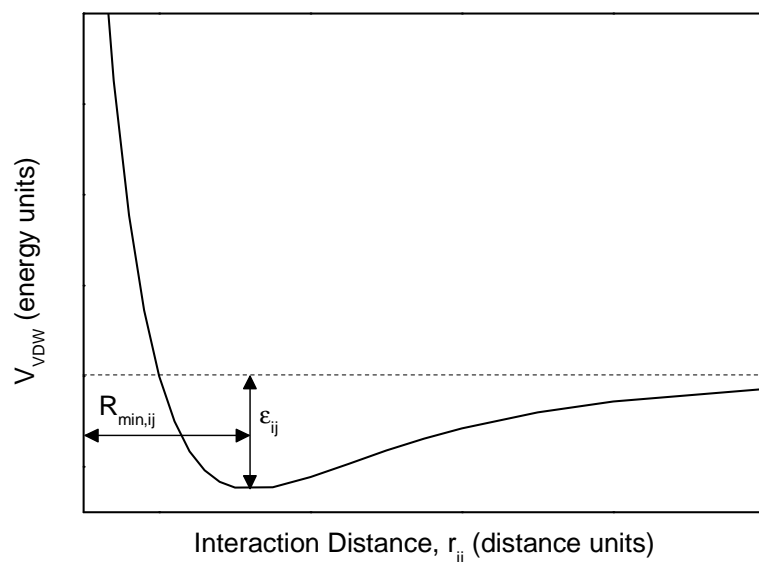
Figure 2-12. Generic representation of van der Waals potential energy diagram.

The second contribution to non-bonded interactions is the coulombic interactions between two charged atoms, and is dependent on the charge (q) of each ion, the distance between them (r_{ij}) and the dielectric constant (ε_D) which is generally equal to 1 (the permittivity of vacuum).

Therefore, once all of the force field parameters are known, the entire potential on each atom is calculated. This process is repeated for all types of atoms in a given system. It is important to note that the equations provided in this section represent a generally-accepted compromise between simplicity and chemical accuracy. Initial positions and velocities are required in order to begin a MD trajectory.

These concepts have been widely applied to the transport of water and ions in ion channels and carbon nanotubes [126, 127, 223-225], but not directly applied to NF. This presents an exciting opportunity to use MD to apply the knowledge of the transport of hydrated ions in biological channels to drinking water contaminants and NF. This fills a gap in current knowledge because it allows the specific examination of ion hydration during ion transport through a pore, which is not considered in existing NF models.

2.6   Review of Research Objectives

This chapter has reviewed the literature available on the properties of inorganic ions in water, NF/RO mechanisms for inorganic solutes, the impact of operating parameters on NF/RO and the modelling techniques available.   In order to understand how the research objectives fit into the existing body of knowledge in this area, a more detailed description than was presented in Chapter 1.6 follows.   The aims and research objectives of each of the four core areas of this thesis are reviewed.

NF/RO mechanisms are highly dependent on solute properties, operating parameters and membrane properties.   While a number of studies have examined mechanisms in very simple systems, understanding membrane performance in real groundwater provides a significant challenge due to complicated groundwater matrices (pH, composition, ionic strength, speciation).   Further, operating a RE-membrane system with no battery storage results in energy fluctuations and varying operating parameters, all of which affect NF/RO mechanisms and performance.   The aim of the first core results chapter, Chapter 4, was to critically evaluate data collected previously during a field trial in Australia in 2005.   The specific objectives were to

- understand the impact of energy variation on retention;
- determine the role of pH in this process (with regard to chemical speciation and system performance);
- determine the dominant mechanisms of ion retention in real groundwater;
- compare system performance at different locations (each with different groundwater); and
- evaluate retention without the influence of complicated groundwater matrices using synthetic water and controlled energy conditions.

The results obtained in Chapter 4 brought to light interesting research questions about the relationship between pH, solute speciation and retention. Although the relationship between pH and retention for fluoride, nitrate and boron has been explored to some extent [49, 51, 54, 107, 240-242], the specific link between solute speciation and retention has not been made for those contaminants. The aim of Chapter 5 was to complete initial work conducted by a previous student in order to thoroughly evaluate

the specific impact of pH on the removal of these contaminants in bench-scale studies. The specific objectives were to

- predict the chemical speciation of boron, fluoride and nitrate as a function of pH;

- measure retention and flux of these solutions as a function of pH with six different NF/RO membranes; and

- determine the relationship between speciation and retention for these contaminants.

The selectivity of monovalent anions observed in Chapter 5 emphasized the hypothesis that ion hydration is a very important parameter in determining retention in NF/RO. This remains an area which is not well-understood in NF/RO, despite anecdotal evidence of retention trends corresponding to hydrated size. As such, a molecular dynamics model was created in order to evaluate the importance of the hydration of monovalent anions (fluoride, chloride, nitrate, nitrite) as the ions transport through narrow cylindrical pores, which was the overall aim of Chapter 6. The specific objectives were to

- determine the hydration structure of the anions in bulk water;

- investigate the hydration of these ions during transport through a generic pore, as a function of (i) pore size; (ii) ion type; and (iii) surface charge; and

- determine the energetic barriers of transport by evaluating free energy profiles in each of these scenarios.

Experimental evidence of dehydration occurring during transport in real NF/RO membranes is an area still yet to be established. The overall aim of Chapter 7 was to gain experimental evidence of dehydration occurring as a proposed transport mechanism in NF by comparing Arrhenius energy barriers to molecular dynamics simulations. The specific objectives were to

- determine the retention and solute flux of monovalent anions as a function of temperature and pressure;

- relate solute flux to energy barriers for different (i) ion types (sodium fluoride, sodium chloride, sodium nitrite and sodium nitrate) and (ii) membrane types (with different effective sizes); and

- link experimental energy barriers with the results from the molecular dynamics simulations discussed in Chapter 6.

Before delving into the results, first the methods and materials used experimentally will be described in Chapter 3.

Chapter 3

Experimental Methods and Materials

This chapter describes the methods and materials used experimentally in this research. The materials included different membrane systems at bench scale (stirred cells, crossflow and diffusion cells) and pilot scale (renewable energy-membrane system). Other materials included commercially-available membranes (and their characteristics) and chemicals. The analytical equipment and techniques used in this project are described in this chapter, including ion selective electrodes, a nutrient analyzer, inductively-coupled plasma optical emission spectroscopy, inductively-coupled plasma mass spectroscopy, total organic carbon analysis and ion chromatography. Common experimental protocols are reviewed here and specific details are discussed when relevant in Chapter 4, 5 and 7. A summary of common experimental calculations and error analysis is included.

3.1 Membrane Systems

A number of experimental systems have been used in the completion of this research project, including stirred cells, crossflow, diffusion cells and a RE-membrane system. Table 3-1 shows a general comparison of the experimental systems used, and a detailed discussion of each system (description, use and experimental protocols) follows.

Table 3-1. General comparison of experimental systems used (for broad comparative purposes only).

System	Primary Use	Membrane Area (cm^2)	Typical Parameter Range Pressure (bar)	Feed Flow (L.min^{-1})	Permeate Flow (L.min^{-1})*
Stirred Cells	Bench-scale filtration	21.2 or 38.5	< 8	--	< 0.008
Crossflow	Bench-scale filtration	46.0	< 30	< 2.0	< 0.1
Diffusion Cells	Diffusion experiments	4.91	0	--	--
RE-Membrane	Pilot-scale filtration	~78000	< 12	< 8.3	< 3.3

*note that permeate flow is strongly dependent on membrane type and water composition

3.1.1 Stainless Steel Stirred Cells

The first type of bench-scale equipment used was a stainless steel stirred cell. Stirred cells were used for two main objectives: (1) to assess the impact of pH on inorganic contaminant removal [171] and (2) to characterize selected membranes. Stainless steel stirred cells are enclosed cylinders used for dead end filtration experiments. A membrane is placed on the base of the cell, which is filled with solution, stirred via a magnetic stir bar and pressurized. Permeate solution then passes through the membrane and collected on the outside of the cell. Two different types of magnetically-stirred stainless steel cylindrical batch cells were used for filtration experiments. A small stirred cell was used in this project for pH experiments (Chapter 5) and larger stirred cells were used for selected membrane characterization (Chapter 3) for consistency and because three could be used at the same time.

The volume of the smaller stirred cell was 185 mL, and the membrane surface area was 21.2 cm^2. The cell contained a plastic magnetic stirrer assembly (Millipore, Watford UK) which was stirred at 300 rpm using a magnetic stir plate (Fisher Scientific, UK). Further details about the cell and the hydrodynamics are provided by Schäfer [243]. The cell was pressurized with compressed air and equipped with a pressure relief valve (Norgren V07-200-NNLG, UK). Pressure was measured using a pressure transducer (OmegaDyne PX219-30V85G5V, USA, accuracy ± 0.25%) and permeate mass measured with an electronic balance (Ohaus Adventurer Pro, UK, accuracy ± 0.1 g).

Pressure and weight were recorded using a data acquisition module (Omega OMB-DAQ-54, Omega Engineering, UK) on a computer using LabVIEW 8.0 (National Instruments, USA). Figure 3-1 and Figure 3-2 show a schematic and photograph of the experimental apparatus, respectively.
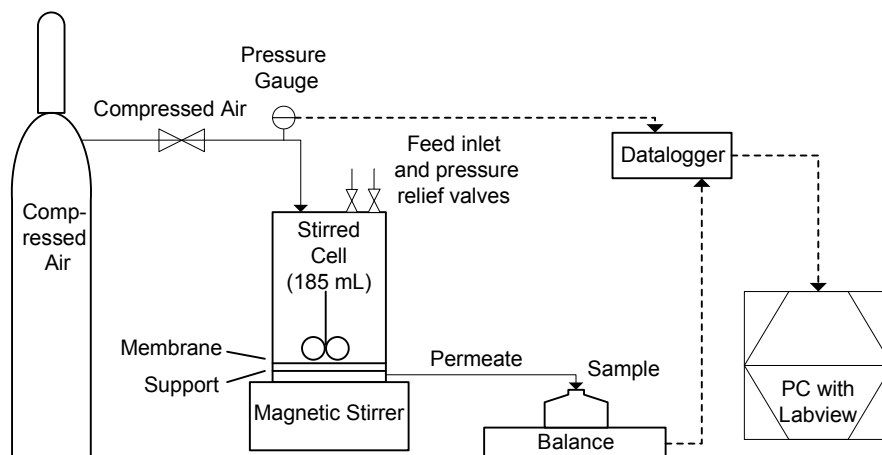
Figure 3-1. Schematic of stainless-steel stirred cell experimental apparatus (note not to scale). Ambient temperature was measured outside of the cell with a probe connected to the datalogger (not shown for clarity).

Figure 3-2. Photograph of the small stainless steel stirred cell.

Larger stainless steel cells were used for membrane characterization. The setup of these stirred cells was nearly identical to what was just described, with the exception that the volume of the cell was 990 mL, and the membrane surface area was 38.5 cm^2. Three of these larger stainless steel cells were used in parallel. Extensive description of these cells is provided by Neale [244].

3.1.2 Crossflow Membrane System

The second type of bench-scale equipment used was a crossflow membrane system. A crossflow rig is used when experiments with flow and pressure across a flat-sheet membrane coupon are desired. A stainless steel crossflow system (MMS, Switzerland) was used for filtration experiments reported in Chapter 7. Extensive modification of this system was required in order to address an oil leak from the pump, and these issues are addressed in detail by Semião [245]. Figure 3-3 and Figure 3-4 respectively show a schematic and photograph of the crossflow system used in this research and then the system details are described.
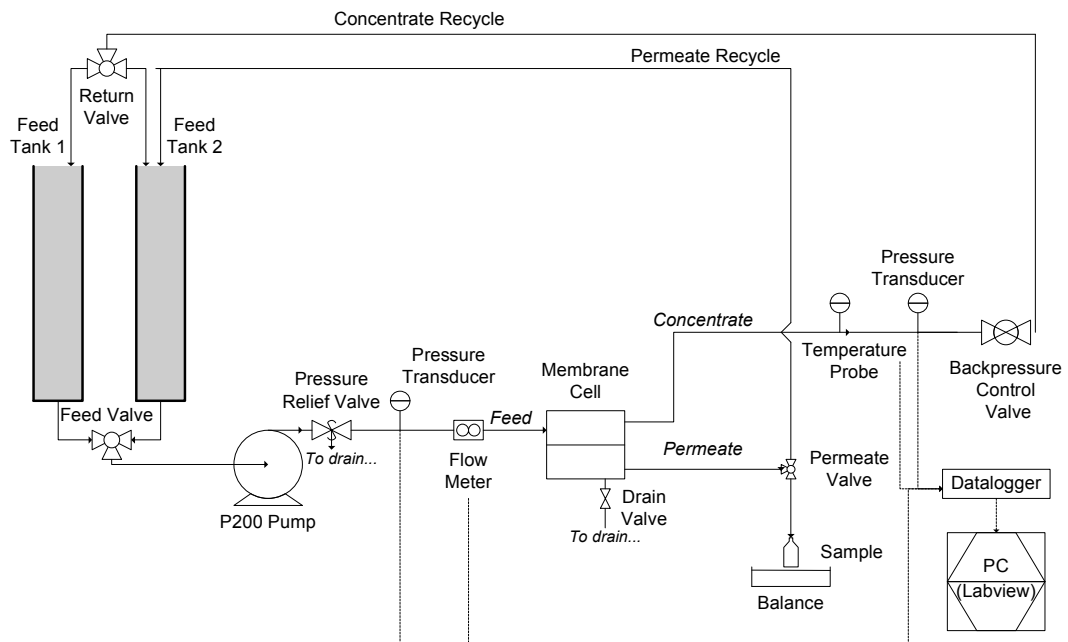
Figure 3-3. Schematic of crossflow membrane system (note not to scale).
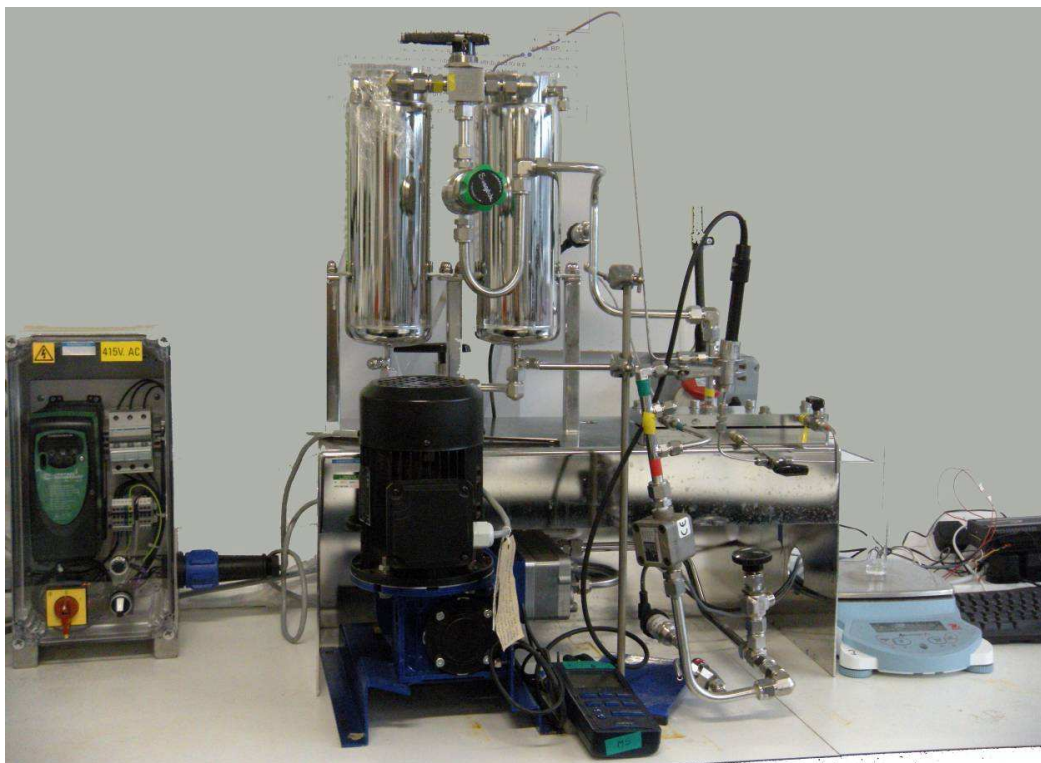
Figure 3-4. Photograph of the crossflow membrane system.

The system contained two 2.5 L feed tanks (of which only one was used at a time) and a high pressure diaphragm pump (Hydra-Cell P200, UK). Feed solution was pumped across and through a flat sheet membrane cell (membrane area 46.0 cm^2). Temperature was controlled by a water bath (Lauda WK 700, Germany) which was piped to a cooling jacket around the feed tanks (0.09 m^2 surface area per feed tank). Pressure was controlled by a back pressure regulator (Swagelok KPB Series, UK). A datalogger (Omega DAQ55, UK) recorded the following in-line monitored parameters: pressure (before and after cell) (S model pressure transducer, Swagelok, UK), feed flow rate (Macnaught M2SSPI, UK) and temperature (Condustrie-Metag WTM Pt 100-0-6, Germany). A conductivity probe (WTW, Germany) was installed in a flow cell in the permeate line just after the membrane cell and attached to a standard meter (WTW, Germany) to monitor conductivity in real time (data was not logged automatically).

The primary purpose of using the crossflow system was to experimentally determine retention, permeability and energy barriers of salt transport through NF/RO membranes, as reported in Chapter 7. The main parameters that can be varied in a crossflow system are solution composition, pressure, flow, and temperature. The selection of operating parameters varied depending on the objectives of the experiment and specifics are listed

in the appropriate chapters and figure captions. The membranes were always compacted before starting an experiment until pure water flux stabilized (at least one hour). Specific protocols will be discussed where appropriate.

3.1.3 Diffusion Cells

The third type of bench-scale equipment used was diffusion cells. Diffusion cells were used to measure the diffusion of various salt solutions across a membrane barrier (Appendix B), as driven by a concentration gradient between the two cells and temperature, and to determine energy barriers of transport. Two glass cells (each 100 mL) were clamped together using joint clip flat flanges (Fisher Scientific, UK). The membrane area was 4.91 cm^2 and dimensions of each cell were as follows: outer diameter (of the flange) 55 mm, inner diameter 25 mm and shank length 204 mm. The volume of the cylindrical sampling port was an additional 26 mL (inner diameter 26 mm, height 50 mm) to the 100 mL cell. A round shaped cross-head stir bar (VWR, UK) was placed in the centre of each cell and stirred with a magnetic stir plate (Fisher Scientific, UK) at approximately 800 rpm. Diffusion cells were supported by standard lab stands (Fisher Scientific, UK) and placed in a water bath where temperature was measured using a thermocouple (Standard ST-9612) and water was mixed with a bubbler to maintain temperature. The water bath was large enough for experiments with two sets of cells to be run in parallel. The diffusion cells were custom-made at Heriot-Watt University. Figure 3-5 and Figure 3-6 show a schematic and photograph of the diffusion cells. Holders are not shown on Figure 3-5 and the water bath is not shown on Figure 3-6 for clarity.
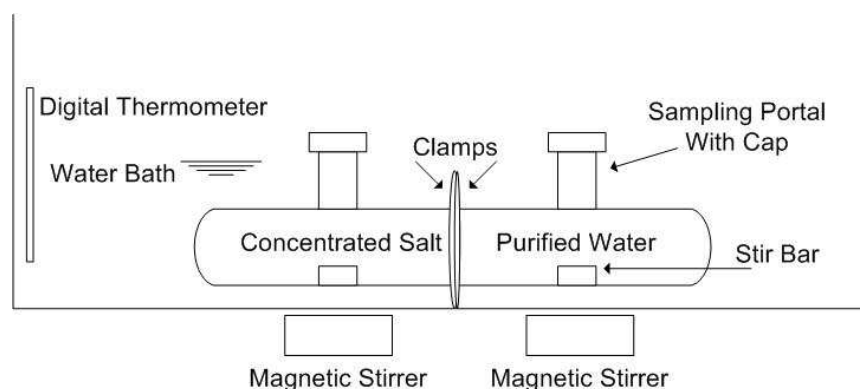
Figure 3-5. Schematic of diffusion cell experimental apparatus (supports not shown for clarity).
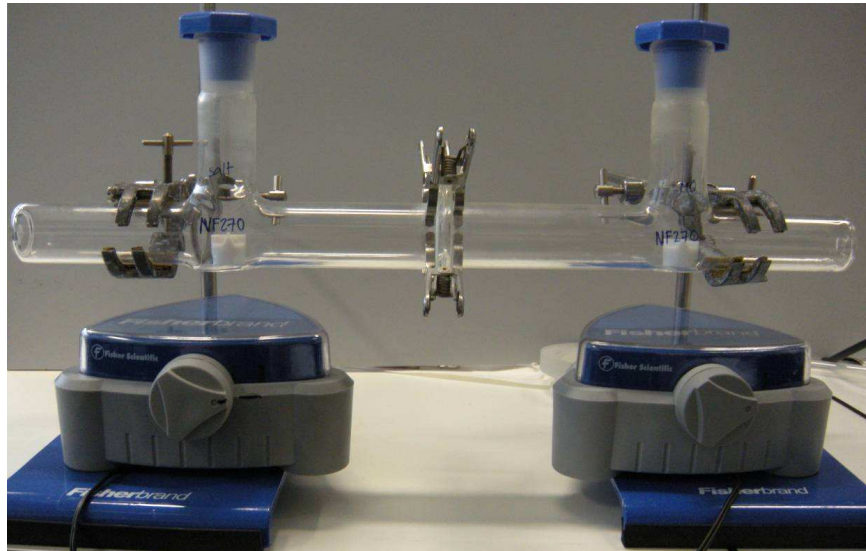
Figure 3-6. Photograph of diffusion cell experimental apparatus (water bath not shown for clarity)

3.1.4   Renewable Energy Membrane System

Prior to the start of the current PhD project, a field trial was conducted using a RE-membrane system. Although the PhD candidate did not take part in the field trial, the data produced from it was critically evaluated by the PhD candidate, which is the subject of Chapter 4. As such, the system will be described in order to put the results in Chapter 4 into context. This same system was later adapted for controlled, laboratory-based experiments, with which the PhD candidate did conduct a limited number of experiments.

The construction of this RE-membrane system has been previously described in detail [74, 246, 247].   The RE-membrane system was a two-staged membrane system combining ultrafiltration (UF) and NF/RO [74]. The system was designed to be suitable for meeting the drinking water needs of remote communities of 50 – 100 people, producing about 1000 L of drinking water per solar day. For field trials, the first filtration stage consisted of six UF membranes (Zenon ZW10) connected in parallel and immersed in a 300 L stainless steel tank. An air bubbler (Nitto LA80a) was used for gentle mixing and for the reduction of solid deposits in the feed tank. A progressive

cavity pump (Mono-Pumps, Australia) drew feedwater through the UF membranes (at around -0.5 bar) and then into the NF/RO module at pressures up to 12 bar. Membrane modules were 4 inch cylinders of spiral wound flat sheet membranes (membrane surface area approximately 7 – 8 m^2 depending on membrane type). A schematic of the RE-membrane system during the field trial is shown in Figure 3-7, and a photograph is provided in Richards *et al.* [248].
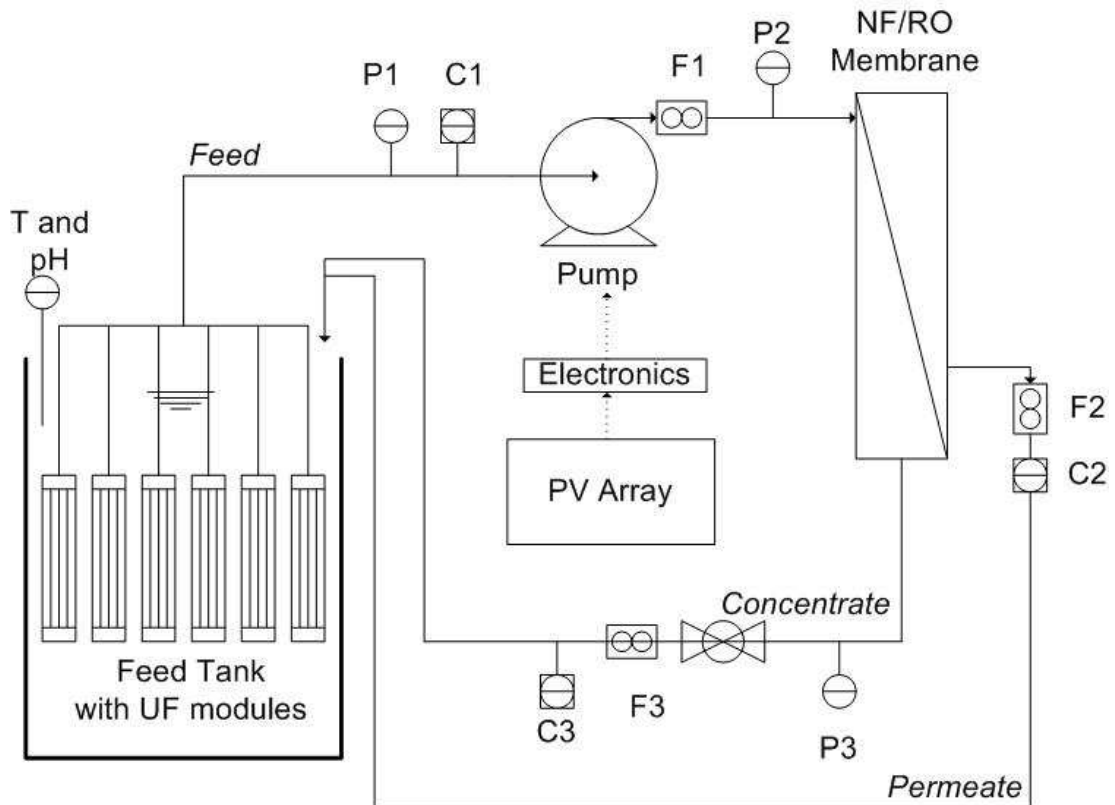
Figure 3-7. Schematic of the RE-membrane system with field trial configuration. Sensors are marked T (temperature), pH (pH), P (pressure transducer), C (conductivity) and F (flow meter).

During the field trial, the system was powered using solar energy via PV panels. Four 24 V_{DC} PV panels (BP Solar, BP3150S) were installed on a 4-wheel drive trailer where the membrane system was mounted. Each of the PV panels provided a maximum power of 150 W and thus only two were required to power the pump (rated at maximum power of 300 W). The panels were mounted on a single axis solar tracker (Mono-Pumps, Australia) which was guided by a global positioning system and thus followed the path of the sun from east to west during the day. An alternative power supply for the system was a backup generator (Honda Eu10i 1kVA) or 240 V_{AC} grid power.

During the field trials a battery bank and charger were used to power peripheral equipment only (such as a laptop computer and data acquisition information).

The system was equipped with a number of sensors to monitor important operating parameters for research purposes (shown on Figure 3-7). Pressure was measured on both sides of the pump and after the NF/RO module on the concentrate line using pressure transducers (Bürkert 8323, Bürkert Fluid Control Systems). Flow sensors (S8011R Farnell type 178-923) were installed on the feed and concentrate lines and manual measurements were made if the flow was outwith the sensor range. Temperature and electrical conductivity were monitored (WTW MultiLine P4) in the feed, concentrate and permeate lines. Pump voltage and current were measured directly from the pump. All parameters were measured with a datalogger (DataTaker DT500) at 5 s intervals and downloaded to a laptop.

For more controlled testing in the laboratory at Heriot-Watt University, the RE-membrane system was configured slightly differently. In order to eliminate random energy fluctuations inherently resulting from renewable energy, power was controlled using a solar array simulator programmable power supply (Agilent Technologies E4350B) that was able to simulate the output of a 300 V PV array. Temperature was controlled using a water chiller system. The power supply was controlled and all data recorded on a personal computer using LabVIEW 8.0 (National Instruments, USA).

3.2 Membranes and Membrane Characteristics

3.2.1 Membranes

The membranes used in this research were all commercially available polymeric RO and NF membranes available from a number of manufacturers. Membrane properties, characteristics and performance varied greatly, and specific parameters are reported here and related to results where appropriate in Chapter 4, 5 and 7. Commercially-available membranes were selected because the research interest was to evaluate membranes that are actually in use and available. For specific experiments, particular membranes were selected based on the desired requirements (*eg.* flux or retention) for a meaningful experiment. All membranes used have a polyamide-based active layer. The

membranes used, along with their classifications, manufacturer and with which system they were used are shown on Table 3-2.

Table 3-2. List of membranes, type, manufacturer and which system they with which they were used for experiments.

Membrane	Type	System[*]	Manufacturer	Information
BW30	RO	RE-Membrane, stirred cell, diffusion cell	Dow	[249]
NF90	NF	RE-Membrane, stirred cell, crossflow, diffusion cell		
NF270	NF	crossflow, diffusion cell		
TFC-S	NF	RE-Membrane, stirred cell	Koch	[250]
TFC-SR2	NF	diffusion cell		
TFC-SR3	NF	diffusion cell		
ESPA4	RO	RE-Membrane, stirred cell	Hydranautics	[251]
UTC-60	NF	stirred cell, diffusion cell	Toray	[252], [253]
UTC-80A	RO	stirred cell, diffusion cell		

[*]Membranes for the RE-Membrane system were 4" spiral would modules; all other were flat sheet membrane coupons

A challenge of working with commercial polymeric membranes lies in that the details of the manufacturing processes are held proprietary and thus it can be difficult to obtain detailed information about membrane properties. Instead, a number of characterization techniques were used to gain information about membrane properties (permeability, retention, effective pore size, molecular weight cutoff, surface charge, chemical composition, surface morphology, active layer thickness, hydrophobicity). Another major challenge is batch variability, where a different batch of the same membrane may well exhibit different properties. This is exasperated because only small coupons are used for bench-scale experiments rather than entire modules. In order to address this, the same membrane batch was used for any set of experiments and characterization was repeated if a new batch was required.

The most important properties for this research on the transport of salts in NF/RO were permeability, retention, effective pore size and surface charge, and these will be the parameters that will be used to describe results in the following chapters. Information about chemical composition, surface morphology and hydrophobicity is included here for the sake of completeness but this data was not extensively considered in the analysis

of filtration results as the other parameters were. The later parameters are more relevant for organic solutes and mechanisms such as adsorption.

Pure water permeability and salt retention were easily measured experimentally (Section 3.2.2). Effective pore size, the thickness to porosity ratio, and molecular weight cutoff (MWCO) were measured (Section 3.2.3) by fitting the hydrodynamic model (Chapter 2.4.1) to experimental data. Membrane surface charge can be measured with streaming potential (Section 3.2.4). Elemental analysis of some of the membranes used was reported in the literature using X-ray photoelectron spectroscopy (XPS) and Rutherford backscattering spectrometry (RBS) (Section 3.2.5). Atomic force microscopy (AFM) was used to determine surface roughness (Section 3.2.6). Transmission electron microscopy (TEM) was used to image the cross section of a membrane (Section 3.2.7). Contact angle gives information on hydrophobicity (Section 3.2.8). Where obtained and/or available in the literature for the membranes used in this research, this data is reported in the following sections. It is important to be informed about membrane properties in order to understand their performance.

3.2.2 Permeability and Retention

The pure water permeability and observed salt retention (0.1 M NaCl, 10 bar) of each membrane was measured and results are shown on Table 3-3. There is a general trade-off between pure water permeability and retention. The membranes with the lowest pure water permeability generally have the highest salt retention, and conversely the membranes with highest permeability have lower retention. Pure water permeability and retention both vary widely depending on membrane type. Detailed retention results for different solutes and under different conditions are given in the relevant results chapters (Chapter 4, 6 and 8). The PhD candidate did the characterization of UTC80A, BW30, TFCS, ESPA4, NF90, NF270 and UTC60, and the remaining membranes were characterized by other members of the Membrane Technology Group (University of Edinburgh).

Table 3-3. Pure water permeability and NaCl retention for membranes used.

Membrane	Pure Water Permeability $(L.m^{-2}.h^{-1}.bar^{-1})$	NaCl Retention, Observed (0.1 M, 10 bar) (%)
UTC80A	2.2	98.4
BW30	4.4	99.8
TFC-SR3	5.7	40.8
TFCS	5.8	86.8
ESPA4	6.5	90.9
NF90	9.7	83.7
TFC-SR2	14.1	22.7
NF270	16.2	42.4
UTC60	32.8	24.7

3.2.3 Effective Pore Radius and Molecular Weight Cut-off

Effective pore radius (R_p, 10^{-10} m), membrane active layer thickness to porosity ratio ($L.\varepsilon^{-1}$, m) and MWCO were determined for the membranes. These parameters are important because they give information about which solutes may be excluded due to size. The retention of neutral organic solutes (25 mg.L^{-1} as C, each of methanol, dioxane, xylose and dextrose) was measured and corrected for concentration polarization to obtain real retention (R_r, %) (see Section 3.5). Solutes were selected according to the expected size of the membrane (*eg.* methanol, the smallest, was used for RO and tight NF and dextrose, the largest, was used for loose NF). Table 3-4 shows the properties of the organic solutes used for characterization.

Table 3-4. Properties of Organic Tracers Used in Characterization.

Organic Tracer	Molecular Weight $(g.mol^{-1})$	Diffusivity $(10^{-10}\ m^2.s^{-1})$ [216]	Stokes Radius $(10^{-10}\ m)$ [216]
Methanol	32	6.0 [254]	1.91
Dioxane	88	9.1	2.34
Xylose	150	7.4	2.90
Dextrose	180	6.6	3.24

The hydrodynamic model (Chapter 2.4.1) was curve fitted to match the variation of real solute retention with permeate flux in order to obtain R_p and $L.\varepsilon^{-1}$, as detailed in the next paragraphs. The methodology described by Nghiem *et al.* [216] was used for BW30, NF90, NF270, UTC60 in the crossflow system, and the same method was adapted for

stirred cells [255] for ESPA4, TFC-S, TFC-SR2, TFC-SR3, UTC-80A. The PhD candidate did the characterization of UTC80A, BW30, TFCS, ESPA4, NF90, NF270 and UTC60, and the remaining membranes were characterized by other members of the Membrane Technology Group (University of Edinburgh).

For characterization, a reduced form of the hydrodynamic model (full form discussed in Chapter 2.4.1) was employed

$$j_i = -D_{i,p} \frac{dc_i}{dx} + K_{i,c} c_i^m J_v,$$
Equation 18

as neutral organic solutes were used and thus there no charge term is required. This therefore assumes that solute retention only occurred through steric exclusion. Integrating Equation 18 over the entire membrane using the concentrations at each end of the pore as boundary conditions and the distribution coefficient, Φ,

$$\Phi = (1 - \lambda_i)^2,$$
Equation 19

where

$$\lambda_i = \frac{R_{Stokes,i}}{R_{pore}}.$$
Equation 20

The integration yields the macroscopic flux equation

$$\langle J_s \rangle = 1 - \frac{\Phi K_{i,c} \langle V \rangle c_m \left[1 - \left(c_p / c_m\right)\exp(-Pe)\right]}{1 - \exp(-Pe)},$$
Equation 21

where Pe is the membrane Peclet number (dimensionless) determined from

$$Pe = \frac{K_{i,c} \langle V \rangle L}{K_{i,d} D_\infty} = \frac{K_{i,c} \langle J_v \rangle}{K_{i,d} D_\infty} \cdot \frac{L}{\varepsilon}.$$
Equation 22

and $\langle J_s \rangle$ is radially averaged solute flux (mol.s^{-1}.m^{-2}), $\langle V \rangle$ is the radial average fluid velocity in the pore (m.s^{-1}), L/ε is the membrane thickness to porosity ratio, c_m is

concentration at the membrane surface (mol.m^{-3}) and c_p is the concentration in the permeate (mol.m^{-3}). Equation 21 can be reduced using real retention (R_r, %) to

$$R_r = 1 - \frac{c_m}{c_p} = 1 - \frac{\Phi K_{i,c}}{1 - exp(-Pe)(1 - \Phi K_{i,c})} . \qquad \text{Equation 23}$$

This theoretical R_r is now a parameter which can be directly compared to the experimental R_r (the calculation of which is shown at the end of this chapter in Section 3.5 with other common calculations used in this thesis). In order to characterize membrane properties, the theoretical and experimental R_r values should be equal, which required fitting the theoretical model to the experimental value of R_r. To do this, the membrane parameters pore radius (R_p) and L/ε were solved for iteratively by minimizing the variance between the theoretical and experimental real retention values with Microsoft Excel Solver. This process essentially determined R_p and $L.\varepsilon^{-1}$ by curve fitting the experimental values for the variation of real solute retention with permeate flux to the pore flow model.

MWCO was determined by measuring the retention of polyethyleneglycol (PEG) of molecular weight 200, 400, 600 and 1000 g.mol^{-1} (again at concentration of 25 mg.L^{-1} as C). MWCO was extrapolated as the point at which 90% retention was achieved. Note that this calculation was invalid for tight NF or RO membranes because the retention of all PEGs tested was greater than 90%. These experimentally characterized membrane properties are listed on Table 3-5. These characteristics also varied according to membrane type. Results are consistent with Table 3-3, showing that membranes with a relatively low permeability and high salt retention have small effective pore sizes and low molecular weight cutoff. These results will be discussed more in detail in the relevant results sections where they can be used to explain experimental data.

Table 3-5. Effective pore radius, active layer thickness to porosity ratio and MWCO for membranes used. Uncertainty in these fitted parameters is estimated to be ± 5%.

Membrane	Effective Pore Radius (R_{pore}, 10^{-10}m)	Active Layer Thickness to Porosity Ratio ($L.\varepsilon^{-1}$, 10^{-6}m)	MWCO
UTC80A	1.9	3.00	n/a[*]
BW30	3.2	6.01	88; 98 [161]
ESPA4	3.3	7.57	n/a[*]
NF90	3.4	1.46	< 88; 100 [161]
TFC-S	3.4	5.29	200 [256]
TFC-SR3	3.8	1.59	167
NF270	3.8	1.01	180
UTC60	4.5	4.70	150 [257]
TFC-SR2	4.6	1.09	425

[*]retention of each organic solute was > 90% and thus MWCO was not calculated

3.2.4 Surface Charge

Membrane surface charge is important because it affects the charge interactions between the membrane and ions. Surface charge of the membrane surface is determined by streaming potential which is measured using an electrokinetic analyzer. Zeta potential result was obtained using an electrokinetic analyzer at Imperial College London (EKA, Anton Paar KG, Austria, with Ag/AgCl-electrodes SE 4.2, Sensortechnik Meinsberg, Germany). Streaming potential was measured in 20 mM NaCl and 1 mM NaHCO$_3$. The electrolyte solution moves through a channel created by a PTFE spacer between the active layers of the membrane samples in order to generate a streaming potential (channel height 0.87 mm). The membrane zeta potential was calculated from the streaming potential using the Helmholtz-Smoluchowski and Fairbrother-Mastin relationships [174],

$$\zeta = \frac{\Delta U_s}{\Delta P} \cdot \frac{\mu}{\varepsilon_{solution} \cdot \varepsilon_0} \cdot \frac{L_{channel}}{A_{x\,section}} \cdot \frac{1}{R_{channel}} \qquad \text{Equation 24}$$

where ζ is zeta potential (mV), U_s is streaming potential (mV), P is applied pressure (bar), μ is dynamic viscosity of the solution (kg.m^{-1}.s^{-1}), $\varepsilon_{solution}$ is the relative permittivity of the test solution (--), ε_0 is the relative permittivity of free space (--),

$L_{channel}$ is channel length (m), $A_{xsection}$ is channel cross-sectional area (m^2) and $R_{channel}$ is channel resistance (m).

The measurement protocol described by Childress and Elimelech was followed [174]. Membranes were rinsed with ultrapure water and equilibrated with the background electrolyte in a beaker for 20 minutes. Then the membrane was mounted in the measuring cell. The protocol was to (1) flush the cell with ultrapure water for 3 minutes; (2) rinse the cell with test solution; (3) equilibrate the cell with test solution for 30 minutes; (4) adjust the pH of the test solution using the autotitrator; (5) recirculate the test solution for 10 minutes or until stable; (6) measure streaming potential; (7) flush the cell with ultrapure water. Eight measurements were taken at each pH (four in each direction). The first two measurements were discarded and the remaining six (three in each direction) averaged to calculate the zeta potential at each pH. The measuring range was from pH 3 to 13. This range was selected in order to span the whole range of typical experimental values used, but it is important to note that Ag/AgCl electrodes are unstable at high pH. Because of this, the measured zeta potential values should be considered relative to each other and not taken as absolute values, especially at high pH. All measurements were taken at room temperature. Zeta potential is shown on Figure 3-8. Zeta potential for each of the membranes decreases from approximately pH 4 to 13. Zeta potential for ESPA4 increases from pH 3 to 4 which is not observed with any other membranes, which could be due to a specific chemical feature of the membrane functional groups. No other zeta potential data for ESPA4 was available in the literature for comparison. Zeta potential for UTC-80A is the most negative at the low pH values and stays more constant throughout the whole pH range when compared to the other membranes. The zeta potential will be discussed in detail and related to retention in Chapter 5. Zeta potential measurements were made by Annalisa De Munari (University of Edinburgh), Dr. Kingsley Ho and Dr. Alexander Bismarck (Imperial College London).
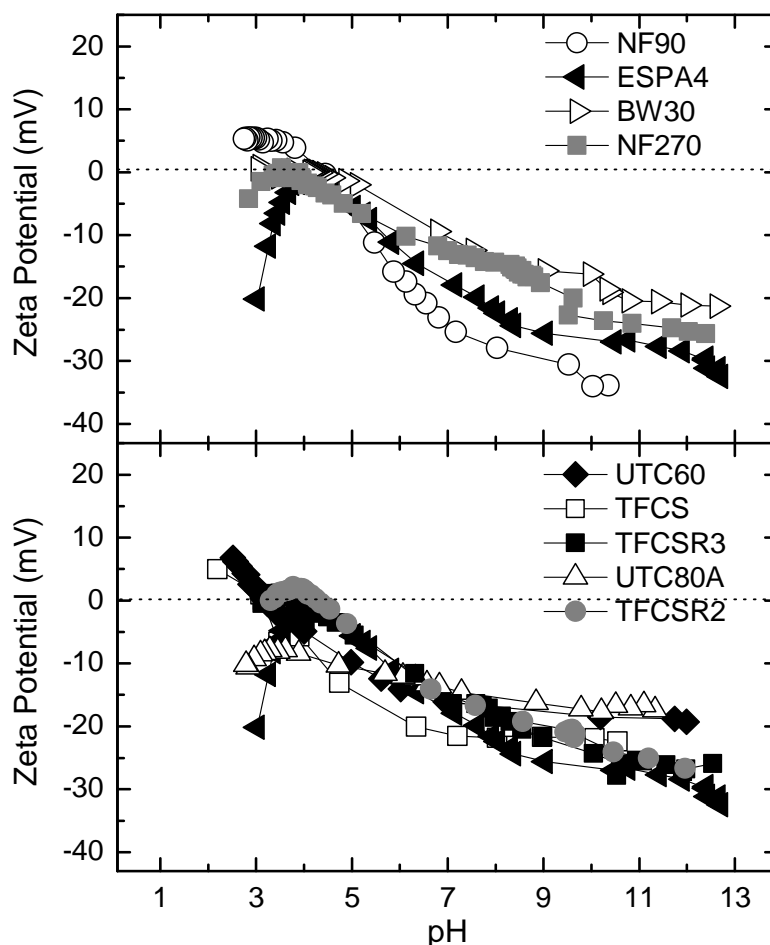
Figure 3-8. Membrane zeta potentials of NF90, UTC-60, TFC-S, BW30, UTC-80A and ESPA4 (in background solution 20 mM NaCl and 1 mM NaHCO$_3$).

3.2.5 Membrane Material and Chemical Composition

All membranes used in this project have a polyamide-based active layer. Specific information about the membrane materials follows as reported in the literature. The Dow Filmtec membranes (BW30, NF90 and NF270) consist of three distinct layers [258]. The base is a polyester support web; the middle layer is microporous polysulphone; and the top (active) layer is an ultrathin polyamide material. NF90 and BW30 are fully aromatic polyamide thin film composite membranes whereas NF270 is a piperazine-based semi-aromatic polyamide thin film [161, 258, 259]. NF90 and BW30 are made from benzezetricarbonyl trichloride and 1-3 phenylene diamine, where as NF270 is made from benzezetricarbonyl trichloride and piperazine [161]. The active layer of these membranes is a few hundred nanometers [260]. UTC-80A has 1,3,5-triaminobenzene as a polyamine component [261].

Mondal and Wickramasinghe conducted elemental surface analysis of BW30, NF90 and NF270 using XPS [258]. With the equipment setup of Mondal and Wickramasinghe [258], XPS allows the sensitive measurement of elemental composition (except hydrogen) on the membrane surface and provides chemical binding information for the top 1 to 10 nm of the membrane surface. Their results for virgin BW30, NF90 and NF270 are reported in Table 3-6. Their objective was to compare virgin membranes with those filtered with oily wastewaters, but only the data for virgin membranes is reported here (and thus the data may include measurement artefacts from the atmosphere because it is taken out of its original context to be comparative). The filtration of oily wastewaters affected the C:O:N ratio of the membranes due to organics absorbing on to the membrane surface [258], but no similar data for inorganics is available.

Table 3-6. Surface elemental analysis (as %) using XPS of virgin samples of BW30, NF90 and NF270 [258].

Membrane	C	O	N	C : O : N ratio	S	Na	Cl	Si
BW30	70.7	22.2	6.1	11.6 : 3.6 : 1.0	--	0.5	0.5	--
NF90	71.0	16.4	11.1	6.4 : 1.5 : 1.0	0.8	0.5	0.2	--
NF270	64.4	22.3	7.5	8.6 : 3.0 : 1.0	1.1	3.7	0.9	--

The elemental analysis of TFC-S [262] and ESPA3 (assumed to be similar to ESPA4) [263] was also reported. The active layer of TFC-S is a polyamide $((CONH_2]^n)$ thin film composite and the composition ratio was determined by Rutherford backscattering spectrometry (RBS) [262]. Results for TFC-S are reported on Table 3-7. Tang *et al.* [263] reported the composition of ESPA (polyamide active layer) and BW30 using XPS and their results are shown on Table 3-8. Both Mondal and Wickramasinghe [258] and Tang *et al.* [263] showed higher O:N ratio than would be expected from a fully cross-linked polyamide layer, which was attributed to either proprietary modifications of the interfacial polymerization or the presence of a coating like polyvinyl alcohol [258]. The active layer material for UTC-60 is a cross linked polyamide [264] and UTC-80 is a cross linked fully aromatic polyamide ultra-thin composite membrane [252] but elemental breakdown for these membranes was not available.

Table 3-7. Active layer elemental composition (as %) of TFC-S determined by model fitting of RBS data of TFC-S [262].

Membrane	C	O	N	C : O : N ratio	S	Cl	Ca
TFC-S	73.1	15.0	10.7	6.8 : 1.4 : 1.0	--	0.9	0.19

Table 3-8. Surface elemental composition (as %) of ESPA3 and BW30 determined by XPS [263].

Membrane	C	O	N	C : O : N ratio
ESPA3	74.3 ± 0.5	12.8 ± 0.8	12.9 ± 1.0	5.8 : 1.0 : 1.0
BW30	67.9 ± 0.6	29.0 ± 1.5	3.1 ± 1.0	21.9 : 9.4 : 1.0

3.2.6 Surface Morphology

Atomic force microscopy (AFM) can be used to determine the roughness of a membrane. The roughness of a membrane is a particularly important parameter for understanding membrane fouling [161]. Although fouling is not the focus of this work, membrane characteristics are important for understanding experimental results. Roughness is used in Chapter 7 to discuss differences between NF90 and NF270. Additionally, surface roughness has implications on more than only fouling, as observed by Hirose *et al.* [265], who showed that a linear relationship exists between permeate flux and surface roughness when filtering NaCl in RO. This was attributed to the unevenness of the top layer causing an enlargement of the effective membrane area [265]. In this light, the roughness will be reported.

Surface roughness was measured using an AFM (Multimode AFM, Veeco, now Bruker Corporation) using a cantilever (Mikromasch CSC38/AIBS type B) in de-ionized water. The AFM uses a tip that slowly moves over the membrane surface (sample size 2.0 μm^2) and determines a roughness profile of the surface by measuring the force it takes for the tip to move. An image of the top surface and the corresponding surface profile is shown for each membrane in Figure 3-9. After determining the profile, the software automatically calculates two parameters which represent the surface roughness. The parameters are *Ra* and *Rq*. *Ra* is the mean roughness which is the arithmetic average of the deviations from the centre plane, and *Rq* is the root mean square roughness which is the standard deviation of two values within a given area. The calculated *Ra* and *Rq*

values are tabulated on Table 3-9. Ime Akanyeti and Dr. Nhan T. Pham (University of Edinburgh) provided the AFM data.

Table 3-9. Membrane roughness measurements using AFM and comparison to literature.

Membrane	Ra $(10^{-9}m)$	Rq $(10^{-9}m)$	Published Roughness $(10^{-9}m)$		
			Ra	Rq	Average
BW-30	67.7 ± 2.4	83.9 ± 3.8		68.3 ± 12.5 [258]	61 [266]
BW-30[*]	63.6 ± 5.0	78.4 ± 6.2			
ESPA-4	86.5 ± 2.3	107.0 ± 3.6			
NF-90	61.7 ± 2.1	78.5 ± 3.6	69.9 [267]	33.1 [161] 129.5 ± 23.4 [258]	70 [266]
NF270	4.2 ± 0.3	5.5 ± 0.4	5.5 [267]	4.2 [161] 9.0 ± 4.2 [258]	4.5 [266]
TFC-S	64.5 ± 6.2	81.5 ± 8.1			
UTC-60	6.6 ± 0.4	8.8 ± 0.5			
UTC-80A	36.9 ± 2.1	45.5 ± 2.5			

[*]compacted at 15 bar

These results show that NF270 and UTC-60 are by far the smoothest membranes. The order of increasing roughness is NF270 < UTC-60 < UTC-80A < NF90 < BW30 (compacted) < TFC-S < BW30 < ESPA4, which is comparable to the literature [161]. Three-dimensional images were not obtained for all of the membranes analyzed, but three-dimensional AFM images are easier to understand conceptually. As such, they are provided in Figure 3-10. These images visually support that NF270 is very smooth compared to BW30 and NF90.

.

(A) BW30
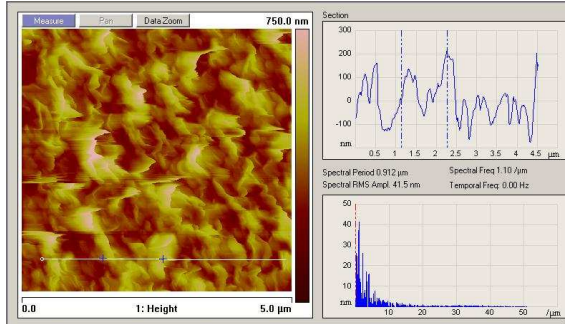
(B) BW30 Compacted
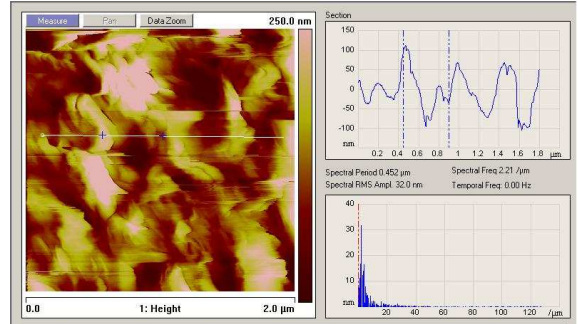
(C) ESPA4
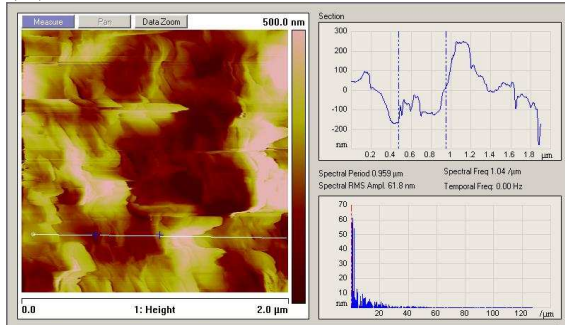
(D) NF90
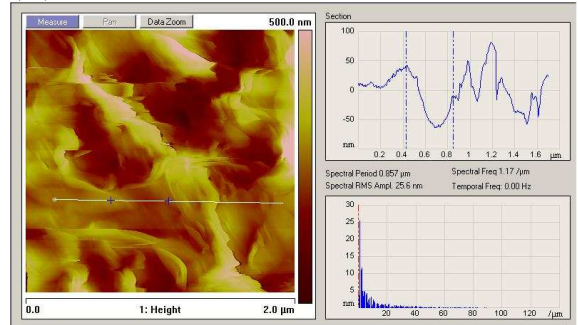
(E) NF270
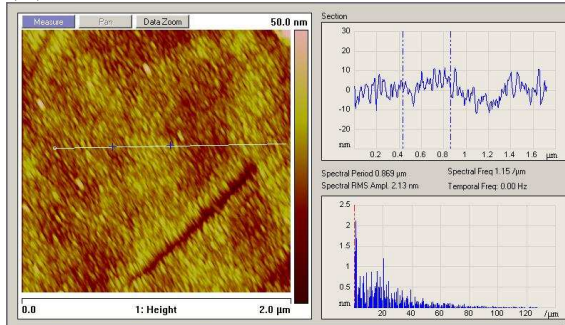
(F) TFC-S
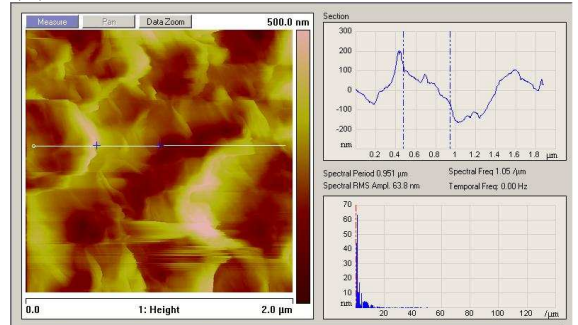
(G) UTC60
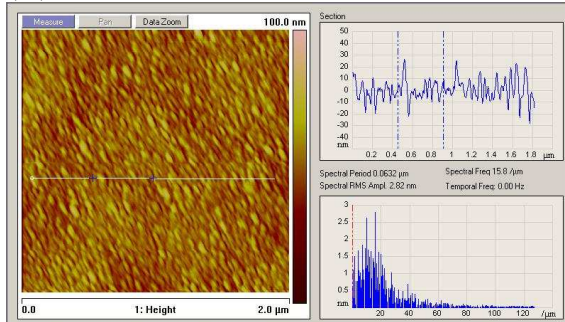
(H) UTC80A
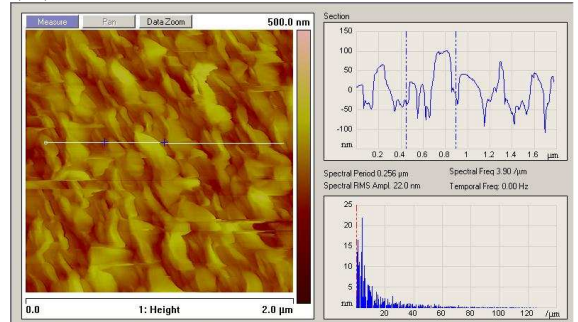
Figure 3-9. AFM images and surface profiles for each of the membranes used.

91
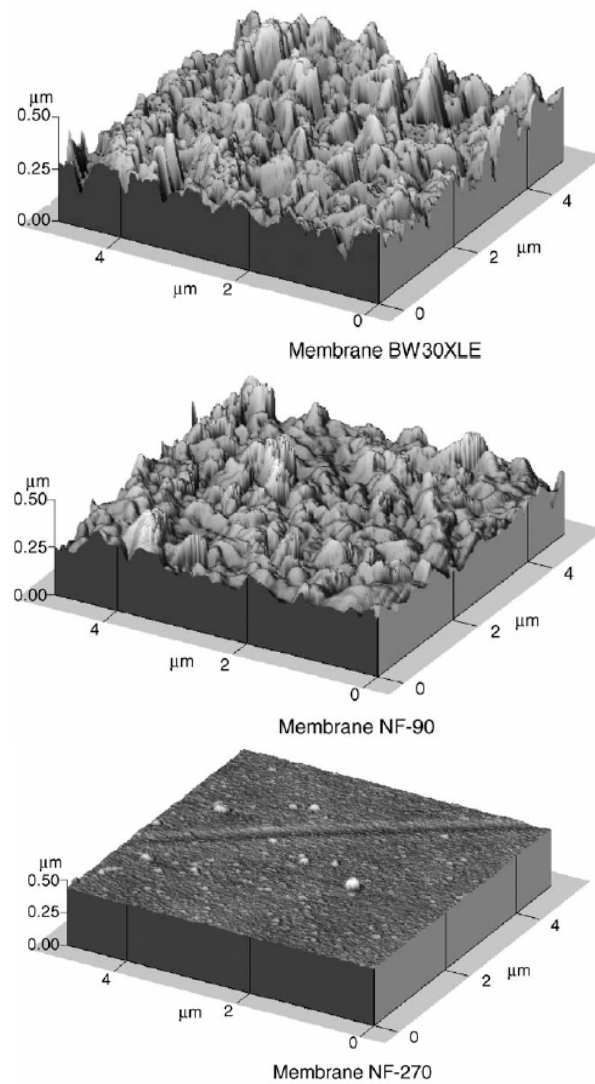
Figure 3-10. Three-dimensional AFM images of BW30XLE, NF90 and NF270 from Boussu *et al.* [161].

3.2.7 Active Layer Thickness

Direct measurement of membrane layers, and in particular the selective active layer, is very difficult because of their very small size. However, the selective active layer is very important because it controls the selectivity and permeability of the membrane. Active layer thickness was used to approximate diffusion coefficients of various salts through NF membranes (Appendix B). NF membranes have an active layer in the range of 15 – 100 nm [260, 268]. High resolution transmission electron microscopy (TEM)

can image the cross-section of a membrane sample but it remains difficult to see the details of the active layer. Although the resolution is not good enough to see pores, these images can assist in the estimation of the active layer thickness. For demonstrative purposes, several TEM images from the literature [263] are shown in Figure 3-11. The polyamide layer of NF270 (Figure 3-11D) can clearly be seen due to the smooth nature of this membrane. Dr. Andrea Semião and Dr. Chris Jeffree (University of Edinburgh) did TEM measurements for NF90 and NF270.

3.2.8 Hydrophobicity

Contact angle provides information on the hydrophilicity or hydrophobicity of a membrane by measuring the interactions between water and the polymeric material of the membrane [110, 153]. More hydrophobic membranes have less interaction with water and hence are less wettable by a drop of water. Low affinity between membrane and water leads to a contact angle greater than 90° and high affinity leads to an angle less than 90°. This is shown on Figure 3-12. While contact angle is commonly used to measure the hydrophobicity of membranes, other membrane properties (such as roughness, pore size and surface tension) affect measurements and thus the data should be used with caution.

Contact angle was measured for selected membranes (BW30, ESPA4, NF90 and NF270) using the sessile drop method and a contact angle instrument (Easy Drop Kruss model FM40, Germany). The membranes were rinsed thoroughly and soaked in deionized water for 24 hours. Then, the membrane surface was dried for at least 8 hours to ensure that the results were not affected by the degree of dryness [269]. The membrane was glued to a glass holder to ensure a plane surface. A pure water drop was placed onto the membrane and it was photographed within 15 seconds and then every minute for at least six minutes, and the contact angle was automatically calculated. At least three measurements for each membrane were taken. Results are reported on Table 3-10 and compared to values reported in the literature. Literature values varied substancially in some cases, which is likely due to variations in measurement methodology and/or manuality of the person taking the measurement. Comparison across one reference is best for this reason. These results show that the hydrophobicity

(A) BW30

(B) ESPA3

(C) NF90 (8k5)

(D) NF270 (40k4)
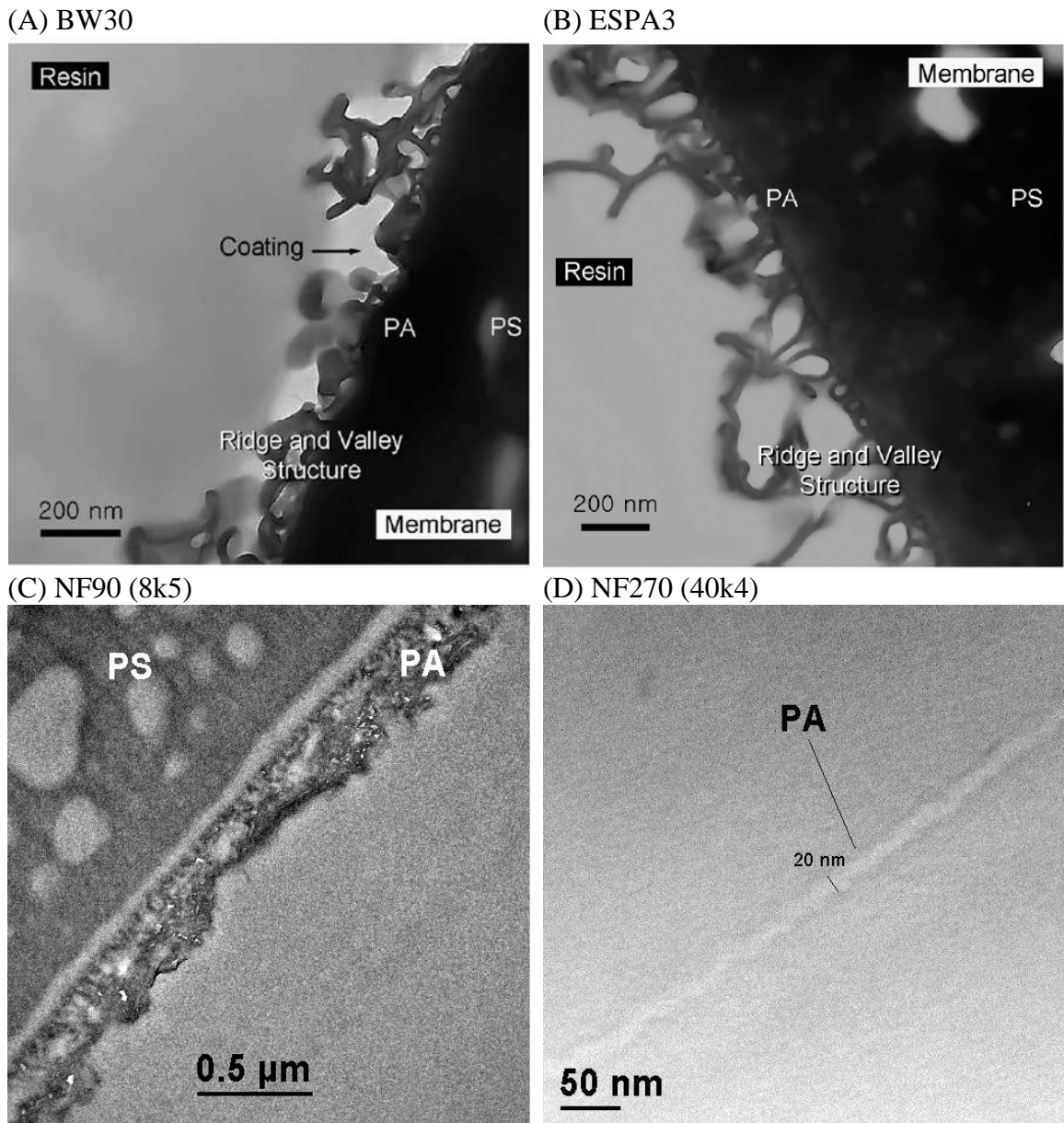
Figure 3-11. TEM images from Tang *et al.* [263] for (A) BW30 and (B) ESPA3 and for (C) NF90 and (D) NF270. Note that the scales are different on each image. PA and PS represent polyamide (active layer) and polysulphone (support layer), respectively.

more hydrophobic
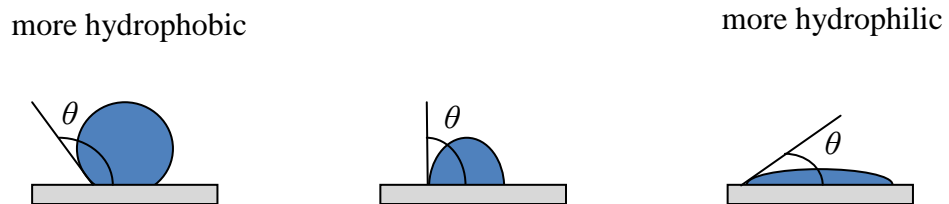
more hydrophilic

Figure 3-12. Significance of contact angle measurements [110, 153].

of the membranes increases in the order of NF270 (most hydrophilic) < BW30 < NF90 < ESPA4 (most hydrophobic) which is consistent with the trend observed in the literature [258]. Contact angle measurements were made by Annalisa De Munari (University of Edinburgh), Dr. Kingsley Ho and Dr. Alexander Bismarck (Imperial College London).

Table 3-10. Membrane contact angle measurements using the sessile drop method and comparison to literature.

Membrane	Contact Angle (°)	Published Contact Angle (°)	
		Sessile Drop Method	**Captive Bubble Method**
BW30	40.3 ± 1.1	60.8 [258], 51 [161]	65 [270]
ESPA4	53.1 ± 2.2	--	--
NF90	47.9 ± 1.7	54.6 [258], 54 [161], 42 [110]	--
NF270	29.1 ± 1.6	42.7 [258], 27 [161], 55 [110]	14.6 [270]
TFC-S	--	30 [110]	--

3.3 Chemicals

All chemicals were of high purity and purchased from Fisher Scientific (UK), Sigma-Aldrich (UK), Acros Organics, Merck or BDH Chemicals. A list of chemicals used along with the general purpose, supplier, and grade/purity is shown on Table 3-11. Ultrapure water (18.2 MΩ.cm^{-1}) (Elga PURELAB Ultra, UK) was used for all experimental and analytical solutions, unless specified otherwise. For particular experiments, the pH was adjusted using 1M NaOH and/or 1M HCl. Concentrations of target contaminants varied depending on the type of experiment and are specified where relevant.

Table 3-11. List of chemicals used with supplier and grade/purity.

Chemical	Purpose[*]	Supplier	Grade/ Purity (%)
acetone (C_3H_6O)	analysis (IC)	Fisher Scientific	99
ammonium chloride (NH_4Cl)	analysis (NA)	Fisher Scientific	99+
boric acid (H_3BO_3)	filtration	Sigma-Aldrich	99.5
dextrose ($C_6H_{12}O_6$)	characterization	Fisher Scientific	99+
dioxane ($C_4H_8O_2$)	characterization	Fisher Scientific	99+
Disodium ethylenediamine tetraacetic acid dehydrate (EDTA, $C_{10}H_{14}N_2Na_2O_8 \cdot 2H_2O$)	analysis (NA)	Acros Organics	99+
glacial acetic acid ($C_2H_4O_2$)	analysis (ISE)	Fisher Scientific	99+
hydrogen chloride (37%) (HCl)	pH adjustment	Fisher Scientific	99+
methanol (CH_3OH)	characterization	Fisher Scientific	99.8 +
multi-element standards	analysis (ICP-OES, ICP-MS)	Merck	--
N-(1-napthyl) ethylenediamine dihydrochloride (NED, $C_{12}H_{14}N_2 \cdot 2HCl$)	analysis (NA)	Acros Organics	98+
nitric acid (67%) (HNO_3)	pH adjustment	BDH Chemicals	--
oxalic acid ($H_2C_2O_4$)	analysis (IC)	BDH Chemicals	99.8
polyethylene glycol (200, 400, 600, 1000) ($H(OCH_2CH_2)_nOH$)	characterization	Fisher Scientific	--
potassium chloride (KCl)	filtration	Sigma-Aldrich	99
potassium fluoride (KF)	filtration	Acros Organics	99
potassium nitrate (KNO_3)	filtration	Fisher Scientific	99+
potassium nitrite (KNO_2)	filtration	Acros Organics	97
sodium hydrogen carbonate ($NaHCO_3$)	analysis (IC)	Fisher Scientific	99+
sodium carbonate (Na_2CO_3)	analysis (IC)	Fisons Scientific	99.9
sodium chloride (NaCl)	filtration, analysis (ISE)	Fisher Scientific	99.9
sodium fluoride (NaF)	filtration	Sigma-Aldrich	99+
sodium hydroxide (NaOH)	pH adjustment, analysis (ISE)	Fisher Scientific	98 +
sodium nitrate ($NaNO_3$)	filtration	Fisher Scientific	> 98
sodium nitrite ($NaNO_2$)	filtration	Acros Organics	97+
sulphuric acid (98%) (H_2SO_4)	analysis (IC)	Fisher Scientific	--
sulphanilamide ($C_6H_8N_2O_2S$)	analysis (NA)	Acros Organics	98
xylose ($C_{10}H_{10}O_5$)	characterization	Acros Organics	99+

[*]IC: ion chromatography; NA: nutrient analyzer; ICP-OES: inductively coupled plasma optical emission spectroscopy; ICP-MS: inductively coupled plasma mass spectroscopy; ISE: ion selective electrode

3.4 Analytical Equipment

A variety of analytical equipment was used to determine chemical composition of experimental samples. A summary of equipment, application and detection limits follows in Table 3-12.

Table 3-12. Analytical Equipment Summary.

Analytical Equipment	Type of Analysis	Measured Units	Typical Range	Detection Limit[*]
Conductivity Meter	electrical conductivity	$mS.cm^{-1}$	1 - 10000	$1~\mu S.cm^{-1}$
pH Meter	pH	--	2 – 13	low: -2.0
Ion Selective Electrodes (ISE)	fluoride, nitrate	mV	10 - 160 mV	$0.1~mg.L^{-1}$
Nutrient Analyzer (NA)	nitrate, nitrite	$mg.L^{-1}$	0.1 - 20 $mg.L^{-1}$	$0.1~mg.L^{-1}$
Inductively-Coupled Plasma Optical Emission Spectroscopy (ICP-OES)	cations, boron	$mg.L^{-1}$	0.1 - 100 $mg.L^{-1}$	$< 0.1~mg.L^{-1}$ [a]
Inductively-Coupled Plasma Mass Spectroscopy (ICP-MS)	cations, boron	$\mu g.L^{-1}$	0.1 - 50 $\mu g.L^{-1}$	$< 0.1~\mu g.L^{-1}$ [a]
Total Organic Carbon (TOC)	organic carbon	$mg.L^{-1}$	0.1 - 25 $mg.L^{-1}$	$0.1~mg.L^{-1}$
Ion Chromatograph (IC)	fluoride, chloride, nitrate, nitrite	$mg.L^{-1}$	0.1 - 2000 $mg.L^{-1}$	$0.05~mg.L^{-1}$

[*]Detection limits are reported as the practical quantitation limit typically used, but this occasionally varied depending on instrument, calibration and sample type. [a] Instrument detection limits were element-specific: $0.1~mg.L^{-1}$ (Mg, Na, B); $0.01~mg.L^{-1}$ (Al, Ca); $0.001~mg.L^{-1}$ (As, Ba, Be, Cr, Cu, Fe, Pb, Li, Mn, Mb, Ni, Se, Sr, S, Ti, U, V, Zn)

3.4.1 Electrical Conductivity and pH

Electrical conductivity (EC, mS.cm^{-1}) and pH were measured using probes (multiline P4 epoxy gel combination pH electrode with automatic temperature compensation immersion probe, WTW, Germany) and a standard meter (WTW, Germany). Conductivity readings were converted to salt concentrations using calibrations made with the particular salt of interest. Calibration details are included in Appendix A. For the results presented in Chapter 4, total dissolved solids (TDS) was estimated by multiplying the electrical conductivity by a conversion factor ($k = 0.64$) which is applicable to Australia groundwater with high sodium content [74, 271].

3.4.2 Ion Selective Electrodes

Fluoride was analyzed for some experiments (specified in the relevant chapters) using an ion-selective electrode (ISE) in conjunction with an Ag/AgCl reference electrode connected to an ion meter (781 Ion Meter, MetrOhm, UK). The electrode was calibrated regularly (once a week during regular use) with calibration standards typically of values 0.1, 0.3, 1.0, 3.0, 10.0 and 30.0 mg.L^{-1}. All standards and samples were mixed with a total ionic strength adjustment buffer (TISAB) to reduce interferences resulting from pH and conductivity. The TISAB buffer consisted of glacial acetic acid, sodium chloride and sodium hydroxide. Note that for analysis of samples containing aluminium there is significant interference with the fluoride measurement using ISE, and thus the TISAB buffer must also include 1,2-cyclohexanedinitrilo-tetraacetic acid ($C_6H_{10}[N(CH_2CO_2H)_2]_2 \cdot H_2O$ or CDTA) in order to reduce those interferences. ISE was only used for fluoride analysis of samples made in lab-grade water without high concentrations of aluminium and thus CDTA was not included in the buffer. Calibration details are included in Appendix A.

3.4.3 Nutrient Analyzer

Nitrate and nitrite were analyzed using a QuickChem 8500 FIA Nutrient Analyzer (Lachat Instruments, Colorado USA). Samples are buffered to pH 8.5 with ammonium chloride (NH_4Cl) before an optional pass through a copperized cadmium column to reduce nitrate to nitrite (this column was used when nitrate was in the samples). Disodium ethylenediamine tetraacetic acid dehydrate (EDTA) is added to the NH_4Cl

buffer solution to reduce possible interferences with other metals present in the samples. The total nitrate (reduced nitrate plus nitrite) is then determined by diazotising with a sulphanilamide colour reagent (converting an amine into a diazo compound of form R-N:N- where R is an aromatic hydrocarbon) followed by coupling with N-(1-napthyl)ethylenediamine dihydrochloride (NED). This process converts the sample to a magenta water-soluble dye which can be read at a wavelength of 520 nm. The resultant peak area is reported in $mV.s^{-1}$. Calibration details are included in Appendix A.

3.4.4 Inductively-Coupled Plasma Optical Emission Spectroscopy

Cations and boron were analyzed with inductively-coupled plasma optical emission spectroscopy (ICP-OES) (Perkin Elmer Optima 5300 DV, Waltham, USA). Calibration standards were typically 0.1, 1.0, 5.0, 10, 50, 100 and 250 $mg.L^{-1}$ (depending on expected sample concentrations) and were prepared from multi-element standards (Merck, Darmstadt Germany). An example calibration is shown in Appendix A. All samples were acidified to below pH 2 with pure Aristar nitric acid and stored in polypropylene centrifugal tubes in order to reduce possible leaching of inorganics into glassware. The analytical rinse solution was 2.8% Aristar nitric acid in MilliQ water (v:v). All samples were analyzed quantitatively by external calibration. Analysis blanks and certified reference standards were analyzed for quality control.

3.4.5 Inductively-Coupled Atomic Emission Spectroscopy

Inductively-coupled atomic emission spectroscopy (ICP-AES) was used to determine cation concentrations for the pH results presented in Chapter 4. Analysis was completed by the Australian Nuclear Science and Technology Organisation (ANSTO) using a Varian Vista AX Simultaneous CCD instrument. ICP-AES samples were acidified and spiked (4000 $mg.L^{-1}$) with cesium to suppress easily ionised elements. All samples were analyzed quantitatively by external calibration. Analysis blanks and certified reference standards were analyzed for quality control.

3.4.6 Inductively-Coupled Plasma Mass Spectroscopy

Analysis of cations and boron at low concentration (typically $\mu g.L^{-1}$ range) for the solar experiments presented in Chapter 4 was conducted with inductively-coupled plasma

mass spectroscopy (ICP-MS) (Agilent 7500ce, USA). Calibration standards were typically 0.1, 1.0, 5.0, 10 and 50 $\mu g.L^{-1}$ and sample preparation and storage was the same as for ICP-OES. Analysis of pH results presented in Chapter 4 was conducted using a different ICP-MS instrument (Agilent 4500, USA) and samples were spiked with indium, yttrium, lithium, scandium, lutetium, bismuth, and rhodium as internal standards. All samples were analyzed quantitatively by external calibration. Analysis blanks and certified reference standards were analyzed for quality control.

3.4.7 Total Organic Carbon

Organic carbon was measured for characterization experiments using a total organic carbon analyzer (TOC-V CPH, Shimadzu, Milton Keyes UK) in non-purgeable organic carbon mode (NPOC). Sample preparation included acidifying samples using 2 M HCl and sparging with nitrogen for 2 minutes prior to injection to remove inorganic carbon. Sources of carbon were neutral organic solutes methanol, xylose, dioxane, dextrose, and polyethylene glycol (200, 400, 600 and 1000 $g.mol^{-1}$). A high-sensitivity column was used and sample concentrations did not exceed 20 $mg.L^{-1}$. Typical calibration standards were 0.1, 1.0, 5.0, 10.0, 25.0 $mg.L^{-1}$, and an example calibration is shown in Appendix A.

3.4.8 Ion Chromatography

Anions for diffusion cell experiments were analyzed using ion chromatography (IC 883, Basic IC Plus, MetrOhm UK). The IC was equipped with a high capacity anion column for the determination of anions in salt solutions. Ions are separated in the column over time according to increasing charge to mass ratio, and concentrations are determined by conductivity spikes at an ion-specific retention time. The eluent used was a carbonate/bicarbonate buffer prepared fresh as needed and at least weekly. Typical standards were made at 0.1, 0.3, 1.0, 3.0, 10.0 and 30.0 and 100.0 $mg.L^{-1}$ of a single salt solution of the desired analyte. Calibration details are included in Appendix A. The analysis of chloride, nitrate and sulfate presented in Chapter 4 was completed by ANSTO with a Dionex DX-600 IC with Eluent Generator. The analysis of nitrate and fluoride for the single feed experiments presented in Chapter 5 was done using a Dionex DX-100 IC (A.I. Scientific) equipped with a Dionex AS9-HC column and the eluent

used was Na_2CO_3 (9.0 mM, pH=10). Analysis blanks and standard checks every 10 samples were analyzed for quality control.

3.5 Standard Calculations

3.5.1 Standard Parameters

Standard calculations reported through this thesis are shown in this section. Other more specialized calculations will be reported as appropriate. Flux (J or J_v, $L.h^{-1}.m^{-2}$) is calculated as

$$J = J_v = \left(\frac{Q_{permeate}}{A_{membrane}} \right), \qquad \text{Equation 25}$$

where Q is the flow of the permeate ($L.h^{-1}$) and A (m^2) is the membrane area. Flux is interchangeably volumetric flux (J_v), because it is based on a volumetric flow. If the subscript such as pure water or solution follows J, it is specifying that the measured flux is of pure water of a specific solution. Flux can be converted to permeability (L, $L.h^{-1}.m^{-2}.bar^{-1}$)

$$L = \left(\frac{Q_{permeate}}{A_{membrane} P_{applied}} \right), \qquad \text{Equation 26}$$

by dividing by applied pressure ($P_{applied}$, bar). Solute flux ($mol.h^{-1}.m^{-2}$) is calculated by

$$J_{solute} = \left(\frac{Q_{permeate}}{A_{membrane}} \right) C_{permeate}. \qquad \text{Equation 27}$$

Retention (R, %) is

$$R = R_o = \left(1 - \frac{C_{permeate}}{C_{feed}} \right) \cdot 100\%, \qquad \text{Equation 28}$$

where C is concentration in the permeate and feed. Retention calculated this way is observed retention (*eg*. no correction for concentration polarization) and unless otherwise specified, retentions reported in this thesis are observed retention. Real retention (R_r) has been corrected for concentration polarization using the relationship

$$\ln \frac{1-R_r}{R_r} = \ln \frac{1-R_o}{R_o} - \frac{\langle J_v \rangle}{k_f} \qquad \text{Equation 29}$$

where k_f is the salt mass transfer coefficient across the membrane (m.s^{-1}) and J_v is the average volumetric flux (L.h^{-1}.m^{-2}). This relationship is based on film theory [216] and was derived in Chapter 2.3.1. The mass transfer coefficient, k_f, was determined experimentally using methods previously published [154, 216] and calculated with

$$k_f = \frac{J_{salt}}{ln\left[\dfrac{\Delta P}{\pi_{bulk} - \pi_{permeate}} \left(1 - \dfrac{J_{salt}}{J_w} \right) \right]} , \qquad \text{Equation 30}$$

where the applied pressure is ΔP, pure water flux is J_w, solution flux is J_{salt}, and the osmotic pressure (π) of the bulk and permeate solutions are calculated from the bulk and permeate salt concentrations using the Van't Hoff equation:

$$\pi = \sum C_i RT , \qquad \text{Equation 31}$$

where C is concentration, R is the gas constant, and T is temperature. By experimentally determining k_f, J_w and J_{salt}, the concentration of salt at the membrane surface ($C_{membrane}$) can be calculated. This allows observed retention to be corrected for concentration polarization to get real retention (R_r)

$$R_r = \left(1 - \frac{C_{permeate}}{C_{membrane}} \right) 100 . \qquad \text{Equation 32}$$

In Chapter 4, a number of operational parameters are reported. Specific energy consumption (*SEC*, kWh.m^{-3}) is calculated using

$$SEC = \left(\frac{I_{pump} \; U_{pump}}{Q_{permeate}} \right),$$

Equation 33

where I is current (A) and U is voltage (V), the product of which is power (W). Trans-membrane pressure (TMP, bar) is calculated by

$$TMP = \left(\frac{p_2 + p_3}{2} \right) - p_{permeate}$$

Equation 34

where p_2 and p_3 are the pressures measured on the feed and concentrate lines (as shown on Figure 3-7).

3.5.2 Error Analysis

Uncertainty (δ) was calculated for selected experiments using standard propagation techniques, according to the general formula (where F is any function):

$$\delta F = F \cdot \sqrt{\left(\frac{\delta A}{A} \right)^2 + \left(\frac{\delta B}{B} \right)^2 + \left(\frac{\delta C}{C} \right)^2},$$

Equation 35

where F is any quantity that depends on A, B and C. The uncertainty for each of the fundamental contributions to the calculations (*eg.* δA or reproducibility of chemical analysis) was taken to be the standard deviation of multiple samples ($n \geq 5$) and assumed to be similar across all experiments (unless otherwise indicated). Table 3-13 shows the values used for uncertainty for standard calculations. It is also important to note that there can be significant variation in membrane coupons, even within the same batch, according to the manufacturing process. In order to reduce this effect, an acceptable pure water flux value was selected for each commonly-used membrane based on experimental flux measurements of a number of coupons of the same membrane type and batch (rather than according to the manufacturer's specification),

and any coupon outwith 10% of that pure water flux value was discarded (the acceptable value is the average permeability shown on Table 3-3 ± 10%).

Table 3-13. Uncertainty values for standard measurements (determined by taking multiple ($n \geq 5$) measurements of a single parameter or analysis).

Parameter, Analysis Type	Uncertainty Estimate (± %)
δ Chloride, IC	2 %
δ Fluoride, IC	2 %
δ Fluoride, ISE	3 %
δ Nitrite, IC	3 %
δ Nitrate, IC	3 %
δ Nitrite, NA	5 %
δ Nitrate, NA	4 %
δ Analysis, ICP-OES	2 %
δ Analysis, ICP-MS	2 %
δ Flux (L.h^{-1}.m^{-2}), --	2 %

Where the propagation calculation could not be directly applied (*eg.* for the fitting procedure in membrane characterization or for calculation of diffusion coefficients), uncertainty was estimated by re-running the fitting procedure or calculation with the largest expected errors in input parameters to determine the variation in the outputs.

3.6   Conclusions

In summary, this chapter explained the methods and materials used experimentally in this research. This included a RE-membrane system and bench scale filtration systems (stirred cells, crossflow and diffusion cells). The commercially-available membranes are described with characteristics that were determined and that were available within the literature. Chemicals were listed and each of the pieces of analytical equipment is described. Common experimental protocols are reviewed, but detailed and specific information is provided in the relevant chapters. A summary of common experimental calculations and uncertainty is included.

Chapter 4

Renewable Energy Powered Membrane Systems

In order to provide safe drinking water in isolated communities where water supply and electrical infrastructure is limited, a solar energy powered desalination system was previously developed using UF followed by NF/RO. During a field trial in 2005 (prior to the start of the PhD candidate), a series of experiments were performed with various NF/RO membranes with natural groundwater in central Australia to assess various influences on system performance, such as varying energy, pH and groundwater type.

The RE-membrane system effectively removed a number of inorganic contaminants over a range of real energy and pH conditions, given sufficient solar availability. At each location, energy fluctuations affected pressure and flow and thus the retention of fluoride, magnesium, nitrate, potassium and sodium where convection/diffusion dominated retention. Retention of calcium, strontium and uranium was very high and independent of solar irradiance, which was attributed to a combination of size and charge exclusion and, for some solutes, sorption and precipitation. The solutes were categorized into two groups (groundwater-specific) according to retention as a function of pH. The first group contained solutes with pH-independent retention (Group 1: arsenic, calcium, chloride, nitrate, potassium, selenium, sodium, strontium, and sulphate). The second group of solutes had pH-dependent retention (Group 2: copper, magnesium, manganese, molybdenum, nickel, uranium, vanadium, and zinc). The retention of Group 1 solutes was typically high and attributed to steric effects. Group 2 solutes had dominant, insoluble species under certain conditions which led to deposition on the membrane surface (and thus varying apparent retention). Variations

in system performance occurred due to changes in solar irradiance, groundwater composition and pH.

Results demonstrated successful use of this system with real water and energy conditions in remote areas, but also highlighted the lack of understanding of fundamental removal mechanisms in NF/RO processes. As such, this chapter brought to light a number of interesting research questions and emphasized the importance of working with simplified systems in order to study fundamental mechanisms, which will be the the subject of the remaining chapters of this thesis.

The RE-membrane system was designed and constructed by the previous research team led by Profs. Andrea Schäfer and Bryce Richards in Australia in 2005. Subsequently, a field trial with the system was conducted in the Australian outback, which included a number of experiments that were planned and carried out by that team. A vast amount of data was produced on this trip, and as such, a series of publications set about to address different aspects of the system operation. The contribution of the current PhD candidate was to specifically evaluate the data relevant to the removal of trace contaminants. This involved critically analyzing a very large set of data collected during the field trial in order to identify interesting results and meaningfully develop a selection of results into manuscript form. This analysis brought to light a number of interesting research questions, which shaped the rest of the PhD. Specifically, the examination of the effect of energy fluctuations and pH on the removal of ions in groundwater ultimately led to mechanistic questions about the role of ion hydration in determining which ions are retained.

4.1 Introduction and Objectives

As discussed in detail in Chapter 1, drinking water treatment and energy consumption are integrally related and need to be addressed together in order to achieve all the United Nations' Millennium Development Goals [4]. A concern with remote drinking water supplies is the presence of naturally-occurring salts and inorganic contaminants such as arsenic, fluoride and nitrate, which can be undesirable above guideline values for both health and aesthetic reasons [11, 24]. NF/RO is capable of retaining many of

these salts and inorganic contaminants, and NF/RO coupled with a renewable energy source may help address drinking water treatment in remote areas without electrical grid connections.

There are many practical advantages of using such a system without battery storage, such as increased efficiency, increased performance at higher temperatures and lower life-cycle costing [72]. However, the lack of battery storage inherently means that the variable renewable energy input will directly impact system operation (in particular flow and pressure) [72]. This subsequently may impact salt and inorganic contaminant retention due to changing conditions near the membrane surface. The impact of renewable energy on the retention of inorganic contaminants in real groundwater remains poorly understood.

In consequence, the aim of the work in this chapter was to evaluate retention of a number of inorganic solutes in real groundwater using NF/RO with five specific objectives:

1. To understand the impact of energy fluctuation on retention
2. To determine the role of pH in this process, with regard to chemical speciation and system performance
3. To determine the dominant mechanisms of ion retention in real groundwater
4. To compare system performance at different locations (each with different groundwater)
5. To evaluate retention without the influence of complicated groundwater matrices using synthetic water and controlled energy conditions

4.2 Experimental Summary

The RE-membrane system was powered by PV panels and comprised of a two-staged membrane process as described by Schäfer *et al.* [74]. Three categories of experiments were conducted: solar experiments, pH experiments and laboratory-based synthetic water experiments, the first two of which were conducted in the field prior to this PhD thesis (October 2005 in Australia).

4.2.1 Field Trial Overview

Because the primary aim of the work was to understand system operation with a real groundwater and natural renewable energy conditions, field trials were conducted. These trials were conducted at six locations in Central (Aileron, Aluyen, Harry Creek, Pine Hill, Ti Tree) and South (Coober Pedy, low salinity borehole) Australia [272] in October 2005. These locations were deemed ideal for the field study due to high average solar irradiance, problems of water scarcity as a result of low precipitation, and no access to grid electricity [273]. A map of the field locations overlain with the annual average peak daily sunshine hours (solar exposure) follows in Figure 4-1, showing that each of the field locations have very high solar irradiance [273].
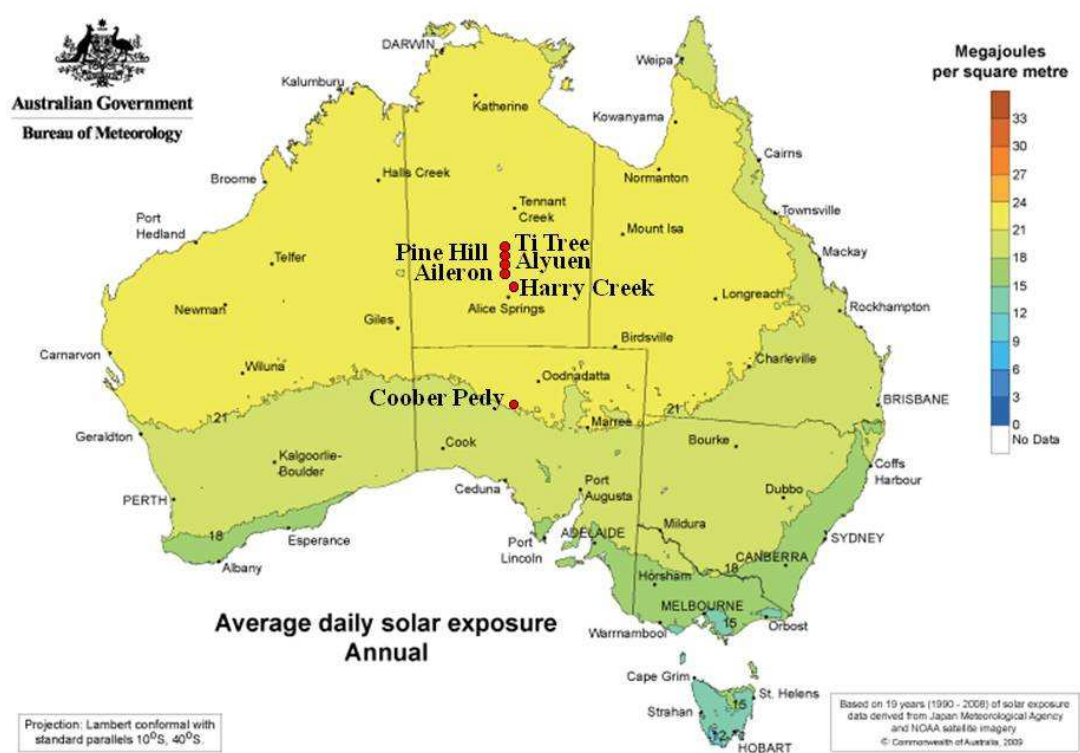
Figure 4-1. Field locations with average daily solar exposure [273].

The first step was to analyze the raw groundwater quality in each of the six field locations to provide a basis for all other experiments, using the analytical techniques described in Chapter 3.4. Chemical speciation of the groundwater was then predicted from experimental measurement of total elemental concentrations using Visual MINTEQ (methods described in Section 4.4). Subsequently, in order to assess each of

the specific effects on system performance, two main types of field experiments were conducted: (1) solar experiments and (2) pH experiments.

4.2.2 Solar Experiments

Solar experiments were designed to assess the impact of naturally varying energy throughout a solar day on salt/contaminant retention at the natural pH of the water. The solar experiments had two main purposes: (1) to obtain in-depth results and chemical analysis for the RO membrane BW30 [249] at Pine Hill and Ti Tree [248], and (2) to compare performance with six different groundwaters with less chemical detail [274]. The system was operated in re-circulation mode. Samples were collected hourly from feed, UF permeate, NF/RO permeate and concentrate and analyzed using the methods (conductivity, pH, ion selective electrodes, inductively coupled plasma optical emission spectroscopy, inductively coupled plasma mass spectroscopy) described in Chapter 3.4. Operating parameters varied depending on location and operation and will be specifically discussed in Section 4.5. Typical values were that solar irradiance varied from $0.01 - 3\,kW.m^{-2}$, motor power from $50 - 300\,W$, TMP across the NF/RO membrane from 2 – 12 bar, and feed flow between $90 - 500\,L.h^{-1}$.

4.2.3 pH Experiments

The objective of the pH experiments was to evaluate the specific impact of pH on contaminant retention, while using constant power (supplied from a diesel generator). Constant power ensured constant flow and pressure, thus isolating pH as the only variable. Four different NF/RO membranes were used (BW30 [249], ESPA4 [251], NF90 [249], and TFC-S [250]) at Pine Hill (for membrane performance comparison). An additional experiment with BW30 was conducted at Ti Tree (for comparison of different groundwaters). During each experiment, the pH of the bore water was adjusted in increasing step-wise increments between 3 and 11 with HCl and NaOH (1 M) and equilibrated (typically for 30-60 minutes) before taking performance readings and collecting samples. Samples were collected from feed, UF permeate, NF/RO permeate and concentrate and analyzed using the methods (conductivity, pH, ion

selective electrodes, ICP-OES, ICP-MS) described in Chapter 3.4. Operating parameters for the pH experiments were set at 9 bar and 400 L.h^{-1}. The feed water temperature in the tank ranged from 24.2 to 26.9°C at Pine Hill and from 29.1 to 32.6°C at Ti Tree on the days of experimentation.

4.2.4 Synthetic Water and Energy Experiments

In order to assess system performance without the influence of complicated groundwater matrices and uncontrolled energy fluctuations (*eg.* not in the field), a limited number of additional experiments were conducted using synthetic brackish water and simulated energy conditions at Heriot-Watt University. The RE-membrane system was configured as described in 3.1.4. Feed water was prepared using deionized water spiked with general purpose grade NaCl (6 g.L^{-1}), NaNO$_3$ (50 mg.L^{-1} as NO$_3$), NaNO$_2$ (10 mg.L^{-1} as NO$_2$), NaF (10 mg.L^{-1} as F), B(OH)$_3$ (10 mg.L^{-1} as B), NaHCO$_3$ (84 mg.L^{-1}) (Fisher Scientific, UK). The membrane was an new NF90 4" module, and a system set-point of 10 bar was selected as described by Park *et al.* [168]. Temperature was controlled at 22.5 °C by constant circulation. Power was held at 75, 100, 160, 220 and 265 W and samples collected at time 0, 1, 2, 3, 5, 10, 20 and 30 minutes after power was adjusted. After 30 minutes, the power was increased to the next level. Chemical analysis was conducted using the nutrient analyzer for nitrate and nitrite, ion selective electrode for fluoride, and ICP-OES for boron. Details of chemical analysis were given in Chapter 3.4.

Having described the various types of experiments conducted, the following sections report the results from these experiments. First an overview of the raw water quality and groundwater speciation in remote Australian communities is given in Sections 4.3 and 4.4, respectively. Then the performance of the RE-membrane system is discussed in detail in Sections 4.5 - 4.7.

4.3 Overview of Water Quality in Remote Australian Communities

This section discusses and compares water quality at each of the six selected field locations. Raw water quality analysis at the different field locations is shown in Table

4-1. The most saline water was Pine Hill (total dissolved solids, TDS = 5700 mg.L^{-1}) and the least saline was Ti Tree (TDS = 1080 mg.L^{-1}), which are levels typical of brackish groundwaters. All groundwaters have a pH between 7.8 and 8.5. Australian Drinking Water Guidelines for NO_3^-, Se, SO_4^{2-} and U (health-based) and Cl^-, Mn^{2+}, Na^+ and TDS (aesthetic) were exceeded at some locations (marked in **bold** font on Table 4-1). All locations exceeded guidelines for at least one contaminant. Associated health concerns for the contaminants exceeding guidelines were reviewed on Table 1-1. For Pine Hill, which will be discussed in detail in Section 4.5, the contaminants exceeding Australian health-based guidelines [24] were selenium (0.015 mg.L^{-1}, guideline (GL): 0.01 mg.L^{-1}), sulphate (889 mg.L^{-1}, GL: 500 mg.L^{-1}), and uranium (0.295 mg.L^{-1}, GL: 0.02 mg.L^{-1}). Where the solute was analyzed but not detected, the result is marked as less than the detection limit (note that detection limit varied because analysis was conducted with different instruments).

Groundwater quality can be affected throughout the year by weather trends (in particular rainfall and temperature) and anthropogenic activities such as agriculture. Therefore, contaminant concentrations could be higher in very dry and hot conditions than when rainfall is high and temperatures are lower due to more dilution and less evaporation.

Average weather information is available for Alice Springs (site number 015590), which is the nearest major town to these field locations [273]. This field study was conducted in October, where the average temperature is 30.9 °C and average monthly rainfall is 21.8 mm. The average monthly temperature varies from 19.7 °C (July) to 36.4 °C (January), and the average monthly rainfall varies from 8.6 mm (September) and 44.3 mm (February). When considering these monthly averages, October would be expected to have higher than the yearly average temperature and approximately average rainfall. While it is expected that contaminant concentrations could be higher at certain points throughout the year, the hottest months (January and February) actually occur when the rainfall is highest too. When these conditions are considered, October seems to be a fair representation of average annual water quality. From an operational standpoint, it is also worth mentioning the daily sunshine averages too. In October, this was estimated to be 10.0 h.day^{-1}, with a minimum of 8.4 (June) and maximum of 10.3 (January).

Table 4-1. Groundwater quality at each of the six field locations in Australia. Concentrations exceeding Australian Drinking Water Guidelines [24] are marked in bold. Associated health concerns for regulated contaminants were previously reviewed on Table 1-1.

Parameter (mg.L^{-1})	Aileron	Aluyen	Coober Pedy	Harry Creek	Pine Hill	Ti Tree	Aust. Guide-line°	WHO Guide-line¤
TDS	**2500**	**1540**	**4780**	**1510**	**5700**	**1080**	500[a]	600[a]
pH (--)	8.2	8.4	8.1	8.2	8.5	7.8	--	--
Al	<0.03	<0.03	<0.03	<0.03	< 0.01	0.107	0.2[a]	--
As	n/a	n/a	n/a	n/a	0.005	0.003	0.007	0.01[b]
Ba	0.0185	0.0505	0.0405	0.0295	0.016	0.04	0.7	0.7
Ca	77.2	38.2	290	31.8	60.1	30.4	--	--
Cl$^-$	n/a	n/a	**1950**	n/a	**2000**	**437**	250[a]	--
Cr	<0.01	<0.01	<0.006	<0.006	< 0.001	< 0.001	0.05	0.05[b]
Cu	n/a	n/a	<0.05	n/a	0.021	0.096	1[a] ; 2	2
F$^-$	2.22	1.27	0.26	0.29	1.10	0.46	1.5	1.5
Fe	<0.01	<0.01	<0.006	<0.006	0.225	0.055	0.3[a]	--
Pb	n/a	n/a	<0.07	n/a	0.004	0.005	0.01	0.01
Li	0.018	0.005	0.132	0.012	0.06	0.007	--	--
Lu	<0.001	0.002	0.001	0.001	<0.001	0.0135	--	--
Mg	59.0	98.3	169	96.7	149	38.1	--	--
Mn	n/a	n/a	**0.296**	n/a	0.007	0.002	0.1[a] ; 0.5	0.4[a]
Mb	n/a	n/a	n/a	n/a	0.005	< 0.001	0.05	0.07
Ni	n/a	n/a	<0.05	n/a	0.003	0.005	0.02	0.07
NO$_3^-$	8.90	21.1	28.0	32.7	19.0	**58.4**	50[c]	50[c]
K	20.6	34.1	66.0	8.6	15.0	26.0	--	--
P	<0.06	<0.06	<0.1	<0.1	<0.1	<0.1	--	--
Sc	<0.001	0.002	<0.001	<0.001	0.001	0.014	--	--
Se	n/a	n/a	n/a	n/a	**0.015**	0.004	0.01	0.01
Na	**660**	**310**	**1050**	**208**	**1650**	173	180[a]	--
St	1.00	0.53	3.31	0.51	1.3	0.475	--	--
S	90.5	36.5	370	24	272	33.2	--	--
SO$_4^{2-}$	n/a	n/a	**940**	n/a	**889**	116	250[a] ; 500	--
Ti	n/a	n/a	<0.001	n/a	< 0.001	< 0.001	--	--
U	n/a	n/a	n/a	n/a	**0.295**	**0.025**	0.02	0.015[b]
V	n/a	n/a	n/a	n/a	0.022	0.0009	--	--
Y	<0.001	<0.001	<0.003	<0.003	<0.006	0.023	--	--
Zn	n/a	n/a	<0.01	n/a	0.222	0.0008	3[a]	--

[a]Aesthetic-based guideline; [b]Provisional guideline due to scientific uncertainties regarding toxicology/epidemiology and/or due to difficulties regarding technical achievability; [c]Guideline recommended to protect against methaemoglobinaemia in bottle-fed infants (short-term exposure); n/a: not analysed; °[24]; ¤[11]

Besides averages, the month of October 2005 experienced the first rain in 18 months and very unusual amounts of it (79 mm at Alice Springs, well above average). These periods of rain and heavy cloud were an unseasonal occurrence. Hence the data may well be different than what one expects based on averages, but the actual performance data obtained will be presented in Sections 4.5 and 4.6.

4.4 Chemical Speciation of Brackish Groundwaters

Chemical speciation of the brackish groundwaters was predicted to understand the dominant chemical forms of each ion in the groundwater. Speciation modelling was conducted using the Visual MINTEQ (version 2.53) software package [275, 276]. Groundwater parameters (concentrations) were entered and 'sweep tests' were utilized based on component activity to determine the chemical speciation of the dominant ionic species over a selected pH range. Assumptions included a fixed carbonate concentration (partial pressure of 3.8×10^{-4} atm), temperature of 25°C, set valence sets based on groundwater information and phase diagrams and a charge difference between cations and anions $\leq 5\%$. Understanding the solubility of each of the compounds in the specific chemical conditions of a particular groundwater (Pine Hill) can help explain the retention results presented later in this chapter in Section 4.6.

Figure 4-2 shows the predicted speciation of fifteen commonly occurring groundwater compounds at Pine Hill by presenting the percentage of relative species of each compound as a function of pH. Several trends can be observed from analyzing these diagrams. Calcium (Figure 4-2B), magnesium (Figure 4-2E), manganese (Figure 4-2F), nickel (Figure 4-2H), and strontium (Figure 4-2L) all have major changes to primarily aqueous carbonate salt species at high pH values. Vanadium (Figure 4-2N) and zinc (Figure 4-2O) also convert nearly completely to carbonate salt species at high pH values, but first go through an intermediate transition stage. Arsenic (Figure 4-2A), fluoride (Figure 4-2D), potassium (Figure 4-2J), and sodium (Figure 4-2K) all exhibit one significant switch in primary species at a pH which corresponds to the chemical properties of the compound (i.e. acid dissociation constant). While the speciation of some compounds such as molybdenum (Figure 4-2G) and phosphate (Figure 4-2I) is quite complicated, the speciation of other compounds is not significantly impacted by

pH. Chloride (Figure 4-2C) speciation is shown as a representative example for chloride, copper, nitrate, selenium, and sulphur, all of which demonstrate this pH independence of speciation.
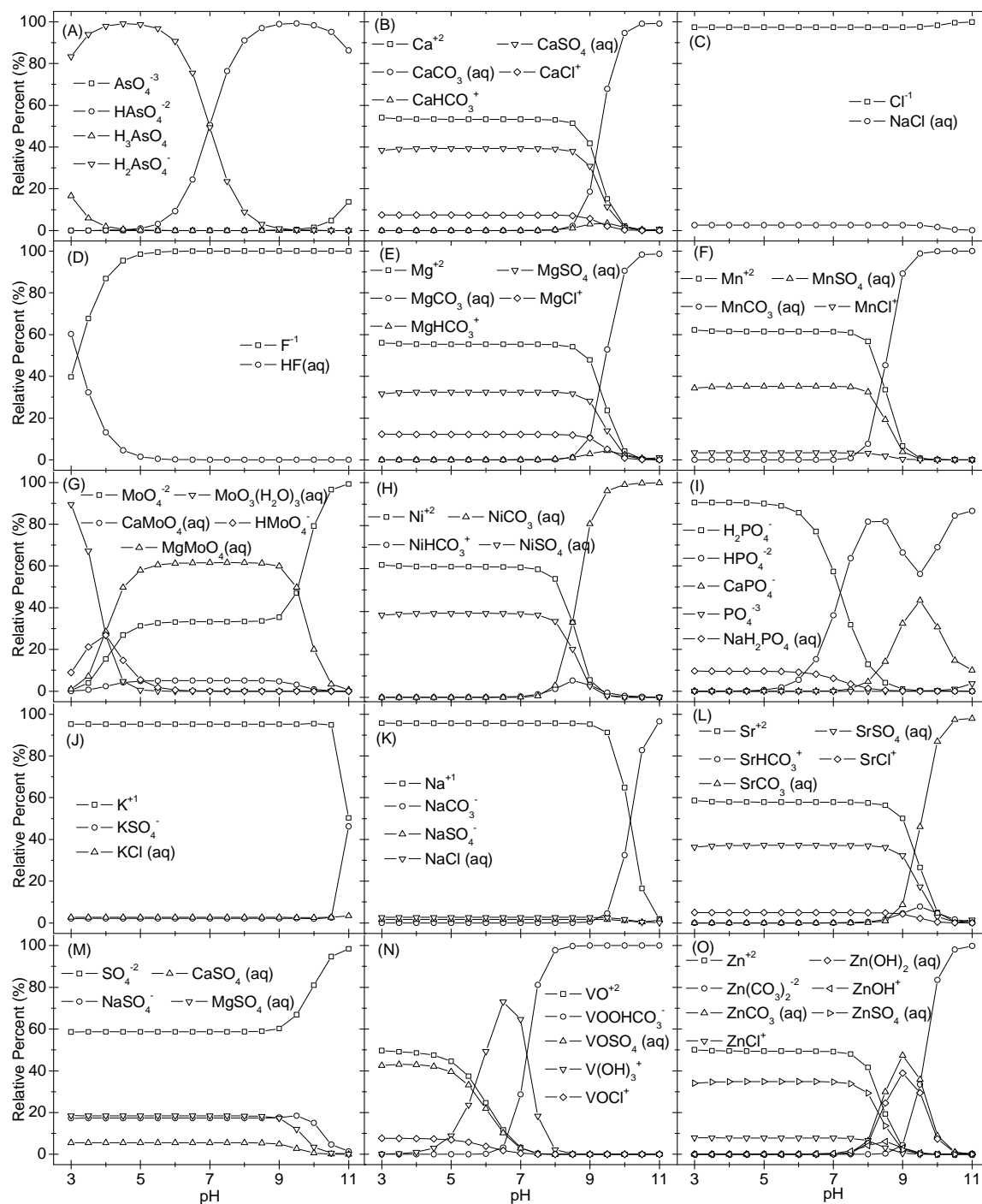

Figure 4-2. Predicted Speciation of Selected Groundwater Compounds at Pine Hill: (A) Arsenic; (B) Calcium; (C) Chloride; (D) Fluoride; (E) Magnesium; (F) Manganese; (G) Molybdenum; (H) Nickel; (I) Phosphate; (J) Potassium; (K) Sodium; (L) Strontium; (M) Sulphate; (N) Vanadium; (O) Zinc

114

Now that the raw water quality and speciation have been discussed, performance of the RE-membrane system will be assessed to see how effective the system is at removing the various chemical contaminants. Solar experiments will first be presented (Section 4.5), followed by the pH experiments (Section 4.6).

4.5   Impact of Varying Solar Conditions on RE-Membrane Performance

This section discusses the effect of varying energy on the RE-membrane system's ability to remove inorganic contaminants. Understanding the impact of varying solar energy on inorganic contaminant removal is critical to evaluating the performance of the membrane system and to determine the safe operating window. During periods with the highest solar irradiance (as per Figure 4-1), power generation from the pump increases, leading to maximum pressure, flow, and therefore high flux while during cloudy periods, pressure and flow decrease and sufficiently low energy levels will lead to pump shut down. Inevitably such variations will affect the retention of solutes. The effect of intermittent operation (wind energy) on TDS retention was examined in depth by Park *et al.* [168]. Discussed here is the effect of varying solar conditions on inorganic contaminant removal specifically at Pine Hill (Section 4.5.1) and Ti Tree (Section 4.5.2), with a summary of all field locations given in Section 4.5.3.

4.5.1   System Performance under Varying Solar Conditions at Pine Hill

The effect of changing solar irradiance on operating parameters at Pine Hill is shown in Figure 4-3. Changes in solar irradiance throughout the day correlated directly with flow, flux, and pressure (Figure 4-3A and B), as expected for a system with no energy storage [72]. The temperature of the feedwater increased nearly 7°C during the solar day from 24.7 to 31.6°C (data not shown on Figure 4-3) due to changes in ambient temperature and pumping heat (water was recycled). The relationship between solar irradiance and retention of common salts (calcium, magnesium, sodium, potassium, and TDS) and inorganic contaminants (uranium, strontium, fluoride, and nitrate) using BW30 is shown in Figure 4-3C and D, respectively. Retention was high and solute specific, with average retention throughout the day being: strontium (99.9 ± 0.1%) ≥ calcium (99.9 ± 0.1%) ≥ uranium (99.9 ± 0.2%) > fluoride (98.5 ± 1.0%) > magnesium (98.1 ± 1.9%) > sodium (97.1 ± 1.4%) > potassium (96.7 ± 1.3%) > nitrate (92.0 ±

1.8%) while TDS was 96.5 ± 3.5%. While very high retention (as achieved here) is desirable for meeting health-based guidelines for contaminants, it is also important to note that sometimes near-complete removal of minerals and salts is not ideal from a taste and possibly health standpoint [272].

Comparison of retention trends with solar irradiance (and thus with flow and pressure) gives information on mechanisms. The retention of some of these salts and contaminants (strontium, calcium, and uranium) was very high (> 99.5%) and did not change with solar irradiance. Under the conditions of the experiment at Pine Hill (pH 7.2), the dominant species of strontium and calcium are Sr^{2+} and Ca^{2+}, respectively [171], both of which have large hydrated radii of $4.12 \cdot 10^{-10}$ m (see Table 2-1, Chapter 2.1) [82]. The large hydrated radii suggest that strontium and calcium retention is dominated by size exclusion. This is significant because safe permeate concentrations of strontium, calcium, and uranium would therefore be expected regardless of operating conditions. The speciation and behaviour of uranium is complex, highly dependent on groundwater type and energy variation, and is specifically dealt with in detail by Rossiter *et al.* [277].

The retention of the other salts and contaminants was impacted by changing solar irradiance. The retention of nitrate, potassium, sodium, and TDS closely followed the trend in solar irradiance, with lowest retention occurring during the lowest solar irradiance both in the morning and evening. The hydrated radii (see see Table 2-1, Chapter 2.1) of nitrate ($3.35 \cdot 10^{-10}$ m), potassium ($3.31 \cdot 10^{-10}$ m), and sodium ($3.58 \cdot 10^{-10}$ m) are relatively low compared to strontium and calcium. This difference in hydrated sizes suggests that different mechanisms are dominant in their removal, which is supported because the operating conditions are more influential on retention than they were for the larger hydrated ions. Convection and diffusion dominate retention for nitrate, potassium, and sodium as is evidenced by an increase in retention (outside of the error range) with increasing pressure (Figure 4-3). Similar behaviour has been previously observed and attributed to convection/diffusion, especially for contaminants with small hydrated size (and thus can enter the membrane 'pore') [107]. As pressure increases, convective drag forces increase due to the solvent flux in the pore even
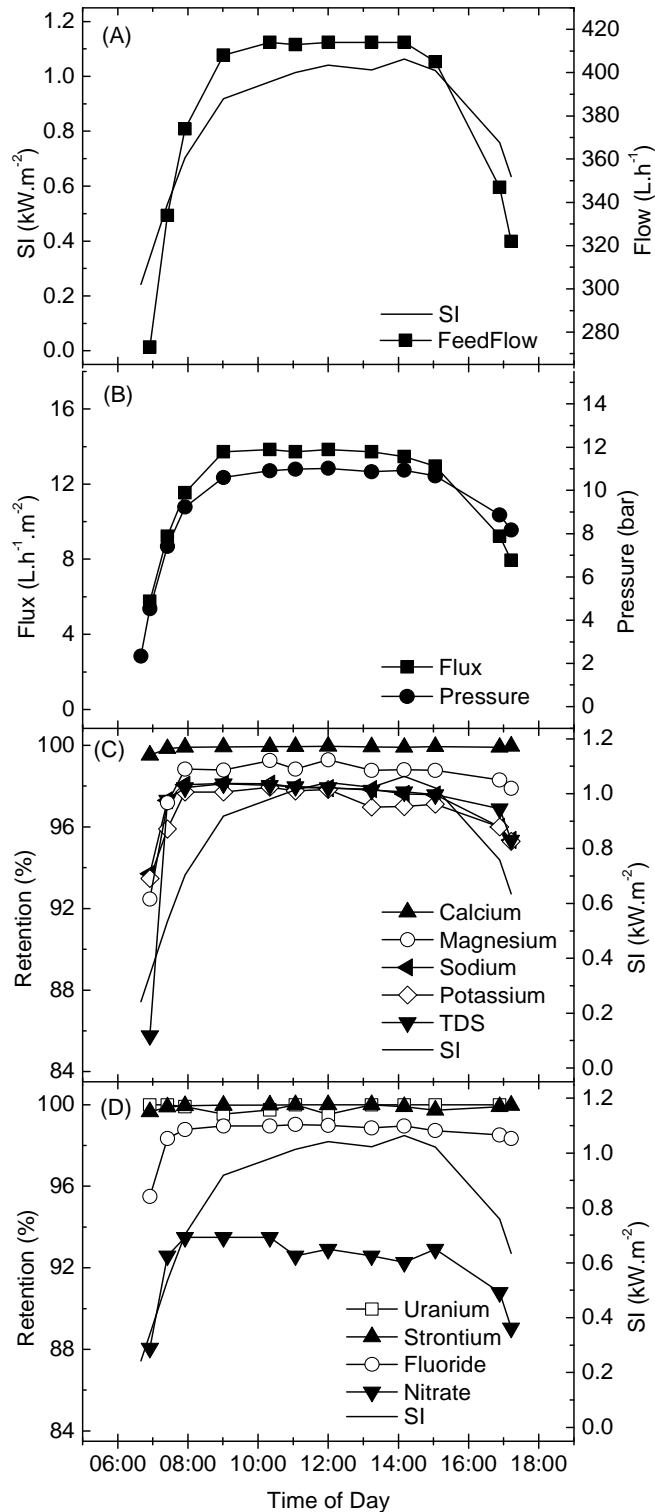
Figure 4-3. Conditions and results for BW30 operating with solar energy at Pine Hill over the course of one solar day (sunrise to sunset). Feed TDS is 5770 mg.L^{-1} and pH 7.2. Figure (A) shows solar irradiance (SI) and flow; (B) flux and pressure; (C) salt retention and SI; and (D) health-threatening contaminant retention and SI. Uncertainty in retention is not shown for clarity but calculated values are reported on Table 4-3 which are assumed to be similar for this data.

117

though surface forces attracting the solute stay constant. Up until a threshold pressure, the surface forces are stronger than the drag forces, and therefore ion flux remains low while solvent flux still increases with pressure, and thus retention increases [107]. Even at the lowest solar irradiance, the lowest retention observed was 88% for nitrate, which indicates that removal is well within acceptable guideline values and thus could be achieved for water with much higher feed concentration.

The retention of fluoride and magnesium closely followed solar irradiance at the beginning of the day, which is explained again by convection/diffusion. However, at the end of the day, retention did not again drop as was observed with nitrate, potassium, and sodium. This could be attributed to concentration polarization and/or changes in the membrane surface (which were not measured) caused by the recirculation of groundwater and thus the build-up of ions near the membrane surface as the day progressed, which resulted in nearly constant retention in the evening despite the decrease in solar irradiance. Correlation of flow and fluoride retention (as observed in the morning) has been similarly reported and attributed to convection/diffusion [241].

4.5.2 System Performance under Varying Solar Conditions at Ti Tree

In order to compare the detailed effect of varying energy with different groundwaters, a similar experiment was conducted at Ti Tree. The results of this experiment are shown in Figure 4-4. The results are similar to those from Pine Hill, where as a result of no energy storage, solar irradiance directly impacted all aspects of operation: pressure, flow, flux and the quantity and quality of permeate produced.

At Ti Tree, the system turned on at approximately 07:00 with $0.09 \, kW.m^{-2}$ solar irradiance. The solar irradiance (Figure 4-4A) increased as the day progressed from 07:00 to 10:00 causing increased feed flow (Figure 4-4A), flux (Figure 4-4B), pressure (Figure 4-4B), and production (Figure 4-4C). From approximately 10:00 to 14:00, feed flow stabilized at around $450 \, L.h^{-1}$, pressure at 10 bar, and permeate flow at $220 \, L.h^{-1}$ (corresponding to a recovery of nearly 50%). This recovery was much higher that the manufacturer's test condition of 15% recovery [249], which is good from a short-term production standpoint but reduces performance (eg. *retention*) [278] and potentially

could be damaging to the membrane module with long term operation due to increased concentration polarization and fouling.

System operation became intermittent when significant cloud cover occurred from 14:00 because solar irradiance became insufficient for operation. When this happened, the system shut off and feed flow and pressure dropped; hence no more permeate was produced (note that sample collected is an average over intermittent operation). Operation was intermittent for the remainder of the day due to partial cloud coverage. Temperature increased from 24 to 33°C during the day due to ambient conditions and pumping heat resulting from recirculation. Specific energy consumption (SEC) (data not shown on Figure 4-4) did not change with solar irradiance and was 1.0 kWh.m^{-3}.

Retention was impacted by varying energy (see Figure 4-4D) as a result of changes in flow and pressure affecting convection/diffusion mechanisms. Retention was stable during consistent system operation but dropped significantly (from > 90% to 20-30%) for all contaminants when operation was intermittent (see sample taken at 18:00). During stable system operation, retention for calcium, magnesium, strontium, potassium, sodium, fluoride, nitrate and TDS was above 90%. Retention of multivalent ions (calcium, magnesium, strontium) was higher than monovalent ions (potassium, sodium, fluoride, nitrate) which is consistent with RO principles [140]. Permeate water quality was acceptable according to guidelines for all contaminants during normal system operation (from 07:00 to 14:00) and not acceptable when operating intermittently due to cloud cover. However, if the very high quality produced during normal operating conditions was mixed with water produced during relatively short periods of intermittent operation, the resulting permeate would still be acceptable.
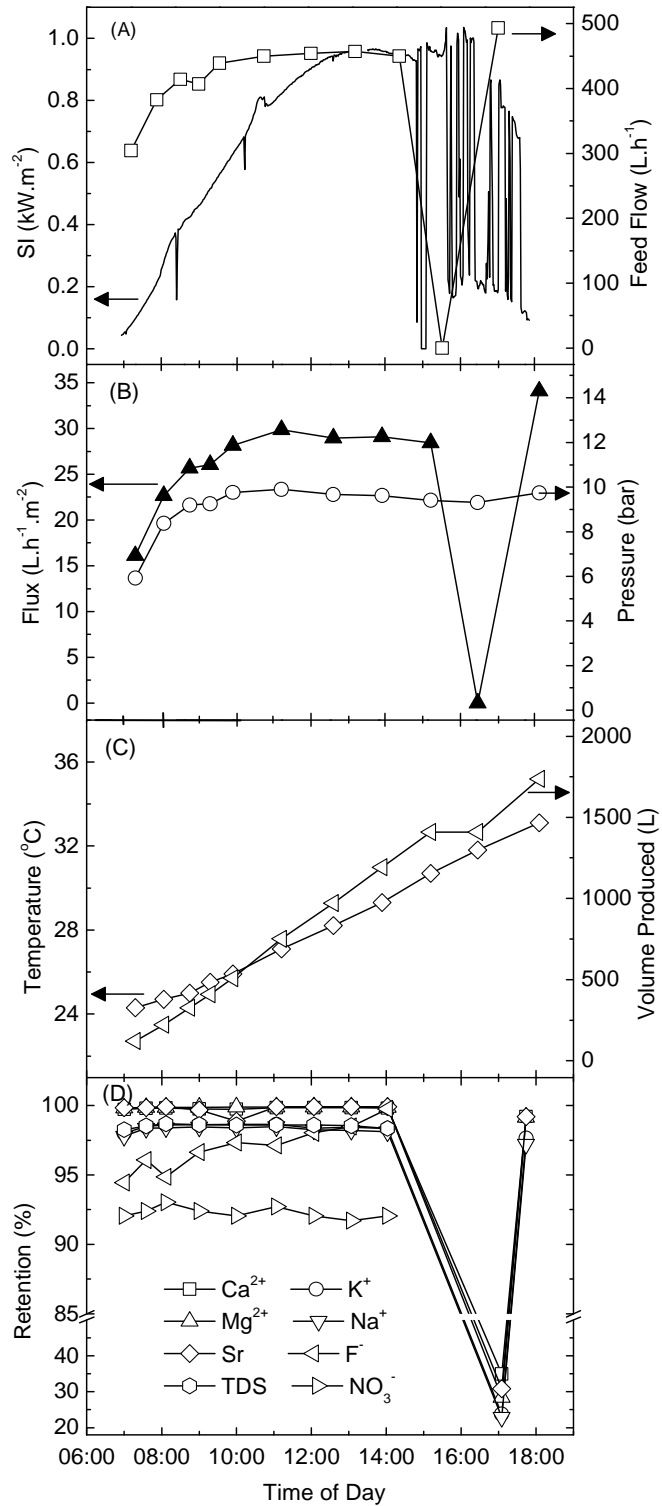
Figure 4-4. Performance of RE-membrane system at Ti Tree using BW30 membrane with operating parameters and ion retention over a solar day (afternoon partial cloud coverage). Uncertainty in retention is not shown for clarity but calculated values are reported on Table 4-3 which are assumed to be similar for this data. Note that there was not enough volume of permeate collected for the final sample of the day for nitrate analysis.

4.5.3 Impact of Groundwater Type on RE-Membrane Performance

Solar experiments were repeated at each of the locations in order to assess the impact of groundwater type on RE-membrane performance. At each location, direct correlation of solar irradiance with operational parameters was observed. A summary of the main performance parameters follows in Table 4-2.

Table 4-2. Comparison of RE-membrane operating parameters by daily average at different field locations using BW30. Note that extensive details of operation at Pine Hill [72, 248] and Coober Pedy [279] have been published elsewhere.

Location	Weather	Solar Irradiance (kWh. $m^{-2}.day^{-1}$)	TMP (bar)	Flux ($L.h^{-1}.m^{-2}$)	Recovery (%)	SEC (kWh. m^{-3})	Volume Produced ($L.day^{-1}$)	Permeate Flow ($L.h^{-1}$)	TDS Retention (%)
Aileron		4.4	5.1	8.5	25.2	1.6	911	61	91.2
Aluyen		10.6	9.2	24.7	43.7	1.2	2120	178	97.9
Coober Pedy [279]		10.7	10.2	9.1	17.5	3.2	764	65	96.3
Harry Creek		10.2	10.0	18.3	36.5	1.6	595	132	97.9
Pine Hill [171, 248]		9.5	9.0	15.4	27.2	2.3	1106	91	96.6
Ti Tree		5.8	9.0	28.4	47.2	1.0	1736	205	98.5

The weather conditions varied at the different locations, making direct comparisons by daily averages difficult. The experiments at Coober Pedy and Harry Creek were fully sunny and thus are the easiest to directly compare. Experiments at Aluyen, Pine Hill and Ti Tree were affected by partial cloud cover during the day and rain occurred at Aileron. Solar irradiance directly correlated with TMP at each of the locations. Aileron had the least solar irradiance and TMP reached a maximum of 6.7 bar during the day, whereas the averages for all other locations were all greater than 9.0 bar. The maximum TMP achieved was 11.6 bar at Harry Creek.

The rest of the parameters on Table 4-2 (flux, recovery, SEC, volume produced, permeate flow, and retention) on were dependent on the feed water in addition to solar irradiance. Because of the similar full-sun weather conditions, Coober Pedy and Harry Creek are compared in detail with regard to water composition. The average flux at Coober Pedy (9.1 $L.h^{-1}.m^{-2}$) was significantly less than at Harry Creek (18.3 $L.h^{-1}.m^{-2}$) which can be attributed to higher TDS at Coober Pedy (4780 $mg.L^{-1}$) than Harry Creek (1510 $mg.L^{-1}$, see Table 4-1) and thus a higher osmotic pressure barrier. The difference

in TDS (and consequentially osmotic pressure barrier) also explains the lower recovery, higher SEC and lower permeate flow at Coober Pedy than Harry Creek. In addition to Coober Pedy's higher TDS, concentrations of magnesium, manganese, calcium, potassium, sodium and strontium were all higher than Harry Creek (Table 4-1) which further explains the lower flux observed. Although the difference in weather conditions affects the TMP, a similar impact of lower TDS leading to high flux, high recovery and lower SEC was observed with Ti Tree and Aluyen where recoveries were again far above the standard manufacturer's test condition of 15% [249].

SEC is particularly interesting and of vital importance for RE-membrane systems [66] because of the implications on capital cost and ability to compare treatment technologies. SEC values range from 1.0 (Ti Tree) to 3.2 (Coober Pedy) kWh.m^{-3}, which was comparable with low range SEC values achieved with other renewable energy brackish water desalination processes [63]. As clearly observed with the comparison between Harry Creek and Coober Pedy, SEC is a function of feed water characteristics such as TDS and concentrations of heavy metals and salts, in addition to solar availability (determines power consumed by the pump).

Average daily TDS retention for each location was above 90%, despite occasional low retention obtained during intermittent operation (for example the drop from >90 to 20-30% as observed at Ti Tree and discussed previously). Likewise, TDS retention dropped to 40% at one sampling point with the poor weather conditions at Aileron, but the daily average remained above 90%. This shows that under these conditions, the system works sufficiently despite the intermittent energy from poor weather.

The differences in selected ion retention for each location are shown in Figure 4-5. The highest retention at all locations occurred with multivalent ions magnesium, calcium and strontium, which was similar to what was observed at Ti Tree and expected due to charge and size exclusion. When operation was continuous (no system shut off), retention was above 85% for these contaminants in each of the groundwaters – which is sufficient to meet drinking guidelines. This is of particular interest because the variation of TDS in the groundwater (between 1080 and 5700 mg.L^{-1}) did not reduce retention to unacceptable levels despite the clear impact on parameters such as flux and SEC (Table 4-2). Similarly, variations in magnesium concentration (169 mg.L^{-1} at

Coober Pedy versus 38 mg.L^{-1} at Ti Tree) did not affect magnesium retention (> 99.5% for both).

Interestingly, retention of nitrate followed solar irradiance at both Aluyen and Pine Hill, with retention lowest at lowest solar availability (early and late day). Solar irradiance impacts convection/diffusion retention mechanisms because of changes in flow and pressure, which consequently affects transport of nitrate (a relatively small ion). However, this trend was not observed at Coober Pedy, as shown on Figure 4-5. This could be explained because Coober Pedy has higher concentrations of large hydrated ions such as calcium and magnesium which could build an ionic boundary layer (concentration polarization) of these larger molecules on the membrane surface and effectively shield the impact of changing operating conditions on smaller ions such as nitrate.

Under very cloudy conditions (Aileron) retention dropped to between 40-50% for one sample at 09:00 due to severe fluctuations (thunderstorms!) but the remainder of samples were retained > 93%. At Ti Tree, retention dropped at 18:00 due to system shut off as discussed previously. A comparison of Aluyen (some fluctuations in solar irradiance) with Coober Pedy (no solar fluctuations) shows no difference in retention, indicating that occasional fluctuations (with a duration of several minutes maximum, occurring every couple of hours) did not impede system performance with regard to contaminant retention, as long as the fluctuation does not cause the power to shut off (as with Ti Tree where the system did not recover). Harry Creek has no data after approximately 12:00 due to the system being down.

Depending on how water is being used/stored, though, periods of unacceptable retention may not have much effect as long as the volumes produced during significantly cloudy/rainy periods are relatively small as compared to when the system is operating well. This is usually the case due to low pressure and hence low flux during reduced energy periods. For example, because the water is treated to such high levels during continuous operation, mixing of ultra high quality water with a small proportion of water that is not treated as well does not make much difference. The issue of intermittent operation is of ongoing research interest [280].

123
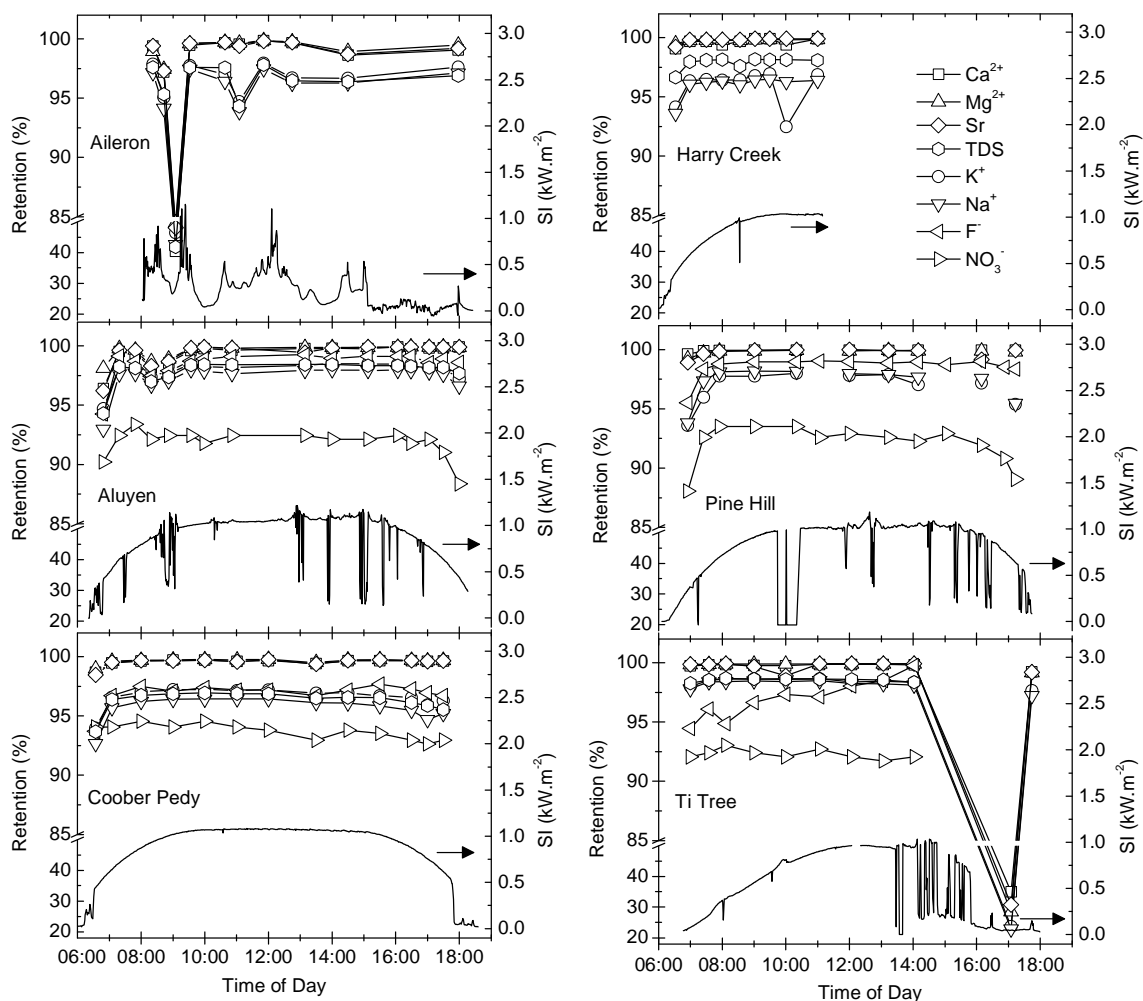
Figure 4-5. Ion retention (calcium, magnesium, strontium, TDS, potassium, sodium, fluoride and nitrate) and solar irradiance (SI) at each of the six field locations over a solar day. Uncertainty in retention is not shown for clarity but calculated values are reported on Table 4-3 which are assumed to be similar for this data.

In summary, these solar experiments have shown that a number of solutes were well-retained ($\geq 85\%$) despite energy variation (solar irradiance between 0.2 and 1.0 kW.m^{-2}) during a typical solar day. Fluctuations in energy led to subsequent changes in flow, pressure, flux, and SEC. Consequently, retention for solutes such as fluoride, magnesium, nitrate, potassium, sodium and TDS was impacted where convection/diffusion dominated retention. For very large hydrated solutes (calcium, strontium, and uranium), retention was very high due to size exclusion and no impact of operating conditions was observed. When different groundwaters were compared, retention of calcium, fluoride, potassium, sodium, nitrate, magnesium, strontium and TDS remained high (>85%) for each site tested (during continuous system operation), despite differences in groundwater composition and solar availability. However, during

periods of severe energy fluctuations (range from 0.02 to 0.8 kW.m^{-2} lasting nearly two hours at Ti Tree), the system shut off and retention dropped significantly to unacceptable levels. This decreased performance during extreme fluctuations has practical implications, especially in locations where such extreme changes occur frequently.

4.6 Impact of pH on RE-Membrane Performance

Because groundwater chemistry changes with pH, performance of the RE-membrane system can also be impacted with regard to ion retention and operation (*eg*. flux). The results from the pH experiments, described in Section 4.2.3, were categorized into two groups according to the observed retention behaviour of the contaminants. The first group is solutes whose retention did not depend on pH (Group 1) and the second group is solutes whose retention was pH-dependent (Group 2).

4.6.1 System Performance for pH-independent Solutes

Group 1 contains solutes whose retention was independent of pH at Pine Hill (arsenic, calcium, chloride, nitrate, potassium, selenium, sodium, strontium, and sulphate). Average retention for each Group 1 solute, membrane, and location throughout the entire pH range are reported in Table 4-3. Results will first be discussed for BW30 at Pine Hill, and then compared to the other membranes and location. Note that Group 1 may contain different solutes in another groundwater, as the pH-dependence is groundwater specific.

Group 1 retention using BW30 at Pine Hill was high and generally above 90% (Table 4-3). Retention correlated both with charge and hydrated size. The hydrated radii sequence for the predicted dominant species of each solute (no data available for arsenic species) is: Ca^{2+} ($4.12 \cdot 10^{-10}$ m) $= Sr^{2+}$ ($4.12 \cdot 10^{-10}$ m) $> SeO_4^{2-}$ ($3.84 \cdot 10^{-10}$ m) $> SO_4^{2-}$ ($3.79 \cdot 10^{-10}$ m) $> Na^+$ ($3.58 \cdot 10^{-10}$ m) $> NO_3^-$ ($3.35 \cdot 10^{-10}$ m) $> Cl^-$ ($3.32 \cdot 10^{-10}$ m) $> K^+$ ($3.31 \cdot 10^{-10}$ m) (see Table 2-1, Chapter 2.1) [82, 171]. Multivalent ions with large hydrated radii (i.e. Ca^{2+}, Sr^{2+} and SO_4^{2-}) were retained more than monovalent ions with smaller hydrated radii (i.e. Cl^-, K^+, and Na^+) at Pine Hill with BW30 (Table 4-3).

Table 4-3. Group 1 retention using BW30, TFC-S, ESPA 4, and NF90 at Pine Hill (for comparison of membrane performance with the same groundwater) as well as BW30 at Ti Tree (for comparison of the same membrane with different groundwater). Operating conditions were set at 9 bar and feed flow 400 L.h^{-1}. Where retention is reported as '≥', the calculation was limited by the analytical detection limit.

Solute	Retention (%) BW30 Pine Hill	Retention (%) TFC-S Pine Hill	Retention (%) ESPA 4 Pine Hill	Retention (%) NF90 Pine Hill	Retention (%) BW30 Ti Tree
Arsenic	≥ 78.9 (± 5.1)	64.2 (± 4.7)	≥ 77.6 (± 4.6)	≥ 77.5 (± 5.9)	≥ 57.6 (± 4.5)
Calcium	99.6 (± 0.2)	95.2 (± 1.1)	98.8 (± 1.3)	99.5 (± 0.3)	99.7 (± 0.2)
Chloride	96.4 (± 2.7)	76.1 (± 1.8)	89.0 (± 1.9)	92.5 (± 3.8)	97.3 (± 2.9)
Nitrate	90.6 (± 6.7)	51.5 (± 6.6)	70.0 (± 7.4)	90.4 (± 2.0)	90.9 (± 6.2)
Potassium	94.9 (± 4.1)	78.9 (± 2.9)	85.7 (± 3.2)	91.0 (± 5.2)	97.4 (± 2.1)
Selenium	≥ 93.8 (± 0.1)	90.0 (± 3.8)	≥ 92.6 (± 2.6)	≥ 92.9 (± 2.6)	≥ 74.3 (± 3.5)
Sodium	96.4 (± 1.5)	77.4 (± 2.9)	79.6 (± 2.2)	87.5 (± 4.9)	96.2 (± 1.4)
Strontium	99.6 (± 0.2)	95.7 (± 0.9)	98.8 (± 1.4)	99.5 (± 0.4)	99.7 (± 0.1)
Sulphate	99.5 (± 0.5)	97.1 (± 0.6)	99.1 (± 0.3)	99.5 (± 0.2)	99.8 (± 0.1)
TDS	94.9 (± 4.5)	77.7 (± 2.7)	87.7 (± 5.9)	91.4 (± 3.7)	94.4 (± 6.9)

The charge of BW30 (as well as each of the other membranes) becomes increasingly negative with increasing pH [161]. Therefore, if charge exclusion was the dominant retention mechanism, retention would be expected to consequently increase with pH [113]. However, because retention did not change with pH, charge is not predicted to be the dominant mechanism for these salts and inorganic contaminants. This is best exemplified with chloride, nitrate, potassium, and sulphate, whose speciation is mostly pH independent between pH 3 and 11 under the conditions at Pine Hill, with dominant species Cl^-, NO_3^-, K^+, and SO_4^{2-}, respectively [171]. The retention of these solutes is pH independent, despite the changing membrane charge with pH. Highest retention is achieved for those with larger hydrated radii. This suggests that charge exclusion is not dominant, and instead, steric interactions dominate Group 1 retention.

The speciation of other Group 1 solutes (arsenic, calcium, selenium, sodium, and strontium) depended on pH [171], but despite the changes in dominant species (and thus differences in charge and hydrated size), the retention remained pH independent. The dominant species of calcium, sodium, and strontium were carbonate forms [171] at high pH and arsenic likely deprotonated between pH 7 and 9 depending on if arsenic was present as arsenic (V), arsenic (III) or a mixture [172]. Arsenic (III) retention has been previously observed to be pH independent and attributed to steric exclusion [172].

Regardless of these changes in species (corresponding to changes in hydrated size and charge) with pH, retention was still constant and for each of these solutes, again supporting that steric interactions dominated retention.

The results for Group 1 solutes with health-based Australian or WHO guidelines (arsenic, nitrate, selenium, and sulphate – see Table 4-1) warrant individual attention given their significance in water supplies. With BW30, the retention of these contaminants was high. Arsenic (total) was well-retained, with an average retention $\geq$ 78.9% (limited by analytical detection limit) and pH-independent. Several studies have evaluated arsenic retention as a function of pH and other operating parameters [26, 177] and found that retention was highly dependent on operating conditions and affected by charge repulsion. There are conflicting studies in the literature with regard to the pH dependence of arsenic retention. In one case, arsenic (III) retention was observed to be pH independent [172]. However, Urase *et al.* observed that arsenic (III) retention was dependent on pH and arsenic (V) was pH-independent [177]. Further conflicting behaviour was observed by Figoli *et al.* who found that arsenic (V) retention was strongly dependent on pH [26]. These studies demonstrate that the dependence of arsenic retention on pH can vary and depends not only on the type of arsenic present but also on other groundwater characteristics. Note that in this study, where pH-independence of arsenic retention was observed, *total* arsenic was measured, rather than a particular species such as arsenic (III) or (V), and most likely the total arsenic present was a mixture of different types. High retention of nitrate (90.6%) was achieved. Selenium and sulphate were the only contaminants above the guideline in the feed, and high retention was again achieved ($\geq$ 93.8% and 99.5%, respectively), resulting in permeate concentrations well below the guideline. Again, selenium and sulphate have relatively large hydrated radii ($3.84 \cdot 10^{-10}$ and $3.79 \cdot 10^{-10}$ m, respectively) [82], which supports that their high retention is due to size exclusion.

Membrane comparison (Table 4-3) showed the TDS retention sequence for Pine Hill is: TFC-S (77.7 $\pm$ 2.7%) < ESPA4 (87.7 $\pm$ 5.9%) < NF90 (91.4 $\pm$ 3.7%) < BW30 (94.9 $\pm$ 4.5%) (note TDS has higher uncertainty than the other parameters because of the many groundwater constituents contributing to this measurement and the changes in their proportion in feed/permeate). The average daily flux sequence (data not shown) varied inversely to the TDS retention: BW30 (13.5 $\pm$ 1.5 L.m^{-2}.h^{-1}) < ESPA4 (23.1 $\pm$ 1.2 L.m^{-}

^{2}.h^{-1}) = NF90 (23.1 $\pm$ 0.6 L.m^{-2}.h^{-1}) < TFC-S (24.3 $\pm$ 0.4 L.m^{-2}.h^{-1}). The retention of specific solutes follows the same trend as TDS for each membrane (see Table 4-3). The lowest retentions occur with TFC-S (which is the 'loosest' of the membranes), and the highest retentions with BW30 (a 'tight' brackish water RO membrane).

Some of these ions presented challenges to the 'loose' TFC-S membrane in terms of retention. In particular, nitrate retention (51.5%) and arsenic retention (64.2%) by TFC-S were low as compared to the retention of other contaminants by TFC-S and to the other membranes' retention of arsenic and nitrate. Because feed concentrations of nitrate and arsenic did not exceed guidelines, this was not unsafe, although the lower retention with TFC-S could be an issue for waters of higher feed concentrations. Size exclusion was a less effective retention mechanism for the 'loose' TFC-S, which explains the lower retention observed and highlights that variation of the effective membrane 'pore' size as compared to contaminants' hydrated radii was significant when different membranes are considered. Retentions with BW30 and NF90 are very similar, which can be explained by the comparable molecular weight cut off values of these membranes (98 and 100, respectively) [161] (and thus similar 'pore' size).

Comparing Pine Hill and Ti Tree waters (Table 4-3) shows the impact of general water characteristics on the performance of BW30. Group 1 retention trends at Ti Tree confirmed results seen at Pine Hill (pH independence and similar retention values). This indicates the consistently high performance of BW30 with Group 1 solutes, and again supports that size exclusion is predominant because of the minimal impact of feed composition. The difference in average feed temperature (31.0°C at Ti Tree compared to 23.8°C at Pine Hill) did not have an observable impact on retention. Nitrate data is of particular significance because it was present above guidelines at Ti Tree (which is a grape farm), and was safely removed to near detection limit. Retention values for those solutes whose permeate measurements were limited by detection (arsenic and selenium) are difficult to compare between groundwaters, but both arsenic and selenium were well below guidelines at Ti Tree.

4.6.2 System Performance for pH-dependent Solutes

The retention of other solutes (Group 2: copper, magnesium, manganese, molybdenum, nickel, uranium, vanadium, and zinc) in the Pine Hill groundwater was impacted by pH, as opposed to the pH-independent Group 1 solutes. Group 2 solutes have insoluble and dominant species under certain conditions, which resulted in their apparent retention being dependent on pH (Figure 4-6). Feed concentration (and thus observed retention) varied significantly between pH 3 and 11, because of deposition on the membrane surface rather than charge or steric retention mechanisms. Precipitation occurs when concentration in the boundary layer exceeds the solubility limit of a particular species [112] at those local conditions.

Magnesium (Figure 4-6B), for example, showed a drastic drop in feed concentration above pH 10, indicating precipitation due to the insolubility of $MgCO_3$ [121, 171]. The deposit of precipitates (M_{dep}) can be calculated from the mass balance:

$$M_{dep} = V_{F,I}C_{F,I} - V_F C_F - V_P C_P - V_N C_N ,$$

Equation 36

where V is volume, C is concentration, and indices F are feed, P permeate, N concentrate, and I the initial reference condition, respectively. Indeed, the mass balance confirmed accumulation on the NF/RO membrane surface, with approximately 78% of the magnesium present in the initial feed solution having deposited at high pH.
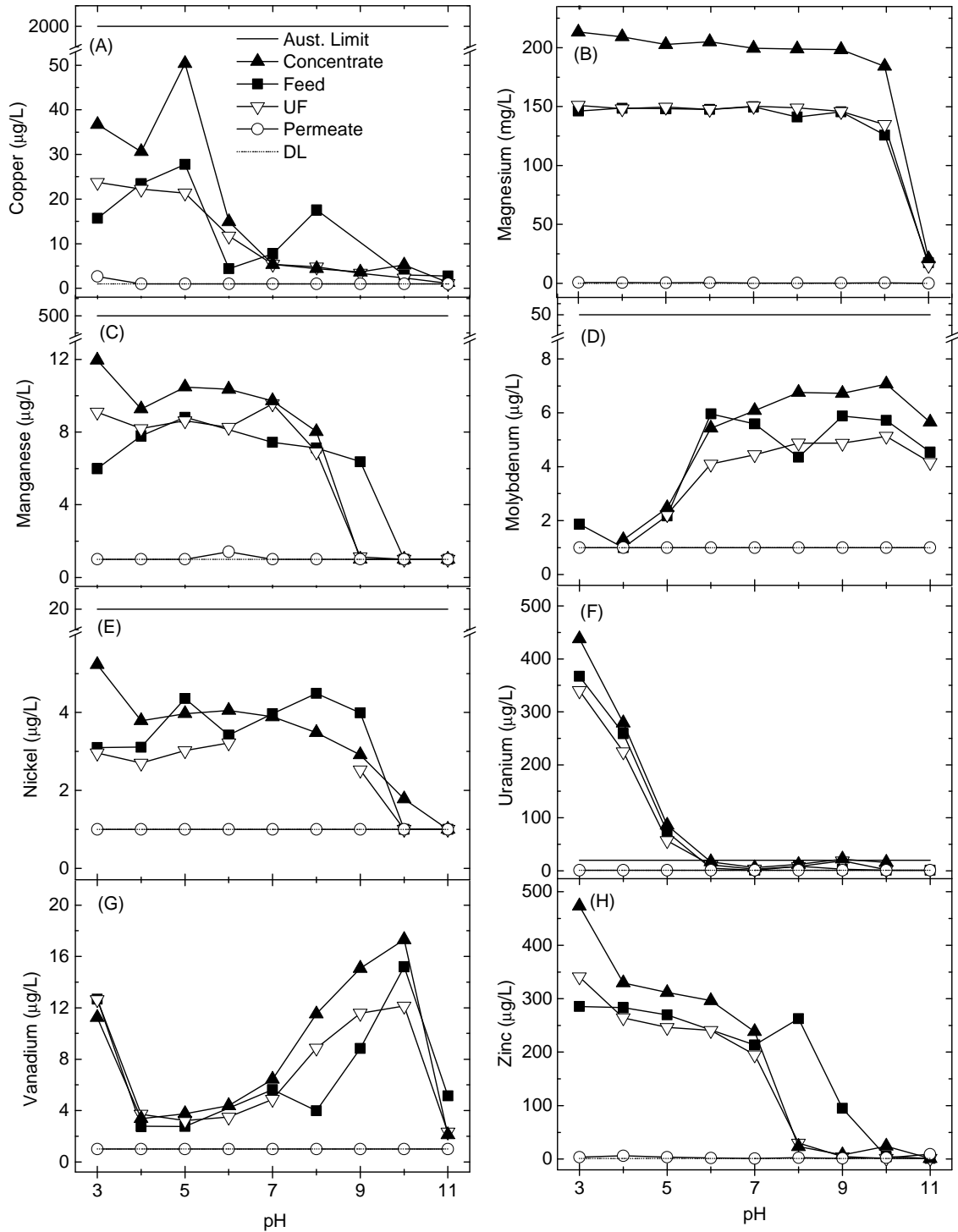
Figure 4-6. Concentration of feed, UF permeate, NF/RO permeate, and concentrate as a function of pH for BW30 at Pine Hill of Group 2 precipitating solutes (A) copper; (B) magnesium; (C) manganese; (D) molybdenum; (E) nickel; (F) uranium; (G) vanadium; and (H) zinc. Australian guidelines (if applicable) and detection limits (DL) are shown.

Similarly to magnesium, deposition occurred for all of the other contaminants shown in Figure 4-6. Manganese (Figure 4-6C) and nickel (Figure 4-6E) deposited on the membrane at high pH, with respective accumulations $\geq 50\%$ and $\geq 3\%$ of the original concentrations (calculation limited by detection). Speciation models indicated that these solutes were present in their carbonate forms $MnCO_3(aq)$ and $NiCO_3(aq)$ at the pH values where precipitation was observed [171]. Copper (Figure 4-6A) and molybdenum (Figure 4-6D) both accumulated on the membrane below pH 7, with respective accumulations of $\geq 68\%$ and $\geq 42\%$ (again constrained by analytical detection limit). Copper was present as either $CuCl^{2-}$ or $CuCl_2^-$, depending on the valence of copper (which was not determined) and molybdenum as $MoO_3(H_2O)_3$ *(aq)*. Accumulation of zinc (Figure 4-6H) was the most significant, with $\geq 96\%$ of the original concentration accumulating on the membrane above pH 8, where zinc was mostly $Zn(OH)_2(aq)$ and $ZnCO_3(aq)$ between pH 8 and 10, and $Zn(CO_3)_2^{-2}$ above pH 10 [171]. Vanadium (Figure 4-6G) showed complex speciation with deposition occurring both at low and high pH (accumulation $\geq 34\%$). Deposition of uranium (Figure 4-6H) on the membrane occurred above pH 5, and the complex speciation of uranium suggests it would dissolve back into solution above pH 8 [23, 171], which was not observed at Pine Hill with BW30. The behaviour of uranium was strongly dependent on both feed water characteristics and operating conditions and specific details were published elsewhere [277].

Removal was achieved (mostly to detection limit) for Group 2 solutes with health-based guidelines (copper, manganese, molybdenum, nickel and uranium - see Table 4-1). Uranium removal to below the guideline is especially notable since the feed concentration was significantly above the recommended level. Although the feed concentrations of copper, molybdenum and nickel did not exceed guidelines, the high removal observed indicates that the process would be effective in treating waters with higher feed concentrations of these solutes. The same general trends were observed for the other membranes tested at Pine Hill (TFC-S, ESPA 4, and NF90) as well as for BW30 at Ti Tree.

The long term consequences of membrane deposition are flux decline, possible deterioration in permeate quality, and increased SEC. During the relatively short experiments (30-60 minutes per pH value), significant flux decline (data not shown) at

high pH was noted for BW30 at both Pine Hill (22%) and Ti Tree (45%). Flux decline for the other membranes was less than 10%. The lowest overall flux (13.5 $L.m^{-2}.h^{-1}$) with BW30 at Pine Hill corresponded to the highest SEC (1.9 $kWh.m^{-3}$). This was due to the high salt concentrations at Pine Hill. For example, calcium in Pine Hill water is approximately double that of Ti Tree water (Table 4-1). In addition to the high retention of BW30 as compared to the other membranes tested which results in higher concentration polarization, higher osmotic pressure and consequently lower flux (which directly impacts SEC). Much of the precipitation was reversible with a change in pH (see vanadium on Figure 4-6G) which may not be the case during long term operation when biofouling may occur as well.

The impact of pH on system operation and specific ion retention at Ti Tree was also evaluated (see Figure 4-7), with the purpose being to compare how varying pH with a different groundwater affected performance. Figure 4-7 shows that above pH 9, flux decreased nearly by 50% and SEC increased almost 200% from 0.95 to 1.8 $kWh.m^{-3}$. The precipitation of carbonate-based contaminants (such as $MgCO_3$, $MnCO_3$ and $CaCO_3$) is theoretically predicted by speciation modelling at high pH [171]. However, unlike Pine Hill, precipitation of these compounds was not observed, as the retention of these large multivalent ions (calcium and magnesium) did not change with pH (Figure 4-7B). The flux decline could be explained by the increased osmotic pressure barrier caused by the addition of NaOH for pH adjustment.

The retention of some ions (nitrate, fluoride and TDS) increased with pH. This is due to increased charge repulsion as the membrane surface charge becomes more negative at higher pH. At low pH, the retention of fluoride is lowest (50%) and then fluoride retention increases to > 98% above pH 8. Nitrate retention is 83% at pH 3 and increases to 94% above pH 8 (which is less than fluoride at the same pH). Because fluoride and nitrate have the same charge and thus would be expected to be repelled in the same manner, this result shows that ion size impacts retention in addition to charge [171], as was demonstrated at Pine Hill.
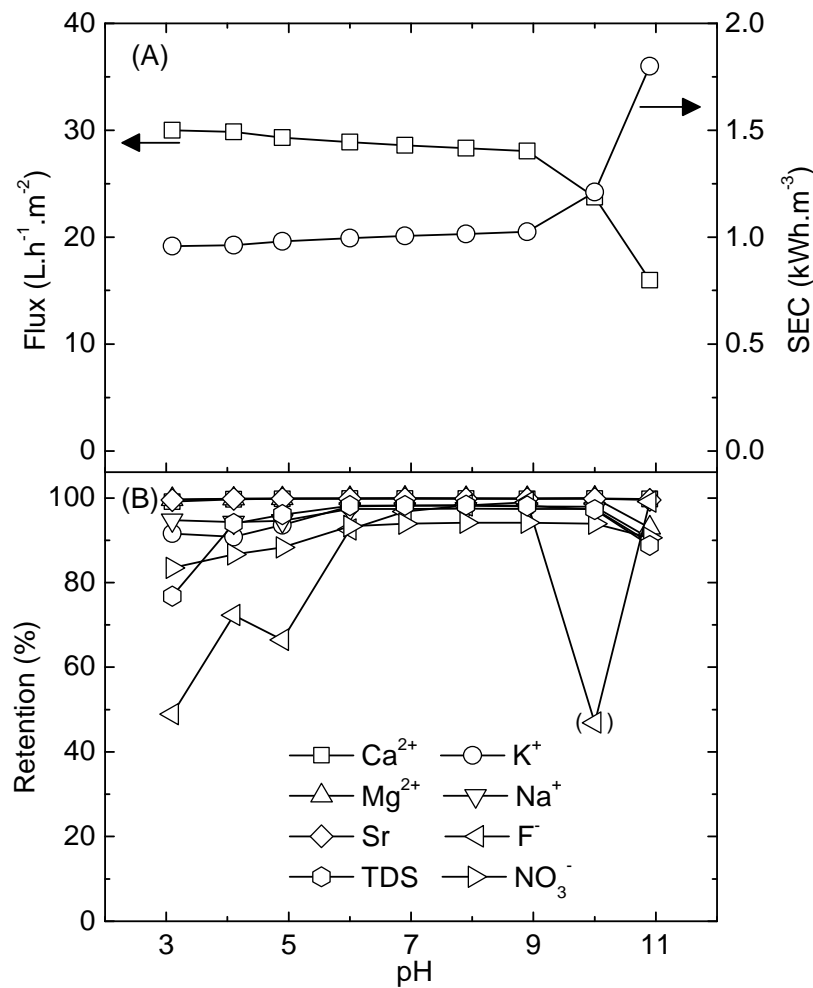
Figure 4-7. Impact of pH on flux, SEC and ion retention at Ti Tree using BW30. Uncertainty in retention is not shown for clarity but calculated values are reported on Table 4-3 which are assumed to be similar for this data.

It is very important to note that the behaviour with regard to the dependence of retention on pH observed at Ti Tree is different for some solutes than was observed at Pine Hill. This means that the groups of solutes presented for pH-dependence and pH-independence are groundwater-specific. For example, at Ti Tree, the retention of nitrate changes with pH although the opposite was observed at Pine Hill (nitrate was in Group 1). Further, at Ti Tree, the retention of magnesium was high and pH-independent, whereas at Pine Hill the behaviour of magnesium was strongly dependent on pH due to precipitation at high pH. The groundwater characteristics thus have an important effect on the pH-dependence of retention of individual solutes, and the groups presented do not apply to every groundwater.

Although the natural pH of the waters tested in the field study only varied from 7.8 to 8.5 (see Table 4-1), some locations have much higher pH where flux decline and precipitation could be a major operational issue. For example, alkaline groundwaters have been identified from pH 9.1 in Tanzania [281] up to pH 12 in Korea [282]. Although precipitation was not observed in Ti Tree, this has been observed in similar groundwaters [283]. In such locations, contaminant retention may be unreliable and flux decline, fouling and membrane cleaning would be major operational barriers. Further, concentration polarization near the NF/RO membrane surface could induce precipitation, or further precipitation, even if none occurred prior to the UF stage or already-present precipitates were small enough to pass through the UF membrane.

In summary, these pH experiments have shown that the retention of some solutes (Pine Hill Group 1: arsenic, calcium, chloride, nitrate, potassium, selenium, sodium, strontium, and sulphate) is independent of pH. The retention of other solutes (Pine Hill Group 2: copper, magnesium, manganese, molybdenum, nickel, uranium, vanadium, and zinc) is strongly dependent on pH. The definition of the groups varies depending on groundwater. Operating parameters such as flux and SEC are also impacted at high pH, which can have negative practical implications.

4.7 System Operation with Synthetic Water and Simulated Solar Power

In order to better understand the system operation and membrane performance without the influence of complex groundwater matrices, a limited number of experiments were conducted using de-ionized water spiked with inorganic contaminants and a solar array simulator to power the system in a controlled manner (as described in Chapter 3.1.4). The experiments determined the retention of each of the inorganic contaminants (at concentrations relevant to brackish groundwaters) at steady state conditions at a number of pump motor power levels. For reference, pump motor power levels of 75, 100, 160, 220 and 265 W corresponded to solar irradiance values of 0.25, 0.34, 0.53, 0.73 and 0.88 $kW.m^{-2}$, respectively. The minimal power level of 75 W corresponded to where the system just began to operate continuously and the maximum neared the maximum capacity of the system. The membrane was an new NF90 4" module, and a system set-point of 10 bar was selected as described by Park *et al.* [168]. Results for steady-state

retention are shown in Figure 4-8 and the average operating conditions (flux, flow, TMP and temperature) at each power level in Table 4-4.
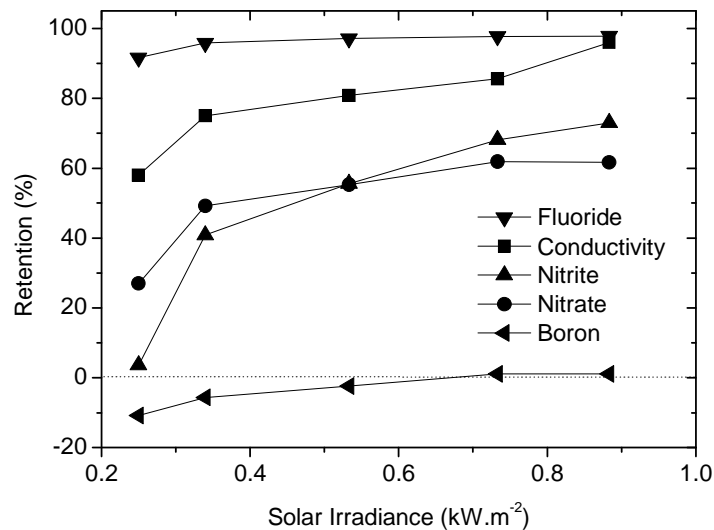
Figure 4-8. Retention at steady-state conditions (30 minutes at each power level) using membrane NF90 and feed composition NaCl (6 g.L^{-1}), NaNO$_3$ (50 mg.L^{-1} as NO$_3$), NaNO$_2$ (10 mg.L^{-1} as NO$_2$), NaF (10 mg.L^{-1} as F), B(OH)$_3$ (10 mg.L^{-1} as B) and NaHCO$_3$ (84 mg.L^{-1}). Uncertainty is approximately ± 3.1% for boron, ± 3.5% for nitrate and nitrite, ± 1.5% for fluoride and ± 1% for conductivity.

Table 4-4. Average operating parameters at steady-state conditions (30 minutes at each power level) using membrane NF90 and feed composition NaCl (6 g.L^{-1}), NaNO$_3$ (50 mg.L^{-1} as NO$_3$), NaNO$_2$ (10 mg.L^{-1} as NO$_2$), NaF (10 mg.L^{-1} as F), B(OH)$_3$ (10 mg.L^{-1} as B) and NaHCO$_3$ (84 mg.L^{-1}).

Solar Irradiance (kW.m^{-2})	Motor Power (W)	Flux (L.h^{-1}.m^{-2})	Flow (L.h^{-1})	TMP (bar)	Temperature (°C)
0.25	75	7.0	54	4.4	23.1
0.34	100	12.8	97	8.1	22.8
0.53	160	25.6	195	10.3	22.8
0.73	220	36.2	275	12.0	22.9
0.88	265	41.5	316	12.0	23.0

Steady-state retention of each of the contaminants increased with power level (and consequently flow and pressure), as shown on Figure 4-8. This is due to the decreased relative importance of diffusion as compared to convection at higher flows and pressures (Table 4-4), and supports the results seen with real groundwater and energy conditions. In these experiments, the power level was increased stepwise, while equilibrating for at least 30 minutes at each level, with a number of samples collected throughout the 30 minute period. Although a hysterisis effect was not checked (*eg.* going down in steps rather than up), this could be tested in future experiments. The

very low retention of boron (and negative values at the lowest pressure) is very interesting, and the mechanistic behaviour of boron remains poorly understood. Negative rejection of boron was observed previously for the membrane ESPA 1 by Oo and Song [284]. The rejection was most negative at the lowest permeate flux (as is the case here), but these results were not explained mechanistically. Besides boron, negative rejections of ions in pressure-driven processes has been proposed to be due to several distinct mechanisms and has been observed before [116, 285]. In many cases, the phenomenon arises by an increased concentration of an ion in the membrane phase, which, in the case of charged membranes, is accompanied by a weakened electric field [285]. This can occur in electrolyte mixtures (as is the case here) due to the presence of different counter ions of different mobilities. Negative rejections can also occur for ions whose concentration is decreased in the membrane phase, which also occurs in electrolyte mixtures due to acceperation of some ions by the electric field of diffusion potential caused by high rejections of other components in the mixture (*eg.* fluoride or chloride here) [285]. The experiments conducted in this section were not sufficiently extensive to be able to comment on possible mechanistic explanations (or a systematic error) for the negative retention of boron under these conditions. However, more detailed analysis of boron retention in bench-scale experiments follows in Chapter 5.

This experiment also confirms interesting results with regard to ion selectivity that were seen in the experiments conducted with real groundwater of complicated chemical composition. In particular, the high retention of fluoride as compared to nitrate and nitrite is of interest. The mechanistic question that results from this observation is in determining why this occurs, since fluoride is a small ion compared to nitrate and nitrite. Hence, size exclusion based on ionic size does not explain these results, nor does charge repulsion since the ionic charges are equivalent. This question will be the focus of the remaining work presented in this thesis.

4.8 Conclusions

In summary, this chapter focussed on the performance of a RE-membrane system with different weather and pH conditions, operating with real water in outback Australia (with the exception of Section 4.7). The work completed here essentially shaped the

rest of the PhD as it brought to light a number of interesting questions with regard to ion selectivity and transport mechanisms in NF/RO.

The main results reported in this chapter showed that a RE-membrane system reliably removed salts and inorganic contaminants (given sufficient solar availability) over a range of real energy and pH conditions via convection/diffusion and precipitation mechanisms. During a typical daily range of solar conditions, a number of solutes were well-retained ($\geq$ 85%) despite energy variation (solar irradiance between 0.2 and 1.0 kW.m^{-2}) and subsequent changes in flow, pressure, flux, and SEC. Consequently, retention for solutes such as fluoride, magnesium, nitrate, potassium, sodium and TDS were impacted where convection/diffusion dominated retention. For very large hydrated solutes (calcium, strontium, and uranium), retention was very high due to size exclusion and no impact of operating conditions was observed. Similar results were obtained when different groundwaters were compared, despite differences in groundwater composition and solar availability. However, during periods of severe energy fluctuations (range from 0.02 to 0.8 kW.m^{-2} lasting nearly two hours at Ti Tree), the system shut off and retention dropped significantly to unacceptable levels. This decreased performance during extreme fluctuations has practical implications, especially in locations where such extreme changes occur frequently.

The retention of a number of solutes (Pine Hill Group 1: arsenic, calcium, chloride, nitrate, potassium, selenium, sodium, strontium, and sulphate) was pH independent between pH 3 and 11. Because retention was stable despite changes in the membrane surface charge (and thus changing electric interactions), steric effects were expected to govern retention. Retention with BW30 at Pine Hill ranged from $\geq$ 78.9% (arsenic) to 99.6% (strontium and calcium) which was attributed to differences in solute properties (*eg.* hydrated size). Retention of other solutes (Pine Hill Group 2: copper, magnesium, manganese, molybdenum, nickel, uranium, vanadium, and zinc) varied as a function of pH due to speciation. The pH-dependence of certain solutes is dependent on the groundwater type, exemplified by nitrate and magnesium demonstrating different behaviour with the different groundwaters at Ti Tree and Pine Hill. Deposition on the membrane surface occurred when concentrations at the membrane surface exceeded solubility limits, and resulted in flux decline. This is a practical problem for long-term operation.

Although the system worked well in a number of cases, the results also highlighted the current lack of understanding of dominant mechanisms of ion transport in NF/RO processes. An improved understanding of the fundamental mechanisms with which ions are removed would be very beneficial to the design and appropriate implementation of such a system. In particular, the results presented in this chapter raised questions on ion selectivity and transport mechanisms, which directed the rest of the PhD. These questions include:

- Why is fluoride highly retained compared to nitrate (Figure 4-3, Figure 4-4, Figure 4-5, Figure 4-8), considering the ionic size is much smaller?

- What explains ion selectivity for ions with the same charge (and hence the same charge repulsion from the membrane surface), such as fluoride, nitrate and nitrite?

- Why is boron rejection negative at the lowest power levels (Figure 4-8), and why does it remain so much lower than any other contaminant at higher power levels?

Because answering these questions requires controlled and systematic studies, further experiments with this large, field-scale RE-membrane system were not pursued (although this certainly could be the subject of future work). Instead, the remainder of this work focussed on conducting systematic experiments with simplified systems. The following chapters will address the role of pH in retention of monovalent anions and boron (Chapter 5). The selectivity of monovalent anions with NF/RO, and in particular the role of hydration in this process, will be addressed with molecular dynamics simulations (Chapter 6) and experimental measurements (Chapter 7).

Chapter 5

Impact of pH on the Removal of Inorganic Contaminants

In Chapter 4, the impact of varying solar energy and pH on a renewable energy powered NF/RO system was evaluated using real groundwaters. These results provided valuable information on the suitability of such a system, and brought up interesting questions about the trends in retention of inorganic contaminants. However, the complexity of groundwater chemistry and the inherent variability in operation of a renewable energy membrane system make it difficult to understand the NF/RO mechanisms which explain the observed behaviour. Thus, more simplified experimental systems are required in order to improve understanding of NF/RO retention mechanisms. The current chapter endeavours to explore the retention of selected ions (boron, fluoride and nitrate) in a controlled laboratory environment and bench-scale equipment. The specific objective of this current chapter was to evaluate the specific impact of pH on boron, fluoride and nitrate retention by linking solute speciation and retention mechanisms.

In this chapter, the pH-dependence of speciation was predicted for health-threatening contaminants boron, fluoride and nitrate in purified water and a background salt solution. The modelled speciation was then compared to results from bench-scale experiments using six different NF/RO membranes (BW30, ESPA4, NF90, TFC-S, UTC-60, and UTC-80A). Retention results were explained with regard to speciation, membrane properties, and ion properties such as charge, hydrated size and Gibbs free

energy of hydration. Flux was independent of pH, indicating that pH did not alter pore size and hence permeability for all membranes except UTC-60. Membrane charge (zeta potential) was strongly dependent on pH, as expected. Boron and fluoride retention depended on membrane type and pH, which correlated closely to contaminant speciation, and was due both to size and charge exclusion. While boron retention at low and neutral pH was a challenge, high boron retention was achieved (>70%) above pH 11. Fluoride retention was generally > 70% above pH 7. Nitrate retention depended on the membrane, and was mostly pH-independent, as was the speciation. The presence of a background electrolyte matrix (20 mM NaCl and 1 mM NaHCO$_3$) reduced nitrate and boron retention (at high pH) due to charge shielding, and enhanced the retention of fluoride in single feed solutions, suggesting preferential transport of chloride compared to fluoride with sodium.

The results obtained here were complimentary to those obtained in Chapter 4. Together, these results have shown the need for detailed analysis of the role of ion hydration in controlling selectivity during transport through a membrane pore, which will be the focus of the remaining work presented in Chapter 6 and 7.

This work was initiated in 2005 by a visiting Master's student (Marion Vuarchère, University of Savoie, France) and Prof. Andrea Schäfer at the University of Wollongong (Australia). Vuarchère conducted speciation modelling, the experiments using BW30, NF90 and TFC-S in single-feed experiments and ESPA-4 and UTC-80A in mixed feed, and the chemical analysis for those experiments [286]. Vuarchère's initial results informed the design of the experiments conducted in the Australian field trial which was the subject of Chapter 4. In 2010, the present PhD candidate picked up this work in order to fill in the gaps and make a clear link between solute speciation and retention mechanisms. The PhD candidate verified speciation predictions, conducted and analyzed remaining experiments (NF90, BW30, ESPA-4 in mixed feed, UTC-80A mixed feed in MilliQ water and all with UTC60) and linked results with membrane properties. The compilation and analysis of the data was completed by the PhD candidate.

5.1 Introduction and Objectives

Groundwater is often considered a viable drinking water resource but, as discussed in Chapter 1, it may contain chemical contaminants which are dangerous to human health and can be difficult to remove. The focus of the work in this chapter is on boron, fluoride, and nitrate, which have respective WHO guidelines of 0.5 mg.L^{-1} (provisional), 1.5 mg.L^{-1}, and 50 mg.L^{-1} (short term exposure), respectively [287]. NF and RO can reduce concentration of each these dangerous contaminants by varying degrees [49-51, 98, 139].

As discussed in detail in Chapter 2.3.5 and shown in Chapter 4.6, solution pH can strongly affect NF/RO because different species in which a solute is present in a solution are pH-dependent, and thus properties such as solute size, charge and hydration can change. For example, if an uncharged solute is deprotonated at its acid dissociation constant (*pK$_a$*), it becomes charged and thus charge exclusion from the membrane surface may become significant. A change in species affects hydration state and consequently hydrated radius, thus impacting retention when size exclusion is important [37, 77]. Therefore, changing solute properties essentially affect all NF/RO mechanisms.

Additionally, the actual membrane characteristics such as charge and pore size can change with pH [143, 174]. Increasing feed water pH results in an increasingly negative surface charge for most polymeric membranes [174]. Subsequently, electrostatic interaction between ionic compounds and the membrane surface vary according to solution pH [143], with minimal retention typically occurring around the isoelectric point of the membrane surface due to the minimized electrostatic effects [104, 111, 138, 141, 172]. Additionally, pH impacts the dissociation of the functional groups on the membrane surface which can impact the "openness" of the pores [143]. Thus, pH can directly impact water flux and solute retention mechanisms (namely charge and size interactions), making pH a very important parameter for ion retention in NF/RO.

The relationship between pH and retention for boron, fluoride, and nitrate has been explored to some extent [49, 51, 54, 107, 240-242], however the focus and novelty of

this chapter was the specific relationship between solute speciation and retention mechanisms for these contaminants. The objective is to systematically evaluate the impact of pH on boron, fluoride, and nitrate retention by comparing speciation with retention using six different NF/RO membranes.

5.2   Experimental Summary

5.2.1   Filtration protocol

To evaluate the impact of pH, experiments were conducted that assess the retention of different membranes when varying the pH. A magnetically-stirred stainless steel batch cell was used for filtration experiments, as described in Chapter 3.1.1. Prior to each experiment, the new membrane was rinsed with ultrapure water and then compacted for one hour with a pressure of 8 bar. Pure water flux was subsequently determined at 5 bar for 30 minutes. Retention experiments were conducted at 5 bar and pH 3, 5, 7, 9, 11 and 12.5. For each batch experiment, 5 samples were collected from the feed (25 mL), concentrate (25 mL), and permeate (3 consecutive samples of 40 mL each for a total filtrate of 120 mL). Retention calculations compensated for the increasing feed concentration and decreasing feed volume as a function of time via mass balance.

Analytical grade boric acid ($B(OH)_3$), hydrochloric acid (HCl), nitric acid (HNO_3), sodium chloride (NaCl), sodium fluoride (NaF), sodium nitrate ($NaNO_3$), sodium hydrogen carbonate ($NaHCO_3$), and sodium hydroxide (NaOH) were obtained from Sigma-Aldrich. $B(OH)_3$ (1 mg.L^{-1} as B), NaF (3 mg.L^{-1} as F), and $NaNO_3$ (100 mg.L^{-1} as NO_3^-) were the target solutes, with concentrations selected to be broadly representative of natural groundwater sources [32, 287, 288]. NaCl (20 mM) and $NaHCO_3$ (1 mM) were used as background electrolyte and buffer, respectively, to roughly represent the matrices of natural waters and allow easier adjustment of pH. HCl (1 M) and NaOH (1 M) were used to adjust pH. All solutions were prepared with purified water (MilliQ).

The flatsheet membranes used were BW30 (RO, Filmtec), ESPA4 (NF, Hydranautics), NF90 (NF, Filmtec), TFC-S (NF, Koch), UTC-60 (NF, Toray), and UTC-80A (RO, Toray). Membrane information is available online from the manufacturers (Filmtec,

Hydranautics, Koch, and Toray) and included in Chapter 3.2. Experiments with BW30, NF90 and TFC-S were conducted both in purified water and background solution in *single contaminant feed solutions* to assess the impact of the background solution on retention. Experiments with UTC-60, UTC-80A, and ESPA 4 were conducted both in purified water and background solution in *mixed contaminant feeds*. Experiments with NF90 were conducted both in single and mixed contaminant feed solutions (with background) to assess the impact of mixed feed. Mixed feed solutions are more representative of what occurs in natural waters, however because interactions can be complex, single feed solutions can give more straightforward insight into retention mechanisms.

5.2.2 Analysis

A number of analytical techniques were used and methods were described in detail in Chapter 3.4. A pH meter was used to analyze pH (Chapter 3.4.1). For single feed experiments, nitrate and fluoride were measured using ion chromatography (Chapter 3.4.8). For mixed feed experiments, nitrate was analyzed with a nutrient analyzer (Chapter 3.4.3) and fluoride with an ion selective electrode (Chapter 3.4.2). Boron analysis was conducted with inductively coupled plasma optical emission spectroscopy (Chapter 3.4.4). Analytical details and sample preparation were discussed in the referred section for each type of analysis.

Zeta potential shows membrane surface charge and was calculated from streaming potential measurements with methods described in Chapter 3.2.4 [174]. Membranes were characterized for pore size using a hydrodynamic model to fit experimental retention of neutral organic solutes (dioxane, xylose, dextrose, and methanol) following the methodology described in detail in Chapter 3.2.3 [36, 216]. Speciation was modelled using Visual MINTEQ (version 2.53), as described in Chapter 4.4 [171, 276].

The results of the experiments will be presented next. First, membrane characterization is discussed (Chapter 5.3), then flux as a function of pH (Chapter 5.4), and finally, speciation and retention of boron, nitrate and fluoride (Section 5.5).

5.3 Membrane Characterization

The properties of the membrane are required to be known in order to understand retention mechanisms. The membrane surface charge was measured using zeta potential, and results for each membrane were shown previously in Figure 3-8. Zeta potential for each membrane changed from positive to negative with increasing pH, with the exception of ESPA4 and UTC-80A which were never positively charged. ESPA4 and UTC-80A followed the same trend of an increase in zeta potential from pH 3 to approximately 4 and then the zeta potential decreased above pH 4, however those two membranes were never positively charged. The point of zero charge (isoelectric point) of the other membranes was 3.1, 3.2, 4.1, 4.2 and 4.3 for TFC-S, UTC-60, ESPA4, BW30 and NF90, respectively. Zeta potential is important for understanding the relative amount of charge repulsion that can occur from the charged membrane surface and how this changes under various conditions.

The other characterized parameters included pore radius and the active layer thickness to porosity ratio ($L.\varepsilon^{-1}$). These experimental results and membrane information applicable to the membranes used in this chapter are summarized in Table 5-1. The pore radius is particularly important because the pore size determines which ions can fit easily through the pore and which are excluded due to their size as a sieve.

Table 5-1. Membrane properties [161, 256, 257, 262].

Membrane	MWCO (Da)	Pore Radius (10^{-10}m)[a]	$L.\varepsilon^{-1}$ (10^{-6}m)[a]	Mat'l	Funct'l Group	Flux[b], PW (L.m^{-2}.h^{-1})	Flux[c], BG (L.m^{-2}.h^{-1})	IEP
TFC-S	200 [256]	3.4	5.29	PA TFC	CONH [262]	29.0	25.4	3.1
UTC-60	150 [257]	4.5	4.70	--	--	164	154	3.2
UTC-80A	--	1.9	3.00	--	--	10.9	6.9	--
BW30	98 [161]	3.2	6.01	PA TFC	COOH; amine [161]	17.2	12.1	4.2
NF90	100 [161]	3.4	1.46	PA TFC	COOH; amine [161]	54.9	36.6	4.3
ESPA4	--	3.3	7.57	PA	--	32.4	18.0	4.1

--: not available; [a] Uncertainty is estimated to be ± 5% for these fitted parameters; MWCO: molecular weight cut-off; PA: polyamide; TFC: thin film composite; [b]Flux of pure water (PW) at 5 bar ; [c]Flux of background (BG) 20 mM NaCl and 1mM NaHCO$_3$ at 5 bar; IEP: isoelectric point

5.4 Flux as a Function of pH

Flux as a function of pH is shown in Figure 5-1 for all experiments conducted. Flux in pure water is shown in Figure 5-1A and with background solution in Figure 5-1B. Permeate flux was independent of pH for all membranes except UTC-60, which suggests this membrane changes with pH. The average flux sequence (Table 5-1) for purified water experiments was UTC-60 > NF90 > ESPA4 > TFC-S > BW30 > UTC-80A. With the background solution, the flux sequence was the same with the exception of TFC-S being greater than ESPA 4. Flux in background was always lower than the corresponding pure water flux with the same membrane, which is attributed to concentration polarization and osmotic pressure effects. The lowest overall flux occurred with UTC-80A, which is an RO membrane developed for high boron retention.
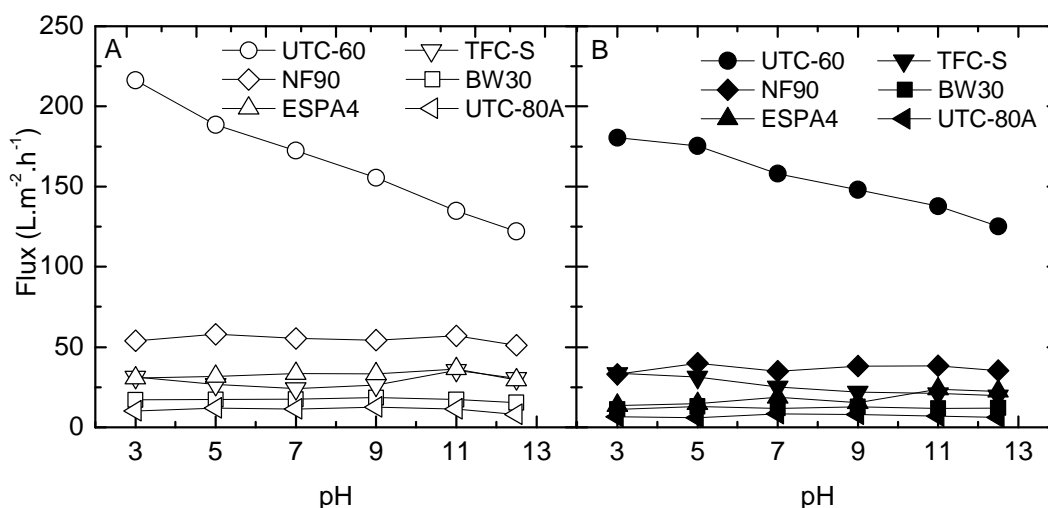
Figure 5-1. pH dependence of flux for BW30, TFC-S, NF90, ESPA4, UTC60, and UTC-80A in (A) purified water and (B) background solution (20 mM NaCl and 1 mM NaHCO₃). Error in flux measurement for one membrane coupon is estimated to be ± 1% but coupons from different membrane batches can vary ± 5 - 10%.

5.5 Speciation and Retention as a Function of pH

Solute characteristics are important to understand which mechanisms might affect the transport of a particular solute. Characteristics of boron, nitrate, and fluoride species are summarized in Table 5-2, including hydrated radii and Gibbs hydration energies where available in the literature to compare hydration strength. Hydrated radii are collected from one data source for consistency where possible [80]. Speciation results for each contaminant are shown in Figure 5-2, Speciation predictions in purified water and background solution were the same for each solute, showing the additional ionic

strength did not impact speciation as sometimes observed at high salt concentration [289]. Speciation (Figure 5-2) and retention for single and mixed feeds (Figure 5-3 and Figure 5-4, respectively) will be discussed for each contaminant individually.

Table 5-2. Characteristics of boron, nitrate, and fluoride and other relevant solutes as reported in the literature [80, 82, 290, 291].

Ion	Molecular Weight (g·mol^{-1})	Crystal Radius (10^{-10}m)	Hydrated Radius (10^{-10}m)	Gibbs Hydration Energies in Water (kJ·mol^{-1})
B(OH)$_4^-$	78.84	2.44 [290]	--	--
B(OH)$_3$	61.83	--	--	-36.9 [291]
Cl$^-$	35.45	1.81 [82]	3.32 [82]	-270 [80]
F$^-$	19.00	1.36 [82]	3.52 [82]	-345 [80]
H$^+$	1.01	--	2.82 [82]	-1015 [80]
HF	20.01	--	--	--
Na$^+$	22.99	0.95 [82]	3.58 [82]	-385 [80]
NO$_3^-$	62.00	2.64 [82]	3.35 [82]	-275 [80]
OH$^-$	17.01	1.76 [82]	3.00 [82]	-345 [80]
--: not available				

5.5.1 Boron

The speciation of boron was strongly dependent on pH (Figure 5-2A). The equilibrium constant of boric acid (B(OH)$_3$) and borate (B(OH)$_4^-$) is 9.27 [121]. This means that boron predominantly existed in aqueous solution as uncharged B(OH)$_3$ below pH 9.27 and as B(OH)$_4^-$ above pH 9.27, as

$$H_2O + B(OH)_3 \leftrightarrow H^+ + B(OH)_4^- \quad (pK_a = 9.27). \qquad \text{Equation 37}$$
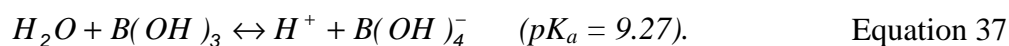
No other forms of boron were predicted to be present in solution, and there was no difference in boron speciation in the background solution.

The influence of pH on boron retention was significant in both purified water and background solution (see Figure 5-3A and B and Figure 5-4A and B). Retention was very low (< 23%) between pH 3 and 9 for all membranes except UTC-80A. With UTC-80A at low pH retention was approximately 50%, both in purified water and background solution, which is significantly higher than the other membranes. At pH 11 and 12.5, retention increased significantly for all membranes. Retention with UTC-60

was significantly lower than all other membranes, even at high pH which is likely due to the more open nature of UTC-60 as shown by its high flux and larger pore size.
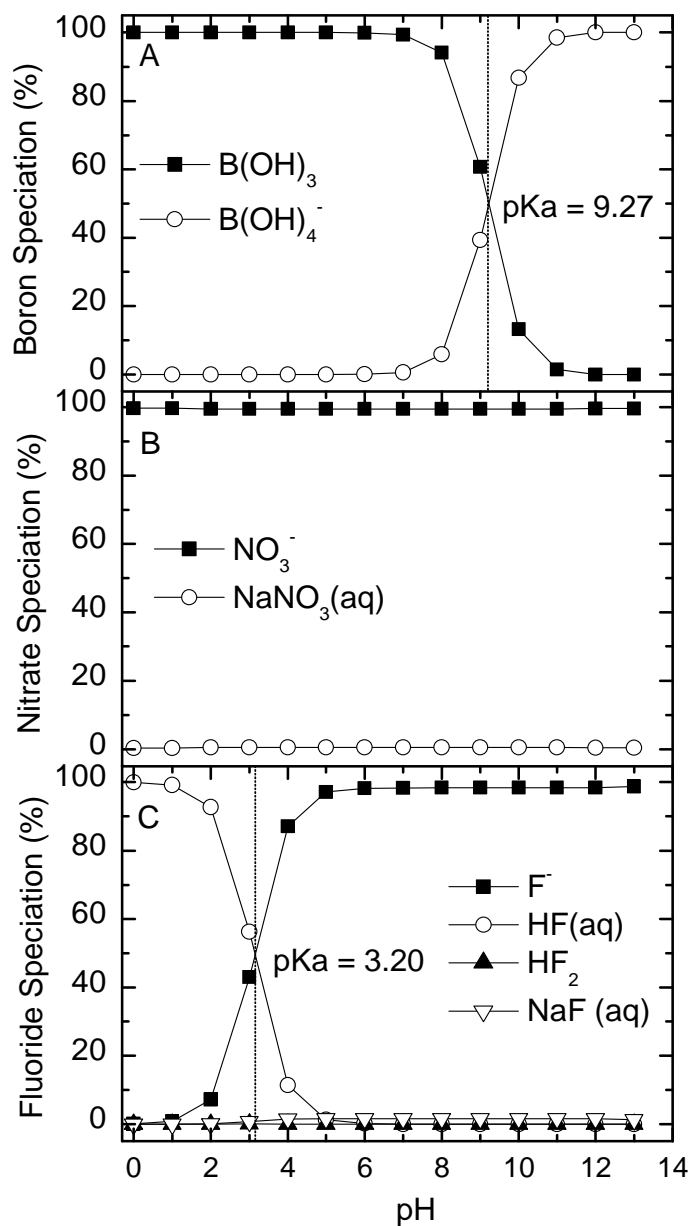
Figure 5-2. Speciation for (A) boron; (B) nitrate; and (C) fluoride. Speciation conditions assumed a fixed atmospheric carbonate concentration (partial pressure 3.8·10⁻⁴ atm) and temperature of 25°C. Speciation results were the same in MilliQ water and with a background solution of 20 mM NaCl and 1 mM NaHCO₃.
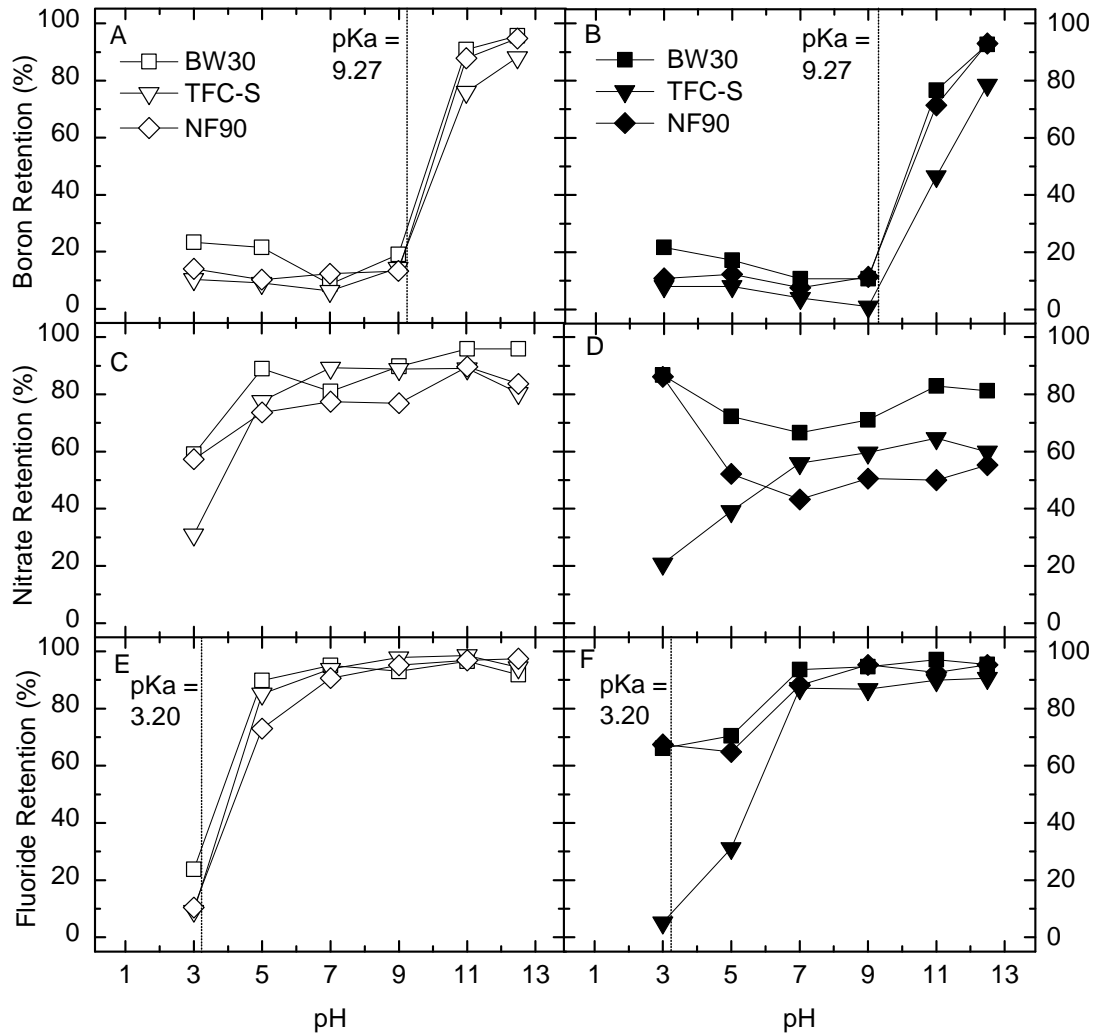
Figure 5-3. Single contaminant solutions (5 bar, feed concentrations: 1 mg.L^{-1} B(OH)$_3$ as B; 3 mg.L^{-1} NaF as F; and 100 mg.L^{-1} NaNO$_3$ as NO$_3$$^{-}$): Observed retention of (A) boron (C) nitrate and (E) fluoride in purified water, (B) boron, (D) nitrate and (F) fluoride in background solution for BW30, TFC-S, and NF90. Uncertainty is approximately ± 3.1% for boron, ± 3.5% for nitrate and ± 1.5% for fluoride.

Similar pH effects on boron retention have been previously reported [49, 50, 289, 292-294], however, data on all membranes used in this study have not been reported and the effects of salinity are often neglected. The improved performance of UTC-80A compared to other membranes at lower pH is significant because the removal of boron at low to mid pH ranges is very challenging for most membranes. Although the performance was even better at pH 10-12.5, the practical issues associated with treating waters of high pH are additional chemical cost and risk of scaling and corrosion [292, 295, 296].

Figure 5-4. Mixed contaminant solutions (5 bar, feed concentrations: 1 mg.L^{-1} B(OH)$_3$ as B; 3 mg.L^{-1} NaF as F; and 100 mg.L^{-1} NaNO$_3$ as NO$_3^-$): Observed retention of (A) boron (C) nitrate and (E) fluoride in purified water, (B) boron, (D) nitrate and (F) fluoride in background solution for UTC-80A, ESPA4, UTC-60, and NF90 (background only). Uncertainty is approximately ± 3.5% for boron, ± 3.5% for nitrate and ± 1.5% for fluoride.

The retention pattern correlated closely with the speciation of boron. At acidic and neutral pH, where retention is lowest, boron was present as boric acid B(OH)$_3$. This neutral species was easily transported through the membrane due both to lack of steric hindrance and lack of charge repulsion. Thus, the higher retention achieved with UTC-80A was likely due to the tight nature of that membrane which is also supported by UTC-80A's low flux.

Above pH 9, retention sharply increased for all membranes (≥ 75% in all cases except for UTC-60 which only reaches 52% in purified water and 30% in background

solution). This increase in retention closely corresponded with the speciation change from $B(OH)_3$ to $B(OH)_4^-$ (see Figure 5-2A), which is anionic as opposed to $B(OH)_3$ [294]. In consequence, the negatively-charged borate ions experienced electrostatic repulsion by the negatively-charged membranes (Donnan exclusion) at pH 11 and 12.5 [292]. Although specific hydration information of both boron species is not currently available, $B(OH)_4^-$ is larger than $B(OH)_3$ [294] so at pH 11 and 12.5 increased retention can further be explained due to size exclusion. However, the hydration energy of $B(OH)_3$ is much lower than the other anions, which is particularly interesting in light of its very low retention. This is an area which warrants further exploration, but more thorough hydration data is required to do so.

Additionally, differences in retention between $B(OH)_3$ to $B(OH)_4^-$ have been attributed to three-dimensional differences in the molecular structure between the two compounds, which resulted in differences in interactions with membrane active groups [292]. $B(OH)_4^-$ has a tetrahedral structure with a sp3 hybrid orbital, in contrast with the trigonal planar structure of $B(OH)_3$ [297], as shown schematically on Figure 5-5. The planar structure enhances hydrogen bridges between $B(OH)_3$ and the membrane functional groups, enabling $B(OH)_3$ to permeate in a similar manner as carbonic acid or water via convection/diffusion [292]. Functional groups are COOH and amine for BW30 and NF90, and COHN for TFC-S (see Table 5-1) but details and functional groups of the other membranes are unknown and proprietary. The hydration structure of borate or boric acid was not available in the literature but this would be helpful information.

Figure 5-5. Chemical structure of boric acid ($B(OH)_3$, trigonal planar on the plane of the page) and borate ($B(OH)_4^-$, tetrahedral, 3D).

Boron retention in purified water was higher than in the background solution at pH 11 and 12.5 (up to 22% different for UTC-60, with most notable differences in the mixed feed solutions). This is because at pH 11 and 12.5, $B(OH)_4^-$ retention was affected by charge repulsion, and in background solution, the increase in sodium ions (from < 1 mM to 20 mM) shielded charge repulsion. The shielding phenomenon is characteristic of charged membranes and has been commonly used to explain decreased anion retention in the presence of increased ionic strength [107, 108, 199, 241]. In single feed solutions, from pH 3 – 9, there was no difference in neutral $B(OH)_3$ retention with and without the background solution, which is consistent with the observation that charge becomes important at pH 11 and 12.5. A comparison of single feed and mixed feed with NF90 in background solution (Figure 5-3B and Figure 5-4B) showed slightly lower retention of $B(OH)_3$ in the mixed feed solution of higher ionic strength (10% in mixed feed; 20% in single feed).

5.5.2 Nitrate

The speciation of nitrate does not depend on pH, with >99.5% present in ionic form (NO_3^-) (see Figure 5-2B). No difference in speciation of nitrate occurs in background solution.

Nitrate retention (Figure 5-3C and D; Figure 5-4 C and D) varied widely from 20 – 96%. Retention was 60-96% and mostly pH independent for RO membranes BW30 and UTC-80A, showing that size exclusion is important when pore size is smaller than or similar to solute size. For other membranes, retention was mostly pH independent above the isoelectric point of the membranes (it shows the same shape for all membranes). Because nitrate was of uniform charge and the charge of all membranes increased with pH, a continuous increase in retention with pH would be expected if charge exclusion was dominant. Minimum retention was observed at low pH near the membrane isoelectric point when charge repulsion is minimal for TFC-S and ESPA4. This was similarly observed by Qin *et al*. [113]. However, retention was mostly pH-independent above pH 5, which suggested that size exclusion was playing a role in addition to charge. The lowest retention was observed with UTC-60, which is the "loosest" membrane. Size exclusion is further supported because NF90 retention for single and mixed feed solutions is similar.

Nitrate retention was generally lower in the presence of the background electrolyte than in purified water (the most notable difference with TFC-S), which has been similarly observed and explained in literature [113, 139]. Because nitrate and chloride have very similar characteristics (charge, hydrated size and hydration strength, see Table 5-2), preferential transport of one of the anions with regard to the other with sodium would not be expected. However, the increase in sodium concentration resulted in enhanced charge shielding and hence reduced retention based on charge repulsion [107, 108, 199, 241]. It is to date unknown if ions such as nitrate permeate membranes in hydrated or unhydrated form, which is subject to ongoing investigations (and will be the subject of Chapter 6 and 7).

5.5.3 Fluoride

The speciation of fluoride was pH dependent and is shown in Figure 5-2C. The equilibrium coefficient of hydrofluoride acid (HF) is $pK_a = 3.2$ [121]. The chemical equation of the acid dissociation is

$$HF \leftrightarrow H^+ + F^- \ (pK_a = 3.20).$$
<div align="right">Equation 38</div>
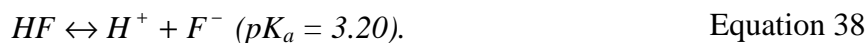
Therefore, above pH 3.2, the charged fluoride ion was dominant and above pH 5 all fluoride existed as F^-. Speciation was identical in background solution.

Fluoride retention (shown in Figure 5-3C and D for single feed solution and Figure 5-4C and D for mixed feed) was impacted significantly by pH and correlated with speciation. Retention for all membranes, in both purified water and background with single feed, was relatively low at pH 3 (from 5 – 65% depending on membrane and conditions) and increased to 95 – 98% at pH 12.5 with pH. Above pH 7, retention in single feed solutions was > 87% and hence higher than that of either boron or nitrate. In mixed feed solutions, an increase in retention with pH was still observed. High fluoride retention has indeed been observed over a range of conditions in a number of studies [51, 54, 240-242].

This suggested that steric effects contribute to fluoride retention. Although fluoride is a very small ion, it is more strongly hydrated because of its high charge density and has a relatively large hydrated radius ($3.52 \cdot 10^{-10}$ m, see Table 5-2) compared to other monovalent anions in solution ($3.32 \cdot 10^{-10}$ m for Cl^- and $3.35 \cdot 10^{-10}$ m for NO_3^-) [51, 82, 242]. Consequently, steric exclusion led to fluoride being more strongly retained by tighter membranes. Retention with UTC-60 was very low with a maximum of 53% in MQ at pH 12.5. Because flux decreased with pH, the change in retention could be attributable to either or both changing charge interactions or the pore size. Retention with NF90 in single and mixed feed solutions was similar, indicating that size exclusion is important for this membrane.

Near the isoelectric point (pH 3-5), fluoride retention was higher in the presence of background solution (near 70% for BW30 and NF90) than in purified water ($< 25\%$) in the single feed solutions (Figure 5-3C and D). At acidic pH, fluoride was not retained by UTC-60 and retention by TFC-S was only 5% and 30% for pH 3 and 5, respectively, and approximately 65% for BW30 and NF90. This can be explained with the fact that chloride rather than fluoride was preferentially transported through the membrane with sodium, which is supported both because the hydrated radius of chloride is smaller than fluoride and because chloride is more weakly hydrated (see Gibbs Hydration Energies on Table 5-2). Interestingly, in the background solution, retention was low at both pH 3 and 5, whereas with purified water, low retention only occurred at pH 3 (this difference is most likely an error). This requires further investigation.

5.6 Conclusions

The objective of this study was to determine the relationship between speciation and retention for boron, fluoride, and nitrate using six different NF/RO membranes. The main conclusions follow.

Flux was independent of pH for all membranes except UTC-60, indicating that pH did not alter pore size and hence permeability and size exclusion characteristics of those membranes. The retention of boron correlated with speciation and was strongly dependent on pH. Below the pK_a of boron ($pK_a = 9.27$), only $B(OH)_3$ was present in

solution, and retention was generally low and due to the small size of the species. At pH $\geq$ 11, retention for all membranes increased sharply (up to 95%) due to charge repulsion of $B(OH)_4^-$ from the negative membrane surfaces. The presence of background solution decreased $B(OH)_4^-$ retention due to charge shielding. The highest boron retention at neutral pH (approximately 50%) was achieved using UTC-80A. The speciation of nitrate was pH independent. Retention varied widely depending on membrane type, and was mostly pH independent above the isoelectric point of the membranes. Data supported that both charge and size mechanisms were occurring. Decreased nitrate retention was observed in the presence of background solution due to the screening effects of sodium. Fluoride speciation and retention were pH dependent, with minimum retention occurring at low pH when HF dominates (this is similar to what happened with boric acid). Fluoride (ion) was better retained than uncharged HF, due to both charge and size mechanisms. Speciation effects were clearer in single feed solutions than mixed feed solutions. In single feed solutions, at low pH, fluoride was better retained with the background solution than in purified water, which can be explained by charge and possibly preferential transport of chloride rather than fluoride to balance the charge of sodium. In single feed solutions, the fluoride ion was more highly retained than nitrate for the same membrane above pH 7, which cannot be explained by the ionic size (fluoride is a smaller ion). This is the same result found in natural groundwaters (Chapter 4) and is of significant interest. More extensive hydration data is needed for species relevant to this study, and this data is not currently available or inconsistent in the literature. In particular, hydrated radius and Gibbs hydration energies for both boron species $B(OH)_3$ and $B(OH)_4^-$, as well as HF, would be valuable to further elucidate mechanisms. Additionally, pH dependent hydration data is needed for all species.

The selectivity of monovalent anions in single feed solutions is the most significant and interesting finding from this work (*eg.* the higher retention of fluoride than nitrate, despite the smaller ionic size of fluoride), and the subject that will be pursued for the remained of this thesis. As such, nitrite will be added as a target contaminant for the remaining work presented, as this is another monovalent anion which is health-threatening, and understanding the selectivity of this ion compared to the others would be valuable. In particular, the role of hydration in determining which ions transport

through pores remains poorly understood, and progress in this area would make a significant contribution to the current knowledge of NF/RO mechanisms. This will be explored using molecular dynamics simulations (Chapter 6) and then further pursued experimentally (Chapter 7).

Chapter 6

The Importance of Dehydration in Determining Ion Transport in Narrow Pores

The previous experimental chapters have demonstrated that mechanisms of salt transport through NF and RO membranes remain unclear. For example, the high retention of fluoride as compared to nitrate, which was demonstrated in Chapters 4 and 5, cannot be explained by size exclusion based on bare ion size. This observation emphasizes that the impact of ion hydration must be important. However, there is no solid evidence about the specific role of ion hydration in determining ion transport in nanofiltration (eg. if ions become dehydrated as they enter a narrow pore), and information on this topic would be very valuable to improving the understanding of mechanisms of transport processes. The transport of hydrated ions through narrow pores is important for a number of applications in addition to desalination, such as the conductance of ions through biological channels. This subject is the focus of the current chapter.

This chapter endeavors to tackle this challenging topic by use of molecular dynamics (MD) simulations which were used to systematically examine the transport of anionic drinking water contaminants (fluoride, chloride, nitrate and nitrite) through model pores ranging in effective radius from $2.5 \cdot 10^{-10}$ to $6.5 \cdot 10^{-10}$ m. The aim was to elucidate the role of hydration in excluding these species during NF. First, an idealized, cylindrical

pore model was created. Bulk hydration properties (hydrated size and coordination number) were determined for comparison with the situations inside the pores. Free energy profiles for ion transport through the pores showed that energy barriers depend on pore size, ion type, and membrane surface charge, and that the selectivity sequence can change depending on the pore size. Ion coordination numbers along the trajectory showed that the process of partial dehydration of the transported ion was the main contribution to the energy barriers. Ion transport was greatly hindered when the effective pore radius was smaller than the hydrated radius, as the ion had to lose some associated water molecules to enter the pore. Small energy barriers were still observed when pore sizes were larger than the hydrated radius due to re-orientation of the hydration shell or the loss of more distant water molecules. These results demonstrate the importance of ion dehydration in transport through narrow pores which increases the current level of mechanistic understanding of membrane-based desalination and transport in biological channels.

This work was conducted at The University of Western Australia by the PhD candidate in collaboration with A/Prof. Ben Corry. Corry has previously worked on the simulation of ions through carbon nanotubes and biological channels and thus shared his knowledge and contributed some code for the development of the model and data analysis. Parameterization, simulations and analysis were conducted by the PhD candidate.

6.1 Introduction and Objectives

Water and ion transport through confined pores is relevant to important applications such as desalination and the understanding of biological ion channels. As described in Chapter 2.2, typical NF models include mechanistic contributions from size exclusion, charge repulsion, diffusion and convection [143, 144, 198, 208-210]. However, a major limitation in current NF models is the definition of solute size. Most models use ionic [210] or Stokes radius [36], which is inherently inaccurate due to the process of hydration. Ions are hydrated by a shell of dipolar water molecules, which means that the mobile entity is the ion with its hydrated shell rather than just the bare ion [76]. Despite the fact that hydration is neglected in NF models, the importance of hydration has been demonstrated numerous times experimentally [77, 85, 122-125] and in carbon nanotube

simulations [126, 127]. Ion hydration is also of critical importance to biological ion channels, where the molecular basis of selectivity is due in part to the ion's hydration properties [230-234, 238, 239].

As discussed in detail in Chapter 2.2, hydration during pore transport processes is not well-understood (and to date completely un-addressed in NF models), for a number of reasons. These reasons include the lack or inconsistent nature of hydration data [80-82, 85], the inaccuracy of applying hydration information in bulk solution to a confined space, and challenges in accounting for an unknown or transient parameter in models [77, 125, 126]. Thus, a more detailed approach is required that incorporates the interaction of water molecules with the ion as well as the interaction between the hydrated ion and the pore.

The overall aim of the work in this chapter was to examine the hydration of a selection of monovalent anions relevant to drinking water purification (fluoride, chloride, nitrate, nitrite) as they transport through nanopores to determine its importance in this process. The specific objectives were to: (1) develop a model using MD to simulation the transport of ions through an idealized pore; (2) determine the hydration structure of the anions in bulk water; (3) investigate the hydration of these ions during transport through a generic pore, as a function of (i) pore size; (ii) ion type; and (iii) surface charge; and (4) determine the energetic barriers of transport by evaluating free energy profiles in each of these scenarios.

The novelty in this study lies in systematically evaluating the dehydration mechanism during pore transport for small ions with molecular dynamics (MD). Rather than attempting the challenge of describing the complexity of realistic membrane pores, simplified channels are used so as to be able to more easily isolate the role of in dehydration in pores of different sizes. By carefully parameterizing the simulations to reproduce ion dehydration energies, many ion types and pore sizes can be examined, which would be difficult with more detailed simulations. This study provides the evidence that dehydration is the determining factor in the transport of ions through pores, and that such effects occur in conditions applicable to desalination and biological pores.

6.2   Molecular Dynamics Model Development

The principles of MD, described in Chapter 2.5, were used to develop a new model to simulate the transport of ions through a pore. The model was developed in light of the primary objective to understand the fundamental role of ion hydration/dehydration during transport through a narrow pore, which is a topic not addressed by current NF models. Specifically, the objective was to assess the transport of anions chloride, fluoride, nitrate and nitrite through narrow pores of sizes relevant to NF/RO. The following sections describe the details of the MD model.

All MD simulations were conducted using the software package NAMD2.7 [226] and VMD1.9 for visualization [298]. NAMD software was selected as it is an appropriate parallel molecular dynamics code commonly used for high-performance simulation of large molecular systems.

There were two main categories of simulations conducted. The first simulation type was in bulk water with no pore and was meant to determine the properties of the ions when in water. The second type of simulation contained a pore and was used to model the transport of ions through the pore. Both types of simulations will be described.

6.2.1   Bulk Water Simulations

The first system was used to determine the unconstrained hydrated size and structure of a target ion in bulk water. A single ion was placed within a simple box of water (type TIP3P [221, 299]) to do this. The system for bulk simulations was minimized for 1-ps and run for 500-ps with a single ion in a water box of $60 \times 60 \times 60 \cdot 10^{-10}$ m at 298 K and 1 atm (controlled with Langevin dynamics). The radial distribution function (RDF) was calculated in order to determine the structure of the hydration shell(s) around the ion. The hydrated radius (R_{hyd}) was defined at the first minima in the RDF. The coordination number is the number of water molecules associated with the ion and this was defined by the average number of water molecules within the hydrated radius.

6.2.2 Pore Simulations

The second type of simulations was similar to the first type with the addition of a pore. Developing the pore representation in the simulations required much effort. A number of different techniques were tried in order to balance surface characteristics with computational efficiency. Ultimately, closely spaced, discrete carbon atoms were selected for the surface representation, as the computation requirements of using analytical functions, grid forces or numerical tables were too high. Although similar simulation systems had been constructed based on carbon nanotubes [127], this current pore representation was selected to be similar to that of an idealized cylindrical nanofiltration pore.

This simulation essentially contained two water reservoirs separated by a pore. This simulation was designed to understand how ions transport through narrow pores. Figure 6-1 shows a side-view representation of this model system. The pore was represented as a smooth, idealized surface to be generic and avoid giving specific chemical characteristics. While the surface representation could have been achieved using analytical functions or numerical tables, closely spaced discrete atoms were selected for computational efficiency. These surface atoms were spaced at an interval of $1 \cdot 10^{-10}$ m as smaller spacing did not influence the LJ interaction as a function of distance from the pore wall. The interaction of water and ions with the wall was through LJ interactions defined by $R_{min/2,surface} = 3.75 \cdot 10^{-10}$ m and $\varepsilon_{surface} = 0.1946$ kcal.mol^{-1} (based upon values for methyl groups in hydrocarbon chains which is of relevance to biological and membrane pores) [300, 301]. The density of atoms on the surface was used to scale $\varepsilon_{surface}$ to reproduce methyl LJ interactions when the atoms are at the density of real methyl groups. A pore of total length $16 \cdot 10^{-10}$ m (selected to ensure that length was more than twice the widest radius and for computational efficiency) was constructed. One simulation with a longer $32 \cdot 10^{-10}$ m pore was also conducted ($R_{eff} = 3.3 \cdot 10^{-10}$ m) and the free energy profile flattened out in the pore. In this case with a relatively small pore radius, the maximum energy barriers flattened at a slightly higher value (~3 kcal.mol^{-1} higher) for the $32 \cdot 10^{-10}$ m pore as compared to the $16 \cdot 10^{-10}$ m pore due to the electric field of the ion dropping away relatively slowly and thus still exerting an influence on the bulk water. This does not affect the ordering of ions and the difference decreases as pore

radius increases. After pore construction, the pore was solvated in a water box of dimensions $40 \times 40 \times 70 \cdot 10^{-10}$ m with periodic boundary conditions for continuity.

The MD pore simulation is very simplified when compared to a real NF membrane. A summary of how the MD pore compares to a real NF membrane is shown on Table 6-1. Because the interest with MD was to assess the specific impact of transport on ion hydration, a simplified model was used which allowed this effect to be determined.
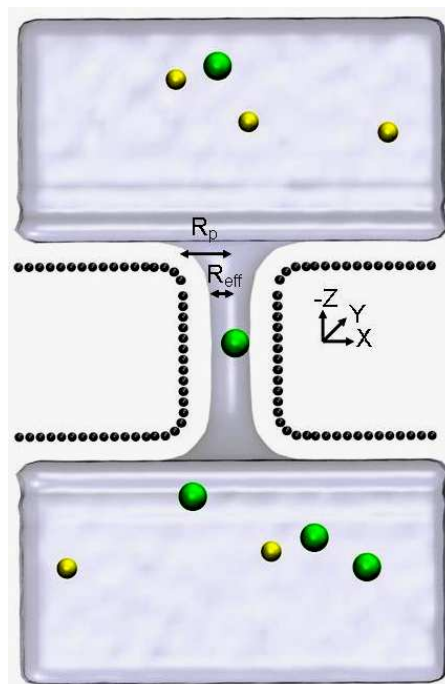

Figure 6-1. Side-view representation of model system with 0.1M NaF and R_{eff} = 3.3 $\cdot 10^{-10}$ m. Light grey region is a volume representation of water; green circles represent fluoride ($R_{ion,fluoride}$ = 1.3 $\cdot 10^{-10}$ m [80]); yellow circles represent sodium ($R_{ion,sodium}$ = 1.0$\cdot 10^{-10}$ m [80]).

Table 6-1. Comparison of MD pore model with a real NF membrane.

Characteristic	MD Model	NF membrane
Pore definition	Idealized cylindrical pore. The effective size of the pore is determined by the space in the pore actually available to water (*eg.* where the LJ interactions between the surface atoms and water molecules allow).	Tortuous void space in the spectrum between discrete pore and dense material, with a distribution of pore sizes. Space available to water is determined by "wetting" which is dependent on the interactions between the polymer material and water.
Material	Pore represented by fixed atoms with the chemical characteristics of carbon atoms in CH_3 groups, hydrophilicity/hydrophobicity not considered	Polyamide $((CONH_2]^n)$ based active layer, typically hydrophilic
Surface Charge	Not considered for the majority of simulations, however limited simulations were conducted with a surface charge of -0.1 $C.m^{-2}$ evenly distributed on the top surface and within pore	Typically negatively charged. A common charge range is approximately -0.05 to +0.01 $C.m^{-2}$ (for reference a zeta potential of -30 mV is approximately -0.01 $C.m^{-2}$ [302])
Functional Groups	Not considered	Commonly present as part of the proprietary manufacturing process of the active layers
Polarity	Not considered	Occurs due to membrane materials, functional groups
Tortuousity	Not considered, however the narrowest part of the NF "pore"is where transport will be controlled	Very tortuous

The effective radius of the pore available to water (R_{eff}) was used to define the pore radius rather than the size defined by the location of the center of the surface atoms (R_p) because R_{eff} was more easily compared to the hydrated radius of each ion. This is easily seen in Figure 6-1. Effective radius was determined by calculating the oxygen density profile within the pore, and adding the distance at which it became zero to the ionic radius of oxygen ($R_{ion,oxygen} = 1.77 \cdot 10^{-10}$ m) in water. This effective radius was always less than the position of the center of the surface atoms due to the LJ interactions between the surface atoms and water (similar to "wetting" in NF). For reference, the effective radii and corresponding radii of the centered surface atoms are shown on Table 6-2. Simulations were initially conducted at $R_{eff} = 2.8$, 3.3, 3.7, 4.3, 5.3 and $6.5 \cdot 10^{-10}$ m [303] and the additional sizes were added on later for comprehensive analysis. Pore radii were selected

to be similar to NF membranes [304] as well as those used in previous simulations of narrow carbon nanotubes [126, 127]. An additional simulation was conducted with surface atoms centered at $R_p = 3.0 \cdot 10^{-10}$ m but a corresponding effective radius could not be calculated because water evacuated from the pore.

Table 6-2. Pore radii (R_p) and corresponding effective radii (R_{eff}) used for pore simulations.

R_p ($\cdot 10^{-10}$ m)	R_{eff} ($\cdot 10^{-10}$ m)
3.75	2.51
4.00	2.81
4.25	3.06
4.50	3.32
4.75	3.52
5.00	3.72
5.25	4.02
5.50	4.33
6.00	4.72
6.50	5.32
7.50	6.53

The pore was neutral for all simulations with the exception of surface charge simulations (at $R_{eff} = 3.3$ and $4.3 \cdot 10^{-10}$ m) where a charge of -0.1 C.m^{-2} was evenly distributed along (i) all atoms on the top surface only, and (ii) all atoms on the top surface and within the pore. The surface charge was implemented by applying a slightly negative partial charge (-0.006240 electronic charge units) evenly to every single atom on the desired surface in order to achieve a net charge of -0.1 C.m^{-2} and a smooth distribution of charge. Ions were randomly placed to yield a net concentration of 0.1 M sodium fluoride, sodium chloride, sodium nitrate, and sodium nitrite (single salt per simulation), with electroneutrality maintained. This meant that there were five cations, five anions and approximately 2400 water molecules per simulation (for a $3.3 \cdot 10^{-10}$ m pore). In the negatively charged pore, one anion was used (the target anion) and ten cations in order to maintain the overall electroneutrality requirement for the system. The pore representation did not account for pore size distributions, tortuousity, and surface characteristics such as functional groups, which can be relevant to transport processes in NF, carbon nanotubes, and biological pores.

6.2.3 Free Energy Profiles

The energetic barriers of the ion transporting through the pore was quantified using free energy profiles, where the free energy of the ion was calculated at a series of locations moving from bulk solution into the pore. At each location, the free energy (or potential of mean force) was determined using umbrella sampling [305]. This technique uses a harmonic potential to set the location of the ion of interest along a trajectory path defined by the distance from the central pore axis r_{radial} and the vertical position Z. The ion was moved from $Z = -15 \cdot 10^{-10}$ m (bulk) to $0 \cdot 10^{-10}$ m (center of pore) along the pore axis (r_{radial} = 0) for all pore sizes in steps of $1 \cdot 10^{-10}$ m. Additional positions were sampled from $Z = -15$ to $7 \cdot 10^{-10}$ m (at $r_{radial} = 4 \cdot 10^{-10}$ m) for $R_{eff} = 2.8$ and $3.3 \cdot 10^{-10}$ m; $Z = -15$ to $0 \cdot 10^{-10}$ m (at $r_{radial} = 4 \cdot 10^{-10}$ m) for $R_{eff} = 3.7$ and $4.3 \cdot 10^{-10}$ m; and $Z = -15$ to $0 \cdot 10^{-10}$ m (at $r_{radial} = 4 \cdot 10^{-10}$ m and $8 \cdot 10^{-10}$ m) for $R_{eff} = 5.3$ and $6.5 \cdot 10^{-10}$ m. For the neutral membranes, the symmetry of the system is used to generate a potential of mean force across the entire length of the pore ($-15 < Z < 15$). The applied force constants were 2 kcal.mol^{-1}.Å^{-2} and 0.2 kcal.mol^{-1}.Å^{-2} in the Z and r_{radial} directions, respectively, and were selected for complete sampling in the system. For each target position, a 250-ps simulation was run, and the coordinate of the ion was recorded every 1-ps.

Table 6-3 shows the configuration parameters used for the simulations. Force field parameters were specified in a protein database file (.pdb) but additional information is needed in order to calculate the interactions between atoms which are far apart. A cutoff distance of $12 \cdot 10^{-10}$ m was specified, meaning that when the distances between two ions are larger than the cutoff distance, the forces and energies are set to zero. In order to eliminate the discontinuity that this creates, switching functions were used to smoothly bring the forces and energies to zero at a switching distance of $10 \cdot 10^{-10}$ m [226]. The pair list distance is used to specify a patch size so that NAMD can create a list of pairs of atoms for which non-bonded interactions should be calculated periodically. The patch size ($13.5 \cdot 10^{-10}$ m) must be defined for the list to be created because of atoms moving into or out of this patch between steps. The scaled 1-4 exclusion policy relates to atoms separated by three bonds (not relevant in this model) and is always used with the CHARMM force field [226]. Constant temperature control is done using Langevin dynamics which balances friction with random noise to drive each atom in the system towards a target temperature. Because periodic boundary conditions were used, full-

system periodic electrostatics and constant pressure (Langevin piston) were used. Harmonic constraints were not used on any atoms in the system and output parameters were recorded every picosecond. The statistical ensemble employed was the NPT ensemble, where pressure and temperature are kept constant. This is implemented in NAMD using Langevin dynamics (details of which are shown in Table 6-3).

Table 6-3. Configuration parameters for pore simulations using NAMD2.7.

Parameter Category	Parameter	Selection
Force-Field Parameters	Exclude	Scaled 1 – 4
	1-4 Scaling	1.0
	Cutoff	$12 \cdot 10^{-10}$ m
	Switching	On
	Switch Distance	$10 \cdot 10^{-10}$ m
	Pair List Distance	$13.5 \cdot 10^{-10}$ m
	Margin	1.0
Constant Temperature Control	Langevin Dynamics	On
	Γ, damping coefficient	5 ps^{-1}
	Temperature	298 K
Periodic Boundary Conditions	--	On
	X-Vector	$40 \cdot 10^{-10}$ m
	Y-Vector	$40 \cdot 10^{-10}$ m
	Z-Vector	$70 \cdot 10^{-10}$ m
PME (full-system periodic electrostatics)	PME	On
	Grid Size X	$75 \cdot 10^{-10}$ m
	Grid Size Y	$75 \cdot 10^{-10}$ m
	Grid Size Z	$95 \cdot 10^{-10}$ m
Constant Pressure Control	Flexible Cell	On
	Constant Area	On
	Langevin Piston	On
	Piston Target	1.01325 bar
	Piston Period	200
	Piston Decay	50
Harmonic Restraints	Harmonic Restraints	Off
Outputs	Restart Frequency	1 ps
	DCD Frequency	1 ps
	XST Frequency	1 ps
	Output Energies	1 ps
	Output Pressure	1 ps

The weighted histogram analysis method (WHAM) [306, 307] was used to calculate two-dimensional free energy profiles with a tolerance of 0.0001 and 30 bins in both *Z* and r_{radial} directions. Conceptually, this method removes the bias placed on the target ion with the umbrella sampling to calculate the energetic requirements, which is the desired end result. Umbrella sampling is a standard technique used in molecular dynamics

simulation. Two-dimensional profiles were integrated at each Z position [127] to determine a one-dimensional profile. All energy profiles were single-ion profiles as no other ions entered the pores during the simulations.

6.2.4 Uncertainty Analysis

The uncertainty in the free energy values was assessed by conducting seven independent trajectories for one case (fluoride at $R_{eff} = 3.3 \cdot 10^{-10}$ m) in order to show error of repeated simulations. The standard deviation of the peak of the energy barrier from the seven independent trajectories was $\pm$ 2.3%, and this was also assumed to be similar for all trajectories. Convergence of the simulations was further evidenced by taking the average and standard deviation of energy outputs over the last 20% of the sample windows of 500-ps (bulk simulations) and 250-ps (per umbrella window). The standard deviation as a percentage of the average value was $\pm$ 0.07% and 1.4% for the 500-ps and 250-ps simulation windows, respectively. To further assess error, the Monte Carlo Bootstrap error analysis [308] feature within WHAM (a standard error technique for umbrella sampling) was evaluated for fluoride at $R_{eff} = 2.8 \cdot 10^{-10}$ m, as determined with 1000 Monte Carlo trials and correlation time of 100. Using this technique, reproducibility of the free energy calculations was estimated to be $\pm$ 0.3 kcal.mol^{-1}. This accuracy was assumed to be similar for all simulations. Because the magnitude of the error bars is small, they are not marked on the figures in Chapter 6.

6.3 Parameterization

Force field parameters required for MD simulations were available for fluoride [83], chloride [83] and water (type TIP3P) [309], but had to be specifically developed for nitrate, nitrite and boric acid using *ab-initio* quantum mechanical and MD techniques [221]. Gaussian03 [310] software was used to conduct geometry optimization (bond length, angle stretch and improper torsion), frequency analysis, and to calculate partial charges with the Merz-Singh-Kollman electrostatic fitting scheme [311]. This was achieved using Hartree Fock theory and a 6-31+G* basis set. Hartree Fock theory utilizes a mean value for electron-electron interactions and the selected basis set 6-31+G*

describes intermolecular interaction energies using split valence and polarization functions on all non-hydrogen atoms [220, 221]. Force constants were determined from potential energy surface scans and adjusted to match the infrared spectra from a MD vacuum simulation to the infrared frequencies obtained from the Gaussian calculation. LJ parameters ($R_{min/2,ij}$ and ε_{ij}) for all non-bonded atoms were systematically adjusted to reproduce the hydration free energies of the ions.

The method of alchemical free energy perturbations (FEPs) [221] was used to validate the ion parameterization by calculating the difference between the Gibbs hydration energies of two ions and comparing to literature values [80]. A single chloride ion was placed in the center of a $40\times40\times40\cdot10^{-10}$ m water box (type TIP3P [221, 299]) and slowly morphed into the target ion (*eg.* nitrate or nitrite) in 20 thermodynamic perturbation steps each lasting 500-ps. The non bonded LJ parameters were adjusted until the simulated hydration free energy of the ions was within 1 kcal.mol^{-1} of the hydration free energies reported in the literature (-71.6 kcal.mol^{-1} for nitrate and -78.8 kcal.mol^{-1} for nitrite [80]).

6.3.1   Fluoride, Chloride and Water

Force field parameters for fluoride [83], chloride [83] and water (type TIP3P) [309], as available in the literature, are shown on Table 6-4. The TIP3P was model was selected as it is commonly used in molecular dynamics simulations for a variety of applications.

Table 6-4. Force field parameters from the literature for fluoride [83], chloride [83] and water (type TIP3P) [309].

Parameter	Fluoride	Chloride	Water (TIP3P)	
			H	**O**
Partial Charges	-1	-1	0.417	-0.834
Non-bonded: $r_{min/2,ij}$ (Å)	2.303	2.513	0.2245	1.7682
Non-bonded: ε (kcal.mol^{-1})	0.0033	0.0356	-0.0460	-0.1521
Bond length, b (Å)	n/a	n/a	H-O: 0.9572	
Bond force constant, k_b (kcal.mol^{-1}.Å^{-2})			H-O: 450	
Angle stretch, θ (deg)	n/a	n/a	H-O-H: 104.52	
Angle force constant, k_θ (kcal.mol^{-1}.rad^{-2})			H-O-H: 55.0	

6.3.2   Nitrate and Nitrite

Force field parameters for nitrate and nitrite were developed using *ab-initio* techniques and FEPs, as described above.   The non bonded LJ parameters were adjusted until the hydration free energy of the ions was within 1 kcal.mol^{-1} of the target value, which was -71.6 kcal.mol^{-1} for nitrate and -78.8 kcal.mol^{-1} for nitrite [80].   The FEP results for nitrate with various LJ parameters are shown in Figure 6-2.
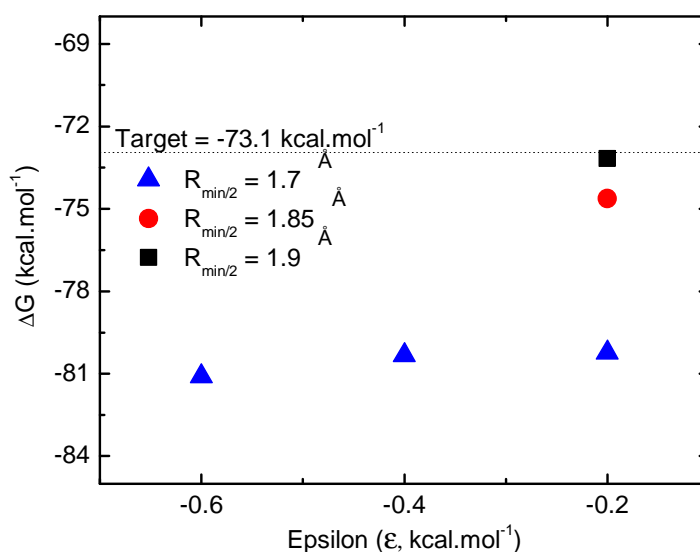
Figure 6-2.   Gibbs free energy values for nitrate obtained from alchemical FEP when a chloride ion was gradually morphed into nitrate in a water box.   The adjusted Lennard-Jones parameters (ε and $R_{min/2}$) are for the oxygen in nitrate.

Alchemical FEP calculations with various combinations of LJ parameters yielded the Gibbs free energies shown on Figure 6-2 for nitrate.   More negative ε and decreasing $R_{min/2}$ led to lower (more negative) Gibbs free energy.   Ultimately, the parameters of $\varepsilon = -0.2$ kcal.mol^{-1} and $R_{min/2} = 1.9 \cdot 10^{-10}$ m were selected for the oxygen in nitrate as this combination yielded the desired free energy of hydration for nitrate [80] and were comparable to values for other bonded oxygen atoms that were already optimized in the available parameter files [226].   A similar fitting procedure was conducted for nitrite. The final optimized parameters for nitrate and nitrite are shown in Table 6-5.

Table 6-5. Optimized ion parameters necessary for pore simulations developed by ab-initio techniques for nitrate and nitrite ("--" is non-applicable).

Parameter	Nitrate		Nitrite	
	N	**O**	**N**	**O**
Partial Charges	1.0323	-0.677	-0.058	-0.471
Non-bonded: $r_{min/2,ij}$ (Å)	1.850	1.900	1.850	1.900
Non-bonded: ε (kcal.mol^{-1})	-0.200	-0.200	-0.200	-0.200
Bond length, b (Å)	N-O:	1.2268	N-O:	1.2254
Bond force constant, k_b (kcal.mol^{-1}.Å^{-2})	N-O:	425	N-O:	264
Angle stretch, θ (deg)	O-N-O:	120	O-N-O:	117
Angle force constant, k_θ (kcal.mol^{-1}.rad^{-2})	O-N-O:	110	O-N-O:	27
Improper torsion, t (deg)	N-O-O-O:	0	n/a	
Improper force constant, k_t (kcal.mol^{-1}.rad^{-2})	N-O-O-O:	163	n/a	

6.3.3 Boric Acid

Geometric optimization, force constants and partial charge determination were also completed for boric acid. These parameters are shown on Table 6-6. Due to the complicated nature of boric acid with seven atoms, parameterization is much more difficult for this molecule and unfortunately there was not sufficient time to complete the parameterization of the LJ interactions. This could be the subject of future work, as the transport of boric acid is poorly understood, and properly parameterizing the molecule for MD simulations would be valuable. Because parameterization was not completed, no further results will be presented for boron in this chapter.

6.4 Ion Behaviour in Bulk Water

The behaviour of ions in bulk water must be understood as a basis for comparison to how water interacts within a confined pore. The ions are placed in bulk water and allowed to interact with the water molecules. After allowing the interactions, a number of properties can be determined. The hydration properties of each ion in bulk water are shown in Table 6-7. Fluoride had the smallest hydrated size ($R_{hyd,fluoride} = 3.4 \cdot 10^{-10}$ m), smallest average coordination number (6.5) and highest hydration energy (-119.7 kcal.mol^{-1}). Nitrate and nitrite had larger hydrated radii ($5.0 \cdot 10^{-10}$ m and $5.1 \cdot 10^{-10}$ m, respectively) and more water molecules associated with them compared to the single atom ions fluoride

Table 6-6. Optimized ion parameters developed by ab-initio techniques for boric acid. Note that Lennard-Jones parameters are not included.

Parameter	Boric Acid		
	B	**O**	**H**
Partial Charges	1.334	-1.096	0.652
Bond length, b (Å)	B-O:	1.3584	
Bond length, b (Å)	O-H:	0.9471	
Bond force constant, k_b (kcal.mol^{-1}.Å^{-2})	B-O:	500	
Bond force constant, k_b (kcal.mol^{-1}.Å^{-2})	O-H:	625	
Angle stretch, θ (deg)	H-O-B:	113.7	
Angle stretch, θ (deg)	O-B-O:	120	
Angle force constant, k_θ (kcal.mol^{-1}.rad^{-2})	H-O-B:	20	
Angle force constant, k_θ (kcal.mol^{-1}.rad^{-2})	O-B-O:	55	
Improper torsion, t (deg)	B-O-O-O:	0	
Improper force constant, k_t (kcal.mol^{-1}.rad^{-2})	B-O-O-O:	31.6	
Dihedral angle, σ (deg)	H-O-B-O:	180	
Dihedral force constant, k_σ (kcal.mol^{-1})	H-O-B-O:	3	

($3.4 \cdot 10^{-10}$ m) and chloride ($3.8 \cdot 10^{-10}$ m). The most weakly hydrated ion was nitrate, which had the highest average coordination number (15.5) and lowest hydration energy (-71.6 kcal.mol^{-1}) meaning that each water molecule was bound weakly to the ion. Note that nitrate and nitrite were not spherical ions, and thus were not spherical when hydrated because water molecules associated at highest density around the polar sites on the nitrogen and oxygen atoms. Also note that the hydrated radii obtained here are somewhat different than reported in very early studies [82] but these new values are more reliable due to their ability to reproduce hydration free energies and will be used for the remainder of the work presented in this thesis. The radial distribution functions and instantaneous distributions of coordination numbers are shown in Figure 6-3.

Table 6-7. Properties of hydration for each ion in bulk water including hydrated radius and average coordination number.

Parameter	Fluoride	Chloride	Nitrate	Nitrite
Ionic Radius, R_{ion} (10^{-10} m)[a]	1.3 [80]	1.8 [80]	3.0	3.0
Hydrated Radius, R_{hyd} (10^{-10} m)[b]	3.4	3.8	5.1	5.0
Average Coordination Number (--)	6.5	7.1	15.5	12.7
Target Hydration Free Energy (kcal.mol^{-1})	-119.7 [86]	-89.1 [86]	-71.6 [80]	-78.8 [80]
Simulated Hydration Free Energy (kcal.mol^{-1})	-119.7 [83]	-89.6 [83]	-71.5	-79.1

[a] For nitrate and nitrite, $R_{ion} = b_{N-O}$ ($1.22 \cdot 10^{-10}$ m) $+ R_{ion,oxygen}$ ($1.77 \cdot 10^{-10}$ m)
[b] For nitrate and nitrite, $R_{hyd} = b_{N-O}$ ($1.22 \cdot 10^{-10}$ m) $+ RDF_{min}$
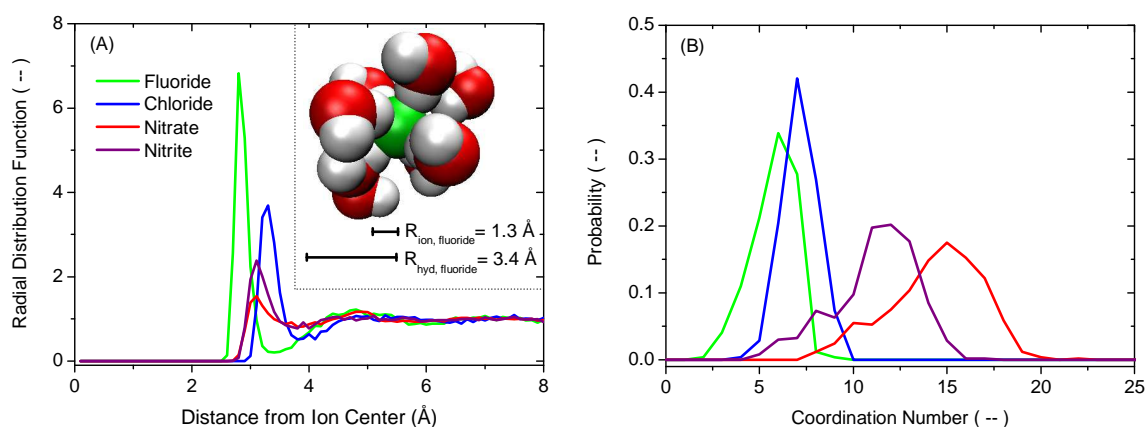

Figure 6-3. Ion behavior in bulk water. (A) Radial distribution function (RDF) for each ion in bulk water. RDF indicates the variation of oxygen (in water) density with distance from the center of the ion, and the size of the hydration shells are defined by the minima of the RDF function. Overlay schematic shows fluoride and its associated first hydration shell ($R_{hyd,fluoride} = 3.4 \cdot 10^{-10}$ m), which is defined by the first RDF minima. (B) Distribution of instantaneous coordination numbers. The probability of each ion having a given coordination number is shown as determined from their relative frequencies within the bulk simulations.

6.5 Ion Transport as a Function of Pore Size

Simulations involving anions transporting through a pore are now considered for the remainder of the chapter. The free energy profiles of fluoride entering pores of different sizes are shown in Figure 6-4A. In the narrowest pore studied ($R_p = 3.0 \cdot 10^{-10}$ m), water evacuated the pore during system equilibration. Such evacuation in small pores has been observed previously [300] and this narrowest pore size was not further pursued in this

study. In the remaining cases, the highest energy barrier for ion transport through the pore (46.9 kcal.mol^{-1}) occurred with the smallest pore where water remained during equilibration ($R_{eff} = 2.8 \cdot 10^{-10}$ m) because ion transport is the most hindered. The energy barrier was not simply a linear function of pore size; there was significant impact of pore size on free energy at $R_{eff} = 2.8$, 3.3 and $3.7 \cdot 10^{-10}$ m but the impact became less prominent at the largest pore sizes $R_{eff} = 5.3$ and $6.5 \cdot 10^{-10}$ m.

A plot of the maximum free energy versus pore size (Figure 6-4B) shows two key regimes that dictate transport. The first regime has a steep slope, as the energy barrier steeply increases as pore radius decreases. This occurred at lower pore radii ($R_{eff} = 2.8$ to $3.7 \cdot 10^{-10}$ m) where transport was highly hindered (energy barrier > 10 kcal.mol^{-1}). The highly hindered regime occurred when the hydrated radius ($3.4 \cdot 10^{-10}$ m) was larger than or similar to the effective radius of the pore meaning that water must be stripped from the ion for it to enter the pore. At larger pore radii ($R_{eff} = 4.3$ to $6.5 \cdot 10^{-10}$ m), transport had smaller hindrance (energy barrier < 6 kcal.mol^{-1}) and the slope of the curve is less because fluoride could fit into the pore with its entire first hydration shell. The dehydration energy does not scale linearly with the number of water molecules, as the first water binds most strongly to the ion. This is apparent in both ab-initio and MD calculations of binding energies [83], but is more evident in the pores where the limited space reduces hydrogen bonding between the coordinating waters as observed previously by Song and Corry, who determined the non-linearity of free energy required to partially or fully dehydration chloride in a pore [126].
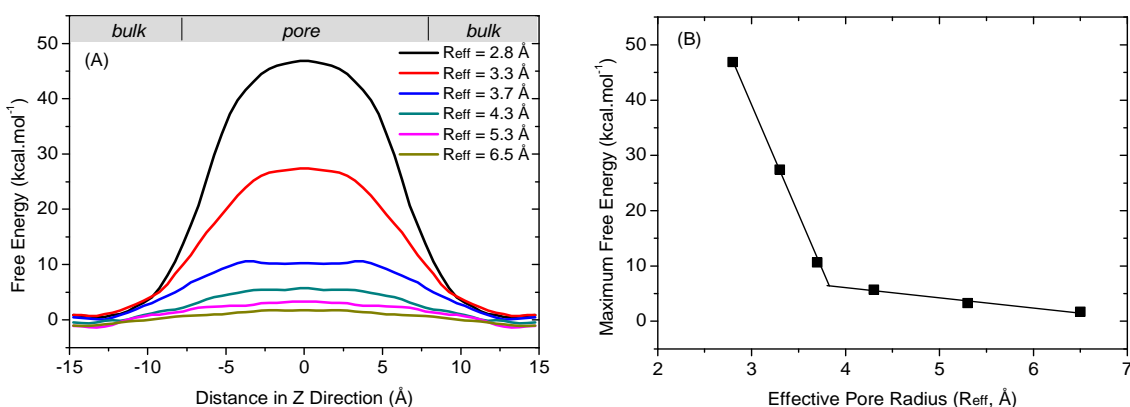
Figure 6-4. Impact of pore size on the free energy of fluoride. (A) Free energy profile of fluoride entering pores of different sizes (center of pore is $Z = 0$). (B) Maximum energy barrier at different pore sizes.

A quantitative and visual analysis of coordination number (Figure 6-5 and Figure 6-6, respectively) clearly showed that these energy barriers were due to dehydration because water molecules were removed from the hydration layer to allow fluoride to "squeeze" into the smaller pores. In the smallest pore ($R_{eff} = 2.8 \cdot 10^{-10}$ m), the coordination number of fluoride decreased from six to two as it moved from bulk into this pore, which means that it was partially dehydrated with the loss of four water molecules from its inner hydration shell, explaining the very large energy barrier. The coordination number remained at two with no deviation inside the pore as there was a single chain of molecules through the pore as shown in Figure 6-6, thus there was no other option for fluoride to coordinate with more than two water molecules once inside.

When the effective pore size was larger than the hydrated radius, fluoride did not have to dehydrate, resulting in a much smaller energy barrier for the transport. Small energy barriers at large pore sizes (for example 1.7 kcal.mol^{-1} at $R_{eff} = 6.5 \cdot 10^{-10}$ m) were due to slight rearrangement of the hydration shell and/or losing water from the second and more distant hydration layer.

These results are reasonable when compared with energy barriers found in carbon nanotubes, NF, RO and biological channels. The energy required to strip water from the hydration shell of sodium as it was entering a carbon nanotube was approximately 8.5

kcal.mol^{-1} per water molecule [126], whereas it is approximately 10 kcal.mol^{-1} per water molecule in this study for fluoride (as calculated by dividing the energy barrier by the decrease in coordination number). Energy barriers of pure water permeation in RO and inorganic NF membranes have been reported in the range of 4.3 to 7.2 kcal.mol^{-1} [183]. The physiological role of biological channels is to transport ions across a membrane and thus most narrow biological pores (such as potassium channels) contain polar groups with which the ions can interact to overcome the dehydration penalty. Biological pores with non-polar lining do exist, but must open wider to pass ions. It has been noted, for example, that the $3.0 \cdot 10^{-10}$ m radius non-polar interior of the closed state acetylcholine receptor presents a 6 kcal.mol^{-1} barrier to sodium and 4 kcal.mol^{-1} to chloride [126, 239, 312].
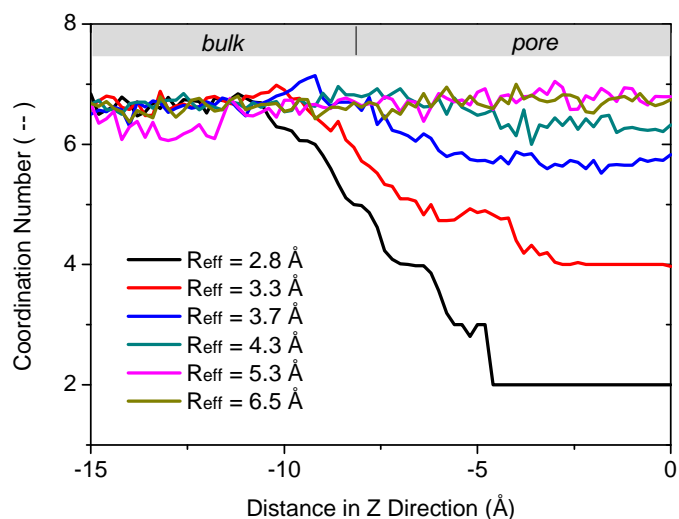

Figure 6-5. **Coordination number of fluoride as a function of distance in the *Z*-direction from bulk water into the pore for each pore size (center of pore is *Z* = 0).**
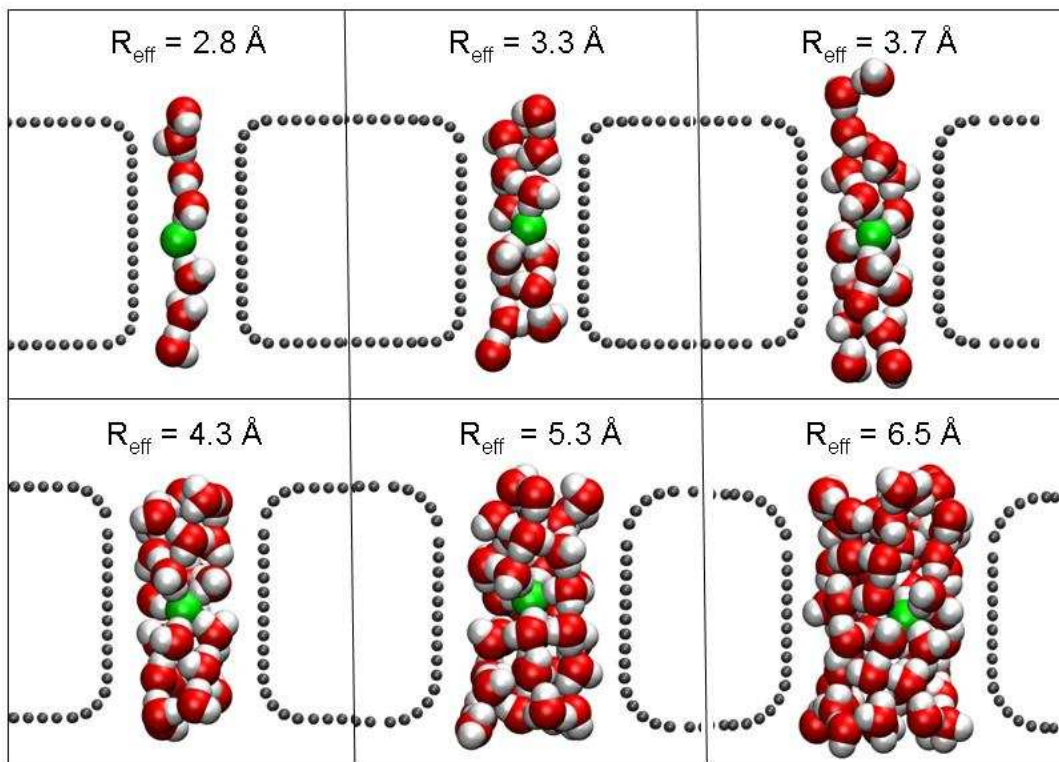
Figure 6-6. Representation of a fluoride ion (green) at the center of the pore ($Z = 0$) and surrounding water for different pore sizes.

6.6 Ion Transport as a Function of Ion Type

The effect of ion type on transport was examined to assess differences in behaviour according to ion properties, as shown in Figure 6-7. The free energy profiles (Figure 6-7A and B) show that the energy barrier is strongly dependent on ion type due to ion size, hydrated size, and hydration strength. In the smaller pore ($R_{eff} = 3.3 \cdot 10^{-10}$ m, Figure 6-7A) fluoride had the highest barrier (27.4 kcal.mol^{-1}), followed by chloride (21.8 kcal.mol^{-1}), nitrite (11.1 kcal.mol^{-1}) and nitrate (6.3 kcal.mol^{-1}). This order matched the trend in hydration energy (Table 6-7), showing that in a very narrow pore, the energy barriers in transport match the hydration energy trends. In the larger pore ($R_{eff} = 4.3 \cdot 10^{-10}$ m, Figure 6-7B) energy barriers decreased for all ion types, which was consistent with the behaviour discussed for fluoride in Section 6.5.

An interesting switch in the trend of the energy barriers occurred with fluoride and chloride with the two pore sizes shown in Figure 6-7. In the larger pore ($R_{eff} = 4.3 \cdot 10^{-10}$ m), chloride had the higher energy barrier, whereas fluoride was the most hindered with the smaller pore ($R_{eff} = 3.3 \cdot 10^{-10}$ m). Plots of the coordination numbers in the pore

(Figure 6-7C and D) can be used to explain these results. In the smaller pore (R_{eff} = $3.3 \cdot 10^{-10}$ m), each of the ions had to partially dehydrate: fluoride partially dehydrated from approximately seven to four associated water molecules; chloride from seven to four; nitrate from fifteen to seven; and nitrite from twelve to six. This shows that partial dehydration resulted in the energy barriers. Nitrate had the lowest energy barrier because even though it lost eight associated water molecules during transport (the largest number of any of the ions), it had the most water molecules associated with it in the bulk (15.5) and the lowest hydration energy (-71.6 kcal.mol^{-1}) so the dehydration did not have a large energetic cost.

In contrast, in the larger pore size (R_{eff} = $4.3 \cdot 10^{-10}$ m) partial dehydration occurred for each ion except fluoride. Fluoride was sufficiently small to fit in the pore without dehydrating (whereas chloride still needed to dehydrate), which explains the switch in fluoride and chloride between Figure 6-7A and B. This is similar to the classic idea of 'size selectivity' but is based upon the size of the hydrated rather than the bare ion or Stokes radii [313, 314]. A similar switch in the order of the energy barriers has been seen for sodium and potassium [126, 239]. Fluoride did not dehydrate, chloride partially dehydrated from seven to six associated water molecules; nitrate from fifteen to ten, and nitrite from twelve to nine. The smaller amount of dehydration required resulted in the lower free energies at R_{eff} = $4.3 \cdot 10^{-10}$ m. These results were consistent with data previously published by Song and Corry, which stated that the free energy required to partially dehydrate chloride to three associated water molecules was 20.3 kcal.mol^{-1} and to six water molecules was 9.50 kcal.mol^{-1} (compared to 21.8 kcal.mol^{-1} at R_{eff} = $3.3 \cdot 10^{-10}$ m and 7.74 kcal.mol^{-1} for R_{eff} = $4.3 \cdot 10^{-10}$ m in this study) [126].

Therefore, this section has shown that free energy barriers were not only dependent on pore size, but also on ion type (and hence hydration properties). Coordination numbers confirmed that partial dehydration is the main determinant of the energy barriers observed.
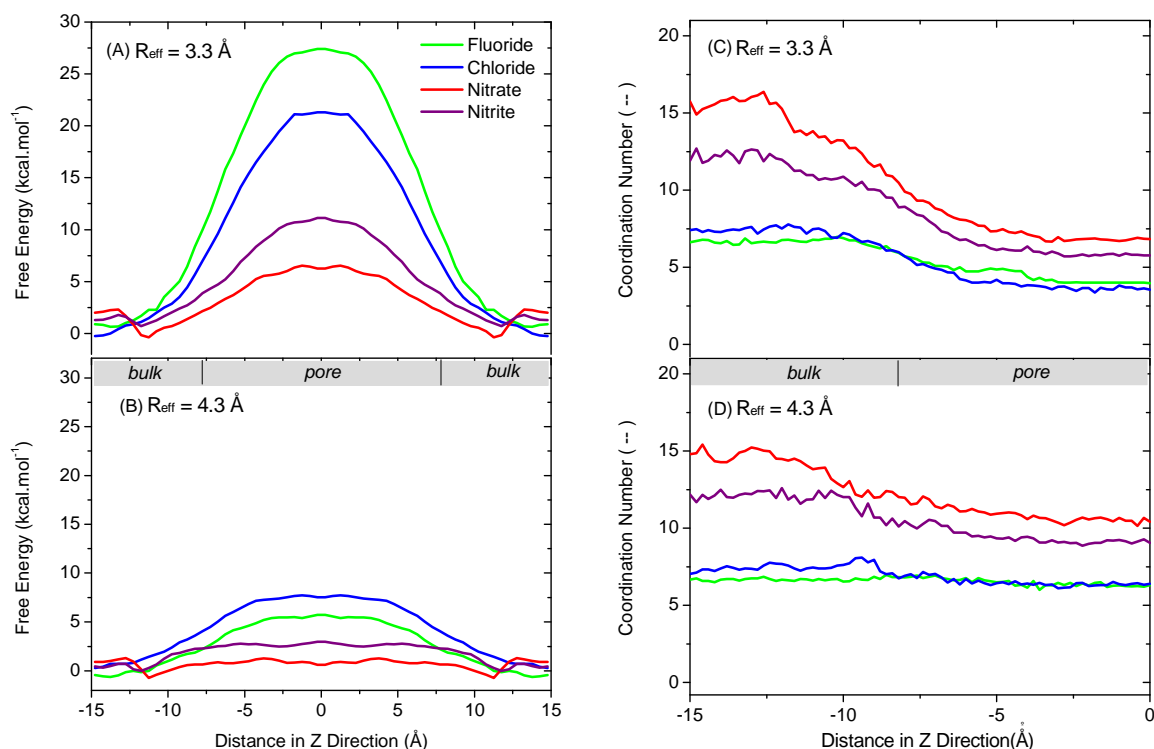
Figure 6-7. Free energy profiles (A and B) and coordination number versus distance (C and D) of different ions for two pore sizes, (A and C) $R_{eff} = 3.3 \cdot 10^{-10}$ m and (B and D) $R_{eff} = 4.3 \cdot 10^{-10}$ m (center of pore is $Z = 0$)

6.7 Ion Transport for Each Ion Type at an Extended Size Range

Because of the very interesting results obtained and discussed in Sections 6.5 and 6.6, additional simulations were conducted for each ion at an extended range of pore sizes. The results for energy barrier of each ion versus effective pore size are shown in Figure 6-8. This figure shows that energy barriers are a very clear function of both ion type and pore size, corroborating the results shown in Sections 6.5 and 6.6. However, this figure also shows some very interesting information in addition to what was already presented in previous sections. In particular, there appear to be three key regimes with regard to ion properties that can be linked to the maximum energy barriers. These key regimes describe regions in which:

1. The ion fits in the pore with its complete hydration shell ($R_{hyd} < R_{eff}$).
2. The pore size is between the size of the bare ion and the hydrated ion ($R_{ion} < R_{eff} < R_{hyd}$).
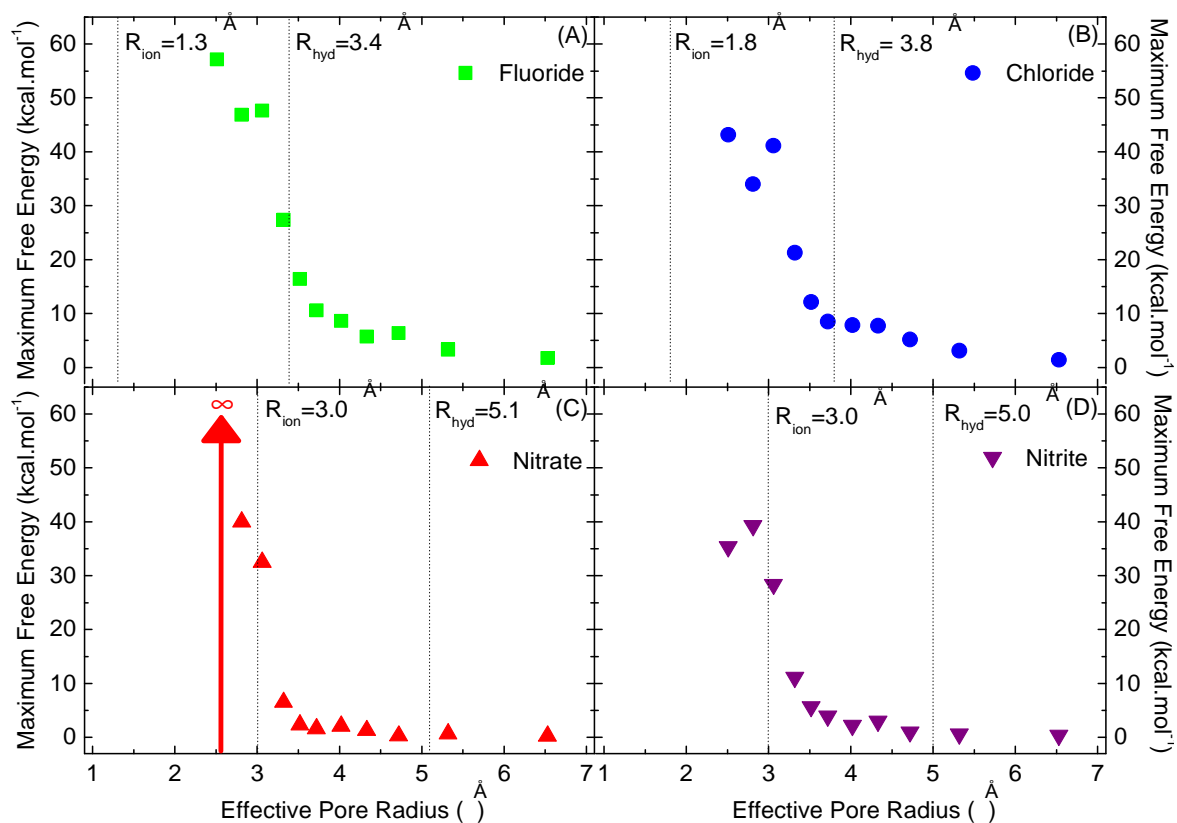3. The bare ion struggles to fit inside the pore ($R_{ion} > R_{eff}$).

Figure 6-8. Maximum energy barriers for fluoride (A), chloride (B), nitrate (C) and nitrite (D) with an extended range of pore sizes.

In the first regime, the ion is able to fit in the pore with its first hydration shell complete. In other words, it is where the effective pore size is larger than the hydrated radius of the ion of interest. This regime is the farthest on the right in Figure 6-8. Energy barriers in this regime are relatively small and are due to rearrangement/reorientation of the first hydration shell or loss of the second and farther hydration shell. The increase in energy barriers with decreasing pore size, even when the ion can fit in the pore with its hydrated shell, is most significant for strongly hydrated fluoride and chloride.

In the second regime, the effective pore size is between the size of the bare ion and the hydrated ion. Here, some dehydration is required in order for the ion to enter the pore with a partial hydration shell. Pore size significantly impacts the energy barriers in this regime due to the energy required to dehydrate. The slope of the line of energy barriers versus pore size can be clearly seen in the middle regime in Figure 6-8. The slope of this line is related to hydration energy. Fluoride, the most strongly hydrated, has a very steep

slope in this regime, followed by chloride, nitrite and nitrate. This trend in slope is the same as the trend in hydration energies as seen on Table 6-7.

The third regime is where the bare ion struggles to fit inside the pore, and hence energy barriers become extremely high or even infinite (as was the case with nitrate in the smallest pore, which is what the up-pointing arrow represents). Fluoride and chloride never reached this third regime because of their very small ionic size (similar to that of water).

The selectivity sequence of ions thus changes according to the pore size, since the regimes for each of the ions are located according to the ion properties (ion size, hydrated size, hydration strength). This ordering is shown on Table 6-8, and will later be compared to experiments (Chapter 7). At the smallest pore size ($2.51 \cdot 10^{-10}$ m), the energy barriers are nitrate > nitrite > fluoride > chloride, assuming the nitrite data point is out of trend. At $2.81 \cdot 10^{-10}$ m, the order is fluoride > nitrate > nitrite > chloride. At $3.06 \cdot 10^{-10}$ m, fluoride > chloride > nitrate > nitrite. From $3.32 \cdot 10^{-10}$ m to $4.02 \cdot 10^{-10}$ m, the order is fluoride > chloride > nitrite > nitrate, which is the inverse order at the hydrated radii. At $4.33 \cdot 10^{-10}$ m and $4.72 \cdot 10^{-10}$ m, the order is chloride > fluoride > nitrite > nitrate, and finally at $5.32 \cdot 10^{-10}$ m and $6.53 \cdot 10^{-10}$ m, the order is fluoride > chloride > nitrite = nitrate. These sequences are directly related to the amount of partial dehydration required, and thus are completely dependent on ion type and pore size. Because each of the ions has a different ionic size, hydrated size and hydration strength, the selectivity sequence will change depending on pore size. This phenomenon was shown and discussed specifically for fluoride and chloride previously on Figure 6-7, where there was a swap in sequence at $R_{eff} = 4.3 \cdot 10^{-10}$ m, due to fluoride being sufficiently small to fit into the pore without dehydrating, but chloride still needed to partially dehydrate which lead to a higher barrier for chloride than fluoride. This same concept results in the changes in selectivity sequences for all ions and all pore sizes discussed here.

Table 6-8. Energy barriers determined for each ion at each pore radius. Error for molecular dynamics results is estimated to be ± 0.6 kcal.mol⁻¹.

Effective Pore Radius (10^{-10} m)	Energy Barrier (kcal.mol⁻¹)						
	Highest						Lowest
2.51	NO_3^- (∞)	>	F^- (57.1)	>	NO_2^- (35.3)	>	Cl^- (43.2)
2.81	F^- (46.9)	>	NO_3^- (40.0)	>	NO_2^- (39.3)	>	Cl^- (34.0)
3.06	F^- (47.7)	>	Cl^- (41.1)	>	NO_3^- (32.5)	>	NO_2^- (28.4)
3.32	F^- (27.4)	>	Cl^- (21.3)	>	NO_2^- (11.1)	>	NO_3^- (6.5)
3.52	F^- (16.4)	>	Cl^- (12.1)	>	NO_2^- (5.7)	>	NO_3^- (2.3)
3.72	F^- (10.6)	>	Cl^- (8.5)	>	NO_2^- (4.0)	>	NO_3^- (1.6)
4.02	F^- (8.6)	>	Cl^- (7.8)	>	NO_2^- (2.2)	≈	NO_3^- (2.1)
4.33	Cl^- (7.7)	>	F^- (5.7)	>	NO_2^- (3.0)	>	NO_3^- (1.3)
4.72	F^- (6.4)	>	Cl^- (5.2)	>	NO_2^- (1.0)	>	NO_3^- (0.3)
5.32	F^- (3.3)	≈	Cl^- (3.1)	>	NO_2^- (0.7)	≈	NO_3^- (0.7)
6.53	F^- (1.7)	≈	Cl^- (1.4)	>	NO_2^- (0.4)	≈	NO_3^- (0.2)

Figure 6-8 showed that maximum energy barrier depended on pore size in three regimes determined by ion properties. These results can be further corroborated by considering the coordination numbers, as shown in Figure 6-9, which confirm that the barriers obtained are due to dehydration. Figure 6-9A shows average coordination number in the center of the pore versus effective pore radii. For the smallest pore sizes, where energy barriers are highest, fluoride and chloride form a single chain with water molecules on either side, making the coordination number limited to two inside the pore. As the pore size increases, more water molecules are able to fit inside the pore with the ions in all cases. At pore sizes larger than the hydrated radii of the ion, the coordination number does not change as the maximum number of water molecules are associated with the ion, independent of being in the bulk water or in the pore. Figure 6-9B shows the direct link between the energy barriers and the dehydration required for each ion. At the smallest pore sizes, where the most dehydration is required, the ratio of the coordination number in the pore to coordination number in bulk is the lowest, and consequentially the energy barrier is the highest. This is the case for all ions evaluated, although the actual values of course depend on the ion properties. This confirms that the energy barriers obtained are due to varying degrees of dehydration.

Further support that barriers are due to dehydration is shown in Table 6-9. Here, the average interaction energy of each ion with the water molecules within its first hydration

shell is reported when the ion is located in the center of the pore. As pore size increases, the attractive (negative) interaction force increases as more water becomes available. The interaction energies reach the same value as in bulk at different pore sizes according to the ion properties. As these results are average interaction energies, they do not include entropic contributions and thus cannot be directly compared to the free energy barriers but they do support that dehydration is important.
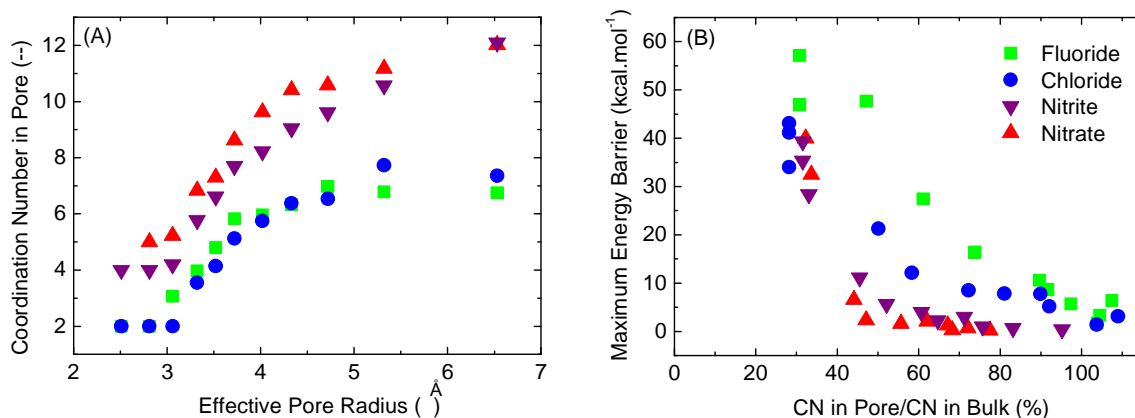

Figure 6-9. Coordination numbers (*CN*) for each ion. (A) is coordination number in pore versus effective pore radius (*R$_{eff}$*); (B) is maximum energy barrier versus % of total coordination as defined by average *CN* in pore divided by average *CN* in bulk.

Table 6-9. Average interaction energy (kcal.mol^{-1}) of each ion with the water molecules within its first hydration shell when located in the centre of the pore.

Effective Pore Size (10^{-10} m)	Average Interaction Energy (kcal.mol^{-1})			
	Chloride	**Fluoride**	**Nitrate**	**Nitrite**
2.51	-32.6	-48.9	--	-23.8
2.81	-32.2	-48.2	-28.2	-27.3
3.06	-31.8	-66.9	-32.6	-39.8
3.32	-49.6	-83.8	-40.6	-55.6
3.52	-56.2	-95.5	-49.3	-68.2
3.72	-68.2	-111.0	-60.3	-79.0
4.02	-72.4	-113.2	-62.7	-80.6
4.33	-74.6	-116.9	-64.1	-81.8
4.72	-77.1	-124.4	-65.8	-81.0
5.32	-83.5	-123.5	-64.8	-84.6
6.53	-83.7	-123.3	-68.5	-84.4
Bulk	-83.9	-121.7	-68.7	-83.7

Finally, the effect of partial ion dehydration is demonstrated visually using a probability density function of water around each ion in the center of the pore (Figure 6-10). Each of the regimes can be seen here. The first regime is shown in Figure 6-10B where the water surrounds the chloride ion in the pore. The second regime is shown for chloride and nitrate (Figure 6-10A and Figure 6-10D, respectively), where the ion must be partially dehydrated to enter the pore (*eg.* $R_{ion} < R_{eff} < R_{hyd}$) and the ion forms a single chain with water on either side. The final regime, where it is difficult for the bare ion to fit, is shown in Figure 6-10C. Here the area that the water in the pore fills is smaller than nitrate, highlighting the unfavorable nature of this regime.
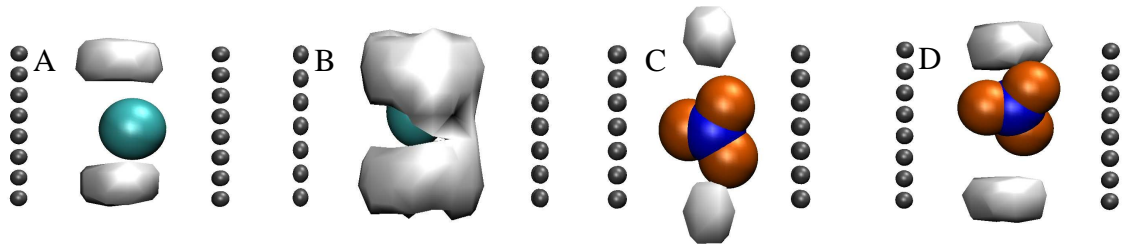

Figure 6-10. Water around the selected ion at the center of a pore as represented by isosurface plots of the average water density. (A) shows chloride at $R_{eff} = 3.3 \cdot 10^{-10}$ m (Regime 2); (B) shows chloride at $R_{eff} = 4.7 \cdot 10^{-10}$ m (Regime 1); (C) is nitrate at $R_{eff} = 2.8 \cdot 10^{-10}$ m (Regime 3); (A) is nitrate at $R_{eff} = 3.3 \cdot 10^{-10}$ m (Regime 2).

6.8   Ion Transport Including Charge Interactions

Most NF membranes contain charged groups on the membrane surface, rather than being neutral, which influences ion rejection through charge repulsion. To compare the importance of ion dehydration with the better characterized mechanism of charge repulsion, additional simulations were conducted with a repulsive charge (-0.1 $C.m^{-2}$) evenly distributed on the top surface. The magnitude of these charges was chosen to be greater than that expected in most NF situations (typical range from approximately -0.05 to +0.01 $C.m^{-2}$) [283] as to compare dehydration with charge repulsion in an extreme case. For reference, a zeta potential measurement of -30 mV, which is approximately the value for NF membranes NF90 and NF270 above approximately pH 12 (Chapter 3.2.4), is -0.01 $C.m^{-2}$ (method of unit conversion in [302]).

The effect of surface charge on free energy profiles is shown in Figure 6-11. The figure shows the free energy profile for fluoride along the z-axis through the center of the pore. The inclusion of negative charge on the top surface led to a higher energy barrier compared to when charge was not considered. This is most likely caused by direct charge repulsion occurring between the negative surface and negative fluoride ion, but could also arise from interactions between water and the charged membrane or entropic changes. However, even though charge contributed by increasing the energy barrier, it is important to note that dehydration remained the dominant effect. The contribution to dehydration on Figure 6-11 is the same as the first half of the free energy profile for fluoride ($-15 < Z < 0$) shown on Figure 6-7. At the smaller pore size ($R_{eff} = 3.3 \cdot 10^{-10}$ m) charge contributed 14% to the maximum free energy (4.5 kcal.mol^{-1} of a total barrier of 31.6 kcal.mol^{-1}) and at $R_{eff} = 4.3 \cdot 10^{-10}$ m, charge contributed 20% to the maximum free energy. Charge had a larger relative effect at the larger pore sizes, because the contribution of dehydration to the total energy barrier was less. These results are important as they demonstrate that dehydration remains the dominant barrier to ion transport as compared to charge repulsion.
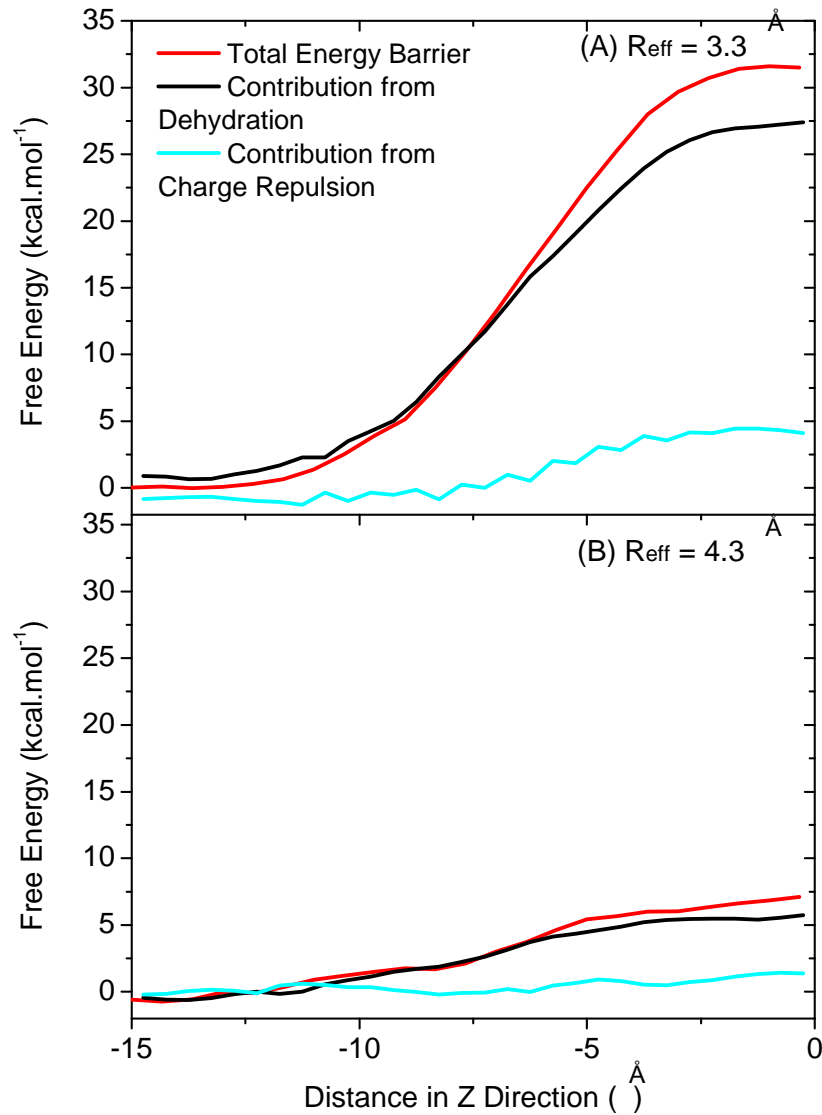
Figure 6-11. Decomposition of free energy profile with a surface charge of -0.1 C.m^{-2} (applied to top membrane surface only) for fluoride with (A) R_{eff} = 3.3·10^{-10} m and (B) R_{eff} = 4.3·10^{-10} m (center of pore is Z = 0).

An additional simulation was conducted to assess the impact of the distribution of charge on the surface of the pore. The results on Figure 6-11 had charge distributed only on the top membrane surface. Figure 6-12 shows the impact of adding charge inside the pore as well. As expected, the presence of charge inside the pore increases the energy barrier due to increased charge repulsion. However, dehydration remains the dominant barrier to pore transport and key to understanding transport mechanisms.
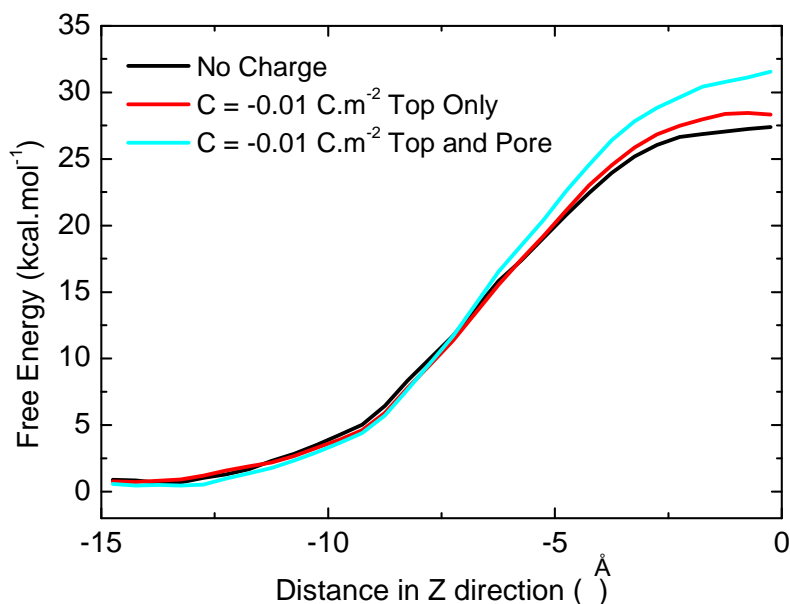
Figure 6-12. Free energy profile with a surface charge of -0.01 C.m^{-2} applied to top membrane surface only and the top surface with the inside of the pore for fluoride with $R_{eff} = 3.3 \cdot 10^{-10}$ m (center of pore is $Z = 0$).

6.9 Relevance to Real Membrane Systems

While these MD simulations are an extremely valuable tool in understanding ion transport, the model cannot exactly replicate a NF pore or membrane. The pore representation used here did not account for pore size distributions, tortuousity and functional groups on the membrane surface. It was meant to be a generic representation of a pore that could thus be used for a number of applications such as NF, carbon nanotubes, and biological pores. Experimental evidence of dehydration occurring during ion transport in a NF membrane is yet to be systematically demonstrated but will provide a complementary and significant step forward in understanding this mechanism. The next chapter in this thesis (Chapter 7) aims to determine energy barriers experimentally using commercial NF membranes in order to gain an indication of the comparison of results obtained with this model to real membrane systems.

6.10 Conclusions

This chapter described MD simulations that were used to examine the hydration of monovalent anions relevant to drinking water purification (fluoride, chloride, nitrate,

nitrite) as they transport through nanopores to determine its importance in this process. Three key conclusions can be drawn from this work. Firstly, energetic barriers were strongly dependent on pore size. Energy barriers were not linearly correlated with pore size; instead, there were three distinct regimes related to the required dehydration. Transport was strongly hindered when the size of the pore was smaller than the hydrated radius.

Secondly, energy barriers depended on ion type (and hence hydration properties) and the selectivity sequence amongst the ions can change depending on the pore size. In general, the transport of small, strongly hydrated ions (such as fluoride) was much more energetically expensive than for larger, less strongly hydrated ions (such as nitrate) due to the required dehydration unless the pore is larger than the size of the hydrated ion. This could have important implications in utilizing the different barriers in order to separate different types of ions, which is especially exciting from the perspective of removing contaminants other than sodium chloride in seawater desalination. Further work is ongoing to pinpoint the pore sizes that enable the best discrimination between the ion types studied, although the issue is complicated when polar groups are present in the pore walls.

Thirdly, and most importantly, these results showed that dehydration was the main barrier to ion transport in the narrow pores. In particular, partial dehydration was the main determinant of the energy barriers for small, strongly hydrated ions whose hydrated radius is larger than the pore size, even when charge repulsion is considered. This explains, for example, why fluoride is rejected by membranes with pore sizes greater than the ionic radius of fluoride. Demonstrating that the process of hydration/dehydration is important in NF will encourage future models to incorporate these interactions. By providing a systematic and novel insight into the role of ion dehydration in pore transport, these results are significant in understanding anionic selectivity in biological channels as well as desalination and removal of various drinking water contaminants with NF. This work provides the theoretical evidence for dehydration occurring as a NF mechanism, and the next chapter (Chapter 7) will aim to show this experimentally.

MD simulations applied to pore transport in NF stand to be developed in a number of ways. It would be particularly interesting to use such methods to understand boron transport, however, complete parameterization of boron species is first required. Additionally, further developing the pore representation to thoroughly account for membrane characteristics such as charge, polarity and functional groups would be very valuable. It is hoped that some of these aims can be achieved in future work.

Chapter 7

Experimental Determination of Energy Barriers to Ion Transport

Using MD simulations, Chapter 6 showed that fluoride, chloride, nitrate and nitrite can partially dehydrate when they transport through narrow pores according to ion type and pore size. This chapter endeavours to show the same effect experimentally. This is a very challenging undertaking due to limitations in what can be measured experimentally (for example it is not possible to measure the hydration structure of an ion as it transports through a membrane pore). However, carefully designed experiments were undertaken using real NF membranes in an attempt to experimentally verify the MD results which suggested dehydration as an important transport mechanism.

The results obtained in this chapter showed that energy barriers can be determined experimentally for anions in a crossflow system. Fluoride, chloride nitrate and nitrite face different energy barriers in the range of 7 – 17 kcal.mol^{-1} according to ion type and membrane type. Fluoride had the highest retention and energy barrier for both NF90 and NF270, which can be explained by its comparatively strong hydration energy and not by size exclusion based on either bare ion or hydrated radius. Besides fluoride, which clearly had a larger barrier than the other solutes, differences in energy barriers for the other solutes were difficult to distinguish outside of the error range. Experimentally-determined energy barriers are within a factor of four when compared to previous MD simulations that demonstrated barriers in idealized cylindrical pores were due to ion

dehydration. The results obtained provide novel experimental indication of dehydration as an important NF mechanism and suggest that NF models would be improved by considering solute hydration.

7.1 Introduction and Objectives

The transport of water and dissolved solutes through NF membranes is substantially hindered because membrane "pores" are similar to the ionic and/or hydrated size of solutes. This hindrance means that any molecule will face an energy barrier which must be overcome if transport through the membrane is to occur. Any mechanism(s) which affects transport contributes to this net energy barrier. As reviewed extensively, accepted mechanisms include size exclusion [77, 105, 106], charge interactions (including maintenance of electroneutrality) [98, 109, 111, 113, 143, 198], sorptive interactions [134-136], diffusion [76, 118-120] and hydrodynamic influences such as convection [94, 198]. However, other, less-established mechanisms (such as the possible dehydration of solutes during transport through the membrane [126, 129, 130, 303]), if important, will also contribute to the net barrier of transport.

As demonstrated in Chapter 5 and 6, not all NF behaviour can be explained by the commonly-accepted NF mechanisms, such as the high retention of fluoride compared to nitrate [139, 283]. The proposed hypothesis is that this selectivity may be due to hydration properties (hydration strength and size) and the process of ions becoming dehydrated while transporting through the membrane [126, 129, 130, 303]. The transport of solutes in NF has been previously correlated with hydrated size and hydration energy [77, 100, 125]. Molecular dynamics simulations in idealized, narrow cylindrical pores (radius 2.5 to 6.5 $\cdot 10^{-10}$ m) discussed in Chapter 6, have highlighted that dehydration is the main contribution to energy barriers of anionic transport [303], and similar dehydration may be important if ions are dissolving into a porous or non-porous dense material. Partial or full dehydration of a solute during transport would reduce the effective size of a solute and thus directly impact size exclusion, diffusion and convection mechanisms. This hypothesis will be tested by experimentally determining energy barriers and linking them with dehydration trends.

Energy barriers can be overcome by any driving force, given that the driving force provides sufficient energy to overcome the barrier. In NF, directional driving forces include pressure and flow (primarily driving convection) and concentration (primarily driving diffusion [76, 118-120]. Temperature provides a non-directional driving force. An increase in system temperature increases diffusion because molecules at higher temperature have more internal energy. By increasing energy, the proportion of solutes with energy greater than the energy barrier of transport is significantly higher, so the overall solute transport increases. In addition to increased diffusion, increase in ion transport with temperature is usually explained by a reduction in solvent viscosity, an increase in polymer chain mobility, or changes in pore size/membrane structure (*eg.* swelling) [136, 183, 185-187]. Temperature is the focus of this chapter because it allows for the quantification of energy barriers using standard techniques.

The standard technique to quantify energy barriers is with the Arrhenius relationship, which describes the temperature dependence of water and solute transport, via

$$\ln(k) = \ln(A) - \left(\frac{E_a}{R} \cdot \frac{1}{T} \right)$$

Equation 39

where k is solute flux (mol.h^{-1}.m^{-2}), A is a pre-exponential factor, R is the gas constant (kcal.mol^{-1}.K^{-1}), T is temperature (K) and E_a is the energy barrier or activation energy (kcal.mol^{-1}) [78]. The slope of a linear plot of $\ln(k)$ versus T^{-1} gives the energy barrier, E_a. The direct inputs from experimental measurements are k and T, and E_a and A are parameters from the linear fit. The main assumptions in this calculation are that (1) the process follows Arrhenius behaviour (validated if the plot is linear) and (2) that the determined energy barrier is a net effect from all contributions. Energy barriers determined with the Arrhenius relationship for the transport of water and various solutes through membranes and dense films have been reported [118, 119, 184, 186, 188-193], with varying objectives ranging from mechanistic to practical considerations of high temperature processes. These were discussed in detail in Chapter 2.3.6. However,

energy barriers in membranes have not yet been linked to dehydration, which is the primary goal of this chapter.

The research objectives are to (1) determine the selectivity of monovalent anions using energy barriers and relate selectivity to hydration; (2) quantify energy barriers using the Arrhenius relationship for different ion types (sodium fluoride, sodium chloride, sodium nitrite and sodium nitrate) and membrane types (NF90 and NF270); and (3) link experimental energy barriers with results from molecular dynamics simulations indicating the dominant impact of dehydration.

7.2   Experimental Summary

The crossflow system was described in Chapter 3.1.2 and used for all experiments in this chapter. Membranes (NF90 and NF270, see next paragraph) were compacted for at least one hour (or until pure water flux stabilized) at 15 bar. The system was operated at a feed flow of 2 L.min^{-1} (recirculated) and pressure was varied from 3, 5, 7, 9, 11 bar for each temperature of 15, 20, 25, 30 and 35 °C. The feed solution consisted of 0.1M single salt (NaF, NaCl, NaNO$_3$, NaNO$_2$, Fisher Scientific, purity on Table 3-11) in MilliQ water with no pH adjustment (pH 6.2). For the ease of referencing, the properties of ions are shown in Table 7-1, which is a consistently-defined set of values for these ions. Samples (25 mL, with the first 5 mL discarded in order to ensure that the sample line had been flushed from the previous sample) were collected from feed and permeate after 30 minutes at a given operating condition. Nitrate and nitrite were analyzed using a nutrient analyzer (Lachat QuikChem 8500, USA, Chapter 3.4.3), fluoride using an ion selective electrode (Metrohm, UK, Chapter 3.4.2), and chloride using ion chromatography (Metrohm 883 Basic IC Plus, UK, Chapter 3.4.8).

Table 7-1. Ion properties (ionic radius, Stokes radius, hydrated radius, hydration free energy and bulk diffusion coefficients) for each ion.

Parameter	Fluoride	Chloride	Nitrate	Nitrite	Sodium
Ionic Radius, R_{ion} (10^{-10} m)[a]	1.3 [80]	1.8 [80]	3.0 [303]	3.0 [303]	1.2 [80]
Stokes Radius, R_{stokes} (10^{-10} m)	1.7 [82]	1.2 [82]	1.3 [82]	1.3	1.6 [83]
Hydrated Radius, R_{hyd} (10^{-10} m)[b]	3.4 [303]	3.8 [303]	5.1 [303]	5.0 [303]	2.4 [83]
Hydration Free Energy (kcal.mol^{-1})	-119.7 [83]	-89.6 [83]	-73.1 [90]	-81.0 [90]	-88.7 [83]
Diffusion Coefficient in Bulk Water at 25°C (10^{-9} m^2.s^{-1})	1.46 [78]	2.03 [131]	1.90 [131]	1.91 [315]	1.33 [316]

[a] For nitrate and nitrite, R_{ion} = b$_{N-O}$ ($1.22 \cdot 10^{-10}$ m) + $R_{ion,oxygen}$ ($1.77 \cdot 10^{-10}$ m)
[b] For nitrate and nitrite, R_{hyd} = b$_{N-O}$ ($1.22 \cdot 10^{-10}$ m) + RDF_{min} (base of the first peak in the radial distribution function of oxygen)

Commercially available NF membranes NF90 and NF270 (Dow Filmtec) were used. Full characterization information was provided in Chapter 3 and a relevant summary is shown in Table 7-2. The two membranes were selected to be of similar effective pore radius to the hydrated radius of the solutes of interest. For example NF90 and NF270 have an average effective pore size very similar to the hydrated radius of fluoride and chloride, and smaller than the hydrated radius of nitrate and nitrite. BW30 was not used because it is tighter than NF90 and a larger effective pore size was desired in order to obtain larger differences in retention (*eg.* retention for all solutes would be expected to be very high and thus difficult to distinguish for BW30). Characterization (effective pore radius, R_{pore}, and the ratio of membrane active layer thickness/porosity, $L.\varepsilon^{-1}$) was obtained by using the hydrodynamic model [36, 105] and methodology as described previously [216, 304]. NF270 is a much smoother membrane than NF90 (Chapter 3.2.6). Temperature dependence of effective pore size was determined using xylose only for NF90 and NF270 by conducting experiments at 15, 20, 25, 30, 35 °C (diffusion coefficients used in the fitting method [216, 304] were adjusted for temperature).

Table 7-2. Membrane characterization.

Membrane	Effective Pore Radius (R_{pore}, 10^{-10} m)[a]	Average Active Layer Thickness: Porosity Ratio ($L.\varepsilon^{-1}$, 10^{-6} m)[a]	Average Active Layer Thickness (L, 10^{-10} m)[b]	Average Porosity (%)[c]	Membrane charge at pH 6.2 (eq.m^{-3})[d]	Ref.
NF90	3.4	1.46	1740	11.9	-502	[283, 304]
NF270	3.8	1.01	350	3.3	-170	[283, 317-319]

[a]Uncertainty is estimated to be ± 5% for both of these fitted parameters; [b]Averaged from the literature (references as in final column); [c]Calculated from experimentally determined $L.\varepsilon^{-1}$ and active layer thickness reported in literature. [d]Measured streaming potential converted to charge density by method in [302].

Real retention was corrected for concentration polarization as described in Chapter 3.5. Energy barriers were calculated in three steps. The first step was that for each temperature, solute flux was plotted against corrected pressure (applied pressure – osmotic pressure) and a line was fit to the plot. The second step was to make an Arrhenius plot of the natural log of the y-intercept of each solute flux fit versus inverse temperature. The third step was to determine the slope of the Arrhenius plot which is the energy barrier. Uncertainty was calculated as described in Chapter 3.5.2. Results were compared to the MD simulations described in Chapter 6.

7.3 *Selectivity of Monovalent Anions in NF*

The first question was to assess the selectivity of monovalent anions in NF and determine how this can be lined to energy barriers. Figure 7-1 shows retention corrected for concentration polarization for each ion with NF90 and NF270. Retention increases with pressure for all ions and for both membranes. An increase of retention with pressure has been observed a number of times [37, 107, 140] and is attributed to higher water flux at higher pressure, leading to lower permeate concentration and higher retention [107]. High selectivity exists between anions for both membranes. Similar ordering of the retention of monovalent anions with NF has been observed previously (retention of fluoride > chloride [242]; retention of fluoride > nitrate [283]; retention of fluoride > chloride > nitrate [139]; retention of sodium chloride > sodium nitrate [106, 107, 136] but trend was opposite for a different membrane in the same study [136]). The highest

retention (fluoride) means that the transport of fluoride has the highest associated energy barrier because transport through the membrane is the most "difficult". Evaluation of the relative contributions of convection, diffusion and electromigration using the Nanofiltran program [164] predicted that diffusive transport strongly dominated the other mechanisms under the conditions of these experiments. Note that all calculations are based on the anion concentrations since the anion (co-ion) is the limiting species that determines overall electrolyte transport through the negatively charged membrane.
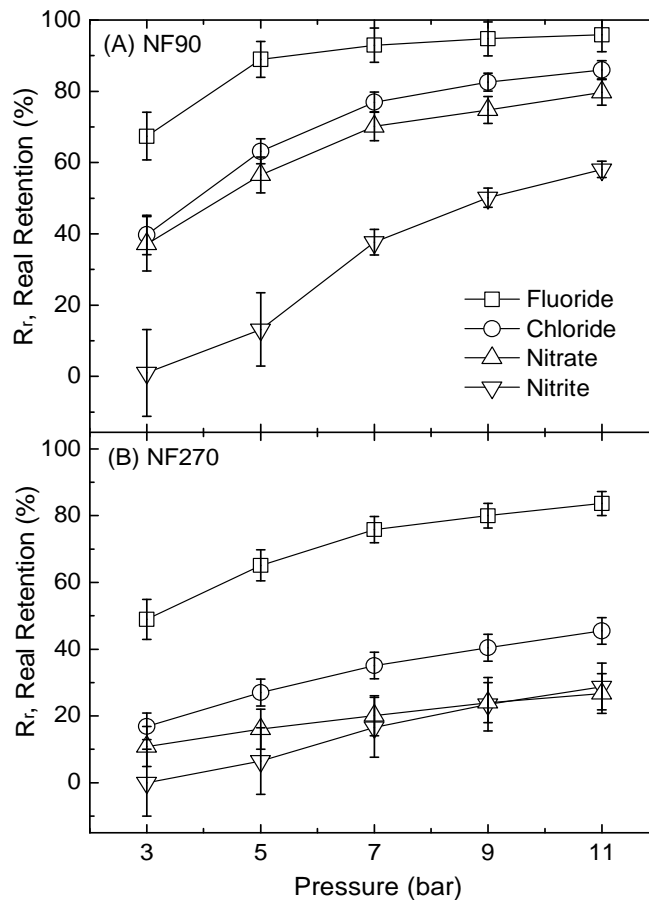

Figure 7-1. Retention corrected for concentration polarization at 25 °C for each anion (as sodium salt, 0.1M in MilliQ water) at pH 6.2 for (A) NF90 and (B) NF270 using crossflow filtration.

There are a number of potential explanations for this ordering that should be considered. The size of the *bare* ion does not explain why fluoride retention is highest, as fluoride is the smallest bare ion (see Table 7-1) yet retention is the highest. The size of the *hydrated* ion does not explain the ordering, as nitrite and nitrate have the largest hydrated radii but their retention is comparatively low. *Stokes* radius does not explain the selectivity either. Although fluoride has the highest Stokes radius and highest retention, chloride, nitrite and

nitrate have very similar Stokes radius and thus this parameter is unable to distinguish sufficiently. Diffusion coefficients also do not explain the selectivity, as chloride has the highest diffusion coefficient so retention would be expected to be lowest in the tightest membrane where diffusion is most important, but this was not observed. Note that Stokes radius and diffusion coefficients are the ion-specific inputs into the hydrodynamic model [164, 198], and neither of these adequately describes the observed behaviour. Simple charge exclusion does not explain the selectivity, because each ion has an equal net charge of -1, so this parameter cannot control selection (differences in charge density or where the charge is located on the ion will be ion-specific but net charge remains the same). Differences in Debye length are expected to be small because they will only be due to concentration/ionic strength in the boundary layer resulting from the different ionic permeabilities (*eg.* a 20% increase in concentration leads to a 9% decrease in Debye length). This shows that none of the well-accepted mechanisms is sufficient to describe this behaviour.

Ion dehydration will be considered as an alternate explanation. Dehydration, in this context, refers to the process in which an ion is forced to become partially or fully dehydrated in order to transport through the membrane. This could occur as a result of limited space availability (when the pore size is smaller or similar to that of the dissolved solute) and is due to forces on the ion driving it through the membrane (*eg.* pressure, concentration gradient, temperature, convection). If dehydration was occurring, retention and transport trends would correlate not with radius as defined either by fully hydration in bulk, nor the bare ion. Rather, the effective radius that controls transport would be somewhere in-between, according to the amount of dehydration required. Further, retention and transport trends would correlate to hydration strength (as is observed with fluoride). Thus, hydration free energies and energetic requirements for transport (*eg.* energy barriers) may be a better descriptor for transport than other mechanisms. In order to test this hypothesis, energy barriers must be quantified. The relationship between solute flux, temperature and pressure will be determined so that the Arrhenius methodology can be used to quantify barriers.

7.4 Solute Flux as a Function of Pressure, Temperature and Anion Type

In order to obtain energy barriers, first the impact of temperature and pressure on solute flux must be determined, as shown on Figure 7-2 for fluoride. Solute flux increases with pressure and temperature as expected.   Solute flux increases with pressure due to increased convective flow.   Solute flux increases with temperature due to increased diffusion and changes in nanostructure morphology [136, 183, 190, 320].   The same process was repeated for all ion types and both membranes (data shown for fluoride in both membranes). One condition was used (7 bar and 25 °C) to compare anions type, as shown on Figure 7-3.

Figure 7-3 shows that solute flux is inversely related to retention (and hence an ion with a low solute flux faces a large energy barrier). Solute flux depends on ion type. For NF90, the solute flux sequence is fluoride (0.3 ± 0.04 mol.h^{-1}.m^{-2}) < chloride (1.3 ± 0.1 mol.h^{-1}.m^{-2}) $\approx$ nitrate (1.2 ± 0.1 mol.h^{-1}.m^{-2}) < nitrite (2.6 ± 0.2 mol.h^{-1}.m^{-2}). For NF270, the sequence is fluoride (1.9 ± 0.15 mol.h^{-1}.m^{-2}) < chloride (2.8 ± 0.2 mol.h^{-1}.m^{-2}) < nitrate (7.7 ± 0.4 mol.h^{-1}.m^{-2}) < nitrite (13.2 ± 0.7 mol.h^{-1}.m^{-2}). Now that solute flux as a function of temperature, pressure, and ion type is known, energy barriers will be quantified according to the Arrhenius expression.
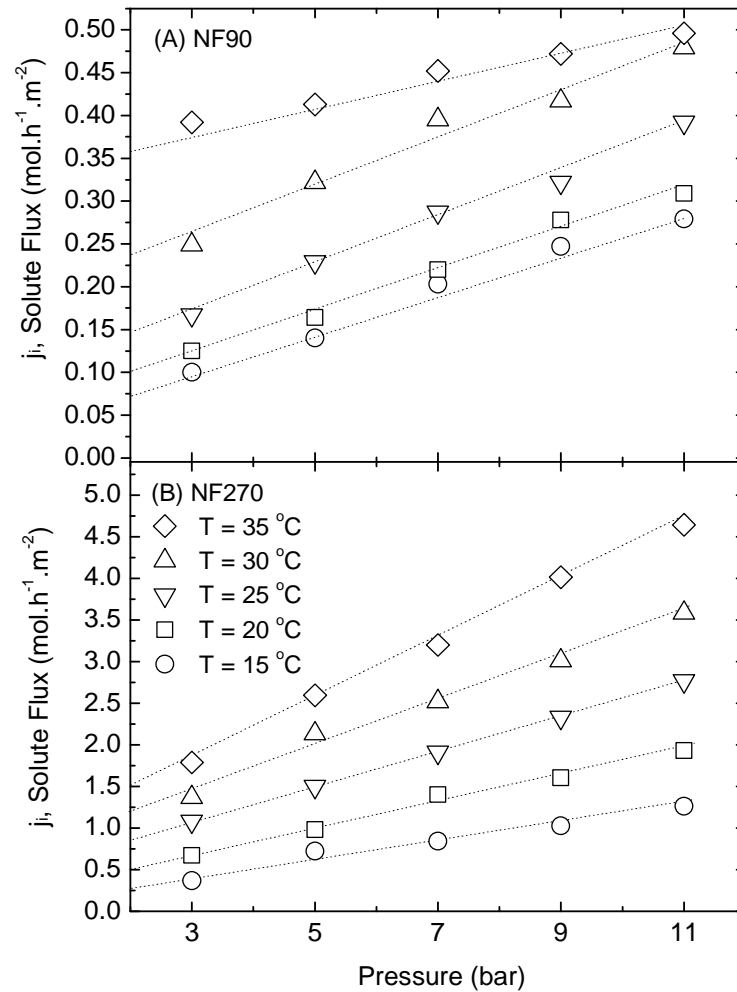
Figure 7-2. Solute flux versus applied pressure for fluoride (as sodium salt, 0.1 M in MilliQ water, pH 6.2) with (A) NF90 and (B) NF270 using crossflow filtration. Error bars have not been included for clarity but are shown on Figure 8-3 and estimated to be ± 0.04 mol.h^{-1}.m^{-2} and ± 0.15 mol.h^{-1}.m^{-2} for NF90 and NF270, respectively. Note that the scales are different for the membranes because of the different magnitude of solute fluxes.
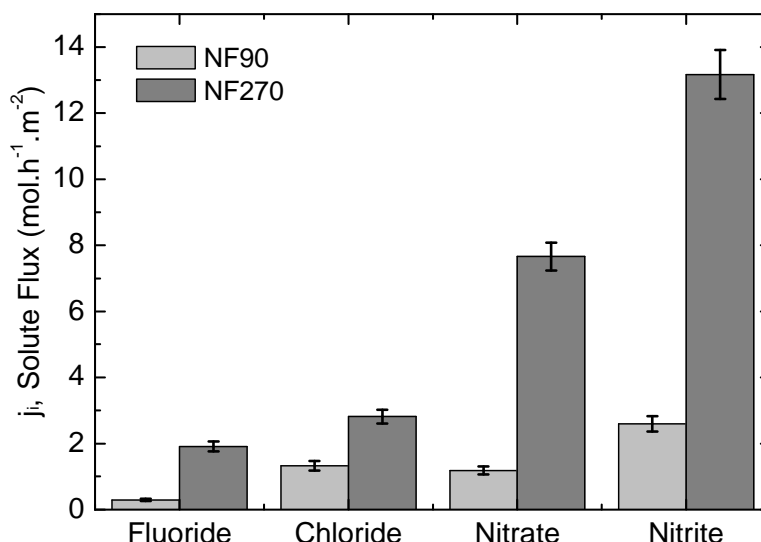
Figure 7-3. Solute flux of fluoride, chloride, nitrite and nitrate (as sodium salts, 0.1M in MilliQ water) at pH 6.2, 25°C and 7 bar.

7.5 *Quantifying Energy Barriers for the Transport of Monovalent Anions in NF*

In order to quantify energy barriers for anionic transport in NF, Arrhenius plots were created for each ion and both membranes (Figure 7-4). Energy barriers depend on ion type and membrane type as expected from retention and solute flux results. Fluoride (the most strongly hydrated ion) has the highest energy barrier, for both membranes, with the following trends. For NF90, the order of energy barriers is fluoride (17.0 ± 2.2 kcal.mol^{-1}) > chloride (9.6 ± 1.3 kcal.mol^{-1}) ≈ nitrate (10.2 ± 1.3 kcal.mol^{-1}) ≈ nitrite (11.0 ± 1.2 kcal.mol^{-1}). For NF270, the order is fluoride (14.3 ± 1.6 kcal.mol^{-1}) > nitrite (11.1 ± 0.9 kcal.mol^{-1}) > chloride (8.0 ± 0.6 kcal.mol^{-1}) ≈ nitrate (7.0 ± 0.6 kcal.mol^{-1}). Conceptually it makes sense that fluoride has the largest barrier because transport is the most hindered and thus fluoride has the lowest solute flux. Fluoride clearly has the highest barrier, which shows that energy barriers can explain the very high retention of fluoride compared to the other solutes, a trend that cannot be explained by other properties or parameters. Differences in the energy barriers between chloride, nitrate and nitrite cannot be adequately distinguished (outside of error), especially for NF90. The energy barriers obtained here are comparable to other barriers reported in the literature for the transport of sodium chloride and sodium nitrate across thin film composite membranes [136] and sodium chloride in various membranes (between 4.4 and 12 kcal.mol^{-1}) [118]. In ion

channels, the transport of chloride in a biological chloride channel was 4 to 4.5 $\pm$ 2 kcal.mol^{-1} [321] and 2 to 3 kcal.mol^{-1} for potassium in a KcsA potassium channel [322].

The energy barriers for the different membranes can be compared. Solute fluxes are smaller and energy barriers larger for NF90 (tighter membrane) than NF270 (looser). Higher water flux in NF270 leads to higher solute flux which leads to lower energy barriers when compared to NF90. Membrane characteristics such as pore size distributions, charge, porosity and surface roughness all may also contribute to the differences between NF90 and NF270. For example, the surface of NF90 is much rougher than NF270, NF90 has a higher thickness to porosity ratio than NF270, NF90 is more hydrophobic than NF270, the surface of NF90 is more negative than NF270 at neutral pH, and the chemical compositions and functional groups of the two membranes are different. Each of these characteristics will contribute to the net energy barriers determined and the specific effect of one membrane characteristic cannot be isolated.

Energy barriers represent the *overall* energetic expense of ion transport, including all membrane effects (pore size, material, surface charge, etc), all operating conditions (pressure, flow, concentration, solution chemistry, etc), all energetic contributions (entropic, enthalpic) and the specific solute. However because the barriers on Figure 7-4 were extrapolated to a "zero pressure" point, convection is not playing a role nor are differences in ion concentrations resulting from concentration polarization. These results suggest that energy barriers may be due to dehydration because the order of barriers is not consistent with other mechanisms such as size exclusion based on either bare ion radius or hydrated radius or simple charge repulsion (since all ions have same net charge and should see similar barriers). Further, the order of barriers is consistent with dehydration because (1) fluoride has the highest barrier for both membranes and (2) the tighter membrane (NF90) has higher barriers.
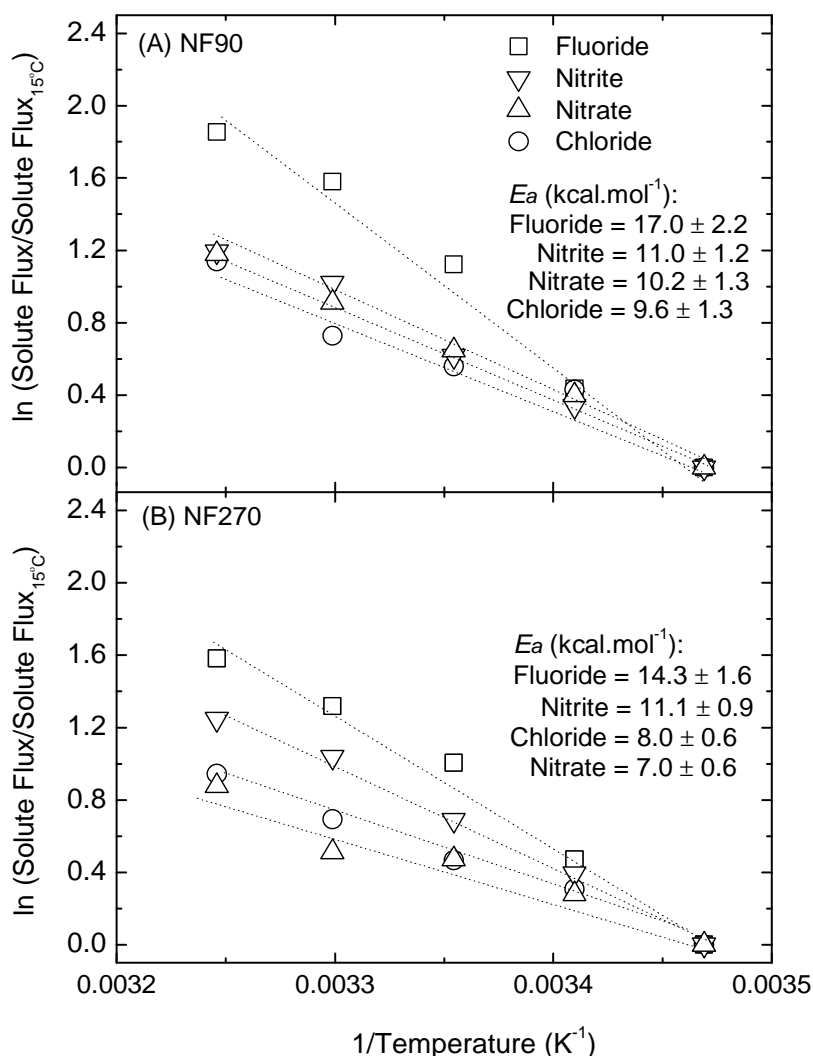
Figure 7-4. Arrhenius plots for anions (as sodium salt, 0.1M in MilliQ water) at pH 6.2 for (A) NF90 and (B) NF270 using crossflow filtration. Each plotted value is the extrapolated y-intercept of a plot of solute flux versus Δpressure (applied pressure – osmotic pressure) for temperatures 15, 20, 25, 30 and 35 °C. Energy barrier (E_a) is the slope of the Arrhenius plot. Error bars of each individual data point are not included for clarity but the propagated error for E_a is shown.

Next, energy barriers were quantified at each pressure (Figure 7-5), rather than from the extrapolated "zero pressure" point. Increasing pressure leads to increasing convection and increasing concentration polarization at the membrane surface. The energy barrier for fluoride decreases with pressure, which is especially notable for NF90. This suggests that pressure/convection/concentration polarization reduce the barriers. In face, at pressures > 5 bar, the dependence of energy barriers on ion type becomes non-distinguishable in NF90. If barriers are indeed due to dehydration, these results suggest

that operating conditions (*eg.* increasing pressure and concentration) make dehydration more likely for some ions (*eg.* fluoride) since the barriers are decreasing with these parameters. Pressure had a less influence on energy barrier for NF270 which is consistent with the fact that this is a more open membrane.
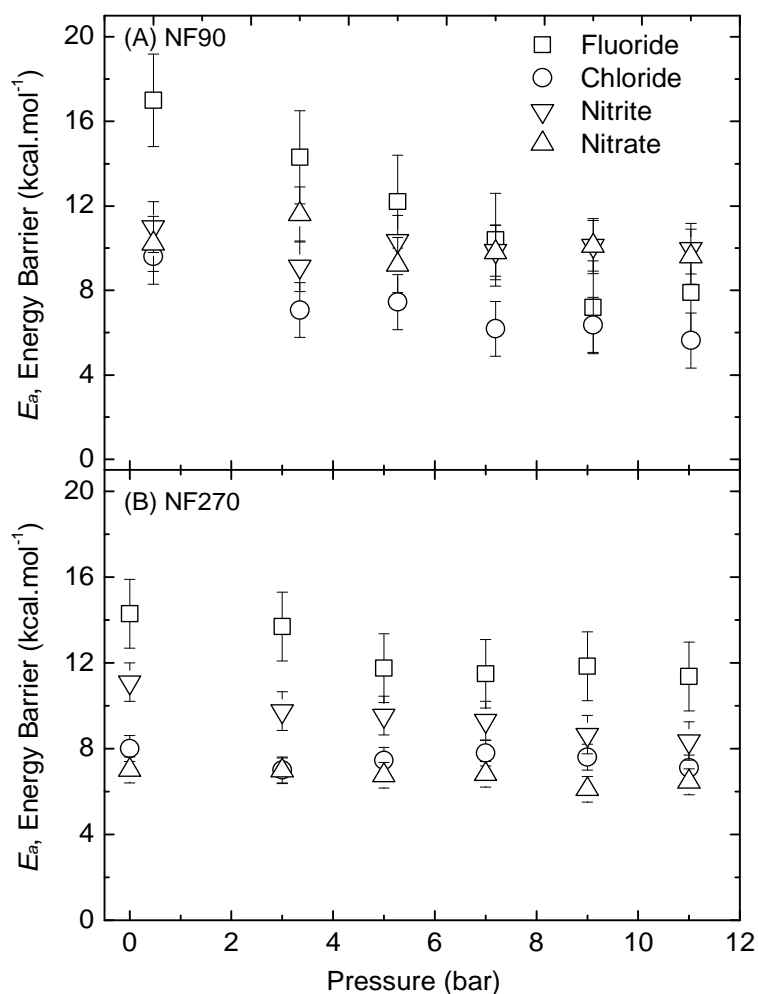
Figure 7-5. Energy barriers calculated directly at each pressure for (A) NF90 and (B) NF270 with 0.1M single sodium salt in MilliQ water at pH 6.2 and from temperature 15 to 30 °C.

The effect of temperature on membrane properties was then assessed (Figure 7-6) in order to understand how changing membrane properties with temperature may affect energy barriers. The effective pore radius and pure water flux increases for both membranes with temperature. Increase in pore size with temperature has been observed before and is attributed to changes in polymer structure [183] (*eg.* polymer expansion/swelling). The increase in pore size with temperature is inherently included in

the Arrhenius calculations because energy barrier is determined by temperature dependence. The increase in pore size with temperature results in the energy barriers quantified in Figure 7-4 and Figure 7-5 being slight over-estimates. Quantification of the impact of the increase in pore size with temperature on energy barriers is currently being examined and will be included in future publications of this work.

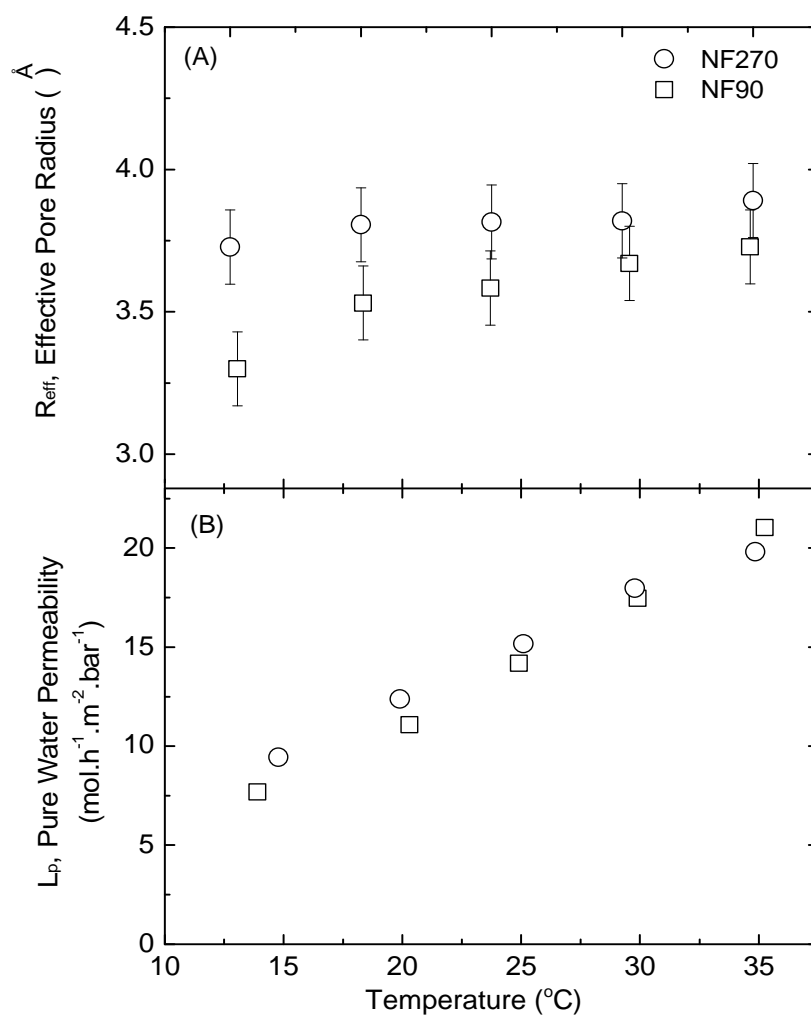**Figure 7-6. (A) Effective pore radius (R_{eff}) and (B) pure water permeability (L_p) for NF90 and NF270. Error on pore size was determined by the carrying out propagated errors through the calculation optimization procedure. Error bars on L_p are not included because they are small (approximately ± 2%), however variation in flux from different batches of the same membrane can be > 10 %.**

7.6   Comparison of Experimental Energy Barriers with MD

In order to interpret the energy barriers, the experimental energy barriers are compared to those obtained using molecular dynamic simulations. Energy barriers determined with MD simulations showed that dehydration was the dominant energetic cost of transport for these ions in an idealized, cylindrical pore [303]. Energy barriers from experiments are compared to MD simulations on Table 7-3.

Table 7-3. Comparison of energy barriers determined experimentally and with molecular dynamics simulations [303, 323]. Error for molecular dynamics results is estimated to be $\pm$ 0.6 kcal.mol^{-1}.

Effective Pore Radius (10^{-10} m)	Energy Barrier (kcal.mol^{-1})						
	Highest						**Lowest**
Membrane							
NF90 (3.4)	F$^-$ (17.0 $\pm$ 2.2)	>	Cl$^-$ (9.6 $\pm$ 1.3)	$\approx$	NO$_3^-$ (10.2 $\pm$ 1.3)	$\approx$	NO$_2^-$ (11.0 $\pm$ 1.2)
NF270 (3.8)	F$^-$ (14.3 $\pm$ 1.6)	>	NO$_2^-$ (11.1 $\pm$ 0.9)	>	Cl$^-$ (8.0 $\pm$ 0.6)	$\approx$	NO$_3^-$ (7.0 $\pm$ 0.6)
MD Simulation							
2.51	NO$_3^-$ (∞)	>	F$^-$ (57.1)	>	NO$_2^-$ (35.3)	>	Cl$^-$ (43.2)
2.81	F$^-$ (46.9)	>	NO$_3^-$ (40.0)	>	NO$_2^-$ (39.3)	>	Cl$^-$ (34.0)
3.06	F$^-$ (47.7)	>	Cl$^-$ (41.1)	>	NO$_3^-$ (32.5)	>	NO$_2^-$ (28.4)
3.32	F$^-$ (27.4)	>	Cl$^-$ (21.3)	>	NO$_2^-$ (11.1)	>	NO$_3^-$ (6.5)
3.52	F$^-$ (16.4)	>	Cl$^-$ (12.1)	>	NO$_2^-$ (5.7)	>	NO$_3^-$ (2.3)
3.72	F$^-$ (10.6)	>	Cl$^-$ (8.5)	>	NO$_2^-$ (4.0)	>	NO$_3^-$ (1.6)
4.02	F$^-$ (8.6)	>	Cl$^-$ (7.8)	>	NO$_2^-$ (2.2)	$\approx$	NO$_3^-$ (2.1)
4.33	Cl$^-$ (7.7)	>	F$^-$ (5.7)	>	NO$_2^-$ (3.0)	>	NO$_3^-$ (1.3)
4.72	F$^-$ (6.4)	>	Cl$^-$ (5.2)	>	NO$_2^-$ (1.0)	>	NO$_3^-$ (0.3)
5.32	F$^-$ (3.3)	$\approx$	Cl$^-$ (3.1)	>	NO$_2^-$ (0.7)	$\approx$	NO$_3^-$ (0.7)
6.53	F$^-$ (1.7)	$\approx$	Cl$^-$ (1.4)	>	NO$_2^-$ (0.4)	$\approx$	NO$_3^-$ (0.2)
MD Weighted Averages (based on log-normal distribution around experimentally determined effective pore radius)							
3.4, distribution	F$^-$ (24.6)	>	Cl$^-$ (19.8)	>	NO$_3^-$ (18.2)	>	NO$_2^-$ (13.7)
3.8, distribution	F$^-$ (16.1)	>	Cl$^-$ (13.4)	>	NO$_3^-$ (8.6)	>	NO$_2^-$ (7.9)

Experimentally-determined energy barriers are within a factor of four of barriers determined from MD simulations based on dehydration. For an effective pore radius of $3.32 \cdot 10^{-10}$ m (similar to NF90), the order of MD barriers was fluoride (27.4 kcal.mol^{-1}) > chloride (21.3 kcal.mol^{-1}) > nitrite (11.1 kcal.mol^{-1}) > nitrate (6.5 kcal.mol^{-1}). For an effective pore radius of $3.72 \cdot 10^{-10}$ m (similar to NF270), the order was fluoride (10.6 kcal kcal.mol^{-1}) > chloride (8.5 kcal.mol^{-1}) > nitrite (4.0 kcal.mol^{-1}) > nitrate (1.6 kcal.mol^{-1}). Ordering in MD models results from ion properties (ion size, hydrated size, and hydration strength) and is due to the requirements for partial dehydration when an ion is

transporting through the cylindrical pore. The changes in ion order with pore size is directly attributable to ion properties and the varying degrees of partial or full dehydration required for the ion to fit in the pore. When a weighted average is taken of MD results (assuming a log-normal pore size distribution), energy barriers are notably comparable to what was observed experimentally (difference of < 10 kcal.mol^{-1}, in the worst case) and ordering matches experimental retentions. This comparison further supports that experimental barriers may be attributed to dehydration.

There are a number of differences between MD simulations and a real membrane, which must be mentioned in order to put the comparison into context. Firstly, pore size distributions were not modelled. Pore size strongly affects dehydration requirements and the ordering of ions. When there are a fraction of pores of different sizes these will all contribute to the net energy barrier measured experimentally and thus it is not expected that values or trends would match up exactly to MD values from one pore size. In order to compensate for this, a weighted average of pore sizes over a distribution was taken and this is a more realistic representation of an actual membrane. Another difference is tortuousity, as simulations use a generic representation of an ideal cylindrical pore. However, the largest energy barriers would be expected to occur at the narrowest part of a tortuous pore/void. Charge and polarity were not considered in the MD results reported on Table 7-3, however negative surface charge would be expected to increase energy barriers with the main contribution remaining dehydration [303]. Functional groups are also not considered in the MD model. Functional groups will affect interactions as the ion nears the membrane surface and may be either attractive or repulsive (which could decrease or increase the energy barriers accordingly). Regardless of these constraints, experimentally determined energy barriers seem reasonable according to dehydration barriers.

7.7 Energy Barriers Determined using Diffusion Cells

In an initial attempt to compare energy barriers obtained with the crossflow system to energy barriers obtained in a system without the complications of flow and pressure, energy barriers were also determined using diffusion cells. These results are included in

Appendix B. The results from diffusion cells largely did not agree with those obtained using the crossflow system. In particular, the result that drew attention was the high energy barriers of nitrate and nitrite as compared to fluoride and chloride, which was not expected either from crossflow results nor MD simulations.

Upon consideration, and unfortunately not until all experiments had been completed, it was realized that the mechanisms of the processes in the diffusion cell and crossflow are fundamentally different, and cannot be meaningfully compared. In a diffusion cell, the diffusion of the ions across the *entire* membrane is measured and the membrane layers are essentially different resistors in series. In a crossflow system, diffusion primarily occurs in the active layer, and then the ions are flushed through the remainder of the membrane along with the convective flow of water. The active layer is extremely small compared to the entire membrane thickness. Even though the support layer is much more porous, the fact that it is so much thicker than the active layer leads to a substantial amount of diffusion required for a solute to transport across the whole membrane thickness (which does not occur in the presence of convective flow). Therefore, measuring diffusion across the entire membrane in diffusion experiments does not predict what is happening in the membrane active layer and cannot be compared with crossflow results. It has been well documented that diffusion experiments using the whole membrane are fundamentally inaccurate due to the overwhelming resistance of the support when compared to filtration experiments [150, 324, 325], which is a reason that diffusion cells have not been used much in recent years for gathering information on salt transport mechanisms in for commercial NF/RO membranes. It is recommended that diffusion cells not be used for determination of energy barriers or for direct comparison with results from any other type of filtration-based experiments.

A recent study by Bason *et al.* [150] has demonstrated that the thin active layer of the membrane can be separated from commercial membranes, and that transport characteristics of this isolated layer are similar to those of the intact active layer within the original composite membrane. Characterizing diffusion across the isolated active layer is much more realistic to the diffusion which occurs during filtration than diffusion experiments with the whole commercial membrane. However, there are still a number of

practical issues that need to be addressed (such as supporting a thin film in a diffusion cell and separating a sufficiently large sample size) before an isolated active layer could be used to measure diffusion as used in this chapter. The area of characterizing membrane active layers for transport properties can be expected to progress rapidly because of its clear relevance to understanding transport in real NF membranes.

7.8   Conclusions

In this chapter, it was demonstrated that high selectivity exists between monovalent anions in NF which is not adequately explained by bare ion radius, hydrated radius, Stokes radius, diffusion coefficients and charge. Energy barriers were determined in a crossflow system in an attempt to explain ion selectivity with regard to hydration properties of the ions and dehydration requirements of transport. Experimentally determined energy barriers depend on anion and membrane type. Fluoride, which has the highest hydration energy and smallest bare ion size, had the highest energy barrier of each anion studied for both membranes (17.0 ± 2.2 kcal.mol^{-1} and 14.3 ± 1.6 kcal.mol^{-1} for NF90 and NF270). Energy barriers for NF90 (smaller effective pore size of $3.4 \cdot 10^{-10}$ m) were larger than for NF270 (larger effective pore size of $3.8 \cdot 10^{-10}$ m), suggesting that transport is more hindered in the tighter membrane.

Energy barriers are partially attributed to dehydration because: (1) ordering of barriers for different ions is not consistent with other mechanisms such as size exclusion based on bare ion size (which would have largest ion with largest barrier), size exclusion based on hydrated ion size or simple charge repulsion (all ions have same charge and should see similar barrier); (2) ordering of ions is consistent with dehydration (fluoride having the highest barrier); (3) energy barriers determined by extrapolating the results to zero pressure meant that convection and concentration changes are not playing a role; and (4) the magnitude of barriers is consistent with MD simulations based on dehydration (Chapter 6). Limitations in the comparison between experiment and simulation such as pore size distributions, tortuousity, charge and functional groups were discussed. These results suggest that incorporating hydration effects into NF models would be beneficial for model development. The final chapter in this thesis (Chapter 8) summarizes the conclusions of this research project and discusses areas for future work.

Chapter 8

Conclusions and Future Outlook

The provision of safe drinking water is critical in an era in which the world's population is increasing rapidly but water supplies remain scarce. One way of addressing this problem is via the desalination of seawater or brackish water with NF/RO membranes. However, the mechanisms by which solutes are retained in NF/RO are not well-understood. Improvements in mechanistic understanding serve to provide membrane designers, chemists, engineers and modellers with information which may improve current technologies and optimize separation performance. The most important contribution of this research was the novel indication of ion dehydration occurring as a mechanism which controls transport in NF, and it is hoped that this work provides a basis for these effects to be incorporated into future membrane models and design considerations.

In this final chapter, a review of the aims and main conclusions of each of the main subject areas are discussed. As this research has been successful in answering some very interesting questions, it has also raised many more. As such, suggestions for future work conclude this thesis.

8.1 Conclusions

In summary, the overall aim of the work presented in this thesis was to improve the understanding of NF/RO, with the motivation that the technical knowledge obtained

could contribute to solutions addressing the world water crisis. The work had four primary sub-aims, and those were to examine: (1) the performance of renewable energy membrane systems; (2) the impact of pH on inorganic contaminant removal; (3) the importance of ion hydration in determining transport in a generic nanopore; and (4) the impact of ion and membrane type on energy barriers in NF. Specific objectives in these areas were met with a combination of experiments and MD simulations. A brief of the conclusions obtained in each of these areas follows.

In Chapter 4, the research objective was to determine how energy fluctuations and groundwater characteristics (in particular pH) affected the performance of a RE-membrane system tested during a previous field trial. During short-term experiments (lasting < 12 hours), the renewable energy membrane system reliably removed salts and inorganic contaminants, given sufficient solar availability, over a range of real energy and pH conditions via convection/diffusion and precipitation mechanisms. During a typical daily range of solar conditions, a number of solutes were well-retained ($\geq 85\%$) despite energy variation and subsequent changes in flow, pressure, flux, and specific energy consumption. Consequently, retention for solutes such as fluoride, magnesium, nitrate, potassium, sodium and total dissolved solids were impacted where convection/diffusion dominated retention. For very large hydrated solutes (calcium, strontium, and uranium), retention was very high due to size exclusion and no impact of operating conditions was observed. The retention of a number of solutes (arsenic, calcium, chloride, nitrate, potassium, selenium, sodium, strontium, and sulphate at Pine Hill) was pH-independent between pH 3 and 11. However, retention of other solutes (copper, magnesium, manganese, molybdenum, nickel, uranium, vanadium, and zinc at Pine Hill) varied as a function of pH, which sometimes led to deposition on the membrane surface and consequential flux decline. The pH-dependence of certain solutes is dependent on the groundwater type, exemplified by nitrate and magnesium demonstrating different behaviour with different groundwaters. During periods of severe energy fluctuations, the system shut off and retention dropped significantly to unacceptable levels. Flux decline and decreased performance during extreme fluctuations have practical implications on system lifetime which need to be thoroughly considered with longer term evaluations. Overall, these results demonstrate that, provided sufficient availability of an energy resource, photovoltaic driven membrane

systems may be a viable solution for remote water applications where contaminants that are difficult to remove by conventional technologies are a concern.

Having demonstrated the importance of pH in the removal of selected inorganic contaminants, a more detailed look at this specific effect was warranted in Chapter 5. The research objective of this chapter was to determine the relationship between speciation and retention for boron, fluoride, and nitrate using six different NF/RO membranes. Flux was independent of pH for all membranes except UTC-60, indicating that pH did not alter pore size and, hence, permeability and size exclusion characteristics of those membranes. Boron was the most difficult to remove and retention strongly depended on pH and speciation, which was suggestive of a dominant charge mechanism. Despite the speciation of nitrate being pH independent, retention varied widely depending on membrane type and suggested both charge and size mechanisms were occurring. Fluoride speciation and retention were pH dependent, with minimum retention occurring at low pH when HF dominates, which again suggested charge and size mechanisms. An interesting result was that the fluoride was more highly retained than nitrate using the same membrane above pH 7, which cannot be explained by the ionic size as fluoride is a smaller ion. This suggests the importance of hydrated size in determining transport, which was the subject of the remaining work presented in this thesis. Overall, this chapter demonstrated that pH is a key factor in determining retention of charged inorganic contaminants, which is directly related to solute and membrane properties, but that there may also be other important factors such as hydration.

The objective of Chapter 6 was to examine the hydration of monovalent anions (fluoride, chloride, nitrate, nitrite) as they transport through idealized, cylindrical pores using MD simulations. Three key conclusions can be drawn from this work. Firstly, energetic barriers were strongly dependent on pore size. Energy barriers were not linearly correlated with pore size; instead, there were distinct regimes related to the number of water molecules which much be stripped away from the ion in order for transport to occur (*eg.* water molecules with the first hydration shell are held much more tightly than outer, more distant water). Transport was strongly hindered when the size of the pore was smaller than the hydrated radius. Secondly, energy barriers depended on ion type (and hence hydration properties). The selectivity sequence amongst the ions

can change depending on the pore size and ion properties. In general, the transport of small, strongly hydrated ions (such as fluoride) was much more energetically expensive than for larger, less strongly hydrated ions (such as nitrate) due to the required dehydration unless the pore is larger than the size of the hydrated ion. Thirdly, and most importantly, these results showed that the required dehydration was the main barrier to ion transport in the narrow pores. In particular, partial dehydration was the main determinant of the energy barriers for small, strongly hydrated ions whose hydrated radius is larger than the pore size, even when charge repulsion is considered. This explains, for example, why fluoride is rejected by membranes with pore sizes greater than the ionic radius of fluoride. By providing a systematic and novel insight into the role of ion dehydration in pore transport, these results are significant in understanding anionic selectivity in biological channels as well as desalination and removal of various drinking water contaminants with NF.

As the theoretical evidence for dehydration occurring as a transport mechanism was demonstrated in Chapter 6, the research aim of Chapter 7 was to obtain experimental evidence of dehydration determining transport in a real NF membrane. This was achieved by determining energy barriers for different anions and membranes in order to link experimental measurements with MD outputs. Energy barriers depended on anion and membrane type. Fluoride, which has the highest hydration energy and smallest bare ion size, had the highest energy barrier of each anion studied for both membranes, and energy barriers for were higher for the tighter membrane. Energy barriers were reasonable (same order of magnitude and general trends) when compared with MD simulations, which corroborated the fact that energy barriers in NF may be due to dehydration. While a one-to-one comparison between real membrane systems and MD is challenging, the results here support conclusions obtained from the fundamental theoretical transport studies. These results demonstrate experimental evidence of the need to incorporate hydration effects into NF models.

8.2 Future Outlook

This work brought to light a number of interesting research topics that would benefit from being the subject of future investigation. To this end, the greatest potential for future work lies in the areas of MD for representation of NF membranes, experimental

work for evidence of the dehydration mechanism, improved NF characterization, and the testing and application of renewable energy membrane systems.

The work completed with MD in this research project was a valuable contribution and stands to be developed in a number of ways. Simplified channels were used in order to isolate the role of ion dehydration in pores of different sizes, but a number of variations could be evaluated in order to better consider the complexity of realistic membrane pores. This could involve designing and running MD simulations which could account for membrane parameters such as polarity, surface charge (on the surface and/or within the membrane pore) and functional groups. Applying the simulations to other contaminants (in particular boron) would be valuable, as would systematically increasing the concentration, which could potentially lead into insight about ion pairing during transport.

The task of demonstrating clear experimental evidence of NF mechanisms in real membranes remains challenging because of limitations in measurements, difficulty in isolating parameters and the heterogeneous nature of polymeric membrane materials. Improved characterization of the porous structure of the active layer of NF membranes would be very useful as it would allow information to be determined the layer which controls selectivity. In particular, more information about the structure (*eg.* discrete pores versus dense film) and chemical properties of this layer is very important. Recent work by Bason *et al.* [150] isolating and characterizing the selective active layer alone shows much promise in this area.

Further, the use of carbon nanotube membranes would be very valuable in the effort to understand mechanisms without the variation in membrane material inherent in polymeric membranes. However, at present suitable membranes of the desired characteristics are still largely in the developmental stages. As soon as feasible, understanding ion transport experimentally in structured membranes would be very valuable in explaining what happens in polymeric membranes, which, although more structurally heterogeneous, are much more widely developed and used.

Gaining clear evidence and understanding of new mechanisms, using the tools of simulation and experiment, gives exciting prospects to the future of desalination. For

example, if it is proven that dehydration is, in fact, a controlling parameter for ion selectivity in NF, future membrane models must take hydration into account. It may be possible, for example, to include energy barriers calculated in MD directly into the continuum transport models commonly used in describing NF. This could also have important implications in utilizing the different energy barriers in order to separate different types of ions, which is especially interesting from the perspective of removing contaminants other than sodium chloride in desalination.

The other main area which warrants future work is in renewable energy powered membrane systems. The integration of membrane technology with renewable energy allows water to be treated to a high standard even in remote locations with no electrical grid connection. This is an excellent solution to the synergetic water-energy problems facing many remote areas of the world. However, further work is necessary to best optimize these systems. In particular, the impact of variable operation on long-term system performance is unknown. This could have consequences for the lifetime of the membrane, and thus needs to be understood for both practical and economic reasons. A comparison of renewable energy membrane systems with traditional point-source treatment methods for a particular location(s) would also be valuable. In order to determine the feasibility of long-term operation of such a system in remote areas, this comparison would need to consider not only technical aspects, but also maintenance requirements, economics, and socio-cultural factors for a complete assessment.

These main areas for possible future work could be summarized by the following questions:

- What are the effects of different water chemistries (*eg.* concentration, pH) on ion hydration properties and thus on potential dehydration during transport through a pore? *(MD simulations)*
- What are the hydration properties of boron species (boric acid and borate, which are relevant in drinking water) and what happens to this hydration during transport through a pore? *(MD simulations)*

- What surface/pore characteristics (*eg.* surface charge, polarity, functional groups) have the largest influence on results and thus are most important in the comparison between MD and real NF membranes? *(MD simulations/NF)*

- How do energy barriers for the transport of anions through carbon nanotube membranes compare to results obtained with MD and NF membranes? (*experimental*)

- How does water composition (*eg.* mixes of feed contaminants or real groundwater) affect energy barriers for the transport of contaminants using NF membranes? *(experimental/field trial)*

- What is the impact of long-term operation on the efficiency and reliability of a RE-membrane system? *(field trial)*

In conclusion, this thesis has provided a thorough evaluation of four important and diverse areas related to the removal of inorganic contaminants with NF and RO. The results achieved provide novel insight into fundamental transport mechanisms and renewable energy powered membrane systems alike. It is hoped that this insight will provide a valuable stepping stone in the endeavour to improve the crisis surrounding the global need for safe drinking water.

Appendix A

Instrument Calibration

Appendix A includes example calibrations for analytical equipment used in this project: electrical conductivity (Figure A-1), fluoride ion selective electrode (ISE, Figure A-2), nutrient analyzer (Figure A-3), inductively-coupled plasma optical emission spectroscopy (ICP-OES) (Figure A-4), total organic carbon (Figure A-5), and ion chromatography (Figure A-6). Calibration curves were made or confirmed by testing a sample of known concentration prior to the analysis of any new set of samples, and test standards were run throughout any sample run (typically every ten samples). Particular ranges of calibrations were selected in order to be appropriate for the concentration range in samples. This means that for the nutrient analyzer or for ICP-OES, for example, samples would be diluted to ensure they were within the range of a linear calibration in order to obtain results without the influence of interferences. For these two instruments, high salt concentrations can interfere with the signal so it was necessary to dilute samples within an acceptable concentration range in order to obtain best instrument sensitivity. The ISE calibration was fit to a log-normal plot, as is standard methodology for this instrument, for a linear calibration.

Example calibrations are included because instrument calibrations can shift slightly depending on, for example, preparation of instrument solutions (*eg.* eluents, buffers), sample matrices (*eg.* pH, concentration of other ions), equipment condition (*eg.* time between cleaning/maintenance) and environmental factors (*eg.* room temperature), which had a larger effect for some instruments (such as the nutrient analyzer) more than others (such as the TOC). Measurements with instruments which required manuality

(such as the ISE) could very slightly vary according to the person taking the measurement due to differences in mixing techniques or amount of time before recording the sample, for example, so a calibration made by the same person who made the measurements was best to ensure consistency. Calibrations were always run on the day of analysis to ensure that the analysis made on that day had a valid calibration, and standards and solutions were made as fresh as possible. Further, analysis of sample standards was conducted frequently in order to monitor any changes of instrument performance over time. Despite all of these things which can influence calibrations, variations remained small if the solutions were made properly and the instrument was working properly. Checking of calibrations was done for quality control.
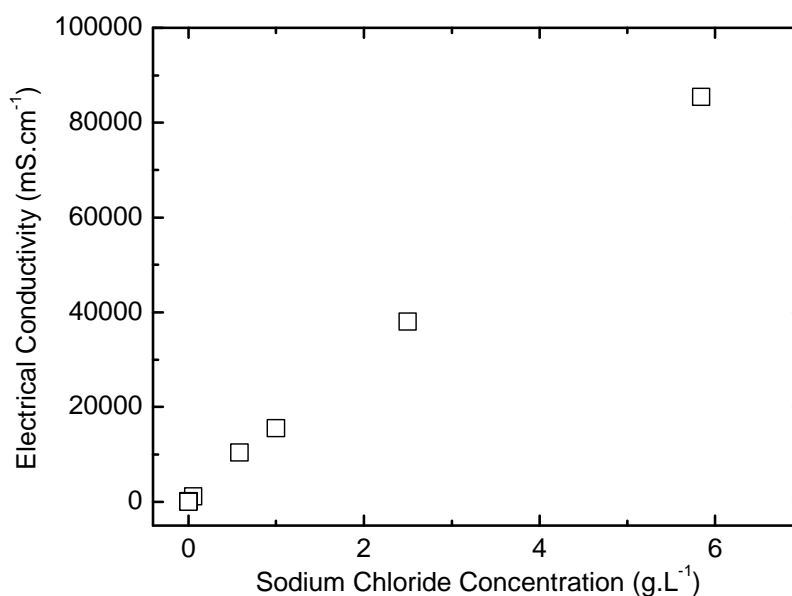

Figure A-1. Electrical conductivity (mS.cm^{-1}) versus sodium chloride concentration (g.L^{-1}) (pH 6.2). Uncertainty in the measurement of multiple samples ($n = 7$) is ± 1%.
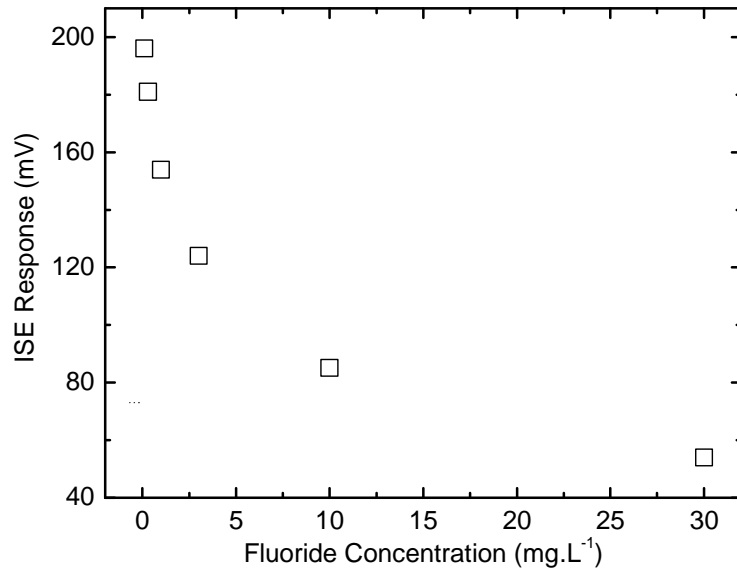
Figure A-2. Ion selective electrode response (mV) versus fluoride concentration (mg.L^{-1}) (pH 7). Uncertainty in the measurement of multiple samples (n = 7) is ± 2%.
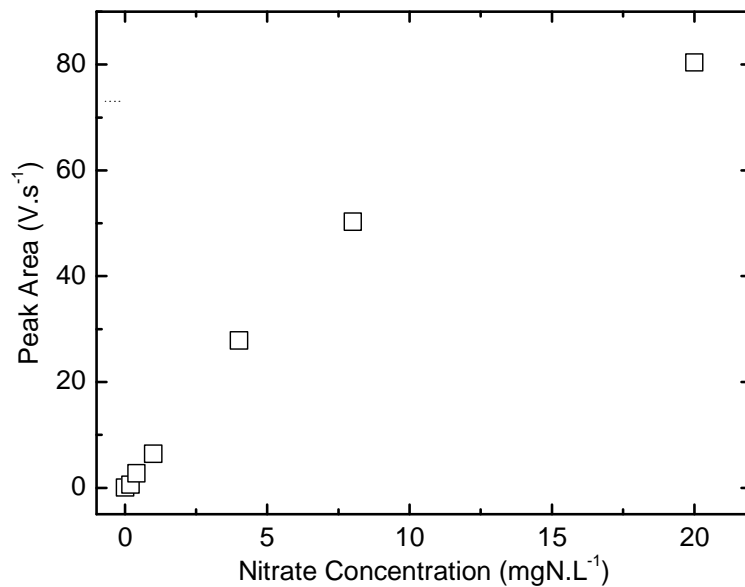

Figure A-3. Nutrient analyzer calibration for nitrate showing peak area (V.s^{-1}) versus nitrate concentration (mg.L^{-1} as N) (pH 7). Uncertainty in the measurement of multiple samples (n = 7) is ± 3%.
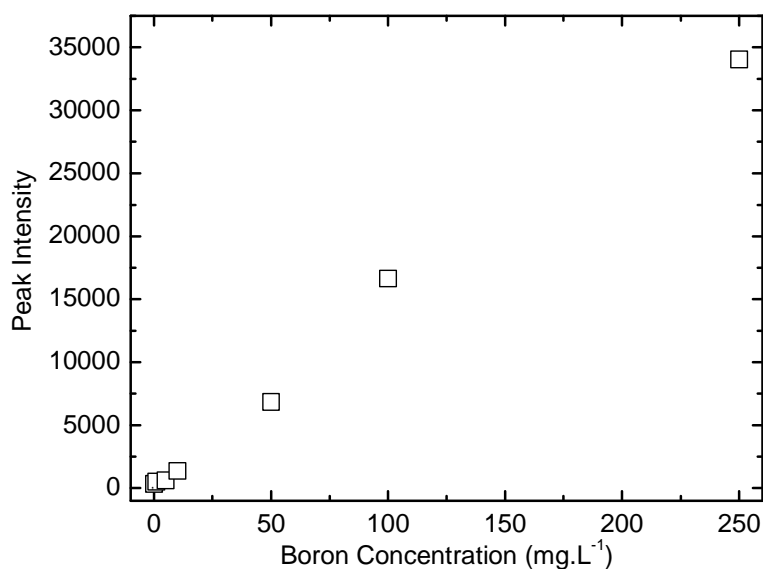
216

Figure A-4. Example ICP-OES calibration for boron showing peak intensity versus boron concentration (mg.L^{-1}) (pH 7). Uncertainty in the measurement of multiple samples (n = 7) is ± 1%.
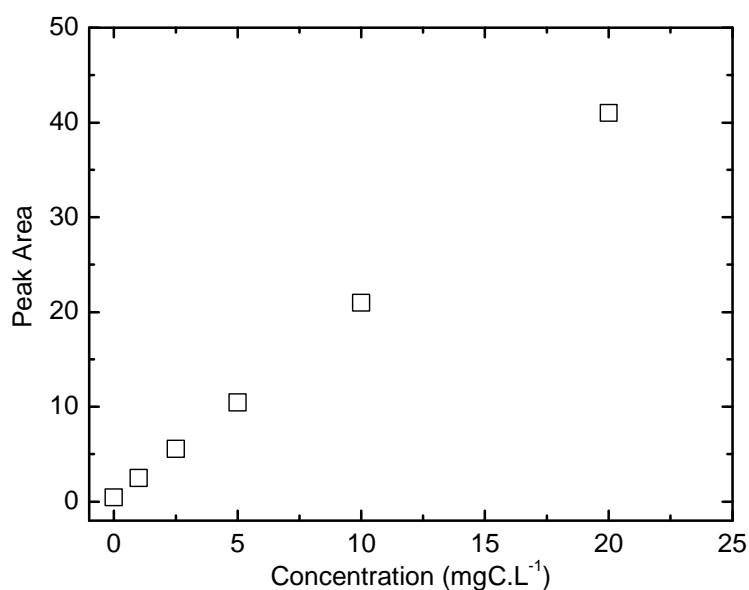

Figure A-5. Example total organic carbon calibration for potassium hydrogen phthalate (PHP) standards showing peak area versus total carbon concentration (mg.L^{-1}) (pH 7). Uncertainty in the measurement of multiple samples (n = 7) is ± 2%.
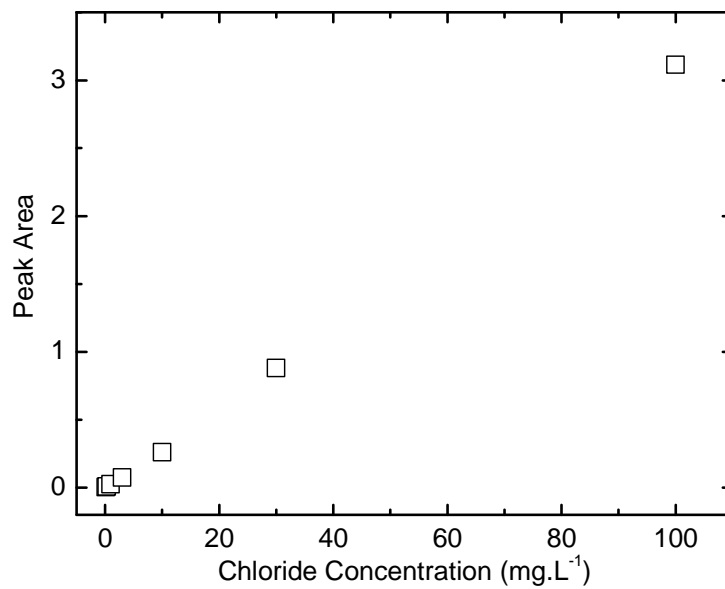
Figure A-6. Example chloride calibration for the ion chromatograph. Uncertainty in the measurement of multiple samples ($n = 7$) is $\pm$ 1%.

218

Appendix B

Energy Barriers and Diffusion Coefficients Determined with Diffusion Cells

B.1   Introduction and Objectives

The purpose of using the diffusion cells was to (1) experimentally determine energy barriers to different ion and membrane types and (2) determine diffusion coefficients. At the time of planning, the objective of these experiments was to determine energy barriers without the complicating effects of pressure and flow (inherent in crossflow filtration) in order to provide complementary information to energy barriers determined with the crossflow system. In hindsight, energy barriers obtained with the diffusion cells only serve to represent the specific conditions of diffusion cells, and cannot be meaningfully compared to the crossflow system due to the presense of flow which changes the mechanisms controlling transport. For the sake of completeness, all diffusion cell results are reported here, but it is important to emphasize that these results cannot be meaningfully compared to the crossflow energy barriers presented in Chapter 7.

B.2   Experimental Summary

The diffusion cells were described in Chapter 3.1.3. A single salt (NaF, NaCl, $NaNO_3$, $NaNO_2$, KF, KCl, KNO_3, KNO_2) at a concentration of 0.1 M was placed in the concentrated cell and ultrapure water in the diluted cell. No pH adjustment was made with the exception of one experiment (Section B.3.2). The cells were clamped together and placed in water bath with temperatures of 15, 20, 25, 30, 35 °C. For each temperature and salt, experiments were run for three hours. Samples were collected

from both the concentrated and dilute cells at 60, 90, 120, 150 and 180 minutes. Ion analysis was done with ion chromatography (Chapter 3.4.8) for anions and inductively coupled plasma optical emission spectroscopy (Chapter 3.4.4) for cations. The energy barriers were determined by the slope of the Arrhenius plot of the natural log of solute flux as a function of inverse temperature. Diffusion coefficients across the membrane were also calculated. Diffusion cell experiments were conducted with commercially available NF membranes UTC80A, BW30, NF90, TFC-SR3, NF270 and TFC-SR2 (characteristics in Chapter 3.2).

B.3 Energy Barriers in Diffusion Cells

Energy barriers were determined in diffusion cells to compare to results obtained with the crossflow system. Since there is no flow or pressure in diffusion cells, the concentration gradient across the cells is the driving force for diffusion. The diffusion of salt from the concentrated to dilute cell was measured at different temperatures in order to calculate an Arrhenius energy barrier to the transport. The rate of diffusion is higher at higher temperatures. Figure B-1 shows the Arrhenius plots for NF270 obtained with diffusion cells, and Figure B-2 shows the energy barriers obtained for NF270 and NF90 for each sodium salt tested.
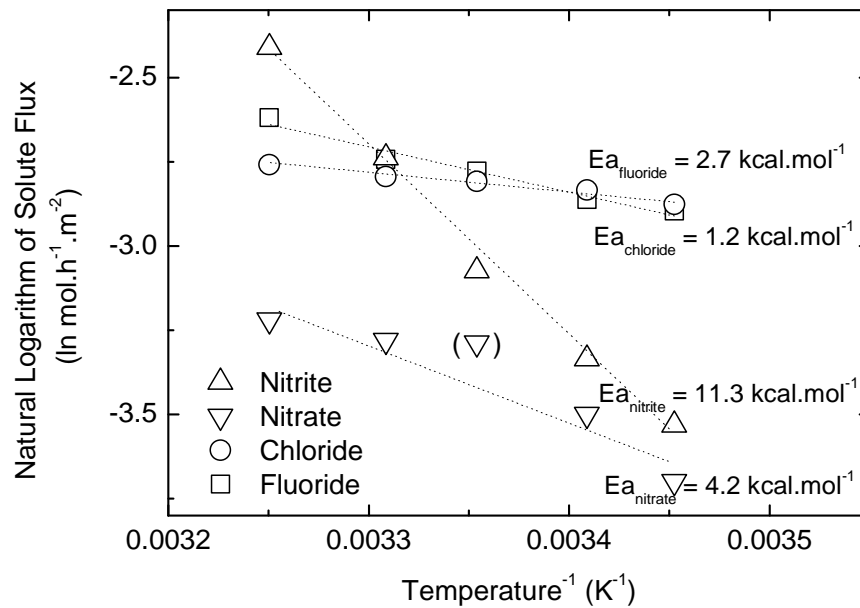

Figure B-1. Arrhenius plots for anions (as sodium salt) for NF270 using diffusion cell methodology.
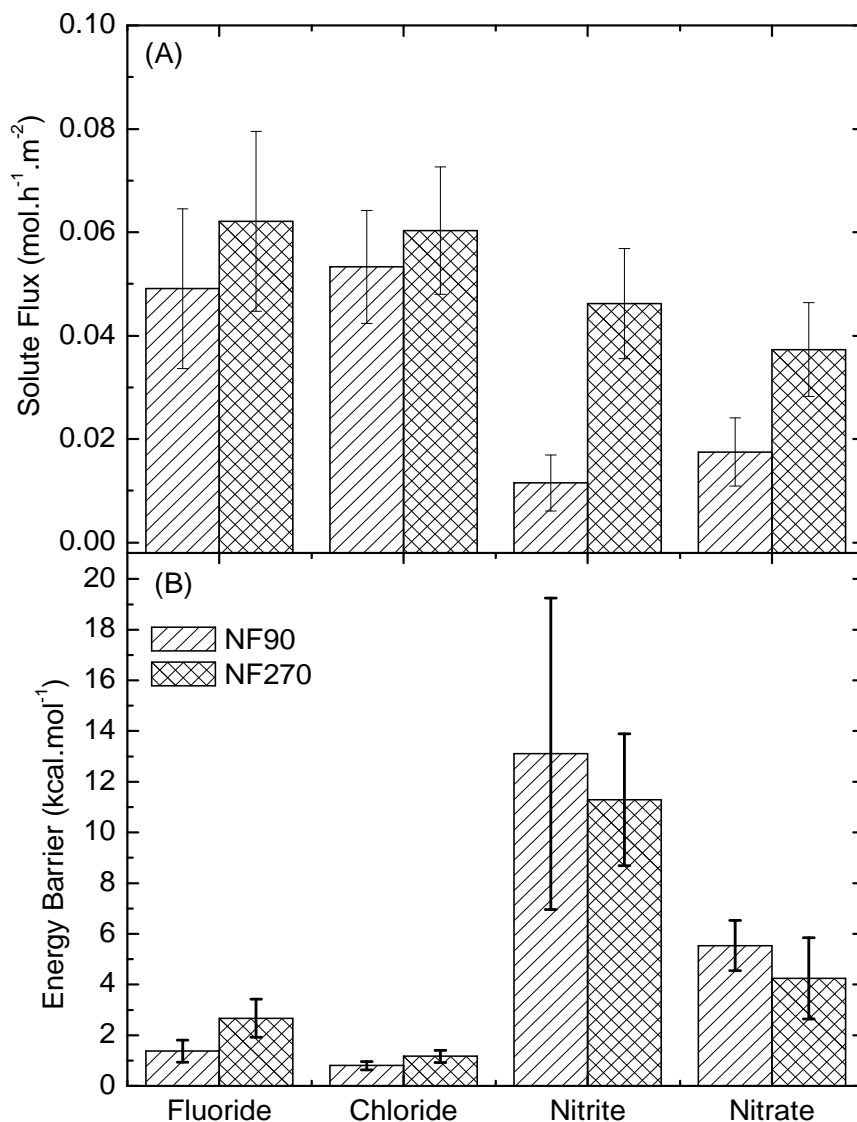
Figure B-2. Solute flux (A) at 25°C and 3 hours of diffusion time and energy barriers (B) for sodium fluoride, chloride, nitrite and nitrate using NF90 and NF270 and the diffusion cell Arrhenius methodology.

These results show that the smaller ions, fluoride and chloride, have higher solute fluxes and lower energy barriers than nitrate and nitrite. This is not explained by the dehydration theory, as molecular modelling predicts that energy barriers for fluoride and chloride are much higher than nitrate and nitrite due to the strong hydration of fluoride and chloride [303]. Fluoride and chloride barriers with NF270 are higher than NF90, which is not expected because NF270 has a larger effective pore size. However, this trend swaps with nitrate and nitrite which have higher barriers with NF90 than NF270, as expected. Mass balance calculations did not suggest any absorption observed within the error of analysis in the three hours of diffusion time. The results here are very different to the results obtained with the crossflow system, despite the dominant effect

221

of diffusion predicted for crossflow experiments using Extended Nernst Planck. This can be explained because the determination of energy barriers using diffusion cells is mechanistically different than when determined with the crossflow system, and these differences are specifically were discussed in Chapter 7.7.

B.3.1 Effect of Membrane Type on Energy Barriers of Fluoride

The energy barriers for fluoride transporting through a number of membranes with different properties were determined. The objective was to compare energy barriers with effective pore sizes. Because it was desired to use to full spectrum of NF pore sizes, two membranes were used for these experiments (TFC-SR3 and TFC-SR2) which were not used anywhere else in this thesis in order to have more characterized pore sizes at the higher end of the spectrum. Figure B-3 shows the results obtained for each membrane. There is no clear trend of fluoride energy barriers and characterized pore size of each membrane, as the method is not suitable in diffusion cells. There are other differences between the membranes that would affect these results, namely the total membrane thickness (which is the total distance the ions must diffuse through) and pore size distributions. However, the active layer thickness alone is also not sufficient to explain results, as exemplified by the fact that the active layer thickness of NF270 ($350 \cdot 10^{-10}$ m) is smaller than that of NF90 ($1740 \cdot 10^{-10}$ m) but the barrier is larger. Pore size distributions [132, 326] may become important if one membrane had a small fraction of large pore sizes, despite a low characterized average pore size, and vice versa. In the first scenario, the fluoride ion would easily transport through the larger pore, which could skew results to have a lower energy barrier than expected from the average pore size alone. With the tightest membrane UTC-80A, no fluoride was detected in the purified water cell after the 3 hours of diffusion cell. These results show that there is no clear trend of the energy barriers with pore size or active layer thickness. Rather energy barriers will be determined by the net membrane properties including a combination of pore size, porosity, material and thickness.
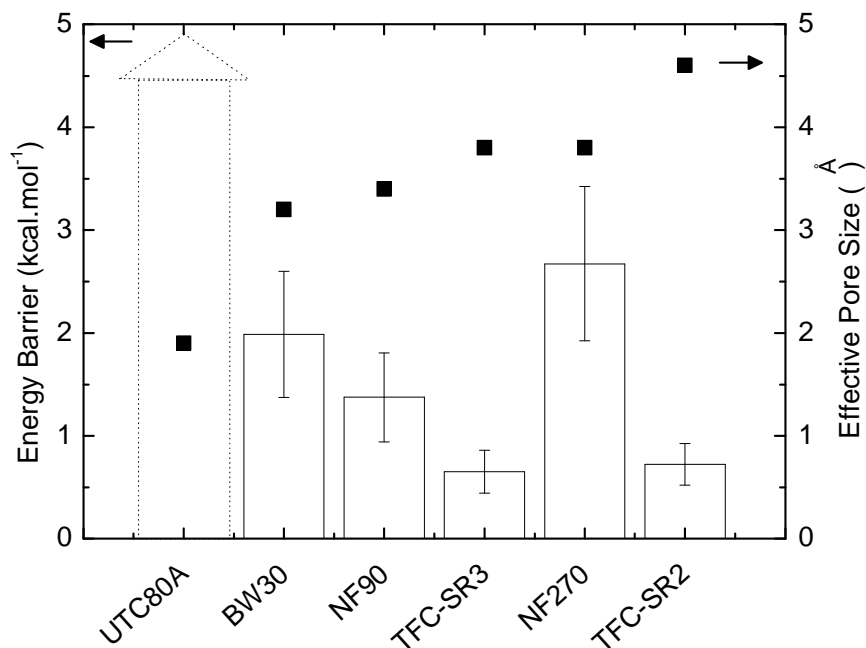
Figure B-3. Energy barriers for sodium fluoride as a function of membrane type (effective pore size on right-hand y-axis) using diffusion cell Arrhenius methodology. No fluoride was detected in the permeate cell for UTC80A, suggesting the energy barrier is very high for fluoride in this very tight membrane (represented by the dotted line).

B.3.2 Effect of pH on Energy Barriers of Fluoride

The effect of pH on the energy barrier of fluoride was tested for NF90 and NF270 at neutral pH (6.2) and very high pH (12.5) where the membranes are highly negatively charged (see Chapter 3.2.4). The results are shown in Figure B-4. This shows that the energy barrier is increased for both membranes at high pH. This is due to the increased charge repulsion from the highly negative membrane surface and anion at high pH. If the values are compared, this shows that charge repulsion contributes approximately 11% and 27% to the overall energy barrier of fluoride transport for NF90 and NF270 respectively, which was similar to modelled results of fluoride transporting through a simplified pore (*eg.* 14% and 19% for a single smooth pore of radius 3.3 and $4.3 \cdot 10^{-10}$ m, respectively) (Chapter 6.8) [303]. However, the pH cannot directly be correlated to the contribution of charge repulsion, as the adjustment of pH affects transport in a number of ways in addition to making the surface charge highly negative. It also means that there are additional sodium hydroxide ions present in the solution (more ions leads to higher ionic strength and more prominent electric fields in solution), an excess of sodium, and possible change in pore size at high pH.
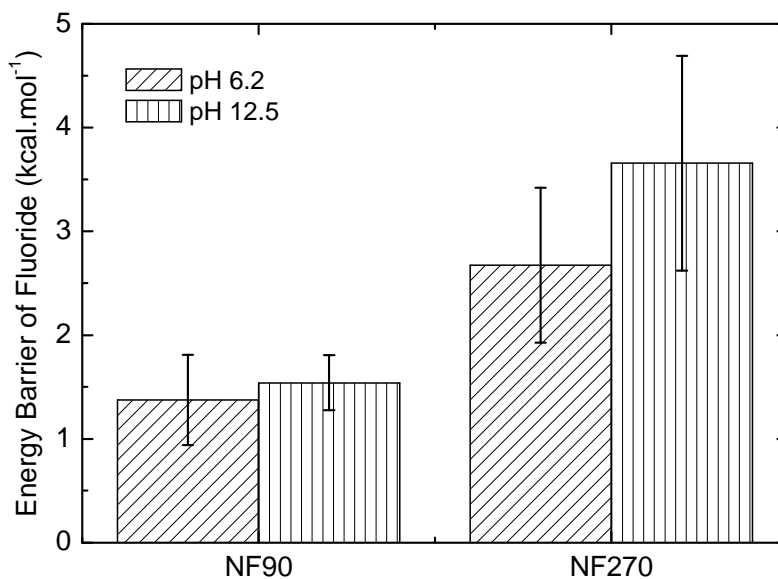
Figure B-4. Energy barriers for fluoride (as sodium fluoride) at neutral and high pH (12.5) where the membrane is highly negatively charged for NF90 and NF270 using the diffusion cell Arrhenius methodology.

B.3.3 Effect of Cation Type on the Energy Barriers of Anions

Selected experiments were repeated using potassium as the cation rather than sodium. The objective was to see if ion pairing or ion pumping played a role in the transport, and thus the cation type was changed in order to see if there was a measurable difference on the transport of the anion. Ion pairing is more likely for potassium than sodium, due to the relatively weak hydration of potassium [86], and is particularly likely for potassium nitrate [76].

Changing the cation does not make a measurable difference for strongly hydrated and small ions fluoride and chloride. However, changing the cation does make a significant difference for nitrate and nitrate. The energy barrier is lower with potassium rather than sodium for these anions. Nitrite and nitrate are more weakly hydrated and pairing between potassium and nitrate or nitrite is much more like than with sodium. If the ions were paired, the new entity would be neutrally charged and thus it could be expected that energy barriers would decrease due to negligible charge effects. However, a much more thorough study would be necessary to validate this hypothesis.
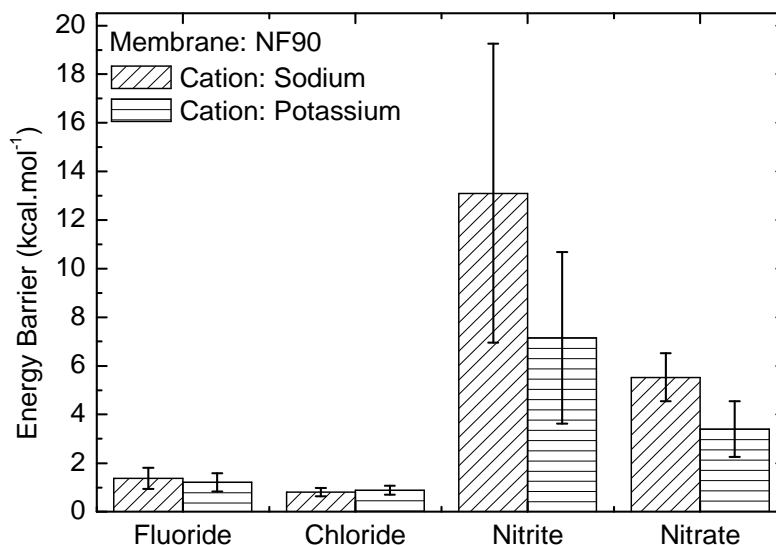
Figure B-5. **Comparison of energy barriers of each of the anions (fluoride, chloride, nitrite and nitrate) with different cations (sodium and potassium) for NF90 using diffusion cell Arrhenius methodology.**

B.4 Determination of Diffusion Coefficients

The data obtained in the energy barrier experiments with diffusion cells was also used to estimate diffusion coefficients for the various salts across NF90 and NF270. The results are shown in Table B-1. Diffusion coefficients are dependent on anion, cation, membrane and temperature. The diffusion coefficients obtained are one to three orders of magnitude slower than in bulk water (typically 10^{-9} $m^2.s^{-1}$ in bulk water), which demonstrates the hindered nature of membrane transport. The error in these results is approximately 10%, which makes any significant changes between ions in one membrane difficult to decipher. The error was estimated by taking the maximum uncertainty in solute flux measurements and re-calculating the diffusion coefficients with the largest expected errors in input parameters to determine the variation in the output (Chapter 3.5.2). Unfortunately, the error in the results makes it difficult to analyze the data meaningfully, and the results obtained also are not relevant to the crossflow results, for reasons which are discussed in Section B.4. Therefore, these diffusion coefficients have little useful significance. When diffusion coefficients are calculated using hindered transport theory, as is used in extended Nernst Planck, the values for hindered diffusion ($D_{i,p}$) in NF90 for sodium fluoride, sodium chloride, sodium nitrite and sodium nitrate are $2.45 \cdot 10^{-10}$ $m^2.s^{-1}$, $8.06 \cdot 10^{-10}$ $m^2.s^{-1}$, $5.75 \cdot 10^{-10}$ $m^2.s^{-1}$ and $5.72 \cdot 10^{-10}$ $m^2.s^{-1}$, respectively. These calculated values of $D_{i,p}$, which estimate

diffusion only in the active layer based on a ratio of pore to Stokes radius and bulk diffusivity, are a better representation of diffusivity in a membrane than diffusion cell measurements of diffusivity across the whole membrane. $D_{i,p}$ is what is used for inputs in diffusion and hydrodynamic models [198].

Table B-1. Experimentally determined diffusion coefficients of anions in NF membranes after three hours. Error in diffusion coefficient is estimated at 10%.

Anion	Cation	Membrane	Diffusion Coefficient of Anion at 25 °C ($m^2 \cdot s^{-1}$)
Fluoride	Sodium	NF90	$3.29 \cdot 10^{-12}$
		NF270	$2.33 \cdot 10^{-11}$
		NF90, pH 12.5	$3.02 \cdot 10^{-12}$
		NF270, pH 12.5	$2.25 \cdot 10^{-11}$
	Potassium	NF90	$3.43 \cdot 10^{-12}$
		NF270	$2.70 \cdot 10^{-11}$
Chloride	Sodium	NF90	$3.57 \cdot 10^{-12}$
		NF270	$2.26 \cdot 10^{-11}$
	Potassium	NF90	$3.91 \cdot 10^{-12}$
		NF270	$2.67 \cdot 10^{-11}$
Nitrite	Sodium	NF90	$7.72 \cdot 10^{-13}$
		NF270	$1.73 \cdot 10^{-11}$
	Potassium	NF90	$7.31 \cdot 10^{-13}$
		NF270	$1.26 \cdot 10^{-11}$
Nitrate	Sodium	NF90	$1.14 \cdot 10^{-12}$
		NF270	$1.31 \cdot 10^{-11}$
	Potassium	NF90	$1.23 \cdot 10^{-12}$
		NF270	$1.43 \cdot 10^{-11}$

B.5   Conclusions

The diffusion cell experiments were originally conducted in order to compare energy barriers in a system without flow and pressure. However, this method was not suitable for comparison due to fundamental mechanistic differences, which were discussed in 7.7 and a result of diffusion occurring across the entire membrane thickness in diffusion cells [150, 324, 325].   It is recommended that diffusion cells not be used for determination of energy barriers or for direct comparison with results from any other type of experimental system, unless the active layer can be isolated and characterized individually which may be possible with new methods in the future [150].

References

[1] T.P. Soubbotina, Beyond Economic Growth: An Introduction to Sustainable Development, Washington DC, 2004.

[2] World Bank, Population Growth Rate, Department Education Program, (2001) http://www.worldbank.org/depweb/, (accessed Nov 2011).

[3] United Nations, GLAAS Report, UN-Water Global Annual Assessment of Sanitation and Drinking Water, (2010) http://www.unwater.org/downloads/UN-Water_GLAAS_2010_Report.pdf, (accessed Nov 2011).

[4] United Nations, The Millennium Development Goals Report New York, (2006) http://unstats.un.org/unsd/mdg/resources/static/products/progress2006/mdgreport2006.pdf, (accessed Nov 2011).

[5] J. Bartram, K. Lewis, R. Lenton, A. Wright, Focusing on improved water and sanitation for health, Lancet, (2005).

[6] R.F. Service, Desalination Freshens Up, Science, 313 (2006) 1088.

[7] M.A. Montgomery, M. Elimelech, Water and sanitation in developing countries: Including health in the equation, Environmental Science & Technology, 41 (2007) 17 - 24.

[8] C.J. Vörösmarty, P.B. McIntyre, M.O. Gessner, D. Dudgeon, A. Prusevich, P. Green, S. Gliden, S.E. Bunn, C.A. Sullivan, C.R. Liermann, P.M. Davies, Global threats to human water security and river biodiversity, Nature, 467 (2010) 555.

[9] International Water Management Institute, Insights from the Comprehensive Assessment of Water Management in Agriculture, Stockholm 2006.

[10] United Nations - Water, International Decade for Action: Water for Life (2005 - 2015), (2006) http://www.un.org/waterforlifedecade/, (accessed Nov 2011).

[11] World Health Organization, Guidelines for Drinking-water Quality: Third Edition Incorporating the First and Second Addenda, Geneva, (2008) http://www.who.int/water_sanitation_health/dwq/gdwq3rev/en/, (accessed Nov 2011).

[12] M.D. Sobsey, Managing Water in the Home: Accelerated Health Gains from Improved Water Supply, World Health Organization, Geneva, (2002) http://www.who.int/water_sanitation_health/dwq/wsh0207/en/, (accessed Nov 2011).

[13] A. Niez, Comparative study on rural electrification policies in emerging economies, International Energy Agency, 2010.

[14] S.J. Kenway, P.A. Lant, A. Priestley, P. Daniels, The connection between water and energy in cities: a review, Water Science & Technology, 63.9 (2011) 1983 - 1990.

[15] M. Elimelech, W.A. Phillip, The future of seawater desalination: energy, technology, and the environment, Science, 333 (2011).

[16] M.A. Shannon, P.W. Bohn, M. Elimelech, J.G. Georgiadis, B.J. Mariñas, A.M. Mayes, Science and technology for water purification in the coming decades, Nature, 452 (2008).

[17] A.M. MacDonald, R.C. Calow, Developing groundwater for secure rural water supplies in Africa, Desalination, 248 (2009) 546 - 556.

[18] I.A. Shiklomanov, J.C. Rodda, World water resources at the beginning of the twenty-first century, Cambridge University Press, 2003.

[19] E. Stewart, How to Select the Proper Human-Powered Pump for Potable Water, Michigan Technological University, 2003.

[20] R.C. Calow, N.S. Robins, A.M. MacDonald, D.M.J. MacDonald, B.R. Gibbs, W.R.G. Orpen, P. Mtembezeka, A.J. Andrews, S.O. Appiah, Groundwater management in drought-prone areas of Africa, Water Resources Development, 13 (1997) 241 - 161.

[21] T. Shah, D. Molden, R. Sakthivadivel, D. Seckler, The Global Groundwater Situation: Overview of Opportunities and Challenges, International Water Management Institute, 2000.

[22] T.R. Green, M. Taniguchi, H. Kooi, J.J. Gurdak, D.M. Allen, K.M. Hiscock, H. Treidel, A. Aureli, Beneath the surface of global change: impacts of climate change on groundwater, Journal of Hydrology, 405 (2011) 532 - 560.

[23] D. Langmuir, Aqueous Environmental Geochemistry, Upper Saddle River, 1997.

[24] National Health and Medical Research Council, Australian Drinking Water Guidelines, NHMRC National Water Quality Management Strategy (Ed.), Canberra 2004.

[25] United States Environmental Protection Agency, National Primary Drinking Water Regulations, United States Environmental Protection Agency (Ed.), 2003.

[26] A. Figoli, A. Cassano, A. Criscuoli, M. Salatul Islam Mozumder, M. Tamez Uddin, M. Akhtarul Islam, E. Drioli, Influence of operating parameters on the arsenic removal by nanofiltration, Water Research, 44 (2010) 97 - 104.

[27] M. Bissen, Arsenic - a Review. Part I: Occurrence, Toxicity, Speciation, Mobility, Acta Hydrochimica et Hydrobiologica, 31 (2003) 9-18.

[28] P.L. Smedley, Arsenic in Rural Groundwater in Ghana, Journal of African Earth Science, 22 (1996) 459-470.

[29] P.L. Smedley, D.G. Kinniburgh, A review of the source, behaviour and distribution of arsenic in natural waters, Applied Geochemistry, 17 (2002) 517-568.

[30] K. Ahmad, S.B. Dampare, D. Adomako, N.N. Opata, R.E. Quagraine, The use of neutrol activation analysis in gold prospecting in small-scale mining in Ghana, Journal of Radioanalytical and Nuclear Chemistry, 260 (2004) 653-658.

[31] World Health Organization, Boron in drinking-water: Background document for development of WHO Guidelines for Drinking-water Quality, Geneva 2009.

[32] J. Fawell, K. Bailey, J. Chilton, E. Dahi, L. Fewtrell, Y. Magara, Fluoride in Drinking-water, World Health Organization, 2006.

[33] World Health Organization, Nitrate and nitrite in drinking-water: Background document for development of WHO Guidelines for Drinking-water Quality, Geneva 2007.

[34] W.M. Edmunds, P. Smedley, Fluoride in natural waters, in: O. Selinus, B. Alloway, J.A. Centeno, R.B. Finkelman, R. Fuge, U. Lindh, P.L. Smedley (Eds.) Essentials of medical geology: impacts of the natural environment on public health, Elsevier, 2005, pp. 301 - 329.

[35] C. Binnie, M. Kimber, Basic water treatment 4th edition, Thomas Telford Limited, London, 2009.

[36] W.R. Bowen, A.W. Mohammad, N. Hilal, Characterisation of nanofiltration membranes for predictive purposes - use of salts, uncharged solutes and atomic force microscopy, Journal of Membrane Science, 126 (1997) 91 - 105.

[37] J. Schaep, B. Van Der Bruggen, C. Vandecasteele, D. Wilms, Influence of ion size and charge in nanofiltration, Separation and Purification Technology, 14 (1998) 155-162.

[38] M. Nyström, L. Kaipia, S. Luque, Fouling and retention of nanofiltration membranes, Journal of Membrane Science, 98 (1995) 249-262.

[39] S. Loeb, S. Sourirajan, Sea water demineralization by means of an osmotic membrane, in: Advances in Chemistry, 1963, pp. Chapter 9, pp 117 - 132.

[40] L. Greenlee, D.L. Lawler, B.D. Freeman, B. Marrot, P. Moulin, Reverse osmosis desalination: water sources, technology, and today's challenges, Water Research, 43 (2009) 2317 - 2348.

[41] R. Singh, Membranes: A review of membrane technologies: Reverse osmosis, nanofiltration and ultrafiltration, Ultrapure Water, (1997) 21 - 29.

[42] P. Eriksson, Nanofiltration extends the range of membrane filtration, Environmental Progress, 7 (1988) 58 - 62.

[43] Van der Bruggen B., C. Vandecasteele, Removal of pollutants from surface water and groundwater by nanofiltration: overview of possible applications in the drinking water industry, Environmental Pollution, 122 (2003) 435-445.

[44] L. Zeman, L. Denault, Characterization of microfiltration membranes by image analysis of electron micrographs. Part I. Model development, Journal of Membrane Science, 71 (1992) 221 - 231.

[45] Y. Yao, S. Guo, Y. Zhang, Surface Properties of Reverse Osmosis Membrane, Journal of Applied Polymer Science, 105 (2007) 1261 - 1266.

[46] R. Semiat, Energy issues in desalination processes, Environmental Science & Technology, 42 (2008) 8193 - 8201.

[47] J. Wagner, Membrane Filtration Handbook, Wagner Publishing, 1996

[48] K.S. Winston Ho, K.K. Sirkar, Membrane Handbook, Kluwer Academic Publishers, 2001.

[49] Y. Cengeloglu, G. Arslan, A. Tor, I. Kocak, N. Dursun, Removal of boron from water by using reverse osmosis, Separation and Purification Technology, 2008 (2008) 141-146.

[50] J. Kim, M. Wilf, J.-S. Park, J. Brown, Boron Rejection by Reverse Osmosis Membranes: National Reconnaissance and Mechanism Study, United States Department of the Interior Bureau of Reclamation, 2009.

[51] M. Mohapatra, S. Anand, B.K. Mishra, D.E. Giles, P. Singh, Review of fluoride removal from drinking water, Journal of Environmental Management, 91 (2009) 67-77.

[52] C.K. Diawara, L. Paugam, M. Pontié, J.P. Schlumpf, P. Jaouen, F. Quéméneur, Influence of chloride, nitrate, and sulphate on the removal of fluoride ions by using nanofiltration membranes, Separation Science and Technology, 40 (2005) 3339 - 3347.

[53] L. Paugam, S. Taha, J. Cabon, G. Dorange, Elimination of nitrate ions in drinking waters by nanofiltration, Desalination, 152 (2002) 271 - 274.

[54] A. Santafé-Moros, J.M. Gozálvez-Zafrilla, J. Lora-García, Performance of commercial nanofiltration membranes in the removal of nitrate ions, Desalination, 185 (2005) 1707-1713.

[55] B. Van der Bruggen, K. Everaert, D. Wilms, C. Vandecasteele, Application of nanofiltration for removal of pesticides, nitrate and hardness from ground water: rejection properties and economic evaluation, Journal of Membrane Science, 193 (2001) 239-248.

[56] K.P. Lee, T.C. Arnot, D. Mattia, A review of reverse osmosis membrane materials for desalination - Development to date and future potential, Journal of Membrane Science, 370 (2011) 1 - 22.

[57] B. Van der Bruggen, C. Vandecasteele, Removal of pollutants from surface water and groundwater by nanofiltration: overview of possible applications in the drinking water industry, Environmental Pollution, 122 (2003) 435 - 445.

[58] A. Al-Karaghouli, D. Renne, L.L. Kazmerski, Technical and economic assessment of photovoltaic-driven desalination systems, Renewable Energy, 35 (2010) 323 - 328.

[59] R.W. Baker, Membrane Technology and Applications, 2nd Edition, John Wiley & Sons, Ltd, 2004.

[60] M. Peter-Varbanets, C. Zurbrügg, C. Swartz, W. Pronk, Decentralized systems for potable water and the potential of membrane technology, Water Research, 43 (2009) 245 - 265.

[61] C. Charcosset, A review of membrane processes and renewable energies for desalination, Desalination, 245 (2009) 214 - 231.

[62] M.A. Eltawil, Z. Zhengming, L. Yuan, A review of renewable energy technologies integrated with desalination systems, Renewable and Sustainable Energy Reviews, 13 (2009) 2245 - 2262.

[63] A. Ghermandi, R. Messalem, Solar-driven desalination with reverse osmosis: the state of the art, Desalination and Water Treatment, 7 (2009) 285 - 296.

[64] E. Mathioulakis, V. Belessiotis, E. Delyannis, Desalination by using alternative energy: Review and state-of-the-art, Desalination, 2007 (2007) 346 - 365.

[65] G. Petersen, S. Fries, J. Mohn, A. Muller, Wind and solar powered reverse osmosis desalination units - design, start up, operating experience, Desalination, 39 (1981) 125 - 135.

[66] R. Robinson, G. Ho, K. Mathew, Development of a Reliable Low-Cost Reverse Osmosis Desalination Unit for Remote Communities, Desalination, 86 (1992) 9-26.

[67] S. Alawaji, M.S. Smiai, S. Rafique, PV-Powered Water Pumping and Desalination Plant for Remote Areas in Saudi Arabia, Applied Energy, 52 (1995) 283 - 289.

[68] W. Gocht, A. Sommerfeld, R. Rautenback, T. Melin, L. Eilers, A. Neskakis, D. Herold, V. Horstmann, M. Kabariti, A. Muhaidat, Decentralized desalination of brackish water by a directly coupled reverse-osmosis-photovoltaic-system - a pilot study in Jordan, Renewable Energy, 14 (1998) 287 - 292.

[69] C.C.K. Liu, J.-W. Park, R. Migita, G. Qin, Experiments of a prototype wind-driven reverse osmosis desalination system with feedback control, Desalination, 150 (2002) 277 - 287.

[70] M. Papapetrou, M. Wieghaus, C. Biercamp, Roadmap for the Development of Desalination Powered by Renewable Energy, ProDes, 2010.

[71] D. Weiner, D. Fisher, E.J. Moses, B. Katz, G. Meron, Operation experience of a solar- and wind-powered desalination demonstration plant, Desalination, 137 (2001) 7 - 13.

[72] B.S. Richards, D.P.S. Capão, A.I. Schäfer, Renewable energy powered membrane technology. 2. The effect of energy fluctuations on performance of a photovoltaic hybrid membrane system, Environmental Science and Technology, 42 (2008) 4563-4569.

[73] E.S. Mohamed, G. Papadakis, E. Mathioulakis, V. Belessiotis, A direct coupled photovoltaic seawater reverse osmosis desalination system toward battery based systems - a technical and economical experimental comparative study, Desalination, 221 (2008) 17 - 22.

[74] A.I. Schäfer, A. Broeckmann, B.S. Richards, Renewable Energy Powered Membrane Technology. 1. Development and Characterization of a Photovoltaic Hybrid Membrane System, Environmental Science and Technology, 41 (2007) 998-1003.

[75] M. Thomson, D. Infield, A Photovoltaic-Powered Seawater Reverse-Osmosis System Without Batteries, Desalination, 153 (2003) 1 - 8.

[76] R.A. Robinson, R.H. Stokes, Electrolyte Solutions, Butterworth & Co., London, 1959.

[77] B. Tansel, J. Sager, T. Rector, J. Garland, R. Strayer, L. Lanfang, M. Roberts, M. Hummerick, J. Bauer, Significance of hydrated radius and hydration shells on ionic permeability during nanofiltration in dead end and cross flow modes, Separation and Purification Technology, 51 (2006) 40-47.

[78] P.W. Atkins, Physical Chemistry Second Edition, Oxford, 1982.

[79] Y. Marcus, A simple empirical model describing the thermodynamics of hydration of ions of widely varying charges, sizes, and shapes, Biophysical Chemistry, 51 (1994) 111-127.

[80] Y. Marcus, Thermodynamics of solvation of ions. Part 5: Gibbs free energy of hydration at 298.15 K, Journal of the Chemical Society, Faraday Transactions, 87 (1991) 2995 - 2999.

[81] J. Burgess, Metal ions in solution, Halsted Press, New York, 1978.

[82] E.R. Nightingale, Phenomenological Theory of Ion Solvation. Effective Radii of Hydrated Ions, The Journal of Physical Chemistry, 63 (1959) 1381-1387.

[83] I.S. Joung, T.E. Cheatham III, Determination of alkali and halide monovalent ion parameters for use in explicitly solvated biomolecular simulations, Journal of Physical Chemistry B, 112 (2008) 9020 - 9041.

[84] K.P. Jensen, W.L. Jorgensen, Halide, ammonium, and alkali metal ion parameters for modeling aqueous solutions, Journal of Chemical Theory and Computation, 2 (2006) 1499-1509.

[85] P. Mukherjee, A.K. Sengupta, Ion exchange selectivity as a surrogate indicator of relative permeability of ions in reverse osmosis processes, Environmental Science and Technology, 37 (2003) 1432 - 1440.

[86] R. Schmid, A.M. Miah, V.N. Sapunov, A new table of the thermodynamic quantities of ionic hydration: values and some applications (enthalpy-entropy compensation and Born radii), Physical Chemistry Chemical Physics, 2 (2000) 97-102.

[87] C.S. Babu, C. Lim, Theory of ionic hydration: Insights from molecular dynamics simulations and experiment, Journal of Physical Chemistry B, 103 (1999) 7958 - 7968.

[88] J. Zhou, X. Lu, Y. Wang, J. Shi, Molecular dynamics study on ionic hydration, Fluid Phase Equilibria, 194-197 (2002) 257-270.

[89] M.Y. Kiriukhim, K.D. Collins, Dynamic hydration numbers for biologically important ions, Biophysical Chemistry, 99 (2002) 155-168.

[90] R. Custelcean, B.A. Moyer, Anion separation with metal-organic frameworks, European Journal of Inorganic Chemistry, (2007) 1321 - 1340.

[91] H.S. Ashbaugh, D. Asthagiri, Single ion hydration energies: A consistent comparison between experiment and classical molecular dynamic simulation, The Journal of Chemical Physics, 129 (2008) 204501.

[92] A.A. Hussain, M.E.E. Abashar, I.S. Al-Mutaz, Influence of ion size on the prediction of nanofiltration membrane systems, Desalination, 214 (2007) 150 - 166.

[93] M.G. Davidson, W.M. Deen, Hydrodynamic theory for the hindered transport of flexible macromolecules in porous membranes, Journal of Membrane Science, 35 (1988) 167 - 192.

[94] A.I. Schäfer, A.G. Fane, T.D. Waite, Nanofiltration - Principles and Applications, Elsevier, Oxford 2005.

[95] C.J. Fennell, A. Bizjak, V. Vlachy, K.A. Dill, Ion pairing in molecular simulations of aqueous alkali halide solutions, Journal of Physical Chemistry B, 113 (2009) 6782-6791.

[96] B. Hess, C. Holm, N. Van Der Vegt, Osmotic coefficients of atomistic NaCl (aq) force fields, The Journal of Chemical Physics, 124 (2006) 164509.

[97] A.A. Chialvo, P.T. Cummings, H.D. Cochan, J.M. Simonson, R.E. Mesmer, Na^+-Cl^- ion pair association in supercritical water, Journal of Chemical Physics, 21 (1995) 9379 - 9387.

[98] S. Choi, Z. Yun, S. Hong, K. Ahn, The effect of co-existing ions and surface characteristics of nanomembranes on the removal of nitrate and fluoride, Desalination, 133 (2001) 53-64.

[99] P. Dydo, M. Turek, J. Ciba, J. Trojanowska, J. Kluczka, Boron removal from landfill leachate by means of nanofiltration and reverse osmosis, Desalination, 185 (2005) 1557-1563.

[100] A. Favre-Réguillon, G. Lebuzit, D. Murat, J. Foos, C.I. Mansour, M. Draye, Selective removal of dissolved uranium in drinking water by nanofiltration, Water Research, 42 (2008) 1160-1166.

[101] K. Košutić, L. Furač, L. Sipos, B. Kunst, Removal of arsenic and pesticides from drinking water by nanofiltration membranes, Separation and Purification Technology, 42 (2005) 137 - 144.

[102] H. Saitúa, M. Campderrós, S. Cerutti, A.P. Padilla, Effect of operating conditions in removal of arsenic from water by nanofiltration membrane, Desalination, 172 (2005) 173-180.

[103] Y. Sato, M. Kang, T. Kamei, Y. Magara, Performance of nanofiltration for arsenic removal, Water Research, 36 (2002) 3371-3377.

[104] C. Bartels, R. Franks, S. Rybar, M. Schierach, M. Wilf, The effect of feed ionic strength on salt passage through reverse osmosis membranes, Desalination, 184 (2005) 185-195.

[105] W.M. Deen, Hindered transport of large molecules in liquid-filled pores, Journal of the American Institute of Chemical Engineers, 33 (1987) 1409-1425.

[106] B. Van der Bruggen, A. Koninckx, C. Vandecasteele, Separation of monovalent and divalent ions from aqueous solution by electrodialysis and nanofiltration, Water Research, 38 (2004) 1347-1353.

[107] L. Paugam, S. Taha, G. Dorange, P. Jaouen, F. Quéméneur, Mechanism of nitrate ions transfer in nanofiltration depending on pressure, pH, concentration and medium concentration, Journal of Membrane Science, 231 (2004) 37-46.

[108] G.T. Ballet, A. Hafiane, M. Dhahbi, Influence of operating conditions on the retention of phosphate in water by nanofiltration, Journal of Membrane Science, 290 (2007) 164-172.

[109] A.E. Yaroshchuk, Non-steric mechanisms of nanofiltration: superposition of Donnan and dielectric exclusion, Separation and Purification Technology, 22 - 23 (2001) 143 - 158.

[110] L.D. Nghiem, Removal of emerging trace organic contaminants by nanofiltration and reverse osmosis, PhD Thesis, Faculty of Engineering, School of Civil, Mining, and Environmental Engineering, University of Wollongong, Wollongong Australia 2005, pp. 214.

[111] C. Bellona, J.E. Drewes, The role of membrane surface charge and solute physio-chemical properties in the rejection of organic acids by NF membranes, Journal of Membrane Science, 249 (2005) 227-234.

[112] L.D. Nghiem, A.I. Schäfer, Chapter 20: Trace contaminant removal with nanofiltration, in: A. Schäfer, A. Fane, T. Waite (Eds.) Nanofiltration - Principles and Applications, El Sevier, Oxford, 2005.

[113] J.J. Qin, M.H. Oo, H. Lee, B. Coniglio, Effect of feed pH on permeate pH and ion rejection under acidic conditions in NF process, Journal of Membrane Science, 232 (2004) 153-159.

[114] J. Schaep, C. Vandecasteele, Evaluating the charge of nanofiltration membranes, Journal of Membrane Science, 188 (2001) 129-136.

[115] G. Hagmeyer, R. Gimbel, Modelling the rejection of nanofiltration membranes using zeta potential measurements, Separation and Purification Technology, 15 (1999) 19-30.

[116] A.E. Yaroshchuk, V. Ribitsch, The use of trace ions for advanced characterisation of transport properties of NF membranes in electrolyte solutions: theoretical analysis, Journal of Membrane Science, 201 (2002) 85 - 94.

[117] A.E. Yaroshchuk, Dielectric exclusion of ions from membranes, Advances in Colloid and Interface Science, 85 (2000) 193 - 230.

[118] J.Y. Chen, H. Nomura, G.G. Wade, Pusch, Temperature dependence of membrane transport parameters in hyperfiltration, Desalination, 46 (1983) 437 - 446.

[119] V. Freger, E. Korin, J. Wisniak, E. Korngold, M. Ise, K.D. Kreuer, Diffusion and water and ethanol in ion-exchange membranes: limits of the geometric approach, Journal of Membrane Science, 160 (1999) 213-224.

[120] A.H. Muhr, J.M.V. Blanshard, Diffusion in gels, Polymer, 23 (1982) 1012-1026.

[121] CRC Handbook of Chemistry and Physics, 76th ed., CRC Press, 1995.

[122] S.M.S. Ghiu, R.P. Carnahan, M. Barger, Mass transfer in RO TFC membranes - dependence on the salt physical and thermodynamic parameters, Desalination, 157 (2003) 385 - 393.

[123] C.T. Matos, R. Fortunato, S. Velizarou, M.A.M. Reis, J.G. Crespo, Removal of mono-valent oxyanions from water in an ion exchange membrane bioreactor: Influence of membrane permselectivity, Water Research, 42 (2008) 1785 - 1795.

[124] P.Y. Pontalier, A. Ismail, M. Ghoul, Mechanisms for the selective rejection of solutes in nanofiltration membranes, Separation and Purification Technology, 12 (1997) 175 - 181.

[125] L. Li, J. Dong, T.M. Nenoff, Transport of water and alkali metal ions through MFI zeolite membranes during reverse osmosis, Separation and Purification Technology, 53 (2007) 42 - 48.

[126] C. Song, B. Corry, Intrinsic ion selectivity of narrow hydrophobic pores, Journal of Physical Chemistry B, 113 (2009) 7642 - 7649.

[127] B. Corry, Designing carbon nanotube membranes for efficient water desalination, Journal of Physical Chemistry B, 112 (2008) 1427 - 1434.

[128] M. Zwolak, J. Lagerqvist, M. Di Ventra, Quantized Ionic Conductance in Nanopores, Physical Review Letters, 103 (2009).

[129] M. Thomas, D. Jayatilaka, B. Corry, The predominant role of coordination number in potassium channel selectivity, Biophysical Journal, 93 (2007) 2635 - 2643.

[130] M. Zwolak, J. Wilson, M.D. Ventra, Dehydration and ionic conductance quantization in nanopores, Journal of Physics: Condensed Matter, 22 (2010) 454126.

[131] H. Matsumoto, R. Yamamoto, A. Tanioka, Membrane potential across low-water-content charged membranes: effect of ion pairing, Journal of Physical Chemistry B, 109 (2005) 14130-14136.

[132] K. Košutić, I. Novak, L. Sipos, B. Kunst, Removal of sulfates and other inorganics from potable water by nanofiltration membranes of characterized porosity, Separation and Purification Technology, 37 (2004) 177 - 185.

[133] P. Mukherjee, A.K. SenGupta, Some observations about electrolyte permeation mechanism through reverse osmosis and nanofiltration membranes, Journal of Membrane Science, 278 (2006) 301-307.

[134] C. Bellona, J.E. Drewes, P. Xu, G. Amy, Factors affecting the rejection of organic solutes during NF/RO treatment - a literature review, Water Research, 38 (2004) 2795.

[135] J.G. Wijmans, R.W. Baker, The solution-diffusion model: a review, Journal of Membrane Science, 107 (1995) 1 - 21.

[136] R.R. Sharma, S. Chellam, Temperature and concentration effects on electrolyte transport across porous thin-film composite nanofiltration membranes: Pore transport mechanisms and energetics of permeation, Journal of Colloid and Interface Science, 298 (2006) 327 - 340.

[137] J.M.M. Peeters, M.H.V. Mulder, H. Strathmann, Streaming potential measurements as a characterization method for nanofiltration membranes, Colloids and Surfaces, A: Physiochemical and Engineering Aspects 150 (1999) 247-259.

[138] M.R. Teixeira, M.J. Rosa, M. Nyström, The role of membrane charge on nanofiltration performance, Journal of Membrane Science, 265 (2005) 160-166.

[139] L. Paugam, C.K. Diawara, J.P. Schlumpf, P. Jaouen, F. Quéméneur, Transfer of monovalent anions and nitrates especially through nanofiltration membranes in brackish water conditions, Separation and Purification Technology, 40 (2004) 237-242.

[140] J.M.M. Peeters, J.P. Boom, M.H.V. Mulder, H. Strathmann, Retention measurements of nanofiltration membranes with electrolyte solutions, Journal of Membrane Science, 145 (1998) 199-209.

[141] M. Mänttäri, A. Pihlajamäki, M. Nyström, Effect of pH on hydrophilicity and charge and their effect on the filtration efficiency of NF membranes at different pH, Journal of Membrane Science, 280 (2006) 311-320.

[142] C. Labbez, P. Fievet, A. Szymczyk, A. Vidonne, A. Foissy, J. Pagetti, Retention of mineral salts by a polyamide nanofiltration membrane, Separation and Purification Technology, 30 (2003) 47-55.

[143] A.E. Childress, M. Elimelech, Relating nanofiltration membrane performance to membrane charge (electrokinetic) characteristics, Environmental Science and Technology, 34 (2000) 3710 - 3716.

[144] A. Szymczyk, C. Labbez, P. Fievet, A. Vidonne, A. Foissy, J. Pagetti, Contribution of convection, diffusion and migration to electrolyte transport through nanofiltration membranes, Advances in Colloid and Interface Science, 103 (2003) 77 - 94.

[145] P. Fievet, C. Labbez, A. Szymczyk, A. Vidonne, A. Foissy, J. Pagetti, Electrolyte transport through amphoteric nanofiltration membranes, Chemical Engineering Science, 57 (2002) 2921 - 2931.

[146] W.R. Bowen, A.W. Mohammad, Characterization and prediction of nanofiltration membrane performance - a general assessment, Trans IChemE, 76 (1998) 885 - 893.

[147] S. Lee, R.M. Lueptow, Membrane Rejection of Nitrogen Compounds, Environmental Science and Technology, 35 (2001) 3008-3018.

[148] S. Bason, O. Kedem, V. Freger, Determination of concentration-dependent transport coefficients in nanofiltration: Experimental evaluation of coefficients, Journal of Membrane Science, 326 (2009) 197 - 204.

[149] S. Bason, V. Freger, Phenomenological analysis of transport of mono- and divalent ions in nanofiltration, Journal of Membrane Science, 360 (2010) 389 - 396.

[150] S. Bason, Y. Oren, V. Freger, Ion transport in the polyamide layer of RO membranes: Composte membranes and free-standing films, Journal of Membrane Science, 367 (2011) 119 - 126.

[151] O. Kedem, V. Freger, Determination of concentration-dependent transport coefficients in nanofiltration: defining an optimal set of coefficients, Journal of Membrane Science, 310 (2008) 586.

[152] A.E. Yaroshchuk, Rejection of single salts versus transmembrane volume flow in RO/NO: thermodynamic properties, model of constant coefficients and its modification, Journal of Membrane Science, 198 (2002) 285.

[153] M. Mulder, Basic Principles of Membrane Technology, Kluwer Academic Publishers, 1996.

[154] I. Sutzkover, D. Hasson, R. Semiat, Simple technique for measuring the concentration polarization level in a reverse osmosis system, Desalination, 131 (2000) 117 - 127.

[155] C.A.C. van De Lisdonk, B.M. Rietman, S.G.J. Heijman, G.R. Sterk, J.C. Schippers, Prediction of supersaturation and monitoring of scaling in reverse osmosis and nanofiltration membrane systems, Desalination, 138 (2001) 259 - 270.

[156] K. Mehiguene, Y. Garba, S. Taha, N. Gondrexon, G. Dorange, Influence of operating conditions on the retention of copper and cadmium in aqueous solutions by nanofiltration: experimental results and modelling, Separation and Purification Technology, 15 (1999) 181 - 187.

[157] B. Van der Bruggen, C. Vandecasteele, Modelling of the retention of uncharged molecules with nanofiltration, Water Research, 36 (2002) 1360 - 1368.

[158] B. Van der Bruggen, C. Vandecasteele, T. Van Gestel, W. Doyen, R. Leysen, A Review of Pressure-Driven Membrane Processes in Wastewater Treatment and Drinking Water Production, Environmental Progress, 22 (2003) 46.

[159] R. Levenstein, D. Hasson, R. Semiat, Utilization of the Donnan effect for improving electrolyte separation with nanofiltration membranes, Journal of Membrane Science, 116 (1996) 77 - 92.

[160] J. Gilron, N. Gara, O. Kedem, Experimental analysis of negative salt rejection in nanofiltration membrane, Journal of Membrane Science, 185 (2001) 223 - 236.

[161] K. Boussu, Y. Zhang, J. Cocquyt, P.V.d. Meeren, A. Volodin, C.V. Haesendonck, J.A. Martens, B.V.d. Bruggen, Characterization of polymeric nanofiltration membranes for systematic analysis of membrane performance, Journal of Membrane Science, 278 (2006) 418-427.

[162] W. Stumm, J.J. Morgan, Aquatic Chemistry: An Introduction Emphasizing Chemical Equilibria in Natural Waters, 2nd Edition, John Wiley & Sons, 1981.

[163] T. Tsuru, K. Ogawa, M. Kanezashi, T. Yoshioka, Permeation characteristics of electrolytes and neutral solutes through titania nanofiltration membranes at high temperatures, Langmuir, 26 (2010) 10897 - 10905.

[164] V. Geraldes, A.M.B. Alves, Computer program for simulation of mass transport in nanofiltration membranes, Journal of Membrane Science, 231 (2008) 172 - 182.

[165] I. Koyuncu, D. Topacik, Effects of operating conditions on the salt rejection of nanofiltration membranes in reactive dye/salt mixtures, Separation and Purification Technology, 33 (2003) 283 - 294.

[166] E.R. Lising, R. Alward, Unsteady State Operation of a Reverse Osmosis Desalination Unit, Desalination, 11 (1972) 261-268.

[167] M.d.S. Miranda, Small-scale Wind-Powered Seawater Desalination Without Batteries, PhD Thesis, Loughborough University (United Kingdom), Loughborough University, 2003.

[168] G.L. Park, A.I. Schäfer, B.S. Richards, Renewable energy powered membrane technology: The effect of wind speed fluctuations on the performance of a wind-powered membrane system for brackish water desalination, Journal of Membrane Science, 370 (2011) 34 - 44.

[169] S. Loeb, E. Selover, Sixteen months of field experience on the Coalinga pilot plant, Desalination, 2 (1967) 75 - 80.

[170] D. Stevens, S. Loeb, Reverse osmosis desalination costs derived from the Coalinga pilot plant operation, Desalination, 2 (1967) 56 - 74.

[171] L.A. Richards, B.S. Richards, H.M.A. Rossiter, A.I. Schäfer, Impact of Speciation on Fluoride, Arsenic and Magnesium Retention by Nanofiltration/Reverse Osmosis in Remote Australian Communities, Desalination, 248 (2009) 177 - 183.

[172] A. Seidel, J.J. Waypa, M. Elimelech, Role of Charge (Donnan) Exclusion in Removal of Arsenic from Water by a Negatively Charged Porous Nanofiltration Membrane, Environmental Engineering Science, 18 (2001).

[173] T. Waite, Chemical speciation effects in nanofiltration separation, in: A. Schäfer, A. Fane, T. Waite (Eds.) Nanofiltration - Principles and Applications, Elsevier, Oxford, 2005.

[174] A.E. Childress, M. Elimelech, Effect of solution chemistry on the surface charge of polymeric reverse osmosis and nanofiltration membranes, Journal of Membrane Science, 119 (1996) 253-268.

[175] R.Y. Ning, Arsenic removal by reverse osmosis, Desalination, 143 (2002) 237-241.

[176] M. Kang, M. Kawasaki, S. Tamada, T. Kamei, T. Magara, Effect of pH on the removal of arsenic and antimony using reverse osmosis membranes, Desalination, 131 (2000) 293-298.

[177] T. Urase, J. Oh, K. Yamamoto, Effect of pH on rejection of different species of arsenic by nanofiltration, Desalination, 117 (1998) 11-18.

[178] M.T. Uddin, M.S.I. Mozumder, M.A. Islam, S.A. Deowan, J. Hoinkis, Nanofiltration Membrane Process for the Removal of Arsenic from Drinking Water, Chemical Engineering Technology, 30 (2007) 1248-1254.

[179] S. Xia, B. Dong, Q. Zhang, B. Xu, N. Gao, C. Causseranda, Study of arsenic removal by nanofiltration and its application in China, Desalination, 204 (2007) 374-379.

[180] D. Prats, M.F. Chillon-Arias, M. Rodriquez-Pastor, Analysis of the influence of pH and pressure on the elimination of boron in reverse osmosis, Desalination, 128 (2000) 269-273.

[181] H. Ozaki, H. Li, Rejection of organic compounds by ultra-low pressure reverse osmosis membrane, Water Research, 36 (2002) 123-130.

[182] P. Berg, G. Hagmeyer, R. Gimbel, Removal of pesticides and other micropollutants by nanofiltration, Desalination, 113 (1997) 205-208.

[183] R.R. Sharma, R. Agrawal, S. Chellam, Temperature effects on sieving characteristics of thin-film composite nanofiltration membranes: pore size distributions and transport parameters, Journal of Membrane Science, 223 (2003) 69 - 87.

[184] D.R. Machado, D. Hasson, R. Semiat, Effect of solvent properties on permeate flow through nanofiltration membranes. Part I: investigation of parameters affecting solvent flux, Journal of Membrane Science, 163 (1999) 93 - 102.

[185] N.B. Amar, H. Saidani, A. Deratani, J. Palmeri, Effect of temperature on the transport of water and neutral solutes across nanofiltration membranes, Langmuir, 23 (2007) 2937 - 2952.

[186] M. Nilsson, G. Trägårdh, K. Östergren, The influence of pH, salt and temperature on nanofiltration performance, Journal of Membrane Science, 312 (2008) 97 - 106.

[187] R.R. Sharma, S. Chellam, Temperature Effects on the Morphology of Porous Thin Film Composite Nanofiltration Membranes, Environmental Science & Technology, 39 (2005) 5022-5030.

[188] C.W. Saltonstall, Practical aspects of sea water desalination by reverse osmosis, Desalination, 18 (1976) 315 - 320.

[189] K.Y. Wang, T.-S. Chung, J.-J. Qin, Polybenzimidole (PBI) nanofiltration hollow fiber membranes applied in forward osmosis process, Journal of Membrane Science, 300 (2007) 6 - 12.

[190] V. Freger, T.C. Arnot, J.A. Howell, Separation of concentrated organic/inorganic salt mixtures by nanofiltration, Journal of Membrane Science, 178 (2000) 185 - 193.

[191] P. Schirg, F. Widmer, Characterisation of nanofiltration membranes for the separation of aqueous dye-salt solutions, Desalination, 89 (1992) 89 - 107.

[192] M. Nilsson, G. Trägårdh, K. Östergren, The influence of sodium chloride on mass transfer in a polyamide nanofiltration membrane at elevated temperatures, Journal of Membrane Science, 280 (2006) 928 - 936.

[193] H.H. Kim, J.H. Kim, Y.K. Chang, Removal of potassium chloride by nanofiltration from ion-exchanged solution containing potassium clavulanate, Bioprocess and Biosystems Engineering, 33 (2010) 149 - 158.

[194] K.S. Spiegler, O. Kedem, Thermodynamics of hyperfiltration (reverse osmosis): Criteria for efficient membranes, Desalination, 1 (1966) 311 - 326.

[195] O. Kedem, A. Katchalsky, Thermodynamic analysis of the permeability of biological membranes to non-electrolytes, Biochimica et Biophysica Acta, 27 (1958) 229 - 246.

[196] N.A. Peppas, D.L. Meadows, Macromolecular structure and solute diffusion in membranes: an overview of recent theories, Journal of Membrane Science, 16 (1983) 361 - 377.

[197] K. Košutić, L. Kaštelan-Kunst, B. Kunst, Porosity of some commercial reverse osmosis and nanofiltration polyamide thin-film composite membranes, Journal of Membrane Science, 168 (2000) 101 - 108.

[198] W.R. Bowen, J.S. Welfoot, Modelling the performance of membrane nanofiltration - critical assessment and model development, Chemical Engineering Science, 57 (2002) 1121 - 1137.

[199] X.-L. Wang, T. Tsuru, S. Nakao, S. Kimura, The electrostatic and steric-hindrance model for the transport of charged solutes through nanofiltration membranes, Journal of Membrane Science, 135 (1997) 19-32.

[200] X.L. Wang, T. Tsuru, S. Nakao, S. Kimura, Electrolyte transport through nanofiltration membranes by the space-charge model and the comparison with Teorell-Meyer-Sievers model, Journal of Membrane Science, 103 (1995) 117 - 133.

[201] G. Jacazio, R.F. Probstein, A.A. Sonin, D. Yung, Electrokinetic salt rejection in hyperfiltration through porous materials. Theory and experiment., Journal of Physical Chemistry, 76 (1972) 4015 - 4023.

[202] T. Tsuru, M. Urairi, S. Nakao, S. Kimura, Reverse osmosis of single and mixed electrolytes with charged membranes: Experiments and analysis, Journal of Chemical Engineering of Japan, 24 (1991) 511 - 517.

[203] R.J. Gross, J.F. Osterle, Membrane transport characteristics in ultrafine capillaries, Journal of Chemical Physics, 49 (1968).

[204] T. Tsuru, S. Nakao, S. Kimura, Calculation of ion rejection by extended Nernst-Planck equation with charged reverse osmosis membranes for single and mixed electrolyte solutions, Journal of Chemical Engineering of Japan, 24 (1991) 511 - 517.

[205] C. Combe, C. Guizard, P. Aimar, V. Sanchez, Synthesis and characterization of mircoporous zirconia powders: Application in nanofilters and nanofiltration characteristics., Journal of Membrane Science, 132 (1997) 109 - 118.

[206] G.M. Rios, R. Joulie, S.J. Sarrade, M. Carles, Investigation of ion separation by microporous nanofiltration membranes, AIChE Journal, 42 (1996) 2521 - 2528.

[207] M. Soltanieh, W.N. Gill, Review of reverse osmosis membranes and transport models, Chemical Engineering Communications, 12 (1981) 379 - 363.

[208] J. Schaep, C. Vandecasteele, A.W. Mohammad, W.R. Bowen, Modelling the retention of ionic components for different nanofiltration membranes, Separation and Purification Technology, 22-23 (2001) 169-179.

[209] A. Szymczyk, P. Fievet, Investigating transport properties of nanofiltration membranes by means of a steric, electric and dielectric exclusion model, Journal of Membrane Science, 252 (2005) 77 - 88.

[210] W.R. Bowen, H. Mukhtar, Characterisation and prediction of separation performance of nanofiltration membranes, Journal of Membrane Science, 112 (1996) 263 - 274.

[211] S. Bandini, D. Vezzani, Nanofiltration modeling: the rold of dielectric exclusion in membrane characterization, Chemical Engineering Science, 58 (2003) 3303-3326.

[212] S. Déon, P. Dutournié, P. Bourseau, Modeling nanofiltration with Nernst-Planck approach and polarization layer, American Institute of Chemical Engineers Journal, 53 (2007) 1952 - 1969.

[213] S. Déon, A. Escoda, P. Fievet, A transport model considering charge adsorption inside pores to describe salts rejection by nanofiltration membranes, Chemical Engineering Science, 66 (2011) 2823 - 2832.

[214] R. Schlögl, Membrane Permeation in Systems Far from Equilibrium, Berichte der Bunsengesellschaft, 70 (1966) 400 - 414.

[215] P.M. Bungay, H. Brenner, The motion of a closely-fitting sphere in a fluid-filled tube, International Journal of Multiphase Flow, 1 (1973) 25 - 56.

[216] L.D. Nghiem, A.I. Schäfer, M. Elimelech, Removal of Natural Hormones by Nanofiltration Membranes: Measurement, Modeling, and Mechanisms, Environmental Science and Technology, 38 (2004) 1888-1896.

[217] P. Dechadilok, W.M. Deen, Hindrance Factors for Diffusion and Convection in Pores, Industrial and Engineering Chemistry Research, 45 (2006) 6953 - 6959.

[218] G. Mavrovouniotis, H. Brenner, Hindered sedimentation, diffusion and dispersion coefficients for brownian spheres in circular cylindrical pores, Journal of Colloid and Interface Science, 124 (1988) 269 - 283.

[219] J. Ennis, H. Zhang, G. Stevens, J. Perera, P. Scales, S. Carnie, Mobility of protein through a porous membrane, Journal of Membrane Science, 119 (1996) 47 - 58.

[220] A.R. Leach, Molecular Modelling: Principles and Applications, Addison Wesley Longman Limited, Essex, 1996.

[221] O.M. Becker, A.D.M. Jr, B. Roux, M. Watanabe, Computational Biochemistry and Biophysics, Marcel Dekker, New York, 2001.

[222] M. Ashcroft, From molecule to malady, Nature, 440 (2006) 440 - 447.

[223] B.J. Hinds, N. Chopra, T. Rantell, R. Andrews, V. Gavalas, L.G. Bachas, Aligned multiwalled carbon nanotube membranes, Science, 303 (2004) 62 - 65.

[224] A. Kalra, S. Garde, G. Hummer, Osmotic water transport through carbon nanotube membranes, Proceedings of the National Academy of Science, 100 (2003) 10175 - 10180.

[225] D. Mattia, Y. Gogotsi, Review: static and dynamic behavior of liquids inside carbon nanotubes, Microfluid Nanofliud, 5 (2008) 289 - 305.

[226] J.C. Phillips, R. Braun, W. Wang, J. Gumbart, E. Tajkhorshid, E. Villa, C. Chipot, R.B. Skeel, L. Kalé, K. Schulten, Scalable molecular dynamics with NAMD, Journal of Computational Chemistry, 26 (2005) 1781 - 1802.

[227] F. Khalili-Araghi, E. Tajkhorshid, B. Roux, K. Schulten, Molecular dynamics investigation of the w current in the Kv1.2 voltage sensor domains, Biophysical Journal, 102 (2012) 258 - 267.

[228] J. Gumbart, C. Chipot, K. Schulten, Free energy of nascent-chain folding in the translocon, Journal of the American Chemical Society, 133 (2011) 7602-7607.

[229] E. Gouaux, R. MacKinnon, Principles of selective ion transport in channels and pumps, Science, 310 (2005).

[230] A. Miyazawa, Y. Fujiyoshi, N. Unwin, Structure and gating mechanisms of the acetylcholine receptor pore, Nature, 423 (2003) 949 - 955.

[231] Y. Zhou, J.H. Morais-Cabral, A. Kaufman, R. MacKinnon, Chemistry of ion coordination and hydration revealed by a K+ channel-Fab complex at 2.0 Å resolution, Nature, 414 (2001) 43 - 48.

[232] O. Beckstein, K. Tai, M.S.P. Sansom, Not ions alone: Barriers to ion permeation in nanopores and channels, Journal of the American Chemical Society Communications, 126 (2004) 14694 - 14695.

[233] P. Linsdell, A. Evagelidis, J.W. Hanrahan, Molecular determinants of anion selectivity in the cystic fibrosis transmembrane conductance regulator chloride channel pore, Biophysical Journal, 78 (2000) 2973 - 2982.

[234] Y. Chen, L. Hu, M. Punta, R. Bruni, B. Hillerich, B. Kloss, B. Rost, J. Love, S.A. Siegelbaum, W.A. Hendrickson, Homologue structure of the SLAC1 anion channel for closing stomata in leaves, Nature, 467 (2010) 1074 - 1080.

[235] R. Dutzler, E.B. Campbell, M. Cadene, B.T. Chait, R. MacKinnon, X-ray structure of a ClC chloride channel at 3.0 Å reveals the molecular basis of anion selectivity, Nature, 415 (2002) 287.

[236] R. Dutzler, E.B. Campbell, R. MacKinnon, Gating the selectivity filter in ClC chloride channels, Science, 300 (2003).

[237] A. Accardi, L. Kolmakova-Partensky, C. Willaims, C. Miller, Ionic currents mediated by a prokaryotic homologue of ClC Cl⁻ channels, The Journal of General Physiology, 123 (2004) 109-119.

[238] D.A. Doyle, J.M. Cabral, R.A. Pfuetzner, A. Kuo, J.M. Gulbis, S.L. Cohen, B.T. Chait, R. MacKinnon, The Structure of the Potassium Channel: Molecular Basis of K^+ Conduction and Selectivity, Science, 280 (1998) 69 - 77.

[239] M. Carrillo-Tripp, M.L. San-Román, J. Hernańdez-Cobos, H. Saint-Martin, I. Ortega-Blake, Ion hydration in nanopores and the molecular basis of selectivity, Biophysical Chemistry, 124 (2006) 243 - 250.

[240] R. Kettunen, P. Keskitalo, Combination of membrane technology and limestone filtration to control drinking water quality, Desalination, 131 (2000) 271-283.

[241] C.K. Diawara, S.M. Lô, M. Rumeau, M. Pontie, O. Sarr, A phenemenological mass transfer approach in nanofiltration of halide ions for a selective defluorination of brackish drinking water, Journal of Membrane Science, 219 (2003) 103-112.

[242] A. Lhassani, M. Rumeau, D. Benjelloun, M. Pontie, Selective Demineralization of Water by Nanofiltration Application to the Defluorination of Brackish Water, Water Research, 35 (2001) 3260-3264.

[243] A.I. Schäfer, Natural Organics Removal Using Membranes, PhD Thesis, UNESCO Centre for Membrane Science and Technology, School of Chemical Engineering and Industrial Chemistry, The University of New South Wales, 1999.

[244] P.A. Neale, Influence of Solute-Solute Interactions on Membrane Filtration, PhD Thesis, School of Engineering, The University of Edinburgh, 2009.

[245] A.J.C. Semião, Removal of Adsorbing Estrogenic Micropollutants by Nanofiltration Membranes in Cross-Flow - Experiments and Model Development, PhD Thesis, School of Engineering, The University of Edinburgh, 2011.

[246] L. Masson, B.S. Richards, A.I. Schäfer, System Design and Performance Testing of a Hybrid Membrane Photovoltaic Desalination System, Desalination, 179 (2005) 51 - 59.

[247] B.S. Richards, L. Masson, A.I. Schäfer, Impact of Feedwater Salinity on Energy Requirements of a Small-Scale Membrane Filtration System, in: Y. Yanful (Ed.) Appropriate Technologies for Environmental Protection in the Developing World, Springer Science & Business Media, 2009, pp. 123 - 138.

[248] L.A. Richards, B.S. Richards, A.I. Schäfer, Renewable energy powered membrane technology: Salt and inorganic contaminant removal by nanofiltration/reverse osmosis, Journal of Membrane Science, 269 (2011) 188 - 195.

[249] DOW FILMTEC Reverse Osmosis and Nanofiltration Elements, http://www.dowwaterandprocess.com/products/ronf.htm, (accessed Nov 2011).

[250] Koch Membrane Systems, Fluid Systems TFC NF Series, http://www.kochmembrane.com/Membrane-Products/Spiral/Nanofiltration/Fluid-Systems-TFC-NF-Series.aspx, (accessed Nov 2011).

[251] Hydranautics, Membrane Element ESPA4-4040 Product Sheet, 2008 http://www.membranes.com/docs/4inch/ESPA4-4040.pdf, (accessed 27 June 2008).

[252] M. Kurihara, Y. Fusaoka, T. Sasaki, R. Bairinji, T. Uemura, Development of crosslinked fully aromatic polyamide ultra-thin composite membranes for seawater desalination, Desalination, 96 (1994) 133 - 143.

[253] Toray Reverse Osmosis and Nanofiltration Elements, http://www.toraywater.com/apac/en/products/products_ro_membranes/products_ro_membranes_overview.aspx, (accessed Nov 2011).

[254] Z.J. Derlacki, A.J. Easteal, A.V.J. Edge, L.A. Woolf, Z. Roksandic, Diffusion Coefficients of Methanol and Water and the Mutual Diffusion Coefficient in Methanol-Water Solutions at 278 and 298 K, The Journal of Physical Chemistry, 89 (1985) 5319.

[255] A. De Munari, A.I. Schäfer, Impact of speciation on removal of manganese and organic matter by nanofiltration, Journal of Water Supply: Research and Technology - Aqua, 59 (2010) 152-162.

[256] I.C. Escobar, S. Hong, A.A. Randall, Removal of assimilable organic carbon and biodegradable dissolved organic carbon by reverse osmosis and nanofiltration membranes, Journal of Membrane Science, 175 (2000) 1-17.

[257] Y. Zhang, B. Van der Bruggen., G.X. Chen, L. Braeken, C. Vandecasteele, Removal of pesticides by nanofiltration: effect of the water matrix, Separation and Purification Technology, 38 (2004) 163-172.

[258] S. Mondal, S. Ranil Wickramasinghe, Produced water treatment by nanofiltration and reverse osmosis membranes, Journal of Membrane Science, 322 (2008) 162 - 170.

[259] C.Y. Tang, Y.-N. Kwon, J.O. Leckie, Fouling of reverse osmosis and nanofiltration membranes by humic acid--Effects of solution composition and hydrodynamic conditions, Journal of Membrane Science, 290 (2007) 86-94.

[260] V. Freger, Nanoscale heterogeneity of polyamide membranes formed by inter-facial polymerization, Langmuir, 19 (2003) 4791.

[261] M. Kurihara, H. Yamamura, T. Nakanishi, High Recovery / High Pressure Membranes for Brine Conversion SWRO Process Development and its Performance Data, Desalination, 125 (1999) 9 - 15.

[262] B. Mi, O. Coronell, B.J. Marinas, F. Watanabe, D.G. Cahill, I. Petrov, Physico-chemical characterization of NF/RO membrane active layers by Rutherford backscattering spectrometry, Journal of Membrane Science, 282 (2006) 71.

[263] C.Y. Tang, Y.-N. Kwon, J.O. Leckie, Probing the nano- and micro-scales of reverse osmosis membranes-A comprehensive characterization of physiochemical properties of uncoated and coated membranes by XPS, TEM, ATR-FTIR, and streaming potential measurements, Journal of Membrane Science, 287 (2007) 146-156.

[264] R. Molinari, P. Argurion, T. Poerio, Comparison of polyethylenimine, polyacrylic acid and poly (dimethylamine-co-epichlorohydrin-co-ethylenediamine) in Cu^{2+} removal from wastewaters by polymer-assisted ultrafiltration, Desalination, 162 (2004) 217 - 228.

[265] M. Hirose, H. Ito, Y. Kamiyama, Effect of skin layer surface structures on the flux behaviour of RO membranes, Journal of Membrane Science, 121 (1996) 205 - 209.

[266] A. Simon, L.D. Nghiem, P. Le-Clech, S.J. Khan, J.E. Drewes, Effects of membrane degradation on the removal of pharmaceutically active compounds (PhACs) by NF/RO filtration processes, Journal of Membrane Science, 340 (2009) 16 - 25.

[267] Q. Li, M. Elimelech, Synergistic effects in combined fouling of a loose nanofiltration membrane by colloidal materials and natural organic matter, Journal of Membrane Science, 278 (2006) 72 - 82.

[268] V. Freger, J. Gilron, S. Belfer, TFC polyamide membranes modified by grafting of hydrophilic polymers: an FTIR/AFM/TEN study, Journal of Membrane Science, 209 (2002) 283 - 292.

[269] W. Zhang, M. Wahlgren, B. Sivik, Membrane characterization by the contact angle technique: II. Characterization of UF-membranes and comparison between the captive bubble and sessile drop as methods to obtain water contact angles, Desalination, 72 (1989) 263 - 273.

[270] D. Norberg, S. Hong, J. Taylor, Y. Zhao, Surface characterization and performance evaluation of commercial fouling resistant low-pressure RO membranes, Desalination, 202 (2007) 45 - 52.

[271] V.H. McNeil, M.E. Cox, Relationship between conductivity and analysed composision in a large set of surface water samples, Environmental Geology, 29 (2000) 1325 - 1333.

[272] M. Werner, A.I. Schäfer, Social aspects of a solar-powered desalination unit for remote Australian communities, Desalination, 203 (2007) 375-393.

[273] Australian Government Bureau of Meteoreology, Climate Maps, (2005) http://reg.bom.gov.au/climate/averages/maps.shtml, (accessed 2010).

[274] L.A. Richards, B.S. Richards, A.I. Schäfer, Renewable energy powered membrane systems: Inorganic contaminant removal from Australian groundwaters, Membrane Water Treatment, 2 (2011).

[275] J.P. Gustafsson, Visual MINTEQ, KTH (Ed.), 2000.

[276] J.D. Allison, D.S. Brown, K.J. Novo-Gradac, MINTEQA2/PRODEFA2, A Geochemical Assessment Model for Environmental Systems: Version 3.0 User's Manual., Georgia, USA, 1991.

[277] H.M.A. Rossiter, M.C. Graham, A.I. Schäfer, Impact of speciation on behaviuor of uranium in a solar powered membrane system for treatment of brackish groundwater, Separation and Purification Technology, 71 (2010) 90-96.

[278] H. Dach, Comparison of nanofiltration and reverse osmosis processes for selective desalination of brackish water: from laboratory scale to industrial pilot, PhD Thesis, Université d' Angers, 2008.

[279] A. De Munari, D.P.S. Capão, B.S. Richards, A.I. Schäfer, Application of solar-powered desalination in a remote town of South Australia, Desalination, 248 (2009) 72 - 82.

[280] G.L. Park, A.I. Schäfer, B.S. Richards, The effect of intermittent operation on a wind-powered membrane system for brackish water desalination, Water Science & Technology, (2011 (in press)).

[281] H. Nkotagu, The groundwater geochemistry in a semi-arid, fractured crystalline basement area of Dodoma, Tanzania, Journal of African Earth Science, 23 (1996) 593 - 606.

[282] J.Y. Lee, S.H. Moon, M.J. Yi, S.T. Yun, Groundwater contamination with petroleum hydrocarbons, chlorinated solvents and high pH: implications for multiple sources, Quarterly Journal of Engineering Geology and Hydrogeology, 41 (2008) 35 - 47.

[283] L.A. Richards, M. Vuachère, A.I. Schäfer, Impact of pH on the removal of fluoride, nitrate and boron by nanofiltration/reverse osmosis, Desalination, 261 (2010) 331 - 337.

[284] M.H. Oo, L. Song, Effect of pH and ionic strength on boron removal by RO membranes, Desalination, 246 (2009) 605 - 612.

[285] A.E. Yaroshchuk, Negative rejection of ions in pressure-driven membrane processes, Advances in Colloid and Interface Science, 139 (2008) 150 - 173.

[286] M. Vuachère, Reverse Osmosis Solar Installation, Inorganic trace contaminants removal using nanofiltration and reverse osmosis, Internal Report, University of Wollongong and Ecole Superieure D'Ingenieurs de Chambery, 2005.

[287] World Health Organization., Guidelines for Drinking-water Quality: First Addendum to Third Edition, Volume 1: Recommendations, 2006.

[288] G. Jacks, V.P. Sharma, Nitrogen Circulation and Nitrate in Groundwater in an Agricultural Catchment in Southern India, Environmental Geology, 5 (1983) 61-64.

[289] H. Hyung, J.-H. Kim, A mechanistic study on boron rejection by sea water reverse osmosis membranes, Journal of Membrane Science, 286 (2006) 286-278.

[290] H. Corti, R. Crovetto, R. Fernandez-Prini, Mobilities and Ion-Pairing in $LiB(OH)_4$ and $NaB(OH)_4$ Aqueous Solutions. A Conductivity Study, Journal of Solution Chemistry, 9 (1980).

[291] A.V. Plyasunov, E.L. Shock, Estimation of the Krichevskii parameter for aqueous nonelectrolytes, Journal of Supercritical Fluids, 20 (2001) 91-103.

[292] A.F.R. M. Rodríguez Pastor, M.F. Chillón, D. Prats Rico, Influence of pH in the elimination of boron by means of reverse osmosis, Desalination, 140 (2001) 145-152.

[293] A. Sagiv, R. Semiat, Analysis of parameters affecting boron permeation through reverse osmosis membranes, Journal of Membrane Science, 243 (2004) 79-87.

[294] M.H. Oo, S.L. Ong, Implication of zeta potential at different salinities on boron removal by RO membranes, Journal of Membrane Science, 352 (2010) 1-6.

[295] Y. Magara, A. Tabata, M. Kohki, M. Kawasaki, M. Hirose, Development of boron reduction system for sea water desalination, Desalination, 118 (1998) 25-34.

[296] P. Glueckstern, M. Priel, Optimization of boron removal in old and new SWRO systems, Desalination, 156 (2003) 219-228.

[297] M. del Mar de la Fuente García-Soto, E. Munoz-Camacho, Boron removal by means of adsorption with magnesium oxide, Separation and Purification Technology, 48 (2006) 36-44.

[298] W. Humphrey, A. Dalke, K. Schulten, VMD - Visual Molecular Dynamics, Journal of Molecular Graphics, 14 (1996) 33 - 38.

[299] W.L. Jorgensen, J. Chandrasekhar, J.D. Madura, Comparison of simple potential functions for simulating liquid water, Journal of Chemical Physics, 79 (1983) 926 - 935.

[300] R. Allen, J.P. Hansen, S. Melchionna, Molecular dynamics investigation of water permeation through nanopores, Journal of Chemical Physics, 119 (2003) 3905 - 3919.

[301] M.G. Martin, J.I. Siepmann, Transferable potentials for phase equilibria. 1. United-atom description of n-alkanes, Journal of Physical Chemistry B, 102 (1998) 2569 - 2577.

[302] M.D. Afonso, Surface charge on loose nanofiltration membranes, Desalination, 191 (2006) 262 - 272.

[303] L.A. Richards, A.I. Schäfer, B.S. Richards, B. Corry, The importance of dehydration in determining ion transport in narrow pores, Small, (2012 (accepted 01/2012)).

[304] A.I. Schäfer, I. Akanyeti, A.J.C. Semião, Micropollutant sorption to membrane polymers: A review of mechanisms for estrogens, Advances in Colloid and Interface Science, 164 (2011) 100 - 117.

[305] G.M. Torrie, J.P. Valleau, Monte Carlo free energy estimates using non-Boltzmann sampling: Application to the sub-critical Lennard-Jones fluid, Chemical Physics Letters, 28 (1974) 578 - 581.

[306] S. Kumar, J.M. Rosenberg, D. Bouzida, R.H. Swendsen, P.A. Kollman, The weighted hisogram analysis method for free-energy calculations on biomolecules. I. The method, Journal of Computational Chemistry, 13 (1992) 1011 - 1021.

[307] B. Roux, The calculation of the potential of mean force using computer simulations, Computer Physics Communications, 91 (1995) 275 - 282.

[308] B. Efron, R.J. Tibshirani, An introduction to the bootstrap, Chapman & Hall, New York, 1993.

[309] A.D. MacKerrell, D. Bashford, M. Bellott, R.L.D. Jr., J.D. Evanseck, M.J. Field, S. Fischer, J. Gao, H. Guo, S. Ha, D. Joseph-McCarthy, L. Kuchnir, K. Kuczera, F.T.K. Lau, C. Mattos, S. Michnick, T. Ngo, D.T. Nguyen, B. Prodhom, W.E.R. III, B. Roux, M. Schlenkrich, J.C. Smith, R. Stote, J. Straub, M. Watanabe, J. Wiorkiewicz-Kuczera, D. Yin, M. Karplus, All-atom empirical potential for molecular modeling and dynamics studies of proteins, Journal of Physical Chemistry B, 102 (1998) 3586 - 3616.

[310] M.J. Frisch, G.W. Trucks, H.B. Schlegel, G.E. Scuseria, M.A. Robb, J.R. Cheeseman, J. J. A. Montgomery, T. Vreven, K.N. Kudin, J.C. Burant, J.M. Millam, S.S. Iyengar, J. Tomasi, V. Barone, B. Mennucci, M. Cossi, G. Scalmani, N. Rega, G.A. Petersson, H. Nakatsuji, M. Hada, M. Ehara, K. Toyota, R. Fukuda, J. Hasegawa, M. Ishida, T. Nakajima, Y. Honda, O. Kitao, H. Nakai, M. Klene, X. Li, J.E. Knox, H.P. Hratchian, J.B. Cross, V. Bakken, C. Adamo, J. Jaramillo, R. Gomperts, R.E. Stratmann, O. Yazyev, A.J. Austin, R. Cammi, C. Pomelli, J.W. Ochterski, P.Y. Ayala, K. Morokuma, G.A. Voth, P. Salvador, J.J. Dannenberg, V.G. Zakrzewski, S. Dapprich, A.D. Daniels, M.C. Strain, O. Farkas, D.K. Malick, A.D. Rabuck, K. Raghavachari, J.B. Foresman, J.V. Ortiz, Q. Cui, A.G. Baboul, S. Clifford, J. Cioslowski, B.B. Stefanov, G. Liu, A. Liashenko, P. Piskorz, I. Komaromi, R.L. Martin, D.J. Fox, T. Keith, M.A. Al-Laham, C.Y. Peng, A. Nanayakkara, M. Challacombe, P.M.W. Gill, B. Johnson, W. Chen, M.W. Wong, C. Gonzalez, J.A. Pople, Gaussian 03, Revision C.02, G. Inc. (Ed.), Wallingford CT 2004.

[311] B.H. Besler, K.M.M. Jr., P.A. Kollman, Atomic charges derived from semiempirical models, Journal of Computational Chemistry, 11 (1990) 431 - 439.

[312] O. Beckstein, M.S. Sansom, A hydrophobic gate in an ion channel: the closed state of the nicotinic acetylcholine receptor, Physical Biology, 3 (2006) 147 - 159.

[313] R. Malaisamy, A. Talla-Nwafo, K.L. Jones, Polyelectrolyte modification of nanofiltration membrane for selective removal of monovalent anions, Separation and Purification Technology, 77 (2011) 367 - 374.

[314] S.U. Hong, R. Malaisamy, M.L. Bruening, Separation of fluoride from other monovalent anions using multilayer polyelectrolyte nanofiltration membranes, Langmuir, 23 (2007) 1716 - 1722.

[315] A. Pinotti, N. Graiver, A. Califano, N. Zaritzky, Diffusion of nitrite and nitrate salts in pork tissue in the presence of sodium chloride, Food Engineering and Physical Properties, 67 (2006) 2165 - 2171.

[316] G. Bargeman, J.M. Vollenbroek, J. Straatsma, C.G.P.H. Schroën, R.M. Boom, Nanofiltration of multi-component feeds. Interactions between neutral and charged components and their effect on retention, Journal of Membrane Science, 247 (2005) 11-20.

[317] V. Freger, Swelling and Morphology of the Skin Layer of Polyamide Composite Membranes: An Atomic Force Microscopy Study, Environmental Science & Technology, 38 (2004) 3168-3175.

[318] K. Boussu, J.D. Baerdemaeker, C. Dauwe, M. Weber, K. G. Lynn, D. Depla, S. Aldea, I. F. J. Vankelecom, V. Carlo, B. Van Der Bruggen, Physico-Chemical Characterization of Nanofiltration Membranes, ChemPhysChem, 8 (2007) 370-379.

[319] M. Mänttäri, T. Pekuri, M. Nyström, NF270, a new membrane having promising characteristics and being suitable for treatment of dilute effluents from the paper industry, Journal of Membrane Science, 242 (2004) 107-116.

[320] G. Seo, F.E. Massoth, Effect of pressure and temperature on restrictive diffusion of solutes in aluminas, AIChE Journal, 31 (1985) 494 - 496.

[321] J. Cohen, K. Schulten, Mechanism of Anionic Conduction across ClC, Biophysical Journal, 86 (2004) 836 - 845.

[322] S. Bemèche, S. Roux, Energetics of ion conduction through the K^+ channel, Nature, 414 (2001) 73 - 77.

[323] L.A. Richards, A.I. Schäfer, B.S. Richards, B. Corry, Quantifying barriers to anion transport in narrow pores, (2012 (in preparation)).

[324] A.E. Yaroshchuk, V. Ribitsch, The uses of non-steady-state membrane characterisation techniques for the study of transport properties of active layers of nanofiltration membranes: theory with experimental examples, Chemical Engineering Journal, 80 (2000) 203.

[325] G. Jonsson, J. Benavente, Determination of some transport coefficients for the skin and porous layer of a composite membrane, Journal of Membrane Science, 69 (1992) 29 - 42.

[326] N. Hilal, H. Al-Zoubi, N.A. Darwish, A.W. Mohammad, Characterisation of nanofiltration membranes using atomic force microscopy, Desalination, 177 (2005) 187 - 199.